UNIVERSITY OF SOUTHAMPTON

FACULTY OF SCIENCE
School of Ocean & Earth Science

A GLOBAL STUDY OF DIURNAL WARMING

Alice Clare Stuart-Menteth

Thesis submitted for the degree of Doctor of Philosophy

April 2004

Graduate School of the Southampton Oceanography Centre

This PhD dissertation by

Alice Clare Stuart-Menteth

has been produced under the supervision of the following persons

Supervisor/s
Professor Ian Robinson

Mr Peter Challenor

Chair of Advisory Panel
Professor Jochem Marotzke

Member/s of Advisory Panel
Dr Tim Henstock

UNIVERSITY OF SOUTHAMPTON

ABSTRACT

FACULTY OF ENGINEERING, SCIENCE & MATHEMATICS,
SCHOOL OF OCEAN & EARTH SCIENCES

Doctor of Philosophy

A GLOBAL STUDY OF DIURNAL WARMING

Alice Clare Stuart-Menteth

The diurnal cycle is a fundamental mode of the climate system associated with solar forcing. Sea surface temperature (SST) is directly affected by the diurnal cycle of the sun's radiation. In clear sky, low wind conditions, strong surface heating creates a stratified stable warm layer in the top few meters of the water column, associated with a rise in SST. The development of a warm surface layer during the day is known as diurnal warming. The presence of the warm layer can complicate the interpretation and application of SST measurements. SST is one of the most important variables influencing short and long term ocean and climate dynamics and is frequently used in ocean and climate research.

This thesis presents a detailed study of the diurnal variability of SST using a variety of data sources from satellites, moored buoys and a 1-D mixed layer model. 10 years of daily day- and night-time satellite data are analysed to provide the first global long-term assessment of diurnal warming patterns. In situ buoy and model data are used to investigate the variability of diurnal warming. A 1-D mixed layer numerical model is used to investigate the sensitivity of the evolution of the diurnal warm layer to the presence of chlorophyll. Under low wind conditions, the distribution of solar energy is largely determined by the optical properties of the water column. Chlorophyll has little impact on the heating within the top few centimetres of the ocean, but below 0.5m, the presence of chlorophyll increases the diurnal heating rate and consequently temperature.

High resolution buoy data are analysed to investigate the sensitivity of the evolution of the diurnal warm layer to fluctuations in the meteorological conditions. Over three hundred individual diurnal cycles of SST, insolation and wind speed are analysed. The results reveal that the evolution of the warm layer is strongly dependent on the time variability of the forcing fields. The shallower the warm layer, the greater its sensitivity to meteorological fluctuations. Under low winds, large differences in SST can occur between the surface and 1m. Based on these results, a new parameterisation is developed to estimate the diurnal variation of SST at the surface and at 1m, taking into consideration the time variability of the forcing fields. The parameterisation has been carefully validated using independent data, showing good agreement and is an improvement over existing parameterisations. The potential implications for this parameterisation and the rest of the results are discussed in detail. The importance of diurnal warming is becoming more broadly recognised in the scientific community and the work presented in this thesis contributes to advances in this field.

For Mum and Dad

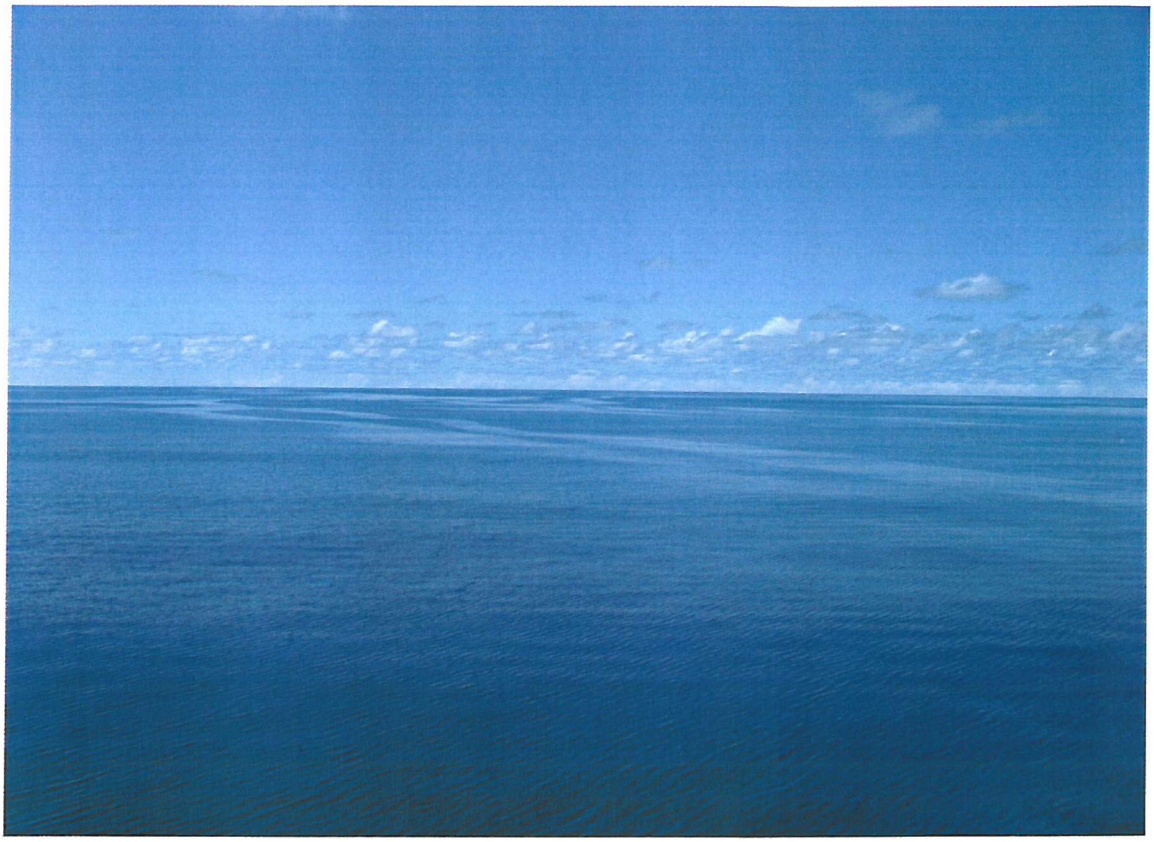

And Grandpit - I may not know much about history, poetry or literature but this proves I do know something!

TABLE OF CONTENTS

List of Figures v

List of Tables xi

Declaration of authorship xiii

Acknowledgements xiv

List of Acronyms xv

CHAPTER 1: Introduction 1

1.1 The climate system..... 1

1.2 Importance of SST..... 2

1.3 Diurnal cycle of SST..... 2

1.3.1 Observations of diurnal warming..... 4

1.3.2 Theoretical studies of diurnal warming..... 6

1.3.3 Implications of diurnal warming..... 7

1.4 Thesis Aim..... 9

CHAPTER 2: Sea Surface Temperature (SST) 12

2.1 Common definition of SST..... 12

2.2 Methods for measuring SST..... 13

2.2.1 Ships..... 13

2.2.2 Buoys..... 15

2.2.3 Satellites..... 15

2.3 GHRSST-PP..... 19

2.4 New Definition of SST..... 21

2.5 Summary..... 22

CHAPTER 3: Global spatial & temporal distribution of diurnal warming events 23

3.1 Background..... 23

3.2 Data..... 24

3.2.1 AVHRR Data..... 24

3.2.2 Ancillary data..... 26

3.3 Method..... 26

3.3.1 Satellite-derived diurnal SST variations..... 26

3.3.2 Dealing with ΔT contamination..... 27

3.3.2.1 Clouds..... 27

3.3.2.2 Advection..... 28

3.3.3 Methodology Limitations..... 29

3.3.4 Model estimated diurnal SST variations..... 31

3.4 Results ... 32
3.4.1 Daily ΔT maps ... 32
3.4.2 Seasonal distribution of diurnal warming events ... 32
3.4.3 Model Comparison ... 37
3.4.4 Interannual distribution of diurnal warming events ... 38
3.4.5 A Climatological view of diurnal warming ... 47
3.5 Implications ... 48
3.6 Summary ... 50

CHAPTER 4: Influence of chlorophyll on diurnal stratification **52**
4.1 Background ... 52
4.1.1 Review of solar irradiance parameterisations ... 54
4.1.2 Review of relevant literature ... 58
4.1.3 Research Aims ... 60
4.2 Data ... 60
4.3 Method ... 63
4.3.1 PWP model ... 64
4.3.2 Model Runs ... 67
4.3.2.1 Optical model intercomparison runs ... 67
4.3.2.2 Main model runs ... 68
4.4 Results ... 69
4.4.1 Observations ... 69
4.4.2 PWP model simulations ... 72
4.4.2.1 Parameterisation inter-comparison ... 72
4.4.2.2 Impact of chlorophyll on diurnal warming ... 78
4.5 Implications ... 83
4.6 Summary ... 85

CHAPTER 5: Sensitivity of the diurnal SST cycle to meteorological variability **87**
5.1 Background ... 87
5.2 Data ... 88
5.3 Method ... 90
5.3.1 Estimating the diurnal cycle at the sea surface ... 91
5.3.2 Fairall et al. (1996) warm layer and cool skin models ... 91
5.3.2.1 Cool skin correction ... 91
5.3.2.2 Warm layer correction ... 92
5.3.3 Data filtering ... 96
5.3.4 Data Analysis ... 98

5.4 Results 99
5.4.1 Differences between diurnal signal at surface and at 1m 99
5.4.2 Sensitivity of the diurnal cycle to wind and insolation variability 101
5.4.2.1 Diurnal shape classification 104
5.5 Implications 108
5.6 Summary 109

CHAPTER 6: A new parameterisation for diurnal warming **110**
6.1 Background 110
6.1.1 Summary of existing diurnal warming parameterisations 110
6.1.2 A new parameterisation 114
6.2 Data 115
6.2.1 1m validation dataset 116
6.2.2 Sub-skin validation dataset 117
6.3 Description of the parameterisation 118
6.4 Derivation of the diurnal warming parameter models 123
6.4.1 Regression dataset 123
6.4.2 Derivation of models and coefficients 123
6.5 Results 129
6.5.1 Comparison against regression dataset 129
6.5.2 Parameterisation intercomparison 131
6.5.3 Validating the parameterisation 134
6.5.3.1 1m parameterisation validation 135
6.5.3.2 Sub-skin parameterisation validation 140
6.6 Potential applications of parameterisation 144
6.7 Limitations of parameterisation 147
6.8 Summary 149

CHAPTER 7: Discussion **150**

CHAPTER 8: Conclusions and Future Work **156**

APPENDIX A: 10 years of monthly mean diurnal warming maps. **161**
APPENDIX B: Monthly climatological diurnal warming maps. **185**
APPENDIX C: Monthly climatological diurnal warming and chlorophyll maps. **187**
APPENDIX D: Matlab code & flow diagram for diurnal warming parameterisation **189**

REFERENCE LIST **195**

LIST OF FIGURES

1.1: Schematic of the evolution of the diurnal warm layer over time in the absence of wind mixing. The colours represent water temperatures in the top 5m of the water column, with temperature increasing from blue to red. The thick black curved arrows represent convective overturning which occurs when the net heat flux is out of the ocean. The warm layer does not fully break down until after midnight..... 4

2.1: Schematic of temperature profile of top 5m of the water column. (a) Well mixed/night-time conditions, (b) diurnal warming conditions..... 13

2.2: Schematic of sampling depth of routine SST instruments over a typical vertical temperature profile during diurnal warming conditions..... 19

2.3: Schematic of temperature profile in top 5m of the water column. The GHRSST-PP definitions of SST are indicated for (a) well-mixed/night-time conditions and (b) diurnal warming conditions..... 22

3.1: Examples of daily ΔT (°C) files for the Arabian Sea during the spring inter-monsoon..... 33

3.2: Seasonal distribution of diurnal warming for 1989. a) Monthly mean ΔT & b) number of occurrences (days) when $\Delta T \geq 0.5$°C (computed from daily day-night SST differences), for January, April, July and October (top to bottom). (See Appendix A for all months and years.)..... 35

3.3: Seasonal cycle of diurnal warming in the Arabian Sea. Monthly mean & maximum ΔT are averaged over a 0.5°x0.5° box in the Arabian Sea to coincide with mooring data at 15.5°N, 61.5°E. Monthly mean in situ ΔT are computed for the local overpass times of the satellite. The continuous line represents the monthly mean ΔT and the dashed line, the monthly maximum ΔT. Black: PFSST and grey: in situ buoy.. 37

3.4: Monthly mean ΔT (°C) for July 1993. a) regression model simulation, b) observed Pathfinder mean..... 38

3.5: Interannual distribution of diurnal warming. Number of occurrences (days)/month when $\Delta T \geq 0.5$°C for July..... 40

3.6: Interannual distribution of diurnal warming. Number of occurrences (days)/month when $\Delta T \geq 0.5$°C for January..... 41

3.7: Interannual distribution of monthly mean ΔT. Monthly mean ΔT (°C) for January..... 42

3.8: The local afternoon overpass time of the AVHRR-NOAA satellite series used in the Pathfinder SST, 1987-1999. Vertical lines mark the transition to a new sensor. * At the end of NOAA-11, there was a gap in the data which was filled by NOAA-9. This was later replaced by NOAA-14 when it became available on 18th January 1995. The dotted horizontal lines mark out 14:30, 15:30 and 16:30 local time..... 43

3.9: Zonally averaged percentage of ΔT for January for the same six years as Figures 4 & 5. The grey lines represent group A years (1989, 1990, 1996-1998), black lines group B years (1987, 1988 & 1993), the black dotted line January 1994 and the grey dotted line represents the NOAA-9 gap during January 1995. The percentage represents the fraction of time, out of the total number of monthly day-night match-

ups, when $\Delta T \geq 0.5°C$..... 44

3.10: SSMI monthly mean wind anomaly fields (m/s) computed from a nine year mean (1988-1998) for January. The satellite was launched in late 1987 so there is no data available for 1987. The black dashed line marks 30°S..... 46

3.11: Interannual distribution of diurnal warming in eastern equatorial Pacific. Number of occurrences (days)/month when $\Delta T \geq 0.5°C$ for April..... 47

3.12: Seasonal climatological mean fields, made up of six years of group A data, for January, April, July and October. (a) Climatological mean ΔT & (b) frequency maps when $\Delta T \geq 0.5°C$... (See Appendix B for all 12 months.)..... 49

4.1: Schematic of influence of chlorophyll pigments on the transmission of solar irradiance through the water column..... 54

4.2: Location of WHOI Arabian Sea Mooring..... 62

4.3:Time series of (a) SST (0.17m), (b) wind speed, (c) downwelling shortwave radiation and (d) chlorophyll concentration. x represent chlorophyll measurements obtained from US JGOFS cruises. The vertical lines mark the two six day periods used in this study..... 63

4.4: Percentage of cumulative irradiance absorbed over depth as a function of chlorophyll concentration ($[I_o - I_z]/I_o$). Irradiance profiles were modelled by the OS00 parameterisation..... 68

4.5: Time series of (i) temperature, (ii) wind speed and (iii) downwelling shortwave radiation for the (a) NEB period and (b) SIM period. The temperature plots show temperature at 0.17m (red), 1m (orange), 1.8m (yellow), 2.5m (green), 3.5m (light blue), 4.5m (royal blue), 5m (navy)..... 69

4.6: Thermal structure of upper 5m of the water column as measured by the WHOI mooring for (a) NEB period and (b) SIM period. Both panels have the same temperature range (1.5°C)..... 70

4.7: Schematic of absorption of heat in the diurnal mixed layer for (i) low chlorophyll and (ii) high chlorophyll conditions for low wind clear sky conditions. (In the presence of chlorophyll, the surface water becomes warmer and reduces the temperature contrast across the diurnal thermocline.)..... 71

4.8a: Total irradiance absorbed (%) as a function of depth (to 5m) for four popular parameterisations. i) low chlorophyll (0.05 mg/m^3 / water type I), ii) moderate chlorophyll (1 mg/m^3 / water type II) and iii) high chlorophyll conditions ($3mg/m^3$ / water type III). Black: Ohlmann et al (2000), dark grey: 9-band Paulson & Simpson (1981), light grey: 3-band Soloviev (1982), dotted line: 2-band Paulson & Simpson (1977)..... 72

4.8b: Same as Figure 4.8a except for top 1m of the water column..... 73

4.9: Taken from Ohlmann & Siegel (2000) Figure 7. Ensemble-average rms error (rmse) profiled for the two-equation model Ohlmann & Siegel (2000) (solid line), the Morel & Antoine (1994: dotted line), the Soloviev (1982: dashed line), and the Paulson & Simpson (1981: dash-dot line) solar transmission parameterisations. The lower x-axis represents the rmse in the transmission and the upper x-axis represents the absolute solar flux (based on climatological surface irradiance of $200Wm^{-2}$)..... 74

4.10: Thermal structure of top 5m during NEB (moderate chlorophyll) period. (a) observations, (b) PWP OS00 and (c) PWP PS77..... 75

4.11: Thermal structure of top 5m during SIM (low chlorophyll) period. (a) observations, (b) PWP OS00 and (c) PWP PS77..... 76

4.12a: Thermal structure of the top 5m of the water column for 8th February. Solar transmission inter-comparison: (i) Observations, (ii) PWP OS00, (iii) PWP PS81, (iv) PWP S82 and (v) PWP PS77..... 77

4.12b: Thermal structure of the top 5m of the water column for 1st May. Solar transmission inter-comparison: (i) Observations, (ii) PWP OS00, (iii) PWP PS81, (iv) PWP S82 and (v) PWP PS77..... 78

4.13: PWP OS00 temperature simulations for (a) a low wind day – 8th February & (b) a moderate wind day – 11th February. (i) 0.25m, (ii) Im & (iii) 3m. The different colours represent different chlorophyll concentrations used in the parameterisation (light grey: 5mg/m^3, grey: 2 mg/m^3, dark grey: 1 mg/m^3, black: 0.1 mg/m^3)..... 79

4.14: PWP OS00 temperature simulations for top 5m of the water column for different chlorophyll concentrations (i) 0.1mg/m^3, (ii) Img/m^3, (iii) 2mg/m^3 and (iv) 5mg/m^3. (a) Low wind day (8th February) & (b) Moderate wind day (11th February)..... 80

4.15: Change in fraction of energy absorbed across depth interval of 0.01m as a function of increasing chlorophyll concentration (referenced from $[chl]$=0), $R_{0.01m}$, for depth intervals down to 1m..... 81

4.16: Change in fraction of energy absorbed across depth interval of 0.01m as a function of increasing chlorophyll concentration (referenced from $[chl]$=0), $R_{0.01m}$, for depth intervals down to Im. (a) OS00, (b) PS81..... 82

4.17: Time series of mixed layer depth from PWP model runs, using OS00 parameterisation, for NEB. Model is run for a range of different chlorophyll concentrations from 0.01 mg/m^3 to 5mg/m^3..... 84

4.18: Monthly climatological $\Delta T_{(day\text{-}night)}$ from Stuart-Menteth et al. (2003) and climatological SeaWiFS chlorophyll maps. Red rings highlight regions of coincident high chlorophyll and frequent diurnal warming. In the diurnal warming frequency maps, colour is only given to frequency values greater than 2 days. (See Appendix C for all 12 months)..... 85

5.1: Location of the WHOI IMET buoys..... 89

5.2: Observed temperature profiles from Arabian Sea mooring and surface temperature values (sub-skin) determined from F96 warm layer model applied to different depths. Black dot: observed $SST_{0.17m}$, light grey *: F96 sub-skin (z=5m), grey triangle: F96 sub-skin (z=2m), dark grey x: F96 sub-skin (z=1m), circle: F96 sub-skin (z=0.17m)..... 95

5.3: Comparison of daily maximum diurnal sub-skin temperature variation, ΔT_{max}, derived from the F96 warm layer model. X-axis shows sub-skin ΔT_{max} derived from F96 using S82 solar transmission parameterisation and depth of measurement z=0.17m. Y-axis shows sub-skin ΔT_{max} derived using (grey x) OS00 parameterisation and z=0.17m and (black *) S82 parameterisation and z=1m..... 96

5.4: (a) Example of diurnal temperature cycle under low wind conditions (u<3 m/s). Light grey: 0.17m, dark grey: 0.5m and black: 1m. (b) Difference between 0.5m and 1m temperatures..... 97

5.5: Time series of 0.17m temperature from the Arabian Sea mooring. Non-local effects are identified in the first five days (marked with X) and consequently these days are removed from the analysis..... 98

5.6: Time series of IMET SST data used in sensitivity study after data filtering (edit in Illustrator). a) Arabian Sea - 1m, b) Equatorial Pacific Western Warm Pool (Coare) – 1m & c) Sargasso Sea (LOTUS) – 0.6m..... 99

5.7: Comparison of diurnal warming variables at the sub-skin (x) and 1m (y). (a) shows the daily maximum ΔT and (b) shows the time of daily maximum SST, t_{max}. Black star: wind speed <3m/s, dark grey triangle: wind speed 3-6 m/s and light grey circle: wind speed >6m/s..... 100

5.8: Observed skin and F96-derived sub-skin SST. Black line: observed skin from R/V Franklin, grey line: F96-derived sub-skin from IMET..... 100

5.9: Two examples of the sensitivity of the diurnal mixed layer to wind fluctuations. Top panel shows temperature at 1m intervals ranging from sub-skin to 4.5m, second row shows wind speed and bottom panel presents the downward shortwave radiation... 102

5.10: An example of a diurnal cycle of temperature (upper panel) and associated wind variability (lower panel) from the TOGA COARE mooring. The warm layer breaks down instantaneously as the wind suddenly increases..... 103

5.11: An example of a diurnal temperature cycle (top panel) from the Arabian Sea mooring. Grey represents the sub-skin and black the 1m temperature. The middle and lower panels show the wind and insolation variability over the same period..... 103

5.12: Observations of classified diurnal shapes from IMET buoy data set for 1m (black) and sub-skin (grey)..... 104

5.13: Frequency of classified diurnal SST shapes observed in IMET dataset..... 108

6.1: Location of buoys used in validation data set. X – TAO/TRITON buoys, + PIRATA buoys, Δ IMET buoys, * Mutsu Bay buoy and the boxes highlight the two cruise regions..... 118

6.2: Schematic of the diurnal SST cycle parameterisation. The day is divided into four parts and six models define the shape of the four curves: *cgrad*, t_{min}, $\Delta T_{12\text{-}tmin}$, t_{max}, $\Delta T_{tmax\text{-}12}$, $\Delta T_{24\text{-}tmin}$. The predicted diurnal warm layer temperature deviation, ΔT, is referenced from the daily minimum SST where $\Delta T_{tmin} = 0$..... 120

6.3: Example of the diurnal cycle parameterisation for 1m (black) and sub-skin (grey) during low wind conditions. In the second plot, wind speed has increased at mid-day after low winds in the morning and the surface water gets mixed down resulting in a sudden drop in sub-skin SST. A different curve is applied to the afternoon time period to represent this..... 123

6.4: a) ΔT_{max} against morning mean wind speed, $U_{8\text{-}12h}$, for different ranges of mean morning insolation values, $Q_{6\text{-}12}$. b) ΔT_{max} against morning mean insolation, $Q_{6\text{-}12}$, for different ranges of mean morning wind, $U_{8\text{-}12h}$. Grey represents sub-skin values and black are 1m values..... 124

6.5a: $\Delta T_{(12\text{-}tmin)}$ against morning wind speed, $U_{8\text{-}12h}$, for $Q_{6\text{-}12h}$ greater than 600Wm^{-2} (grey) and for $Q_{6\text{-}12h}$ between 350 and 450Wm^{-2} (black). The dots represent 1m $\Delta T_{(12\text{-}tmin)}$ and the crosses represent the sub-skin values. The lines are the model predictions for $Q_{6\text{-}12h}$ 650Wm^{-2} (grey) and 400Wm^{-2} (black)..... 125

6.5b: $\Delta T_{(tmax\text{-}12)}$ against afternoon wind speed, $U_{12\text{-}15h}$, for $Q_{12\text{-}18h}$ greater than 600Wm^{-2} (grey) and for $Q_{6\text{-}12h}$ between 350 and 450Wm^{-2} (black). The dots represent 1m $\Delta T_{(12\text{-}tmin)}$ and the crosses represent the sub-skin values..... 126

6.6: Model variables against wind and insolation values. All are derived from the regression dataset. a) Cooling gradient, *cgrad*, against $U_{0\text{-}6h}$. b) Time of daily minimum SST, t_{min}, against (i) $U_{8\text{-}12h}$ and (ii) $Q_{6\text{-}12h}$. c) Morning diurnal heating amplitude, $\Delta T_{(12\text{-}tmin)}$, against (i) $U_{8\text{-}12h}$ and (ii) $Q_{6\text{-}12h}$. d) Time of daily maximum SST, t_{max}, against (i) $U_{8\text{-}12h}$, (ii) $Q_{6\text{-}12h}$, (iii) $U_{12\text{-}15h}$ and (iv) $Q_{12\text{-}18h}$. e) Afternoon diurnal heating amplitude, $\Delta T_{(tmax\text{-}12h)}$, against (i) $U_{12\text{-}15h}$ and (ii) $Q_{12\text{-}18h}$. f) Residual stratification at midnight, $\Delta T_{(24h\text{-}tmin)}$, against (i) $U_{16\text{-}24h}$ and (ii) ΔT_{max}..... 127

6.7: Diurnal warming variables derived from regression dataset against the modelled parameter values for (a) 1m, (b) sub-skin. (i) $\Delta T_{(12\text{-}tmin)}$, (ii) $\Delta T_{(tmax\text{-}12)}$, (iii) t_{max}..... 130

6.8: Example of the parameterisation (ΔT = diurnal variation from daily minimum SST). Bold lines represent the parameterisation and thin lines represent observations. Grey lines represent sub-skin and black lines represent 1m..... 131

6.9: Example of the ΔT parameterisation intercomparison results using the Arabian Sea IMET data. Black line: observed 1m ΔT, green line: SM (new) ΔT, blue line: G04 ΔT, pink dotted: KK02 ΔT_{max} and orange dotted line: KK03 ΔT_{max}..... 132

6.10a: KK02, KK03 and G04 ΔT_{max} over a range of daily mean wind speeds. The parameterisations were run with same values for Q_{sw_max}, Q_{sw} and Q_{lat}. Q_{sw_max} = 1100Wm^{-2}, Q_{sw} = 350Wm^{-2} and Q_{lat} = -100Wm^{-2}..... 133

6.10b: Same as Figure 6.10a using the corrected low wind coefficients for KK03..... 133

6.11: Comparison of model ΔT_{max} for Toga Coare and Arabian Sea IMET datasets. Negative KK03 ΔT_{max} values have been set to zero. Green *: SM (new), blue Δ: G04, pink x: KK02 and orange o: KK03..... 134

6.12a: Validation of 1m diurnal variation parameterisation from MLML91 data (33W, 60N). Nine consecutive days are shown where non-local affects did not dominate the diurnal cycle. Black line: observed 1m SST, light grey line: new Stuart-Menteth (SM) parameterisation, dark grey line: Gentemann G04 1m parameterisation and dark grey dotted line: KK02 1m ΔT_{max}..... 136

6.12b: Same as Figure 6.12a, except validation data for 20 days from Subduction IMET buoy (22W, 33N). Twenty consecutive days are shown here..... 136

6.12c: Same as Figure 6.12a, except validation data for 20 days from TAO/TRITON buoy at 140W, 0N. Twenty consecutive days are shown here..... 137

6.12d: Same as Figure 6.12a, except validation data for 20 days from TAO/TRITON buoy at 95W, 5S. Twenty consecutive days are shown here..... 137

6.12e: Same as Figure 6.12a, except validation data for 20 days from PIRATA buoy at 10W, 10S. Twenty consecutive days are shown here..... 138

6.13: Scatter plots of observed 1m ΔT_{max} against modelled ΔT_{max} for new (SM) parameterisation (green), KK02 (pink) and G04 (blue) for a range of different oceanic regions. The first buoy (0N, 140W) is located east of the cold tongue along the central Pacific equator. The second buoy (10S, 10W) is located in the tropical East Atlantic and the third buoy (5S, 95W) is in the equatorial Pacific cold tongue..... 140

6.14a: Validation of sub-skin diurnal variation parameterisation using the RV Franklin data. Black line: observed skin SST, green line: new Stuart-Menteth (SM) parameterisation, blue line: Gentemann G04 TMI parameterisation, pink dotted line: KK02 skin ΔT_{max} and the orange dotted line: W96 ΔT_{max}..... 141

6.14b: Same as Figure 6.14a except using the RRS Charles Darwin skin data..... 142

6.14c: Same as Figure 6.14a except using the Mutsu Bay 0.02m data..... 143

6.15: a) Model validation for 4th day of RRS Charles Darwin (Figure 6.14b) and the associated time series of b) wind speed and c) downward shortwave radiation (Wm^{-2}).. 143

6.16: Scatter plots of observed sub-skin ΔT_{max} against modelled ΔT_{max} for new (SM) parameterisation (green *), KK02 (pink x), W96 (red +) and G04 (blue Δ) for a range of different oceanic regions..... 144

A.1-12: Monthly mean ΔT for 12 months (January to December), computed from daily AVHRR SST data (Chapter 3)..... 161

A.13-24: Number of occurrences (days)/month when $\Delta T \geq 0.5$°C for 12 months (January to December), computed from daily AVHRR SST data (Chapter 3)..... 173

B.1: Climatological ΔT maps from 6 years of AVHRR Pathfinder data..... 185

B.2: Climatological diurnal warming frequency maps from 6 years of AVHRR Pathfinder data. Frequency = no. days / month $\Delta T \geq 0.5$°C..... 186

C: Monthly climatological $\Delta T_{(day\text{-}night)}$ from Stuart-Menteth et al. (2003) and climatological SeaWiFS chlorophyll maps..... 187

D: Flow diagram of diurnal warming parameterisation..... 189

LIST OF TABLES

1.1: Summary of diurnal warming field studies reported in the literature. Maximum ΔT values are listed when available. In some cases the magnitudes are approximate..... 5

2.1: List of main SST-Measuring Platforms..... 15

2.2: Current SST-Measuring Satellites. IR: InfraRed, PM: Passive Microwave. (See list of Acronyms for full sensor and satellite names.)..... 18

3.1: Coefficients for determination of ΔT_{max} from [3.3]..... 32

4.1: Coefficients for Paulson & Simpson (1977) bi-modal downward irradiance parameterisation..... 56

4.2a: Coefficients for Paulson & Simpson (1981) 9-band downward irradiance parameterisation..... 57

4.2b: Coefficients for 1st band of Paulson & Simpson (1981) 9-band downward irradiance parameterisation, for different water types (Soloviev & Schluessel, 1986)..... 57

4.3a: Coefficients for Soloviev (1982) 3-band downward irradiance parameterisation..... 57

4.3b: Coefficients for 1st band of Soloviev (1982) 3-band downward irradiance parameterisation, for different water types..... 57

4.4: Linear regression coefficients for determination of the eight model parameters used in the clear sky solar transmission parameterisation (from Ohlmann & Siegel, 2000)..... 66

4.5: Approximate correspondence between Jerlov's Water Type classification and chlorophyll concentrations (from Morel (1988))..... 68

5.1: Details of buoy data sets..... 90

5.2: List of diurnal warming variables derived from the buoy dataset used in this chapter. 99

5.3: Differences between sub-skin and 1m ΔT_{max} and $Time_{SSTmax}$ (sub-skin – 1m)..... 100

5.4: Wind speed thresholds used to categorise diurnal warming shapes into groups described in Section 5.4.2.1..... 108

6.1: Coefficients for determination of ΔT_{max} from [6.1]..... 111

6.2: Coefficients for determination of ΔT_{max} from [6.2]..... 112

6.3: Coefficients for determination of ΔT_{max} from [6.3]..... 113

6.4: Details of data used in the validation dataset..... 117

6.5: List of diurnal warming variables & parameters derived from the buoy dataset..... 121

6.6: Coefficients for the regression models described in Table 6.7. Coefficients in grey represent the different coefficients that are applied to the 1m diurnal models under certain low wind conditions..... 129

6.7: Statistics of derived models against IMET buoy data. Bias = observation – model. Black: 1m model, grey: sub-skin model..... 130

6.8: Statistics from ΔT_{max} intercomparison using Arabian Sea and Toga Coare IMET data..... 134

6.9: Statistics of parameterisation validation and inter-comparison against independent buoy data sets. Bias = observed – model. Units for bias, standard deviation and rmse are °C..... 139

6.10: Statistics from sub-skin ΔT_{max} intercomparison. Units for bias, standard deviation and rmse are °C..... 143

6.11: Bias and standard deviation of satellite-measured SST and the foundation temperature with & without the sub-skin model diurnal variations (DV) corrections. SST(t): satellite SST at overpass time (t), SST_{min}: daily SST minimum, SST_c: corrected SST (SST-DV), SST_{cu}: corrected SST with point wind measurement at time (t) used for $U_{8\text{-}12h}$ & $U_{12\text{-}15h}$ instead of a mean value. (Number of data points used, n=270.)..... 147

DECLARATION OF AUTHORSHIP

I, *Alice Stuart-Menteth*, declare that the thesis entitled

A Global Study of Diurnal Warming

and the work presented in it are my own. I confirm that:

- this work was done wholly or mainly while in candidature for a research degree at the University;
- where any part of this thesis has previously been submitted for a degree or any other qualification at this University or any other institution, this has been clearly stated;
- where I have consulted the published work of others, this is always clearly attributed;
- where I have quoted from the work of others, the source is always given. With the exception of such quotations, this thesis is entirely my own work;
- I have acknowledged all main sources of help;
- where the thesis is based on work done by myself or jointly with others, I have made clear exactly what was done and what I have contributed myself;
- Parts of this work have been published as:

  Stuart-Menteth, A. C., I. S. Robinson & P. G. Challenor, A Global study of diurnal warming using satellite-derived sea surface temperature, J, Geophys. Res., 108, doi:10.1029/2002JC001534, 2003.

  Gentemann, C. L., C. J. Donlon, A. C. Stuart-Menteth & F. J. Wentz, Diurnal signals in satellite sea surface temperature measurements, Geophys. Res. Letters, 30, doi:10.1029/2002GL016291, 2003.

Signed: ...[redacted].....

Date: .....30/6/2004.....

ACKNOWLEDGEMENTS

I would like to thank the following people who have made this work possible:

My supervisors Professor Ian Robinson and Peter Challenor for their support and advice. Thank you Ian for your enthusiasm and confidence in my abilities and for encouraging me to pursue opportunities that came my way.

Simon Josey for his great support, advice and friendship throughout my Ph.D. and for his helpful and thoughtful comments when reading my thesis.

Craig Donlon for his enthusiasm and for allowing me to be part of the GHRSST-PP project.

Bob Weller, Chelle Gentemann, Peter Minnett, Gary Wick, Ken Casey, Ed Armstrong, Ian Barton, Nick Rayner, Mark Pritchard, Brian Ward, Yoshimi Kawai and the GHRSST-PP Science Team for their encouragement and support.

To those who provided data for my research: PODAAC Pathfinder Team, WHOI UOP Group, Chelle Gentemann, John Marra, Chris Kinkade and Yoshimi Kawai.

Lisa Redbourn-Marsh for downloading and storing the Pathfinder SST data and Helen Snaith for helping me with data management issues.

Graham Quartly, Andrew Shaw, Paolo Cipollini, Dave Woolf and Andrew Coward for always being on-hand to answer my endless Matlab, Adobe Illustrator, Fortran questions etc.

George Nurser & Bob Weller for their helpful discussions and for reading some of my thesis chapters.

Robin Pascal and Adrian New for giving me a place on the CD135 Indian Ocean Cruise - my greatest life-time experience to date.

Nico Caltabiano for his support during my Ph.D., especially at the beginning when he gave me a lot of help and advice and introduced me to the world of satellite SST.

James Harle for always being there to answer my questions and discuss science and life!

My regular lunch mates: Phil, Ago and Zoë and my office mates: Nico, Isobel, Martin, Ana-Paula and Dohyung.

Zoë Howard-Bond for being a great best friend. It's a shame our oceanography paths have to separate now after eight years but our friendship won't.

My family for always supporting me and encouraging me to aim high.

Barclay for relaxing me at weekends and always believing in me.

LIST OF ACRONYMS

AATSR	Advanced Along Track Scanning Radiometer
ADEOS-II	ADvanced Earth Observing Satellite - II
AMSR	Advanced Microwave Scanning Radiometer
ATLAS	Autonomous Temperature Line Aquistion System
ATSR	Along Track Scanning Radiometer
AVHRR	Advance Very High Resolution Radiometer
COADS	Comprehensive Ocean-Atmosphere Data Set
COARE	Coupled Ocean Atmosphere Response Experiment
CSIRO	Commonwealth Scientific and Industrial Research Organisation
DML	Diurnal Mixed Layer
ENSO	El Nino Southern Oscillation
ENVISAT	ENVIronment SATellite
ERS	European Remote Sensing satellite
GCM	General Circulation Model
GHRSST-PP	GODAE High Resolution Sea Surface Temperature – Pilot Project
GODAE	Global Ocean Data Assimilation Experiment
GOES	Geostationary Operational Environmental Satellite
IMET	Improved METeorological
IR	Infrared
JGOFS	Joint Global Ocean Flux Study
KPP	K-Profile Parameterisation
LOTUS	LOng Term Upper ocean Study
LST	Local Solar Time
MJO	Madden-Julian Oscillation
MODIS	MODerate resolution Imaging Spectroradiometer
MVMS	Multi Variable Moored System
NBDC	National Buoy Data Centre
NEB	North East Bloom
NOAA	National Oceanic & Atmospheric Administration
NPOESS	National Polar Orbiting Environmental Satellite System
NWP	Numerical Weather Prediction
PALACE	Profiling Autonomous Lagrangian Circulation Explorer
PFSST	Pathfinder Sea Surface Temperature
PIRATA	Pilot Research Moored Array in the Tropical Atlantic
PM	Passive Microwave
PWP	Price, Weller & Pinkel (1986)

R/V	Research Vessel
RAL	Rutherford Appleton Laboratory
RRS	Royal Research Ship
SeaWiFS	SEA viewing Wide Field of view Sensor
SIM	Spring Inter Monsoon
SISTeR	Scanning Infrared Sea surface Temperature Radiometer
SkinDeEP	Skin Depth Experimental Profiler
SOC	Southampton Oceanography Centre
SSMI	Special Sensor Microwave Imager
SST	Sea Surface Temperature
TAO	Tropical Ocean Atmosphere
TMI	Tropical rainfall measuring mission Microwave Imager
TOGA	Tropical Ocean Global Atmosphere
TRITON	TRIangle Trans Ocean Buoy Network
TRMM	Tropical Rainfall Measuring Mission
UOP	Upper Ocean Processes
WHOI	Woods Hole Oceanographic Institution
WPWP	Western Pacific Warm Pool

CHAPTER 1: INTRODUCTION

1.1 THE CLIMATE SYSTEM

The Earth's climate system is driven by the sun's radiation. Approximately two thirds of incoming short-wave radiation is absorbed by the Earth, which is balanced by out-going long-wave infrared radiation. The planet is heated unevenly with excess heating at the equator relative to the poles creating a meridional temperature gradient which drives the motion in both the atmosphere and ocean. The dynamic processes that transfer heat to the poles have long term mean and fluctuating components which shape our climate.

The ocean plays an intimate role in the dynamics of the climate due to its large heat capacity. The upper ocean mixed layer stores thirty times more heat than the entire atmosphere (Henderson-Sellers & Robinson, 1983). The ocean stores and redistributes heat, forcing atmospheric convection and winds. It also absorbs and releases gases (e.g. dimethylsulphide, carbon dioxide (CO_2) and other greenhouse gases), enhancing its importance in the climate system. Phytoplankton absorb CO_2 making the ocean a huge sink for this greenhouse gas and the biological control is believed to be damping the Greenhouse Effect and reducing the rate of 'global warming'.

Over the last couple of decades, climate research has been in the spotlight with the phenomenon of 'global warming'. Air and sea temperature records show that temperatures have been rising quite dramatically over the last few decades (e.g. Jones et al., 1986; Houghton et al., 2001; Luterbacher et al., 2004). The cause of this trend has yet to be agreed, with some climate scientists believing it is purely a result of anthropogenic forcing while others state it is part of the climate system's natural variability. The climate has its own natural variability, which occurs on all time scales (from diurnal, seasonal and interannual to decadal and centennial). In order to establish whether we really are experiencing anthropogenic climate change, it is important to understand the climate's natural variability on all timescales to be able to distinguish and separate human-induced climate trends.

This PhD is concerned with understanding one particular aspect of the ocean-atmosphere system: the variability of sea surface temperature (SST) at diurnal timescales. In low wind, high insolation conditions, the temperature of the sea surface

can increase by several degrees during the daytime. This variability is investigated using a combination of satellite, buoy and model data. The details of the thesis aims are described in Section 1.4.

1.2 IMPORTANCE OF SEA SURFACE TEMPERATURE

Sea surface temperature is one of the most important variables influencing short and long-term ocean and climate dynamics. Its significance has long been recognised with SST measurements dating back to the 1850's. SST plays a major role in the heat and gas transfer through the marine boundary layer, coupling the ocean-atmosphere system. It influences upper ocean physical and biogeochemical processes and acts as an indicator of climate change both directly and indirectly. SST plays an important role in climate and seasonal forecasting, management of shelf/coastal areas, the fishing and offshore industry and navy applications. The importance of SST is highlighted by the decision of the future US National Polar-orbiting Operational Environmental Satellite System (NPOESS) to classify SST as one of six key performance parameters out of a total of 57 environmental variables.

SST observations are used directly to monitor and investigate oceanic and climate variability, and they are applied to modelling studies. SST has several key applications in modelling studies from simple 1-D models up to complex general circulation models. It is used:

- as a lower boundary condition for atmospheric models.
- for data assimilation in operational ocean models.
- as a relaxation term in coupled ocean-atmosphere and ocean-only models.
- for validation of coupled and ocean-only models.

1.3 DIURNAL CYCLE OF SEA SURFACE TEMPERATURE

The diurnal cycle is a fundamental mode of the climate system associated with solar forcing. SST is directly affected by the diurnal cycle of the sun's radiation. As the radiation enters the ocean, it is absorbed and scattered by water- and suspended particles (Ivanoff, 1977). The absorbance of light is wavelength dependent with the red end of

the spectrum absorbed most strongly and the remaining visible (blue/green) light penetrating deeper. Almost half the incoming irradiance is absorbed within the top metre of the water column and in the absence of wind (turbulent mixing), the strong surface heating creates a highly stratified stable warm layer in the top few metres of the water column, separated from the uniform mixed water below. The warm layer is associated with a strong diurnal thermocline, a shallow mixed layer depth and an increase in SST during the daytime.

The warm layer evolves shortly after dawn once the solar heating exceeds the heat flux out of the ocean. SST will typically peak two to three hours after mid-day (Price et al., 1986; Yokoyama et al., 1995) at which point the warm layer gradually begins to break down. The timing of the break down of the warm layer is dependent on the balance between the opposing stabilising and mixing forces. In the absence of wind mixing, free-convection is believed to dominate the erosion of the warm layer (Pritchard & Weller, 2004). As the net heat flux changes sign and the ocean loses heat to the atmosphere, the near surface layer will become thermally unstable as the energy accumulated during the daytime is released to the atmosphere (by surface cooling via the latent, sensible and longwave heat fluxes) and the water below the diurnal warm layer (by convective overturning and turbulent kinetic energy dissipation). The schematic in Figure 1.1 presents a typical example of the evolution of a diurnal warm layer under very low wind conditions.

In reality, wind stress will oppose the positive buoyancy forcing and will act to break down the thermal stratification and distribute the daily solar heating over a greater depth. The depth to which the diurnal warming penetrates is therefore dependent on the balance between the positive buoyancy flux, related to the incoming solar radiation, and the turbulent energy available to mix the upper layer, primarily provided by the wind stress at the ocean surface. In high wind conditions, the turbulent energy mixes the surface water deep into the water column, distributing the daytime heat over a great depth and destroying any trace of a diurnal warm layer.

The phenomenon of diurnal warming relates to conditions when solar heating dominates turbulent mixing (calm, clear sky conditions), creating shallow warm layers at the surface and causing SST to vary over the day. The weaker the wind, the shallower the

diurnal mixed layer and the larger the increase in SST. As wind speeds approach zero, there is a transition from a shear driven regime to a free convective mixing regime and the diurnal mixed layer may vanish completely. Under the free convection regime, buoyancy forcing is so strong that the surface layer can decouple from the mixed water below. Kudryavtsev & Soloviev (1990) reported that the suppression of turbulent mixing reduced the friction at the interface between the buoyant warm layer and the water below, resulting in the diurnal mixed layer 'slipping' over the water below.

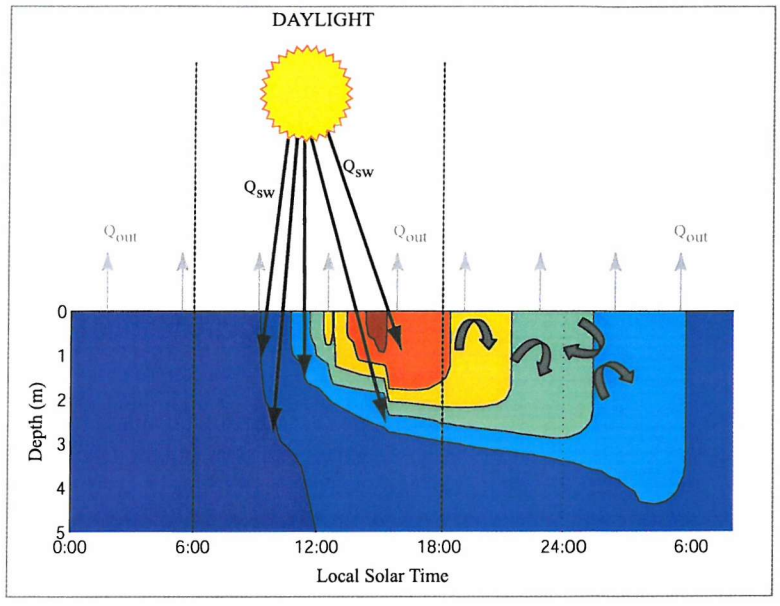

Figure 1.1: Schematic of the evolution of the diurnal warm layer over time in the absence of wind mixing. The colours represent water temperatures in the top 5m of the water column, with temperature increasing from blue to red. The thick grey curved arrows represent convective overturning which occurs when the net heat flux is out of the ocean. The warm layer does not fully break down until after midnight.

1.3.1 Observations of Diurnal Warming

Diurnal warming was first reported in the 1970's (e.g., Stommel et al., 1969; Halpern & Reed, 1976; Kaiser, 1978) with local diurnal variations of SST reaching over 1°C. Deschamps & Frouin (1984) observed large areas of diurnal increases in SST using satellite images of the Mediterranean Sea. No in situ observations were available to confirm their results and consequently oceanographers were reluctant to consider the effect seriously. However, since then, diurnal warming has been reported in many localised areas: Sargasso Sea (Stramma et al., 1986; Price et al., 1987), western North Atlantic (Cornillon & Stramma, 1985), Mediterranean Sea (Deschamps & Frouin, 1984; Bohm et al., 1991), western North Pacific (Kawai & Kawamura, 2002; Tanahashi et al., 2003), off the west coast of California (Price et al., 1986) and the equatorial tropical

Pacific (Webster et al., 1996; Soloviev & Lukas, 1997). As listed in Table 1.1, these studies have reported diurnal warming, in some extreme cases as large as 6.6°C (Flament et al., 1994), using a variety of observational techniques.

Table 1.1: Summary of diurnal warming field studies reported in the literature. Maximum ΔT values are listed when available. In some cases the magnitudes are approximate.

Study	SST measurement	Location	Maximum ΔT
Stommel (1969)	In situ	Sargasso Sea	
Halpern & Steed (1976)	In situ	Subtropical North Atlantic	1.4°C
Kaiser (1978)	In situ	Sargasso Sea	
Deschamps & Frouin (1984)	Satellite	Mediterranean Sea & North Sea	5°C
Cornillon & Stramma (1995)	Satellite	Sargasso Sea	4°C
Cornillon et al. (1986)	Satellite & in situ	Sargasso Sea	3.5°C
Price et al. (1986)	In situ	Off California	2°C
Price et al. (1987)	In situ	Sargasso Sea	3°C
Bohm et al. (1991)	Satellite	Mediterranean Sea	
Ramp et al. (1991)	In situ	Off California	4°C
Hawkins et al. (1993)	Satellite	Subtropical N. Atlantic	4°C
Yokoyama et al. (1993, 95, 96)	In situ and satellite	Mutsu Bay	4°C
Flament et al. (1994)	In situ and satellite	Off California	6.6°C
Fairall et al. (1996)	In situ	Western Warm Pool	4°C
Soloviev & Lukas (1997)	In situ	Western Warm Pool	3°C
Wu et al. (1999)	Satellite	Western Atlantic	3°C
Kawai & Kawamura (2002)	In situ	Western Pacific	2°C
Tanahashi et al. (2003)	Satellite	Western Pacific	
Stuart-Menteth et al. (2003)	Satellite	Global	
Pritchard & Weller (2004)	In situ	Western Warm Pool	

Cornillon, Stramma et al. (1985, 1986) were some of the first people to follow on Deschamps & Frouin's work (1984). Stramma et al. (1986) used a combination of satellite and in situ data to look at the size, frequency and spatial extent of diurnal warming in the Sargasso Sea. They found that satellite and in situ observations agreed very well, observing maximum diurnal temperature variations, ΔT, of 3.5°C and concluding that the area had a 20% chance of diurnal warming greater than 0.5°C. Satellites were advantageous in mapping out the extent of the warming, which in cases covered 100,000 km^2, and the area was found to correspond well with atmospheric pressure patterns. In some extreme cases, the effect of diurnal warming could be seen at night, where the heat gain during the day exceeded heat loss at night

The spatial distribution of diurnal warming patches agrees well with areas of low wind speed and little/no cloud coverage (Cornillon & Stramma, 1985). Several studies have commented that the shape and position of warming patches vary rapidly in response to the evolution of the wind field (Flament et al., 1994). In the case of equatorial regions, in particular the western equatorial Pacific, freshwater lenses and salinity gradients near the surface can also determine the spatial distribution of the warming (Soloviev & Lukas, 1997). The presence of freshwater will strengthen the stability of the upper ocean, further suppressing turbulence. Under very low winds, the influence of freshwater is unimportant as the upper ocean has reached its full stratification through the thermal heating (Webster et al., 1996). However in moderate wind conditions, rainfall can help to promote diurnal warming. Internal processes can also affect the distribution in the diurnal thermocline on account of the buoyancy adjustment and internal waves (Pritchard & Weller, 2004).

These studies have reported large diurnal warming events at a range of locations. However, there still remain unresolved issues regarding the diurnal cycle of SST. No global long-term view exists of diurnal warming to put these results into the broader context. Furthermore, little attention has been paid to distinguish the difference between the diurnal variations observed at the true sea surface and those occurring just below, in order to understand the distribution of heat through the diurnal warm layer. Most studies have focused on the maximum amplitude of the diurnal signal while the phase of the signal has received little attention.

1.3.2 Theoretical studies of diurnal warming

There have been many theoretical studies on the diurnal warm layer (e.g. Price et al., 1986; Anderson et al., 1996; Fairall et al., 1996b; Soloviev & Schluessel, 1996; Webster et al., 1996; Zeng et al., 1999; Kawai & Kawamura, 2002; Pritchard & Weller, 2004). One of the most widely quoted studies is by Price et al. (1986), who parameterised the warm layer effect using a modified instability model. The model represents the mixed layer depth as shoaling very rapidly as solar radiation increases during the first few hours of the morning. The depth to which it shoals is defined as the depth where the absorbed solar radiation exactly compensates the surface heat loss. As the mixed layer shoals, shear stress at the base of the mixed layer can generate Kelvin-Helmholtz instability. Once this instability exists, the mixing depth is controlled by the turbulence

rather than the balance between the incoming and outgoing heat flux. The warm layer onset occurs about an hour after sunrise though it usually takes a further few hours for the effects to become noticeable.

Other mixed layer models have also been used to investigate diurnal warming and each model has its own weakness (Pritchard & Weller, 2004). An important aspect of modelling and understanding the evolution of the diurnal warm layer is to correctly parameterise the distribution of heating through the water column. A wide range of parameterisations exists to predict the vertical profile of irradiance but a detailed intercomparison of the different parameterisations has not been carried out to date. In addition, differences in the way each model describes turbulent mixing processes will also contribute to discrepancy between models.

1.3.3 Implications of diurnal warming

The diurnal cycle of SST has a range of implications. They can crudely be broken down into two categories: 1) the impact on the interpretation and application of SST measurements and 2) the impact on physical processes - upper ocean dynamics and air-sea interaction.

1) Impact of diurnal warming on the interpretation and application of SST observations

As discussed above, SST has a wide range of applications. In general most SST users require either the upper ocean mixed layer temperature or the temperature at the air-sea interface, known as the skin temperature. For some applications, the presence of diurnal warming can create noise and contaminate the SST signal under investigation. The presence of a diurnal warm layer will be imposed on top of the surface mixed layer temperature and therefore measurements taken within the warm layer will not be representative of the true mixed layer temperature. Several studies in the past have demonstrated that diurnal heating can mask SST fronts and eddies (e.g. Katsaros et al., 1983; Deschamps & Frouin, 1984; Bohm et al., 1991). These studies advised that regions of diurnal heating should be excluded from SST analyses. Furthermore, diurnal warming can create its own horizontal temperature gradients which reflect meteorological dynamics and not oceanic processes (Robinson & Donlon, 2003). The diurnal signal also acts as noise for long-term climate change studies. Climate research and its prediction is one of the most important areas of oceanographic research at the

moment as the evidence of global warming builds up. For climate change studies, highly accurate SST's are required, as the results need to be quantitatively reliable. The CLImate VARiability and predictability (CLIVAR) Implementation Plan (1999) called for SST to be accurate to 0.1°C for monitoring long term climate, while Allen et al. (1994) advised that SST should be stable and accurate to 0.1°C/decade to confidently detect climate change. Given the large temperature variations that can be associated with diurnal warming, it can potentially introduce large biases into climate SST records.

2) Impact of diurnal warming on upper ocean dynamics and air-sea interaction

Diurnal SST variability can have important implications for upper ocean and coupled air-sea dynamics. Diurnal variations are important over the diurnal period but can also rectify to longer timescales. Although the heat content in the diurnal warm layer is small in comparison with the mixed layer, it is not in comparison with the heat content of the atmospheric boundary layer. Diurnal variations in temperature are most likely to have greatest impact in the tropics since the high temperatures associated with this region are more sensitive to changes in SST. Webster et al. (1996) suggested that large diurnal warming can lead to increased convection in the atmospheric boundary layer and that feedbacks between the atmosphere and ocean potentially operate on diurnal time scales. Heat and gas fluxes are dependent on SST and underestimating the magnitude of SST over the diurnal cycle can affect estimates of heat and gas exchange between the ocean and atmosphere. Cornillon & Stramma (1985) commented that diurnal warming only has a small impact on the monthly mean air-sea heat flux (~5 Wm^{-2}), but that the impact is always biased in the same direction, towards a lower net heat flux into the ocean, and can often occur over large regions. Heat losses over a 24 hour period will be much larger. This result was also confirmed by Zeng & Dickinson (1998) for the tropical Pacific. They concluded that large diurnal flux variations could have a significant impact on the diurnal variability of tropical clouds and precipitation. Most atmospheric models are forced with monthly/weekly bulk SST or by ocean model SST values that do not resolve the diurnal cycle or distinguish between the temperature at the air-sea interface (skin) and at depth (bulk). With regards to gas fluxes, McNeil & Merlivat (1996) reported that the presence of the diurnal SST cycle would enhance CO_2 evasion from the ocean in areas of super-saturation and reduce invasion in areas of under-saturation, which could lead to a net asymmetry. Quantifying and understanding

CO_2 uptake is key to climate change prediction. By ignoring global diurnal variations of SST, the amount of CO_2 being drawn down by the ocean could be overestimated.

Shinoda & Hendon (1998) and Bernie et al. (2003) discuss the rectification of the diurnal cycle to longer timescales. If winds are low during the night as well as during the day, then the heat trapped during the daytime in the diurnal warm layer will be distributed over a shallower depth at night as less energy will be available to mix the heat deeper. This in turn will increase the mean SST and if conditions persist for several days, the diurnal variations will continue to increase the mean SST each night. In addition, in the absence of wind mixing, some irradiance will penetrate below the diurnal mixed layer and warm the water below, which again will contribute to shallower nocturnal mixing and a warmer mean SST. Shinoda & Hendon (1998) and Bernie et al. (2003) suggest that the diurnal cycle should be considered in order to correctly simulate and predict the intraseasonal SST variability associated with the Madden-Julian Oscillation. Bernie et al. (2003) report that the diurnal cycle of SST contributes to a third of the intraseasonal SST variability. These SST anomalies are capable of organising atmospheric convection on intraseasonal timescales (Woolnough et al., 2001). Coupled models have difficulty in replicating the atmospheric variability, which has been related to inadequacies in the representation of the upper ocean (Inness & Slingo, 2003). The exclusion of large diurnal variations in SST and heat fluxes and their impact on the intraseasonal SST have been suggested as a cause for the model inadequacies and research is currently being carried out to investigate this (Woolnough, personal communication).

1.4 THESIS AIMS

As detailed above, the diurnal cycle of SST has a broad range of implications. Despite its significance it has often been ignored until recently. A major reason for this is that diurnal warming was not considered to be a global problem. The first aim of this project has been to investigate the frequency of diurnal warming events on a global scale to reveal the temporal and spatial distribution of diurnal warming patterns and help evaluate its impact on SST. While there have been many studies of diurnal warming in the past, there has not been a long-term global assessment. One of the major motivations for this study comes from the Global Ocean Data Assimilation

Experiment (GODAE) High Resolution SST - Pilot Project (GHRSST-PP) (Donlon, 2002a), which was being established at the time this Ph.D. programme commenced. This international project is concerned with providing a new generation SST product to meet the wide range of SST user needs. Given the noise that diurnal warming can create for some applications, the question was raised as to the significance of the phenomenon. Could it be ignored or did it need to be investigated and resolved? The results from this first part of the work led on towards the content of the later chapters, which focus on improving our understanding of the diurnal SST cycle and characterising it in more detail. Throughout this thesis, the results are related to the implications for SST measurements and their interpretation and for coupled air-sea dynamics.

Despite the variety of past studies on diurnal warming, there is still more to be investigated and understood. The inspiration for the new work presented in this thesis comes from these earlier studies where certain issues were raised but remain unresolved. Several key questions will be addressed in this thesis:

- Where and when does diurnal warming regularly occur?
- What controls the shape of the diurnal cycle? What influences the timing of the daily maximum SST? How do the phase and amplitude of the diurnal signal vary through the diurnal warm layer?
- How important is sea water clarity for diurnal warming?
- How can the diurnal signal 'contamination' be addressed in SST datasets?

Before presenting the new work, more background information is given to develop the history and complexity of SST. SST is frequently and mistakenly believed to be well understood. Chapter 2 will discuss the issues within the SST community and highlight the recent advances in the field. Then follow four chapters which present the substantive original contributions contained in the thesis. In each of these, the relevant literature is discussed briefly in greater detail to provide the basis for the new results. Chapter 3 presents a global analysis of diurnal warming to describe the large-scale temporal and spatial distribution of diurnal warming patterns. In the following chapters, the dynamics of the diurnal warm layer are addressed in more detail using high

resolution buoy data and a mixed layer model to investigate the influence of water clarity on the diurnal warm layer (Chapter 4) and the sensitivity of the diurnal cycle to time variability of the forcing fields (Chapter 5). Finally Chapter 6 ties the results from the previous chapters together and presents a new parameterisation for diurnal warming to help evaluate the diurnal signal present in satellite and in situ measurements. The final two chapters discuss the implications of the new results for SST applications and consider how this work fits into the exciting advances in this research field and identify directions in which the work could be taken further.

CHAPTER 2: SEA SURFACE TEMPERATURE

2.1 COMMON DEFINITION OF SST

Care must be taken when defining sea surface temperature (SST). SST is often referred to as either a bulk or a skin temperature. The skin temperature refers to the temperature at the air-sea interface, in the upper microns of the ocean, where turbulent motion is inhibited. The air-sea interface acts as a boundary and so in order for heat to pass through the interface, it must be transferred by molecular conduction along a temperature gradient (e.g., Woodcock, 1941; Saunders, 1967). Subsequently, a strong temperature gradient exists at the air-sea interface resulting in the skin temperature being slightly cooler than the water millimetres below it, typically by 0.17°C (Donlon et al., 2002b). The bulk SST refers to the temperature of the upper ocean mixed layer where it is assumed that the water column is well mixed by turbulent wind forcing. In practice, this has been interpreted to include any measurement taken below the oceanic skin layer in the top 10m.

A major weakness of this definition is that it assumes that the temperature below the skin layer is always uniform and well mixed. In diurnal warming conditions, the upper few metres of the water column stratify during the daytime, and can create very strong thermal gradients with differences of several degrees across the diurnal warm layer. These thermal gradients complicate the definition of SST. It is no longer as simple as distinguishing between skin and bulk SST. This is demonstrated in Figure 2.1 where the well-mixed temperature profile (Figure 2.1a) is compared to a typical diurnal warm layer temperature profile (Figure 2.1b). In diurnal warming situations, the definition of bulk SST becomes meaningless as measurements in the top few metres will not represent the mixed layer temperature. In general, SST users are either only concerned with the skin SST or the true mixed layer surface temperature. The upper ocean mixed layer temperature is regarded as an important indicator of heat storage and the thermal capacity of the ocean, while skin SST is important for heat fluxes and air-sea interaction. Depending on the depth and time of day of the measurement, temperatures measured at a point location over a 24-hour period could vary greatly. Thus, the diurnal signal has the potential to add bias and noise to measurements supposed to represent the mixed layer SST.

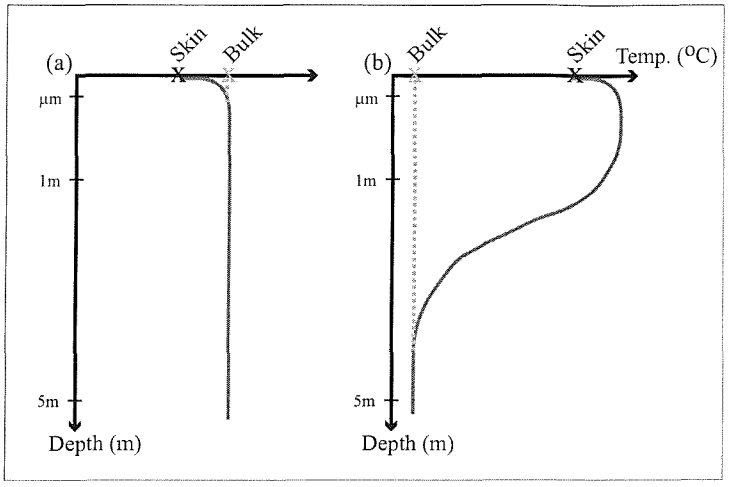

Figure 2.1: Schematic of temperature profile of top 5m of the water column. (a) Well mixed/night-time conditions, (b) diurnal warming conditions

2.2 METHODS FOR OBSERVING SST

The significance of SST for oceans and climate has long been recognised. SST measurements date back to the 1850's, which have enabled the scientific community to study the mechanisms behind past oceanic and climatic changes and predict its future state. Over the last 150 years, temperature-measuring instruments have developed and improved considerably. Historically, SST referred to a bulk near-surface in situ ocean temperature but with the advent of satellites, skin SST has also been measured.

There are three main platforms for measuring SST: ships, buoys and air/space-borne sensors (Table 2.1).

2.2.1 Ship Measurements

One of the first techniques used to measure SST was to throw a bucket over the side of a ship to obtain a water sample and measure its temperature with a thermometer. Ship data has restricted coverage since it depends on the shipping routes. Coverage was fairly widespread in the Atlantic and Indian Oceans but sparse in the Pacific until the 1930's. The Southern Ocean has the poorest sampling since few vessels operate in that area. There are several concerns regarding the accuracy of bucket SST measurements. For example, biases can be caused by the insulation properties of the buckets, from taking the water sample from the ship's wake or from leaving the bucket on deck for a period of time before recording the temperature. The design and insulation of the buckets has evolved over time from un-insulated canvas buckets to partially insulated

wooden buckets and finally insulated rubber buckets in the 1970's. Suitable corrections have been applied to compensate for the differing insulation properties (Folland & Parker, 1995), though doubts still remain concerning how the temperature was actually measured and what proportion of measurements are from the different types of buckets.

During World War II, bucket measurements were replaced by measuring the temperature of the water drawn in to cool the ship's engine, known as the engine intake method. There are also concerns associated with this technique such as the range of depths from which the water is drawn in (3-10m), whether this water is representative of that depth, the size of the ship intake, the configuration of the engine room and the point where the measurement is taken (Kent et al., 1993). Kent et al. (1993) reported warm biases, typically 0.35°C, caused by the ship's engines warming the water. More recently hull-mounted thermistors have been attached to ships either externally or internally. If the sensor is internally mounted, this method can be limited by the damping of the sensor response time due to the effect of the ship's hull. The number of hull-mounted sensors is small in comparison to the engine intake method.

Bucket measurements are still carried out today by some Ships of Opportunity and Voluntary Observing Ships, although the more common techniques are now hull-mounted temperature probes and engine intake measurements. Although corrections have been developed and applied to historical data, some doubts remain about the adequacy of corrections to the historical data. These measurements can not be disregarded as they make up a large and important part of the historical SST time series. To improve the record, more information on the distribution of the different instruments and the timing of the switch from bucket measurements to engine intake and between canvas to wooden buckets is needed, and differences between the individual measurement techniques must be assessed (Kent, personal communication).

Research vessels provide another source of ship SST measurements. SST instruments tend to be more sophisticated on scientific ships and therefore more accurate measurements can be obtained. However research ship datasets make up only a very small contribution to the ship SST data record.

2.2.2 Buoy Measurements

Since the 1970's, SST has also been measured by moored buoys (e.g. ATLAS in the equatorial Pacific) or drifting buoys (e.g. PALACE), which measure SST at 0.3m-1.5m depth. There is now a huge network of moored and drifting buoys in the oceans, which provide near real-time accurate SST. Their coverage is again restricted and they can become trapped in stable current fields (Minnett, 1990). However they are able to access more remote areas which has helped improve sampling, particularly in the Southern Ocean and they have superior accuracy over most ship data. There are many different buoy designs with different sensor packages and a variety of hull designs. Recently Emery et al. (2001) reported biases in buoy data, but they still remain the best currently available bulk SST standard on a global scale.

2.2.3 Remotely Sensed Measurements

In the late 1970's, remotely sensed SST became available with the advent of Earth Observing satellites. For the first time, synoptic views of the ocean's surface were obtained, bringing with it fundamental revelations about the ocean, the most notable being the discovery of ocean eddies. The unique capability of satellites to monitor SST on a global synoptic scale has led to the rapid development of satellite platforms and sensors. Satellite images have been used to monitor ocean currents, eddies and fronts, for over two decades, providing a clearer picture of the spatial and temporal scales of these oceanic features and processes. A key advantage of satellite data is that with its near global coverage, there is no significant hemispheric or regional sampling bias.

Table 2.1: List of main SST-Measuring Platforms

Instrument	Spatial sampling	Temporal sampling	Depth sampling	Accuracy
Research Vessel	Very sparse	continuous	Not fixed	<0.1 K
Voluntary Ship	Track-limited, sparse	1 day	1-10m	0.5 K
Buoy	Distributed, sparse	1 hr -1 day	0.3-1.5m	0.1 K
Polar orbiting infrared satellite	Global coverage	12 hrs	Skin 10μm	0.3 K

SST can be measured from space using two different parts of the electro-magnetic spectrum: infrared and microwave. Infrared radiation is emitted from the ocean's skin (microns) and microwave radiation is emitted from just below the skin (millimetres),

often referred to as the sub-skin. In accordance with the general definition of SST, infrared sensors measure the skin and passive microwave sensors measure the bulk SST. In reality, passive microwave instruments do not always measure the mixed layer temperature. Under diurnal warming conditions, the sub-skin temperature, detected by microwave sensors, is not representative of the mixed layer SST.

Satellites have a range of resolutions depending on their orbit type and footprint. There are three main types of satellite orbit for Earth Observation satellites: polar orbiting, geostationary and low inclination orbit. Polar orbiting satellites are sun-synchronous and consequently measurements of SST for each overpass are taken at approximately the same local time each day. Depending on the sensor footprint some satellites cover the whole globe daily (e.g. Advanced Very High Resolution Radiometer - AVHRR) whilst others can take a few days to get full global coverage (e.g. Along Track Scanning Radiometer - ATSR). Geostationary satellites (e.g. Geostationary Operational Environmental Satellite - GOES) on the other hand, take readings every half an hour but their coverage only extends to a maximum of ± 50 degrees latitude and longitude. Some satellites have a lower inclination orbit which allows the overpass time to precess each day (e.g. Tropical rain fall measuring mission Microwave Imager - TMI). In this case, the coverage is limited latitudinally (e.g. TMI is restricted to ± 40°). Passive microwave satellites are limited in resolution by the size of their footprint, which is at least 50km, although they sample every 25km (Robinson & Donlon, 2003). In contrast, infrared sensors can measure SST to a resolution of 1.1km.

Satellites are handicapped by less accurate SST measurements as corrections and algorithms must be applied to the data to derive SST (Robinson & Donlon, 2003). The sensor initially measures the top-of-atmosphere brightness temperature, T_b, which must be recovered from the signal by direct calibration of the sensor, using on board black body targets of a known temperature (Brown et al. 1985). Next the measurement must be corrected for atmospheric effects. Due to the different nature of the infrared and microwave radiation, the different techniques require separate corrections. The atmospheric transmittance of infrared radiation is dependent on the levels and types of aerosols and gases present. The atmosphere, in particular water vapour, absorbs infrared radiation and therefore T_b is cooler than the temperature of the sea surface. The

correction for water vapour is particularly important since it is highly variable both temporally and spatially (Kilpatrick et al., 2001). Aerosols (e.g. desert dust, volcanic aerosols) also have a similar effect, which must be accounted for (Merchant et al., 1999).

Clouds absorb the infrared radiation emitted from the sea surface and consequently infrared sensors can not measure SST through clouds. Clouds need to be detected and flagged to prevent cloud contaminated pixels being interpreted as SST (Jones et al., 1996). This is a major limitation of infrared SST. In a similar way to water vapour, clouds will create a cool bias. In regions of large SST gradients, the spatial characteristics of clouds and SST are similar making it extremely difficult to account for all cloud-contaminated pixels. Cloud detection techniques are carefully designed and applied to satellite data to ensure that as many cloud-contaminated pixels are identified and flagged as possible.

Passive microwave's greatest advantage over infrared techniques is that it is not limited by cloud. It uses a combination of different microwave wavebands, including the 10.7GHz and preferably the 6.7GHz channels which are transparent to the atmosphere. Microwave retrievals are therefore insensitive to atmospheric water vapour and are not affected by aerosols. However the microwave signal is affected by rain and can not retrieve SST under wet conditions. The amount of rain-contaminated pixels for microwave techniques is negligible in comparison to the cloud-contaminated pixels in infrared retrievals (Stammer et al., 2003). Microwave's main contamination comes from sea surface roughness effects (Wentz, 1997). Both wind speed and direction will affect the brightness temperature received by the sensor.

Each infrared and microwave sensor has its own processing algorithms to apply the necessary corrections and produce the final SST. The structure of these algorithms also plays a role in the accuracy of SST. The data processing creates biases unique to each satellite, which must be taken into consideration. For example, some infrared satellites (e.g. AVHRR) convert their skin measurement to 'bulk' SST using specially designed algorithms (e.g. Walton et al. 1998), matched to SST measurements from buoys, to keep up the continuity with historical SST records. Their accuracy depends on how well the differences between the skin and in situ measurements are understood and modelled.

This relationship is complicated under diurnal warming conditions, as the true skin-mixed layer temperature difference is harder to measure. The cool skin difference is the difference between the skin and the water just below the skin (known as the sub-skin). Under diurnal warming conditions, this is different from the skin - mixed layer temperature difference. This is highlighted in Figure 2.2 which shows the diurnal warming temperature profile and the variety of depths at which SST is typically sampled from current measurement techniques.

Table 2.2 summarises the main SST satellites currently operating in space and lists their design strengths and weaknesses. During the course of the work presented here, several new satellites have been launched almost doubling the variety and sources of SST measurements from space. As can be seen from the table, each sensor has its own advantages and disadvantages: no satellite is perfect. While AVHRR has excellent coverage and validation, its accuracy is still under question since it relies on regression to in situ buoy match-ups which can be regionally and seasonally biased (Ajoy et al., 2000). ATSR produces accurate SST but researchers are reluctant to use it since it measures the skin SST and is not routinely validated (Robinson & Donlon, 2003).

Table 2.2: Current SST-Measuring Satellites. IR: InfraRed, PM: Passive Microwave. (See List of Acronyms for full sensor and satellite names.)

Sensor	Satellite	Orbit Type	Spatial Resolution	Temporal Resolution	Depth Sampling	Accur-acy	SST product
AVHRR IR	NOAA 1988 -	Polar-orbiting	Global, 1km Cloud limited	12 hr Daily coverage	~10 μm	0.5°C	1m
(A)ATSR IR	ERS, ENVISAT 1991 -	Polar-orbiting	Global, 1km Cloud limited	12 hr 35 day coverage	~ 10 μm	0.3°C	Skin
GOES IR	METEO-SAT 1994 -	Geostat-ionary	±45 °, 2-6km Cloud limited	30 mins	~ 10 μm	0.3-0.5°C	1m
TMI PM	TRMM 1997 -	Polar-orbiting	± 38 °, 50km	12 hrs - 2days	~ 1mm	0.5-1°C	Sub-skin
AMSR/E PM	AQUA 2002 -	Polar-orbiting	Global, 25km	12 hr Daily coverage	~ 1mm	0.5°C	Sub-skin
AMSR PM	ADEOS-II 2002-03	Polar-orbiting	Global, 25km	12 hr Daily coverage	~ 1mm	0.5°C	Sub-skin
MODIS IR	AQUA (2002 -) TERRA (2000 -)	Polar-orbiting	Global, 1km Cloud limited	12 hr Daily coverage	~ 10 μm	0.3°	Skin

In 2002, the Global Ocean Data Assimilation Experiment (GODAE) set up a High-Resolution SST steering group to develop a new generation of SST datasets, primarily to match the requirements of modern operational oceanography, drawing upon the advantages of each satellite/sensor to produce a superior SST product (Donlon, 2004a).

For example, AVHRR is generally accepted to be the superior infrared satellite as it has the best coverage and resolution, although its accuracy requires improvement (Robinson & Donlon, 2003). By flying the highly accurate ATSR simultaneously with AVHRR, AVHRR could be tuned with the robust calibration of ATSR, thus improving its accuracy. Geostationary satellites (e.g. GOES) could be useful to detect and remove cloud from images since the satellite can follow the progression and movement of clouds with its half hourly coverage and microwave satellites (e.g. AMSR-E) could provide information about SST under cloud persistent regions, to fill in the gaps in the global field.

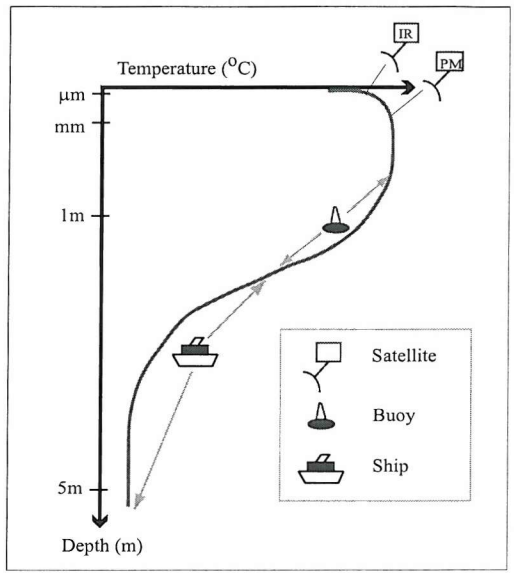

Figure 2.2: Schematic of sampling depth of routine SST instruments over a typical vertical temperature profile during diurnal warming conditions.

2.3 GODAE HIGH RESOLUTION SST – PILOT PROJECT

This new international project is called the GODAE High Resolution Sea Surface Temperature – Pilot Project (GHRSST-PP) (Donlon, 2004a). The aim of the project is to develop a system that will deliver a new generation of global coverage high resolution SST data products in real time. The products will be derived by combining complementary satellite and in situ observations to improve spatial coverage, temporal resolution, cross-sensor calibration stability and SST accuracy. This is clearly the best way forward to exploit the full potential of satellite data. Even the next generation of satellites, which have already been designed, will not be able to provide the perfect package, and they will need to be used in synergy to produce a superior SST data set.

To bring together and merge different satellite measurements is a considerable challenge for satellite oceanographers as many issues must be considered and resolved. Some of the main challenges are:

- differences in spatial and temporal sampling of satellites
- problems of data gaps due to clouds, rain or lack of data
- individual sensor biases
- differences between geophysical measurements – skin v sub-skin
- diurnal SST variability
- derivation of true mixed layer SST

The GHRSST-PP is half way through its demonstration phase and the project has already been successful in raising considerable scientific interest and support (Donlon, personal communication). This project has thoroughly re-evaluated SST and has made considerable effort to communicate with SST users to assess user requirements. The GHRSST products will be developed to meet the full range of SST applications from real time high resolution SST for operational purposes, to highly stable and accurate SST for climate studies.

Climate research and prediction is one of the most important areas of oceanographic research at the moment as the evidence of global warming builds up. Satellite-derived SST has the potential to contribute to climate research. Reynolds (1999) warned that satellite-derived global SST products should be used with great care in climate research since there still exist small uncertain biases in the data. Hurrell & Trenberth (1999) intercompared four principal global SST data sets based on in situ or a combination of in situ and satellite measurements and noted that each one had its own weaknesses and uncertainties, due to the different sources of data and the processing/interpolation techniques employed. These results demonstrate the complexity of SST analyses and highlight the uncertainties that still remain. For a meaningful long term record of SST, it is necessary to combine detailed statistical analyses and modelling to remove any bias between different data series. Each SST time series is different: there is no standard analysis.

2.4 NEW DEFINITION OF SST

Through GHRSST-PP, the definition of SST has come under serious scientific review. The GHRSST-PP science team have defined a set of SST variables in order "*to achieve the closest possible coincidence between what is defined and what can be measured operationally, based on the current understanding of the near surface thermal structure of the ocean*" (Donlon, 2004a). Employing these new definitions will allow SST to be applied with more confidence to its range of applications.

GHRSST-PP has suggested a new SST definition to describe the true mixed layer surface temperature. This temperature is called the Foundation Temperature (T_{fnd}) and refers to a well mixed temperature value free from cool skin and warm layer effects. The project also defines skin SST and sub-skin SST in recognition of infrared and passive microwave satellites which will make up the majority of future SST records (Figure 2.3). All in situ measurements should be defined with their depth, SST_z, to ensure that the depth of the measurement is known to avoid mis-interpretation. Relating these back to the original skin and bulk SST definitions, the skin definition still exists, but now the bulk SST is referred to as the more precise foundation temperature. Under high winds or cloudy/weak insolation conditions, microwave satellite and in situ measurements (regardless of their depth below the skin layer) will represent T_{fnd} but in diurnal warming conditions, only ships with deep engine intakes may record the true T_{fnd}. Since satellites and buoys make up the majority of the present day SST data records, it highlights the importance of recognising the bias associated with diurnal warming. All buoy and satellite data used to make a bulk SST record are potentially biased by diurnal warming. The GHRSST-PP aims to resolve this problem and will develop methods to deal with the diurnal SST variability, so that the true foundation temperature can be determined.

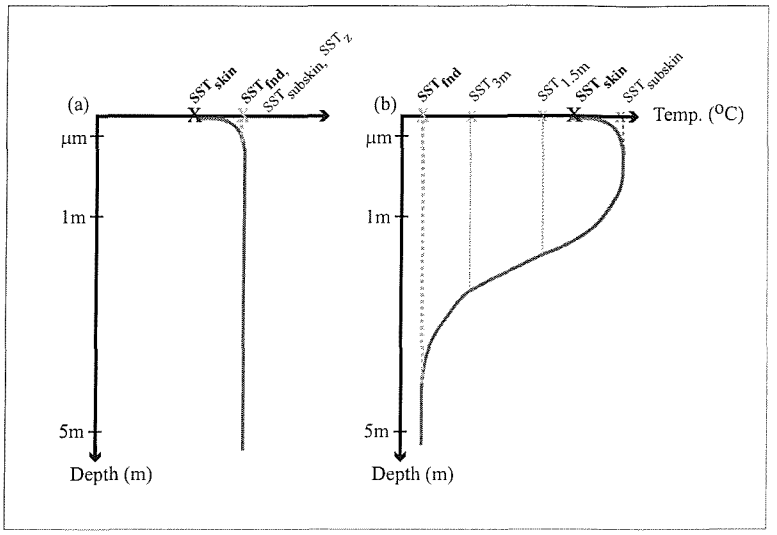

Figure 2.3: Schematic of temperature profile in top 5m of the water column. The GHRSST-PP definitions of SST are indicated for (a) well-mixed/night-time conditions and (b) diurnal warming conditions.

2.5 SUMMARY

This chapter has shown the significant uncertainties that still exist within SST measurements. There are many methods to measure SST which each deliver a potentially biased SST dataset dependent on the particular technique used. Historical records are made up of data from a combination of different ship-based instruments. Their coverage is not uniform and some regions of the Southern Ocean have very little data coverage, which can introduce hemispheric and regional biases into the data. More recently buoy and satellite measurements have become available greatly improving data coverage. Satellites offer full global synoptic views of the oceans and improve the sampling of many remote areas.

There is no longer a simple definition of SST. Bulk SST has been the conventional definition of SST in the past and it is important to keep up the continuity. However this chapter has highlighted the uncertainty in the generality of 'bulk' measurements when diurnal stratification is considered. This uncertainty is not acceptable for climate records. In order to study the sensitivity of climate and detect very small changes in temperature, we must be able to confidently separate measurement biases from climate trends. It is important to be aware of the complexity of SST. Through the new definitions proposed by GHRSST-PP, the true meaning of SST is becoming clearer and should lead to more stable SST records, providing future generations of earth scientists with a clearer understanding of this key climate variable.

CHAPTER 3: GLOBAL SPATIAL & TEMPORAL DISTRIBUTION OF DIURNAL WARMING EVENTS

3.1 BACKGROUND

As discussed in the previous chapter, diurnal warming signals can bias mixed layer SST measurements. This is not acceptable for climate quality data records. While some of the scientific community has been aware of the potential impact of diurnal warming, it was thought that it could be ignored for global applications. Diurnal warming has been reported in many localised areas (Table 1.1) using a combination of in situ and satellite data. While reporting large diurnal amplitudes of SST, these studies have been limited in time and space. There has not been a long term observational study to identify the global temporal and spatial patterns of diurnal warming. Given the implications of diurnal warming for SST measurements, it is important to have a global view of this phenomenon. In this chapter, infrared satellite-derived SST from the Advanced Very High Resolution Radiometer (AVHRR) is used to investigate and identify, for the first time, the temporal and spatial characteristics of diurnal warming over all ocean basins. Part of the motivation for this works comes from the GODAE High Resolution SST – Pilot Project (GHRSST-PP, Section 2.3) where the question was raised whether the diurnal variation of SST was important for generating accurate and stable SST measurements.

There are two crucial factors determining whether diurnal warming will be detected: the depth and time of the measurement. With regards to depth, satellites will always detect the warm layer since they measure the surface temperature. In situ measurements may or may not, depending on the depth of the observation, though most instruments are likely to measure some degree of diurnal warming but probably to a weaker extent than satellites. In all cases, it will also depend on the time of the measurement. The diurnal peak of SST has been observed from pre-noon to late afternoon. Price et al. (1986) reported that surface warming typically peaks around 14:30 local solar time (LST) but noted considerable scatter and in some cases, the warming peaked before noon.

Satellites possess the temporal and spatial resolution to investigate global diurnal SST variations which no other observing platform can claim. Stramma et al. (1986) used a

combination of satellite and in situ data to investigate diurnal warming and found that satellite and in situ observations agreed very well, observing a maximum day-night temperature difference, $\Delta T_{day\text{-}night,}$ of 3.5°C. Satellite data were advantageous in mapping out the extent of the warming, which in cases, covered 100,000's km^2, and the area was found to correspond well with atmospheric pressure patterns.

This chapter investigates a global view of the temporal and spatial characteristics of diurnal warming derived from AVHRR SST. Seasonal, interannual and climatological diurnal warming patterns are presented and the implications of the results, which will be useful in a variety of contexts, including remote sensing, ocean and climate modelling and air-sea fluxes, are discussed.

3.2 DATA

To carry out a global long-term study of diurnal warming demands strict data requirements. The data must have global resolution with adequate temporal resolution to sample across appropriate parts of the diurnal cycle. Only satellites possess the temporal and spatial resolution to investigate global diurnal warming patterns. The data processing techniques employed by each satellite must also be considered to ensure that data can be used with confidence for this type of work. Some processing schemes treat day and night SST differently which can introduce noise into the diurnal signal under investigation.

3.2.1 AVHRR data

Ten years of daily day-time and night-time Advanced Very High Resolution Radiometer (AVHRR) SST data, processed by the Pathfinder program, are used in this study (1987-1990, 1993-1998). At the time of the study, no data was available for 1991 and 1992 since extra processing was required due to contamination from the Mount Pinatubo volcanic eruption in 1991. The version V4.1, 18km, all-pixel daily Pathfinder SST (PFSST) product is used (Kilpatrick et al., 2001).

The AVHRR/NOAA satellite was chosen over other satellites for three main reasons. Firstly for its spatial resolution: it is one of the few satellites to provide daily global

coverage. Secondly for its temporal resolution: it has two overpasses a day during early morning and afternoon and thirdly for its choice of algorithm and method of data processing.

The AVHRR is an infrared sensor which measures the skin temperature of the ocean. It has been placed on board a series of National Oceanic & Atmospheric Administration (NOAA) sun-synchronous, polar orbiting satellites since 1981 which orbit the earth twice a day: once during the day and once at night. Between 60°N and 60°S, the time of the satellite overpass is at approximately the same local time each day (~02:00 and 14:00), making the satellite useful for investigating the diurnal cycle.

The objective of the Pathfinder Project is to re-process the entire AVHRR SST database in a consistent manner making it suitable for climate research. The dataset contains infrared radiances from several different satellites and versions of AVHRR sensors and algorithms, so it is necessary to cross-calibrate data from the different sensors to allow the data to contribute to a long-term stable climate database. To meet user requirements and to keep up with historical continuity, atmospheric attenuated brightness temperature measurements of the ocean skin are converted to a pseudo-bulk SST using a simple empirical algorithm. The coefficients of the Pathfinder SST (PFSST) algorithm are determined by matching satellite measurements against co-located in situ drifting and moored buoys from the global buoy network. Coefficients are estimated for monthly periods and the same set of coefficients is applied to both day and night time data. This detail is very important for this study. Since day- and night-time overpasses are processed in an identical manner, with the same coefficients, it removes any uncertainty and doubt that differences in algorithms could create non-geophysical differences between the two measurements.

The accuracy of the PFSST, when compared to the matchup database, is approximately 0.02 ±0.5°C (Kilpatrick et al., 2001). Results from Kearns et al. (2000), who compared PFSST with skin SST from the Marine Atmospheric Emitted Radiance Interferometer (M-AERI), found the accuracy to be 0.07 ±0.31°C. While the differences in bias may reflect differences between the in situ instruments, the improved standard deviation suggests that despite the regression to in situ observations, the final product is more

characteristic of a skin measurement than a bulk observation. While the magnitude of the mean PFSST is closer to the bulk mean, its variability is characteristic of the skin. The regression of the satellite skin to buoy measurements can be interpreted as bringing the satellite mean value towards the buoy. It will have no influence on the variability of the signal.

3.2.2 Ancillary Data

Monthly mean wind speed and short wave radiation data are also used in this study to predict where diurnal warming should occur using a simple regression model and verify the satellite results. The wind data are taken from version 5 of the Special Sensor Microwave Imager (SSMI) satellite dataset (Wentz, 1997). The satellite data have been processed using a unified physically based algorithm to produce a stable long-term record of wind speed (1987-present, resolution 1°, accuracy ~1m/s). Short-wave radiation is taken from the Southampton Oceanography Centre (SOC) flux data set (Josey et al., 1998). The SOC fields are derived from in situ meteorological reports from the Comprehensive Ocean-Atmosphere Data Set (COADS), spanning the period 1980-1997, using a simple empirical formula and has a resolution of 1°.

3.3 METHOD

3.3.1 Satellite-derived diurnal SST variations

In order to investigate the diurnal variations of SST, day-night temperature differences, ΔT, are computed using the daily Pathfinder data [3.1]. Despite the fact that the Pathfinder product is a pseudo-bulk, the diurnal signal described in this study is assumed to represent the diurnal amplitude of the skin and not at 1 metre, since the algorithm corrections do not alter the variability of the signal, only the mean.

$$\Delta T = \mathrm{SST}_{\mathrm{day}} - \mathrm{SST}_{\mathrm{night}} \tag{3.1}$$

The number of day/night matchups is limited to where the overpass paths overlap and cloud-free regions. To improve the number of matchups, if a ΔT matchup for the day and following night does not exist, then the night before is referred to. Consequently the final ΔT product is made up of a combination of:

$$\Delta T_{(d\text{-}n)} = SST_{day} - SST_{night} \quad \text{and} \quad \Delta T_{(d\text{-}(n\text{-}1))} = SST_{day} - SST_{(night\text{-}1)} \tag{3.2}$$

From these daily ΔT files, monthly averaged ΔT and ΔT frequency fields are produced. The frequency fields represent the number of occurrences (days) in a month when ΔT was greater or equal to 0.5°C, for each pixel. This gives an indication of where warming is occurring regularly and may influence the long term mixed layer SST. The 0.5°C threshold was chosen because it marks the minimum temperature difference that can be reliably detected in the data. Furthermore, this threshold also rules out the influence of the cool skin effect (Saunders, 1967). Generally the cool skin effect applies equally to day and night data and any offset is not expected to be more than a few tenths of a degree and therefore is within the noise and can be ignored.

Binning the data to improve the confidence of the statistics and increase the number of day-night matchups was considered. The length-scale of diurnal warming is variable depending on the forcing fields, but is expected to be on the order of at least 10's km and therefore it is reasonable to average the data over a 3x3 to a 6x6 pixel box. However, while increasing the number of observations, improves the confidence of the statistic, it can also introduce error into the result. In boxes where no co-located day-night matchups exist, taking the day-night difference from different pixels within the box could result in the difference being taken across a surface thermal gradient, particularly at the edge of a diurnal warm patch on the ocean, and therefore the day-night difference would not purely represent diurnal warming. For this reason, the data is kept at 18km resolution and not binned.

3.3.2 Dealing with ΔT contamination

The day-night SST differences computed from AVHRR data can be contaminated by non-local heating and cooling processes. The two main sources of contamination are undetected cloud and advection of water masses.

3.3.2.1 Clouds

Undetected cloud will create a cool bias in a SST measurement. Jones et al. (1996) reported that cloud detection can be less successful at night because the visible channel

of the sensor is unavailable. Therefore, cloud-contaminated night-time pixels could create a positive ΔT which does not represent diurnal warming. To address this issue, the dataset is filtered to include only high quality data. The all-pixel Pathfinder product provides quality flags for each pixel ranging from 0 (bad) to 7 (good), based on a series of statistical tests (Kilpatrick et al., 2001). In this study, only pixels with a quality flag greater than four are used. Even with the quality control used in the study, the influence of cloud contamination will not be fully removed and it is therefore likely to create noise in the results. However the noise should be small compared to the strong diurnal warming signal.

3.3.2.2 Advection

Advection of warm water masses can also produce a positive ΔT. Regions of high surface variability (e.g. western boundary currents, eddies) can produce rapid shifts in SST over very short periods of time. Tanahashi et al. (2003) noted that small regions of anomalously high ΔT values, derived from satellite data, were caused by advection of water in high SST gradient regions. The overall influence of advection is not expected to have a positive day-night bias. The amplitude and sign should be random, creating negative ΔT as well as positive differences.

Previous studies of diurnal warming have addressed this influence by removing/identifying any possible advection-related ΔT data points either visually or by simple tests. Stramma et al. (1986) considered positive ΔT only when both $\Delta T_{(d\text{-}n)}$ and $\Delta T_{(d\text{-}(n\text{-}1))}$ were greater than 0.5K. This approach was applied to our data but since the number of ΔT matchups was already quite limited, the technique substantially reduced the final number of ΔT matchups and so was not used. Instead some simple tests were carried out to investigate the influence of advection. These tests included looking at the SST gradient and standard deviation within 3x3 and 5x5 pixel blocks to see if regions of high SST variability coincided with the diurnally warmed regions. These tests helped rule out any obvious influence of heat advection. No data was eliminated as advection contamination since the main regions of high variability did not correspond with the observed regions of diurnal warming. Some advection contamination is still expected which may contribute to the noisiness of the data, but it is not expected to overshadow the large scale warming patterns which are the focus of this chapter.

3.3.3 Methodology limitations

There are limitations to the methodology. First, daily ΔT fields do not have global coverage and contain missing data in regions where there are no day-night data matchups. The number of matchups is limited to where ascending and descending overpasses overlap and also to where regions are cloud free. Consequently, this method can not reveal complete global information about diurnal warming. In some regions, this has little impact as diurnal warming will not occur under cloudy conditions but it will affect tropical regions which are cloudy while still highly susceptible to diurnal warming. The results are likely to underestimate the real frequency of warming. Given the variability in the number of matchups, the number of diurnal warming occurrences (sometimes referred to as the 'frequency') is presented in this paper rather than monthly percentages of warming, to avoid any misinterpretation.

A more statistically meaningful representation of the 'frequency' of diurnal warming, such as a monthly probability or percentage of diurnal warming events, was considered. If the number of day-night matchups and the number of diurnal warming events are independent, then the true 'frequency' could be estimated by:

$$\text{True 'frequency'} = \frac{\text{No. of occurrences } \Delta T \geq 0.5°C}{\text{No. day/night matchups}} \tag{3.3}$$

However, since day-night matchups are limited to clear sky conditions (favourable for diurnal warming), the number of matchups and the number of diurnal warming events will be correlated. Consequently, without having a full time series of day-night matchups for every day of the month, it is not possible to estimate a true 'frequency' and for this reason, the 'frequency' is represented as the number of occurrences per month when $\Delta T \geq 0.5°C$. These fields provide an objective measurement which the reader can immediately relate to. Percentage/probability maps would require further information to interpret the results. Given the variability of the number of matchups, the 'frequency' results should be interpreted with caution and regarded as the minimum number of diurnal warming occurrences per month.

The second limitation is that ΔT, as defined from the Pathfinder SST product, is only a snapshot of the full diurnal cycle. It is unlikely to represent the maximum diurnal amplitude given the reported variability in the timing of the peak SST (Price et al., 1987). Stramma et al. (1986) matched AVHRR data with in situ observations and reported that the satellite-derived ΔT captured 40% to 95% of the full diurnal amplitude, with a mean of around 70%. Therefore, the ΔT computed in this study is likely to be smaller than the maximum diurnal amplitude. This effect is amplified further by the way the AVHRR data is quality checked. In one of the first quality flag steps, the SST pixel is compared against the weekly Reynolds & Smith (1994) 1° SST product. If the difference between the two is greater than 2°C, the data is flagged as bad quality. This step will dampen the diurnal warming signal present in the data. However, the focus of this study is not on the absolute amplitude but the frequency and spatio-temporal distribution of diurnal warming events. The method will reveal the regions being influenced by the diurnal cycle and provide a good indication of the strength of the warming. However it is important to be aware that the ΔT values are likely to be underestimated.

While this study can not provide complete details of the amplitude of the diurnal SST signal nor the true spatial extent of the warming because of missing ΔT values, it still provides the most comprehensive study into the global temporal and spatial distribution of diurnal warming. Over the last year, polar orbiting passive microwave satellites have been launched (e.g. AMSR-E on AQUA). These satellites have the potential to fill in the gaps since they can see through cloud. At present there are still technical algorithm issues to be resolved before the data can be confidently used for this type of study. The great advantage of AVHRR data is that due to its long lifetime and popularity, most issues have been resolved in the Pathfinder SST products. The 10 year ΔT record demonstrates the variability of the regions of warming, not only seasonally but also at interannual timescales to provide a global, and almost climatological, view of diurnal warming.

3.3.4 Model estimated diurnal SST variations

To verify that the results are consistent with expected diurnal warming and are not artefacts of the data processing or measurement errors, a simple regression model is

used to predict the regions susceptible to warming on the common assumption that it should only occur in regions of low wind and high insolation (Price et al., 1986). The aim of the comparison is to verify that the observed warming regions match the model results.

The model used in this study is that of Kawai & Kawamura (2002) who derived a simple regression equation to evaluate the maximum diurnal amplitude of SST, ΔT_{max}, based on daily mean wind speed and peak insolation measurements. Their model is based on a similar regression model by Webster et al. (1996). While Webster et al.'s model is derived from data from the Tropical Ocean Global Atmosphere (TOGA) Coupled Ocean-Atmosphere Response Experiment (COARE) for the tropical western Pacific, Kawai and Kawamura's model uses drifting and moored buoys from the tropics and mid-latitudes, yielding a better representation of ΔT_{max} outside the tropics. The model estimates the maximum diurnal amplitude of SST from the peak incoming radiation and the daily averaged wind speed, in the form:

$$\Delta T_{max} = a + bS^2 + c\log U + dS^2\log U \tag{3.4}$$

where a, b, c and d are coefficients (Table 3.1), ΔT_{max} is the predicted diurnal SST amplitude (°C), S is the daily peak incoming insolation (Wm^{-2}) and U is the daily averaged wind speed (m/s).

In this study, the model is used to estimate a monthly mean ΔT_{max}, $\Delta T_{max\text{-}mon}$, using monthly mean wind speed and short wave radiation. This method is not technically correct since the model is designed for daily fields. However the aim of the model comparison is not to compare the diurnal warming amplitudes and test the accuracy of the model but to use the model to predict where diurnal warming should occur given the mean wind and insolation conditions. The results are used as a qualitative spatio-temporal comparison to increase our confidence in the method used to produce the Pathfinder ΔT results and confirm that the observed ΔTs are consistent with the correct meteorological conditions. The absolute modelled ΔT values are not of interest.

Table 3.1: Coefficients for determination of ΔT_{max} from [3.3]

	Coefficient	$U_{0\text{-}24h} > 2.5$m/s	$U_{0\text{-}24h} \leq 2.5$m/s
SKIN	*a*	-7.3287×10^{-2}	-3.6700×10^{-1}
	b	3.2708×10^{-6}	5.6814×10^{-6}
	c	-7.9982×10^{-2}	4.0052×10^{-1}
	d	-1.3329×10^{-6}	-3.9637×10^{-6}
1m	*a*	-1.4236×10^{-1}	-1.0322×10^{-1}
	b	2.3989×10^{-6}	1.9361×10^{-6}
	c	5.7289×10^{-2}	1.4576×10^{-2}
	d	-9.2463×10^{-7}	-4.1966×10^{-7}

The wind and insolation data are interpolated onto a finer grid to match the Pathfinder SST resolution by using the 'nearest neighbour' technique. Since the model uses monthly fields rather than daily data, the coefficients are re-estimated by least squares fit to the observations. While this invariably tunes the model predicted amplitude of ΔT_{max_mon} to match the observations, it cannot significantly influence the spatial distribution of where warming occurs, since this is dominated by the coincidence of high insolation and low winds.

3.4 RESULTS

3.4.1 Daily ΔT maps

The focus of this work is on the large scale seasonal patterns of diurnal warming. Daily ΔT maps are not analysed individually. An example of the daily ΔT maps is shown in Figure 3.1 for six consecutive days during April 1989 in the Arabian Sea to reveal the characteristics of the daily ΔT data. The figure demonstrates the gaps in the field due to cloud and where the overpass paths do not overlap. The daily ΔT maps have been analysed in more detail by the Satellite Applications Group at the UK Met Office (Horrocks et al., 2003a). While daily ΔT maps reveal the characteristics of individual warming events, in order to look at the large scale temporal and spatial distribution of diurnal warming, which is the aim of the work, monthly fields are more useful.

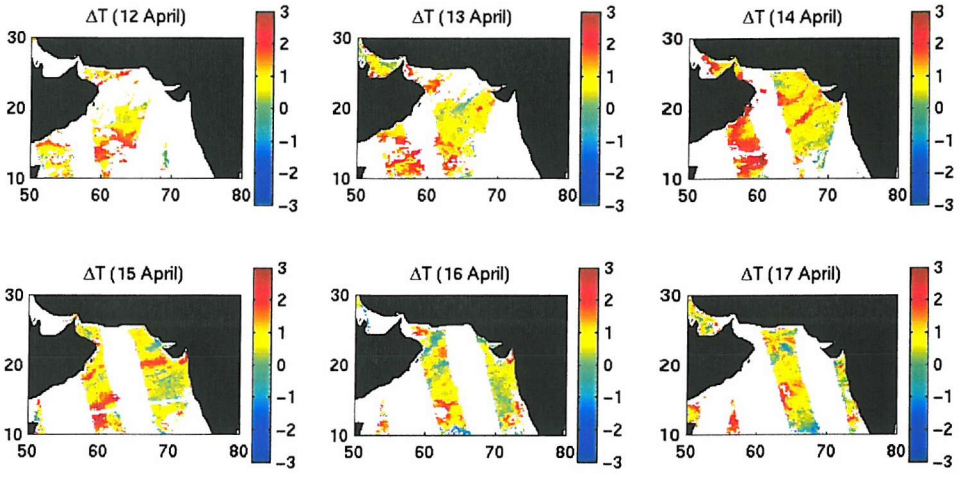

Figure 3.1: Examples of daily ΔT (°C) files for the Arabian Sea during the spring inter-monsoon.

3.4.2 Seasonal distribution of diurnal warming events

The work presented has been published as Stuart-Menteth et al. (2003)[1]. In that paper, four months of the year were presented to investigate the seasonal variations of the warming patterns: January, April, July and October. An example of the seasonal diurnal warming patterns is shown in Figure 3.2 for 1989. Other years can be found in Appendix A, as can figures for the full 12 months. Figure 3.2a reveals the distribution of the monthly averaged ΔT and Figure 3.2b shows the associated frequency of warming events greater or equal to the threshold of 0.5°C for a given month. Attention must be drawn to the fact that by averaging ΔT over a month, we are losing the information in which we are most interested: extreme diurnal amplitudes. However, the average will give an indication of how much the diurnal variability is affecting the monthly mean. Consequently these figures should be looked at in conjunction with the number of occurrences of diurnal warming to reveal the regions being frequently affected by diurnal warming which may not be obvious from the monthly average. The number of observations that make up the mean will vary greatly depending on the number of matchups. Typically the extra-tropics and mid-latitudes have the highest number of matchups in a month (>15) whereas regions in the tropics and high-latitudes may only have two to five matchups. The monthly mean ΔT maps are expected to be quite noisy compared to the frequency fields due primarily to the influence of cloud contamination.

[1] This work was carried out by Alice Stuart-Menteth. The co-authors only provided editing support when the manuscript was written.

Therefore any unrealistic values of ΔT near regions with no matchups should be ignored and treated as noise.

Figure 3.2a shows the spatial and seasonal distribution of diurnal warming events. White regions represent missing data where there are no day-night matchups over the whole month due to persistent cloud cover. There is a clear seasonal pattern with warming occurring in the summer mid-latitudes, in the tropics, particularly the western Pacific warm pool (WPWP) and the Indian Ocean, and in the northern Indian Ocean related to the inter-monsoon periods. In January, the most noticeable warming is around 20°S-40°S related to the austral summer high pressure systems. In April, warming is observed throughout the tropics, in particular the WPWP and Indian Ocean and in the northern Indian Ocean. April typically falls into the period of the Indian spring inter-monsoon which is characterised by clear skies and low winds (Dickey et al., 1998). Some warming is also present at mid-latitudes in the northern hemisphere. In July, the strongest warming is evident in the northern hemisphere mid-latitudes, again related to high pressure systems (e.g. Bermuda-Azores High). Warming is also evident in some parts of the tropics but its detection in this region is limited by cloud. Insolation can still be high in the tropics, in spite of the cloud, as the cloud is often patchy and has its own diurnal cycle (Yang & Slingo, 2001). In October, the main warming is in the tropics and the northern Indian Ocean. Warming in the Indian Ocean is related to the autumn inter-monsoon, which has similar meteorological conditions as the spring inter-monsoon but weaker incoming radiation (Dickey et al., 1998). This is consistent with the results where we observe smaller ΔT in October compared to April.

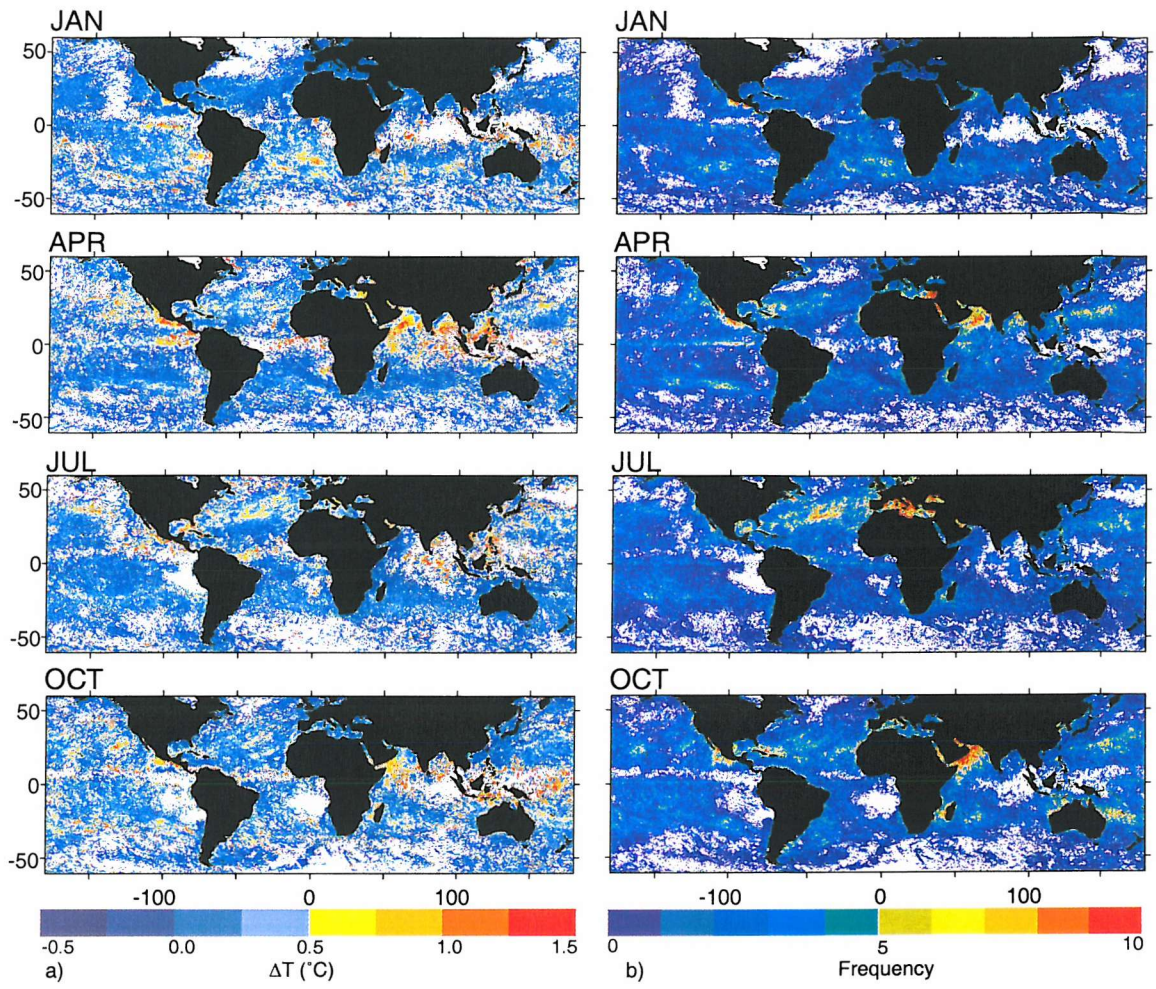

Figure 3.2: Seasonal distribution of diurnal warming for 1989. a) Monthly mean ΔT & b) number of occurrences (days) when $\Delta T \geq 0.5$°C (computed from daily day-night SST differences), for January, April, July and October (top to bottom). (See Appendix A for all months and years.)

Referring to the number of diurnal warming occurrences (Figure 3.2b), in January parts of the southern mid-latitudes and the northern extra-tropics (e.g. off the west coast of Mexico, Arabian Sea) show repeated warming. In April, the Arabian Sea and Bay of Bengal stand out, as well as other northern extra-tropical regions in the western Pacific and west of Mexico. Some repeated warming is also noted west of Madagascar and in the southern mid-latitudes of the Pacific Ocean. In July, northern mid-latitudes are frequently warmed, in particular the Mediterranean Sea and the mid-Atlantic. In October, frequent warming occurs in the Arabian Sea, west of Madagascar, north and east of Australia and again west of Mexico. Very little repeated warming is noted in the tropics due to clouds. It is important to consider that the tropical regions may also be highly susceptible to diurnal warming, which can not be detected using the infrared data. The combined interpretation of the monthly mean ΔT and frequency fields provides the most useful information about the distribution and variability of diurnal

warming. The monthly mean fields will reveal diurnal warming in places with very few monthly day-night SST matchups, while the frequency maps highlight clear sky regions that are susceptible to regular diurnal warming.

Figure 3.3 provides a closer look at the seasonal variability of the diurnal warming signal. The Arabian Sea is chosen as an example since it shows a strong seasonal warming pattern. The monthly mean ΔT is averaged over a 0.5°x0.5° box centred at 15.5°N, 61.5°E, in the north western part of the Arabian Sea, which coincides with the location of a Woods Hole Oceanographic Institution mooring, deployed during an Arabian Sea field experiment from October 1994 to October 1995. The description of the mooring data is given in Weller et al. (1998). Data from the uppermost thermistor (measuring SST), at 0.17m, is used to calculate $\Delta T_{d\text{-}n}$ at the corresponding overpass times of the satellite. The figure shows the monthly mean (continuous line) and maximum (dotted line) ΔT for both the PFSST (black) and the mooring observations (grey). There is a clear seasonal signal in the diurnal variability, related to the monsoon wind patterns which agrees well with observations from Weller et al. (1998). The mean ΔT approaches 1°C during the spring intermonsoon and decreases rapidly during the Southwest (SW) monsoon in the summer. The satellite observations show excellent agreement with the in situ ΔT measurements. While the skin is expected to have the larger diurnal cycle since ΔT decreases with depth, the results suggest that such differences in the diurnal ΔT amplitudes are cancelled out by cool skin effects in the surface microlayer. For most of the year, the monthly satellite and in situ means are almost identical. There is disagreement towards the start of the autumn intermonsoon in September where the PFSST shows very weak warming compared to the in situ data. Investigation into these months revealed that there were very few matchups available for this period due to cloud coverage and so the small ΔT are likely to be a result of these cloudy conditions or possibly the consequence of cloud contamination producing unrealistic results. The PFSST generally has a higher maximum ΔT amplitude which is expected since it represents the diurnal variability of the skin. The skin shows a maximum ΔT of 2.7°C in March and the in situ SST at 0.17m, a maximum ΔT of 2.3°C in April.

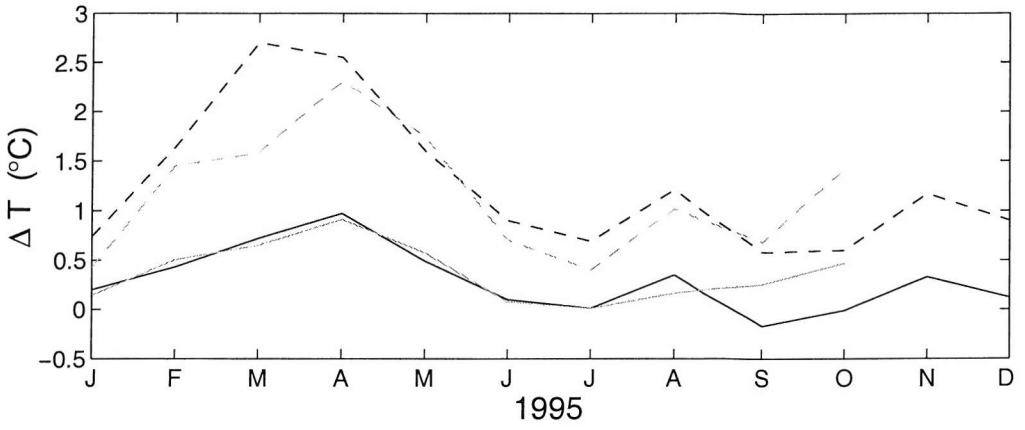

Figure 3.3: Seasonal cycle of diurnal warming in the Arabian Sea. Monthly mean & maximum ΔT are averaged over a 0.5°x0.5° box in the Arabian Sea to coincide with mooring data at 15.5°N, 61.5°E. Monthly mean in situ ΔT are computed for the local overpass times of the satellite. The continuous line represents the monthly mean ΔT and the dashed line, the monthly maximum ΔT. Black: PFSST ΔT and grey: in situ ΔT.

3.4.3 Model Comparison

To further increase confidence that the results represent diurnal warming, a monthly mean ΔT_{max} ($\Delta T_{max\text{-}mon}$) was modelled using only monthly averaged wind speed and insolation. An example of this is shown in Figure 3.4, which compares the modelled ΔT_m (Figure 3.4a) with the observed ΔT field (Figure 3.4b) for July 1993. As previously discussed in section 3.3.4, the predicted $\Delta T_{max\text{-}mon}$ values should not be expected to precisely match the observed ΔT fields. It is the spatial distribution of the warming that is of interest. Focusing on the regions with $\Delta T_{max\text{-}mon}$ around 0.5°C, one can identify the strong similarity between the two figures. There are some warming regions predicted by the model which do not appear in the observed ΔT field and these absences can mostly be ascribed to a lack of satellite day-night matchups (e.g. central Indian Ocean and parts of the tropical Atlantic). The same good agreement is seen for other months and years (not shown) implying that the satellite ΔT does represent diurnal warming.

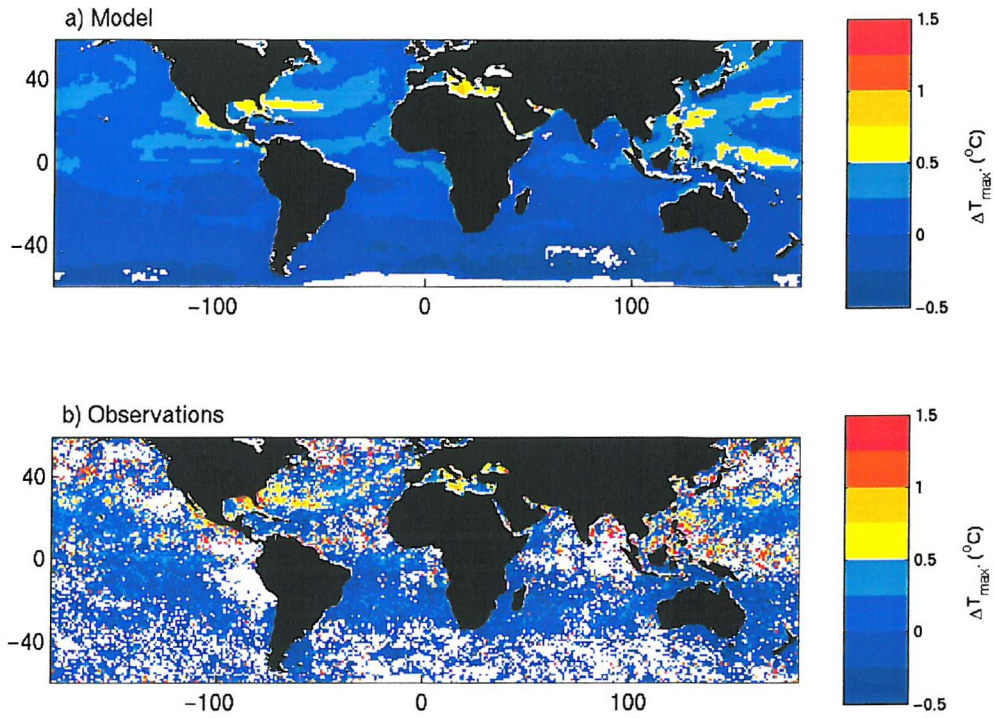

Figure 3.4: Monthly mean ΔT (°C) for July 1993. a) regression model simulation, b) observed Pathfinder mean.

3.4.4 Interannual distribution of diurnal warming events

To investigate the interannual variability of the warming patterns and to assess how typical the seasonal warming patterns described above are, other years are examined. Figure 3.5 presents the number of occurrences of diurnal warming for July for the ten years analysed in this study. The figure shows similar diurnal warming patterns across all years. The same regions are frequently affected: primarily the Mediterranean Sea, mid North Atlantic and the west Pacific. This consistency is not noted for all months. The results for January are examined in Figure 3.6. For this month there are noticeable differences in the diurnal warming maps between the different years. The warming patterns are typically in the same place but the frequency and strength of ΔT shows variability. From this figure, the frequency maps can be separated into three types, with years 1987, 1988, 1993 & 1994 revealing more frequent warming and years 1989, 1990, 1996-1998 showing a weaker pattern and finally 1995 showing almost no warming. 1987, 1988, 1993 and 1994 show a much stronger signal than the other years as well as more frequent warming as revealed in Figure 3.7, which presents the monthly mean ΔT for January. Again 1995 shows very weak warming. January 1994 reveals strong diurnal warming patterns outside the southern hemisphere mid-latitudes. This unusual pattern is discussed in more detail below.

Analysis into the full times series of monthly diurnal warming patterns for all months and years (Appendix A) reveals that 1993 & 1994 sometimes show quite different patterns from the other years, particularly from September 1993 to April 1994. Several months from 1987 & 1988 also show similar features. For ease of description, the data are divided into two groups to identify these differences. Group A refers to years 1989, 1990, 1995-1998 and Group B refers to years 1987, 1988, 1993 & 1994.

Investigation into these patterns revealed that years with the larger ΔT signals (Group B) coincide with periods when the satellite orbit had drifted. The orbit of the NOAA satellites gradually drifts over time, which results in a later overpass time. The two different types of warming patterns were found to coincide with the years with and without a significant orbit drift. Figure 3.8 shows the drift in the local afternoon overpass time for the NOAA satellites used in the Pathfinder SST time series from 1987 to 1999. The figure shows the gradual drift in the overpass time of each sensor until it is replaced by the next satellite. NOAA-9 was replaced by NOAA-11 in November 1988, which continued until its demise during September 1994. To bridge the gap between the launch of the next satellite, data from NOAA-9 was used until NOAA-14 became available on the 19th January 1995. At that time, the afternoon overpass time for NOAA-9 had drifted to around 9pm. Relating this to the two different warming groups, Group A refers to $\Delta T = T_{\sim 14:00} - T_{\sim 02:00}$ and Group B to $\Delta T = T_{(15:30\text{-}17:00)} - T_{(03:30\text{-}05:00)}$. The stronger and more frequent warming associated with group B may be attributed to the later overpass times. As the overpass time becomes later in the afternoon, the satellite may capture increased warming. The timing of the night-time overpass is not believed to be important in this context. Although in principle, cooling continues through the night, the change in temperature between midnight and dawn is expected to be small in comparison to SST changes during the afternoon. The weak warming during the reversion to NOAA-9 (14/09/1994 - 18/01/1995), as observed for January 1995 (Figures 3.6 & 3.7), is due to the very late overpass times.

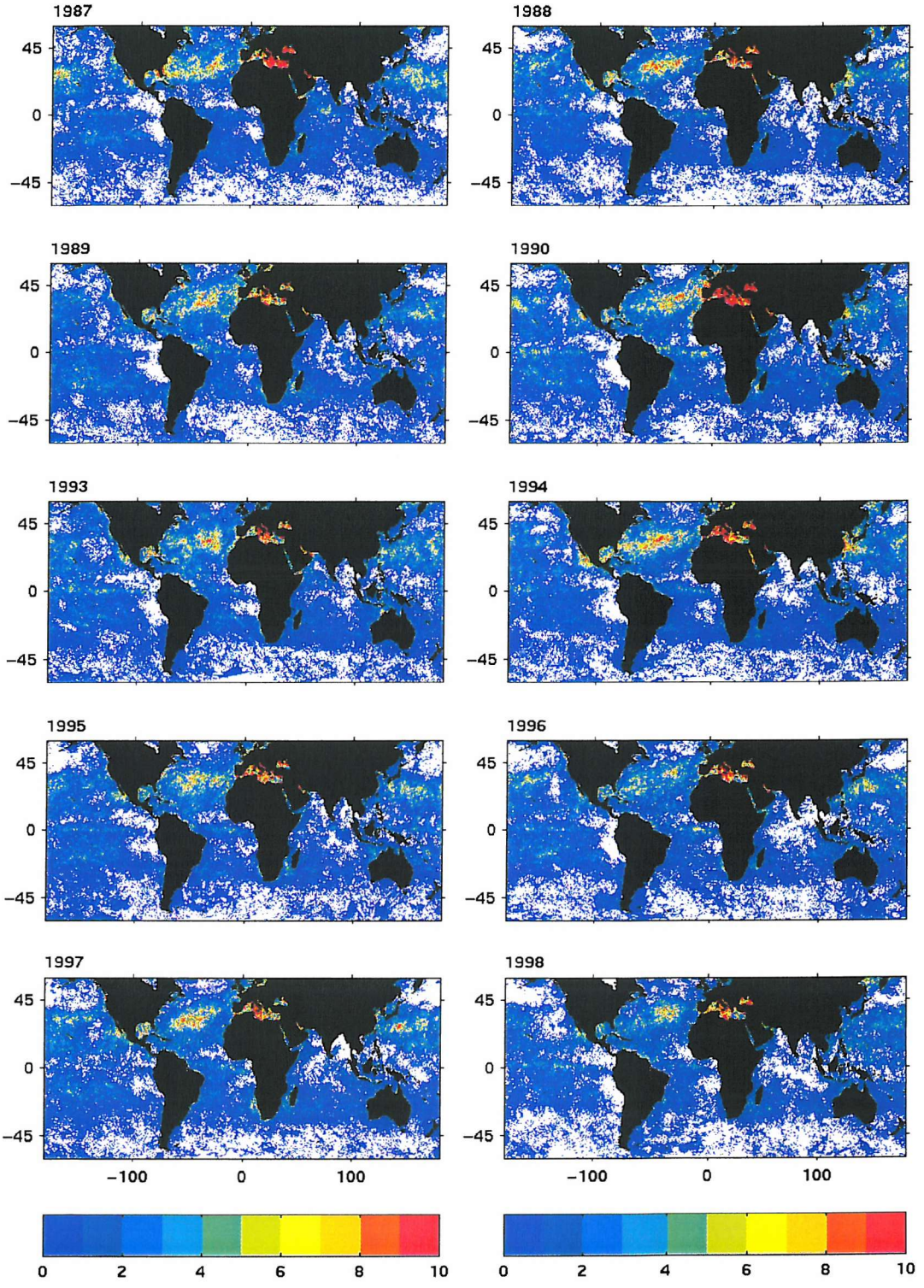

Figure 3.5: Interannual distribution of diurnal warming. Number of occurrences (days)/month when $\Delta T \geq 0.5$°C for July.

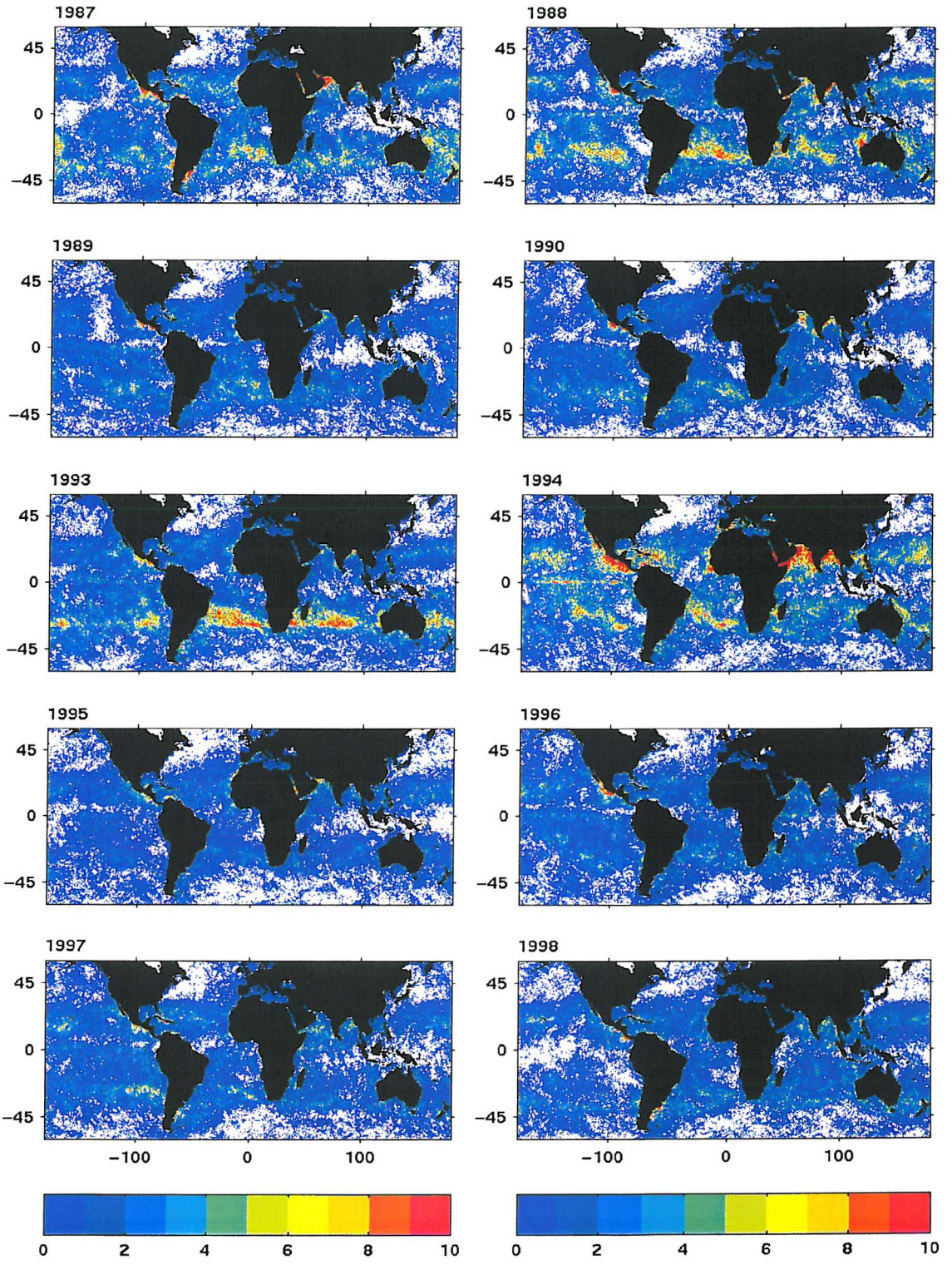

Figure 3.6: Interannual distribution of diurnal warming. Number of occurrences (days)/month when ΔT $\geq$ 0.5°C for January.

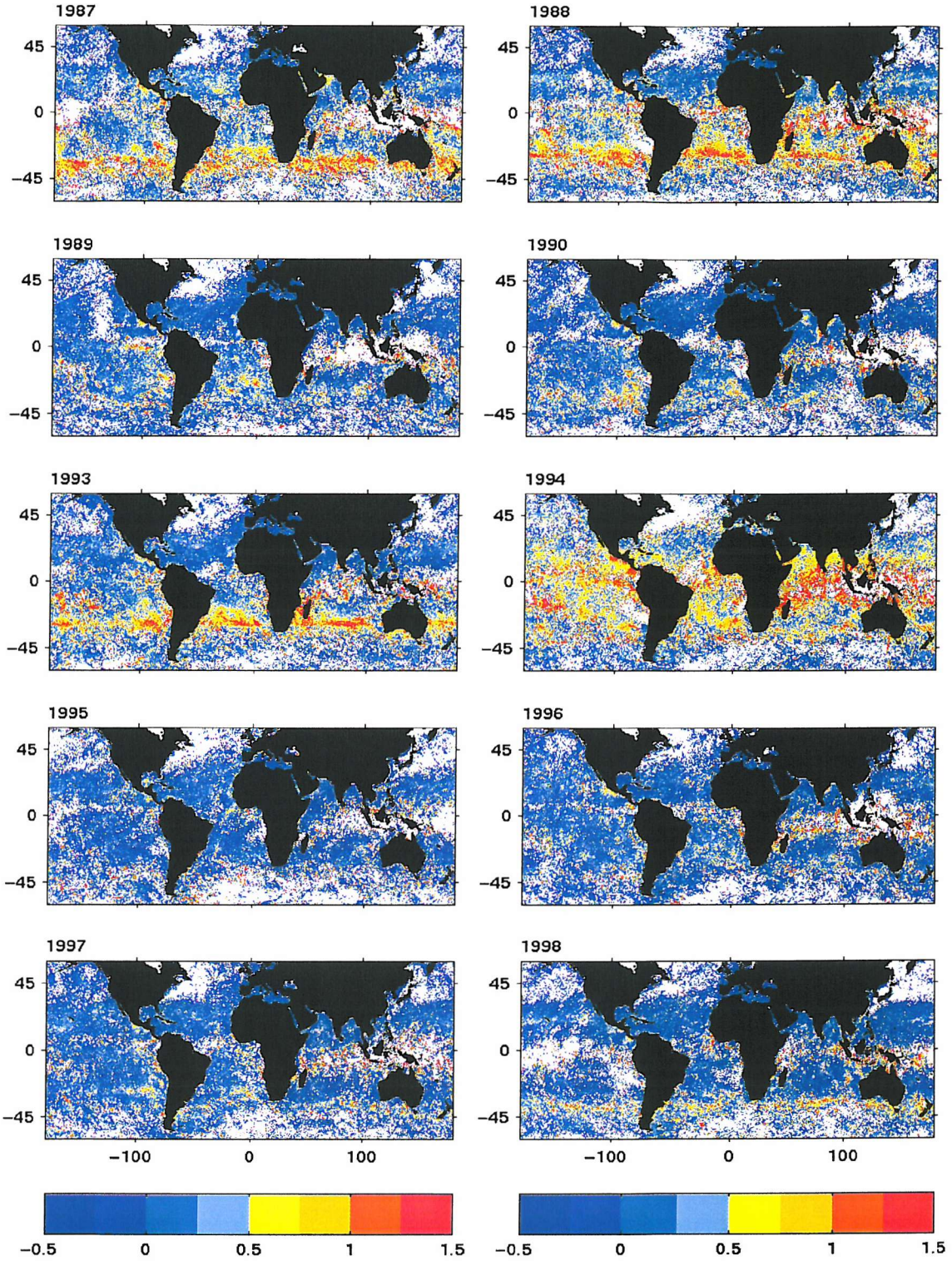

Figure 3.7: Interannual distribution of monthly mean ΔT. Monthly mean ΔT (°C) for January.

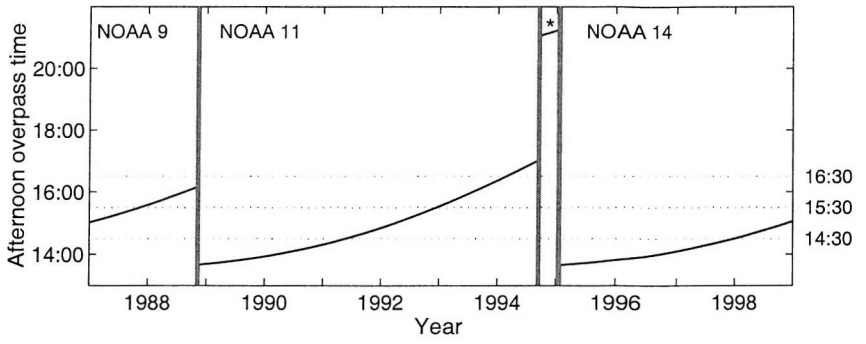

Figure 3.8: The local afternoon overpass time of the AVHRR-NOAA satellite series used in the Pathfinder SST, 1987-1999. Vertical lines mark the transition to a new sensor. * Between NOAA-11 and NOAA-14, there was a gap in the data which was filled by NOAA-9. The dotted horizontal lines mark out 14:30, 15:30 and 16:30 local time.

To rule out the possibility that the strengthened warming patterns could be attributed to shifting cloud patterns and therefore related to the distribution of day-night matchups at different local times of the day, the percentage of the warming is investigated. Figure 3.9 shows the zonally averaged percentage of warming greater than or equal to 0.5°C computed from the number of occurrences of diurnal warming for January for the same six years discussed in Figures 3.6 & 3.7. The black lines represent the Group B years (1987, 1988, 1993 & 1994) and the grey lines, Group A (1989, 1990, 1995-1998). The grey dotted line indicates 1995 and the black dotted line, 1994. Although 1995 belongs to Group A, two thirds of January 1995 falls in the NOAA-9 gap when the overpass times were much later in the day. Consequently 1995 shows the smallest percentage of warming. The Group B years show a much higher percentage of warming at the southern mid latitudes than the other years, confirming that, regardless of the number of matchups, the satellite is detecting stronger and more frequent warming. These results follow on from work by Privette et al. (1995) who warned that the AVHRR orbit drift could affect afternoon overpasses.

If the change in the local time of the overpass is believed to explain the variations in the signal for the southern hemisphere in January, one would expect other regions to show enhanced ΔT signals during the years associated with the orbit drift. Enhanced patterns are not observed throughout the year. They are mainly evident during autumn to early spring in the southern hemisphere mid-latitudes. This suggests that the time of the overpass cannot fully explain the interannual variability.

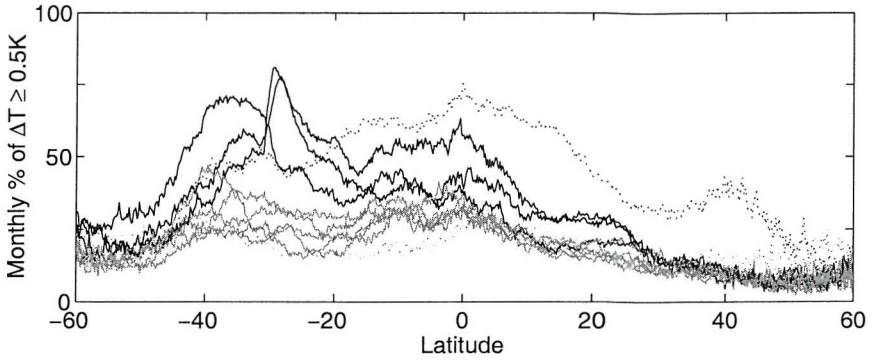

Figure 3.9: Zonally averaged percentage of ΔT for January for the same six years as Figures 4 & 5. The grey lines represent group A years (1989, 1990, 1996-1998), black lines group B years (1987, 1988 & 1993), the black dotted line January 1994 and the grey dotted line represents the NOAA-9 gap during January 1995. The percentage represents the fraction of time, out of the total number of monthly day-night match-ups, when $\Delta T \geq 0.5$°C.

There are two other factors that should also be considered. With relation to the orbit drift, Cao et al. (2001), reported that AVHRR SST were affected by regional solar contamination effects on the satellite's radiometric system, which resulted in regional and seasonal biases. It is unclear from this research where and when the biases occur but they may contribute to the ΔT signal. The contamination effect is only suggested to be ± 0.3°C and therefore should only amplify the signal and would rarely create a strong ΔT on its own. The final consideration is whether the differences reflect interannual variability in the forcing fields. The Group B years coincide with El Nino years but so however do 1997 and 1998 (Group A). Using monthly mean SSMI wind fields, a nine year mean and the corresponding monthly mean anomalies were computed. The SSMI wind data only start in 1988 so there are no data available to investigate 1987. The wind maps show that anomalously low winds conditions coincide with the strong diurnal warming signals during January 1988 and 1993 (Figure 3.10). It does not appear to explain the patterns in 1994 and there are no data for 1987. 1994 shows some of the most anomalous diurnal warming results (Figure 3.7 & Appendix A), revealing increased warming in the northern hemisphere sub-tropics which are not observed during any other year.

The results suggest that these interannual ΔT patterns can be due to a combination of factors. ΔT variability exists but at times it is hard to separate the effects of the amplification from meteorological forcing, the change in measurement time and external problems associated with solar contamination. The unexpected patterns in

September 1993 – April 1994 suggest that the signal is not purely geo-physical and that solar contamination may be influencing the SST signal. The differences are less obvious at other times during these years and during 1987 and 1988. The SSMI wind anomaly fields (Figure 3.10) support the increased warming signals during 1988 and 1993 and suggest calibration problems are not responsible. These complications reduce the confidence of the results for these years. For this reason Group B years should be interpreted with caution.

The concern relating to the orbit drift makes it harder to investigate and identify true interannual signals in the data. An obvious example to look for is the El Nino Southern Oscillation (ENSO). One would expect to detect variability in the diurnal warming patterns in the tropics related to the change in the oceanic and meteorological conditions during El Nino or La Nina. Initial analyses have detected some evidence of ENSO events in the data. Figure 3.11 shows the interannual diurnal warming variability for April for the tropical Pacific. For most years, a small band of diurnal warming is observed along the equator in the cold tongue region. Analysis of some historical satellite cloud and wind data from the Tropical rain measuring mission Microwave Imager (TMI) (not shown) confirm that these patterns coincide with low wind and clear skies. For three years, no diurnal warming pattern is evident (1987, 1993 & 1998). These three years coincide with El Nino years when the atmospheric patterns completely reverse from clear, dry conditions to wet convective periods. There are other interesting signs of interannual variability in the data. The Arabian Sea and Bay of Bengal show variability in the warming patterns which may provide useful information about the behaviour and timing of the monsoon system.

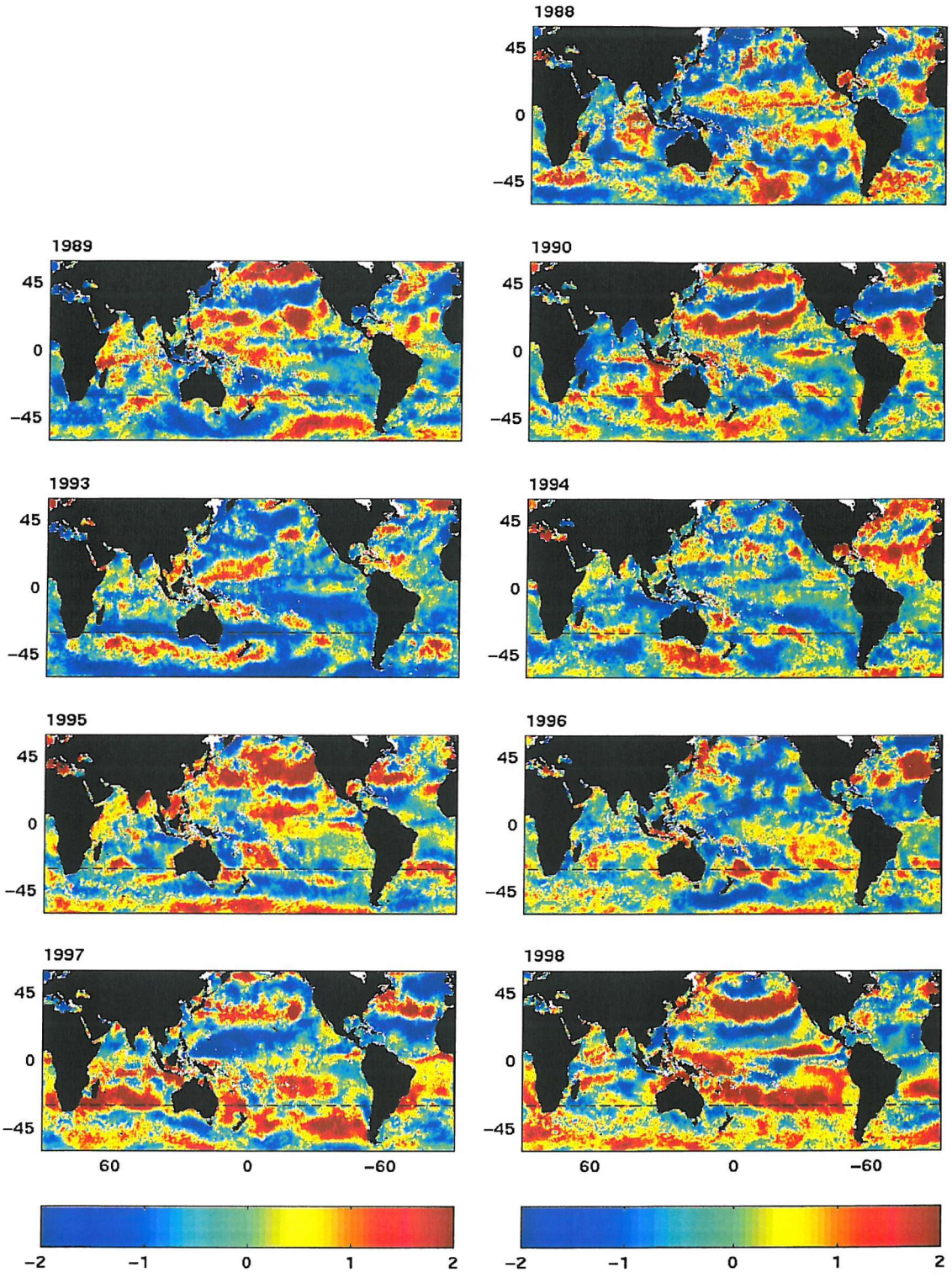

Figure 3.10: SSMI monthly mean wind anomaly fields (m/s) computed from a nine year mean (1988-1998) for January. The satellite was launched in late 1987 so there is no data available for 1987. The black dashed line marks 30° S.

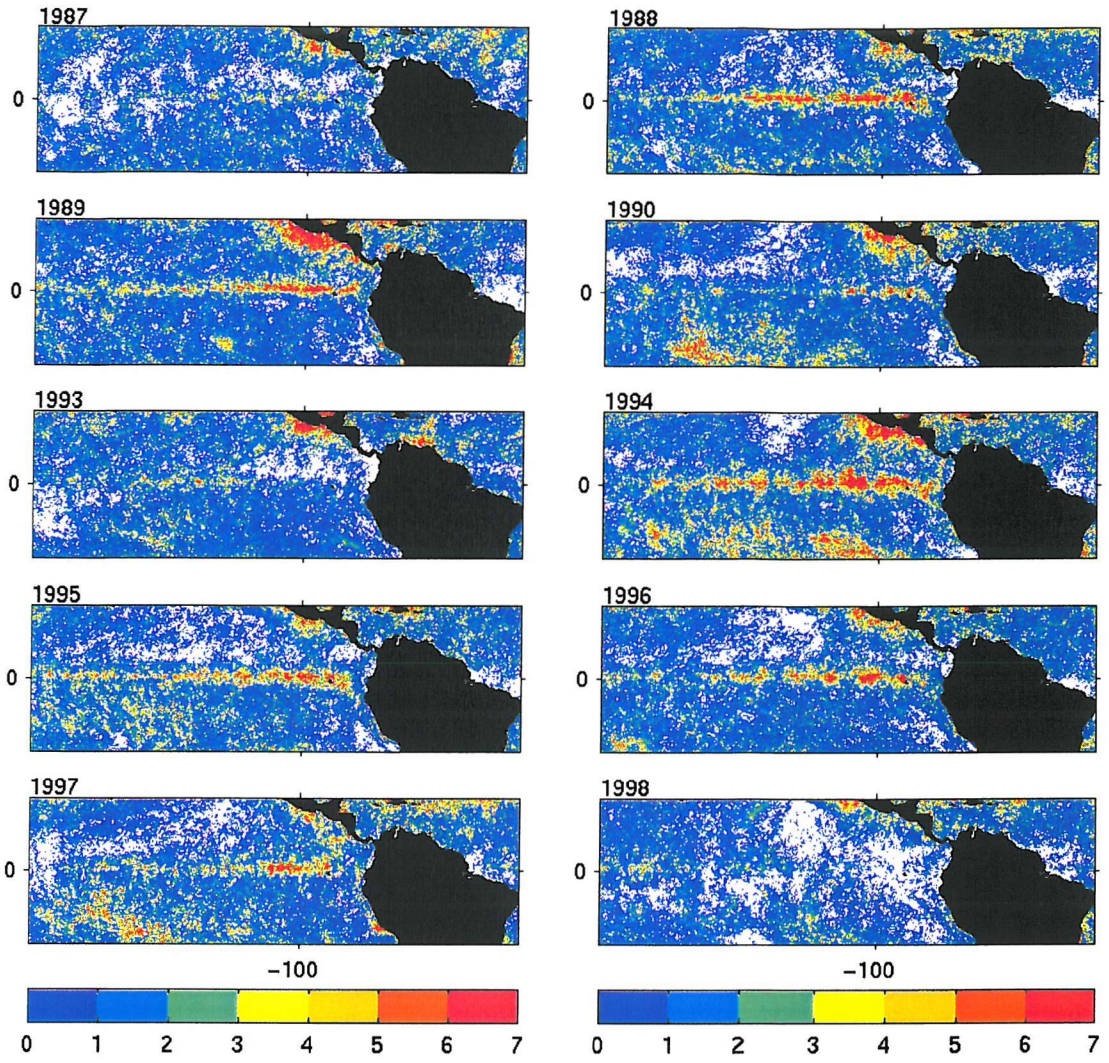

Figure 3.11: Interannual distribution of diurnal warming in eastern equatorial Pacific. Number of occurrences (days)/month when $\Delta T \geq 0.5$°C for April.

3.4.5 A climatological view of diurnal warming

Having identified the large scale temporal and spatial variability of the diurnal warming patterns and evaluated them against model fields and in situ data, six years are averaged to produce climatological maps of the warming patterns (Figure 3.12) for the mean ΔT and the number of occurrences when ΔT is greater or equal to 0.5°C. The full 12 months are presented in Appendix B. The average is made up of only Group A years with overpass times around 2am and 2pm to avoid using data which may be affected by non-geophysical processes as discussed in Section 3.4.4. This long term mean has its limitations regarding data coverage as already discussed but this is the best method possible at this time to approximate a climatology of diurnal warming. This climatology is only a starting point and it is hoped that by using these overpass times, it can be built upon as more data from AVHRR and other future satellites become

available. For example, the polar-orbiting AMSR-E has great potential to fill in the gaps in the cloudy tropical regions. Also the long time series of data recorded by the TAO/TRITON and PIRATA arrays, in the tropical Pacific and Atlantic respectively, could be used to fill in the gaps. The climatology shows a more complete view of the warming patterns. Persistent warming is evident in the tropics throughout the year while the extra-tropics and mid-latitudes show the seasonal patterns discussed earlier. Climatological ΔT values exceeding 0.5°C are typical and regions such as the tropical western Pacific warm pool and parts of the Indian Ocean and the sea off the west coast of Mexico reveal diurnal variability greater than 1°C. The frequency maps (Figure 3.10b) highlight the clear sky regions highly susceptible to diurnal warming, bringing out features that are not obvious from the mean ΔT fields. The frequency fields do not reveal the true frequency of warming events in the tropics, which can also be susceptible to regular warming in spite of cloud. The two maps should be interpreted together to provide the fullest understanding of the diurnal warming variability.

3.5 IMPLICATIONS

There are two main conclusions from this work. Firstly, the results have revealed that large regions of the world's ocean are susceptible to diurnal warming, consistent with the prediction of a simple empirical model. The spatial extent of these regions is considerable and can extend over the order of 10,000's km^2. The results show strong seasonal variability in the diurnal warming patterns related to the seasonal wind patterns and the solar insolation cycle. The distribution of diurnally warmed regions is generally dictated by the orientation of the overlying wind fields. In the open ocean, the orientation of the patterns is East-West coinciding with the large scale wind fields. This is an extension of the results found by Cornillon & Stramma (1985) for the Sargasso Sea. In the northern Indian Ocean, the distribution is driven by the monsoon cycle. Interannual variability is also present but its detection is complicated due to possible satellite orbit drift effects on the sensor. The long time series builds up a climatological view of the diurnal warming patterns providing concrete evidence of the regularity of the seasonal warming patterns.

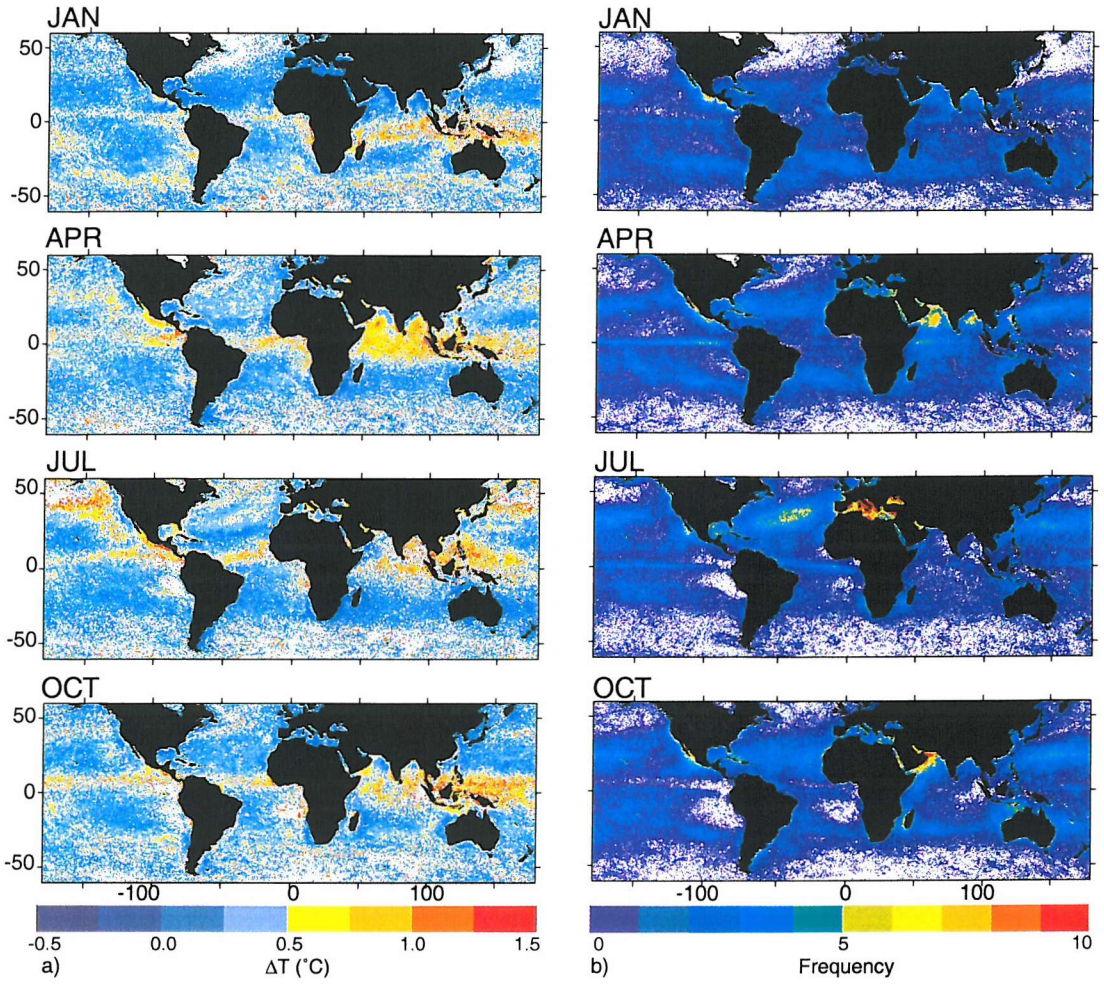

Figure 3.12: Seasonal climatological mean fields, made up of six years of Group A data, for January, April, July and October. (a) Climatological mean ΔT & (b) frequency maps when $\Delta T \geq 0.5$°C. (See Appendix B for all 12 months)

Persistent diurnal warming can rectify to longer timescales, influencing the intraseasonal SST and upper ocean heat content. Modelling studies in the tropics have already reported that the inclusion of diurnal forcing improves model solutions (Shinoda and Hendon, 1998; McCreary et al., 2001). The results presented here now demonstrate the extent of some of the regions affected by warming, highlighting where the oceans are strongly influenced by diurnal forcing. The results support modellers' suggestions that the diurnal cycle should be included in numerical models. Diurnal variations will have implications for heat and gas exchanges across the air-sea interface at short and longer timescales. The tropics are particularly sensitive to diurnal SST variability and studies by Webster et al. (1996) and Zeng & Dickinson (1998) have discussed the biases that can be introduced into the heat balance by not including the diurnal variations. Including the diurnal variability will increase the net heat flux out of the ocean. The

transfer of gas across the air-sea interface is also dependent on SST. McNeil & Merlivat (1996) report that diurnal variability can result in a reduction of soluble CO_2 and therefore higher atmospheric concentrations. These implications will be discussed in more detail in Chapter 7.

The second outcome of this work is the confirmation that diurnal warming signals exist in SST measurements. These results have important implications regarding the stability and accuracy of SST records. As research advances, SST users require highly accurate and stable records of SST. The results presented in this chapter have revealed the true importance of diurnal warming which many SST users have underestimated or ignored in the past. SST measurements can be biased depending on the local time of the measurement. While this study has only revealed the warming patterns for satellite-derived SST at the ocean's surface, one would expect a weaker but still significant diurnal cycle down to at least 1m. Therefore both satellite and most in situ SST can be 'contaminated' by the diurnal signal, questioning the stability of SST records. These diurnal amplitudes can easily be aliased into the climate signal and should not be ignored. The results also show additional biases caused by the solar contamination effects which have clearly not been fully addressed in the Pathfinder re-processing project.

3.6 SUMMARY

This chapter has presented a global view of the temporal and spatial distribution of diurnal warming using 10 years of AVHRR satellite data. The main points are summarised below:

- This is the first global assessment of diurnal warming. Although there have been studies in the past, they have been restricted to a fixed point or small region and limited in time. The results have shown that large regions of the oceans are frequently susceptible to diurnal warming, at mid-latitudes as well as the tropics. There is a strong seasonal signal in the distribution of the warming patterns related to the wind variability and the solar insolation cycle, which is observed each year.

- The results are consistent with a simple empirical model, based on the assumption that large diurnal SST variations occur only under low wind and high insolation conditions.

- There is evidence of interannual variability caused by meteorological patterns. The most outstanding variability is observed in the southern hemisphere during the austral summer months. Some of the patterns are coincident with anomalously low wind conditions but the interpretation of the signal is complicated by uncertainties caused by the orbit drift. There is evidence of ENSO-related variability and suggestion of changes associated with the timing of the Indian Ocean monsoon.

- A six year seasonal $\Delta T_{14:00\text{-}02:00}$ climatology has been presented for the first time, which highlights the strong spatial and temporal distribution of diurnal warming events.

CHAPTER 4: INFLUENCE OF CHLOROPHYLL ON DIURNAL STRATIFICATION

4.1 BACKGROUND

The aim of the next two chapters is to look at the sensitivity of diurnal warming and understand what factors influence its magnitude and phase. While there have been many studies on low wind processes, two areas have received little attention. Chapters 4 & 5 will look at the influence of water clarity and the time variability of the forcing fields on the evolution of diurnal stratification. Both these topics have been identified in the literature but have received limited attention.

The objective in this chapter is to investigate the influence of chlorophyll on the evolution of the diurnal warm layer. Several modelling studies of diurnal warming have discussed the importance of correctly parameterising the transmission of solar irradiance through the water column (e.g. Dickey & Simpson, 1983; Price et al., 1987; Stramska & Dickey, 1993). In the radiative regime when no wind mixing is present, the distribution of heat in the diurnal warm layer depends almost entirely on the vertical distribution of irradiance in the water column. As the sun's radiation enters the ocean, part of it is reflected away at the sea surface (albedo). The remaining incoming solar radiation penetrates the sea surface and is absorbed and scattered by water and suspended particles (Ivanoff, 1977). The absorbance of light is wavelength dependent, red light being absorbed first and the remaining visible (blue/green) light penetrating deeper. Almost half the incoming irradiance is absorbed within the top metre of the water column. The precise penetration depth of light is strongly dependent on the optical properties of the water column.

Chlorophyll plays an important role in the optical properties of the water column. Phytoplankton pigments strongly absorb blue light changing the spectral nature of the penetrating irradiance and the distribution of heat. If little or no chlorophyll is present, blue wavebands of light can penetrate deep into the water column. In the presence of chlorophyll, the irradiance is quickly absorbed by photosynthetic pigments, trapping more heat near the surface and causing the surface layer to heat up and become more stratified while the water below remains cooler. This is represented in the simple

schematic in Figure 4.1. The left side corresponds to oligotrophic conditions where blue light can penetrate deep into the water column, even below the mixed layer. The right-hand side represents chlorophyll-rich waters where the blue light is absorbed by chlorophyll pigments near the surface and heat is trapped in a shallower layer. In this situation, the SST can be expected to be warmer than the oligotrophic case, the mixed layer is shallower and the thermocline is more pronounced. Below the thermocline, the water is expected to be cooler than the oligotrophic case and there is an increased temperature contrast between the mixed layer and the water below.

The aim of this chapter is to assess if the presence of chlorophyll and its corresponding influence on the vertical irradiance profile will modify the diurnal cycle of SST. Modelling studies often report that they are unable to reproduce very large diurnal warming events under low winds which suggests that the distribution of irradiance in the top few metres of the water column is important for the evolution of the diurnal warm layer.

Over the last fifteen years, many studies have investigated the influence of penetrative solar radiation on the upper ocean heat budget, reporting that solar radiation absorption and radiant heating are influenced by the abundance of phytoplankton pigments (Dickey & Simpson, 1983; Lewis et al., 1990; Sathyendranath et al., 1991; Stramska & Dickey, 1993; Morel & Antoine, 1994; Siegel et al., 1995; Ohlmann et al., 1996, 1998, 2000; Ohlmann & Siegel, 2000; Nakamoto et al., 2000, 2001; Murtugudde et al., 2002). All these studies have been model-based, using solar transmission parameterisations to investigate the influence of chlorophyll pigments on the distribution of radiant energy through the water column.

The majority of these studies have focused on the impacts of chlorophyll on upper ocean dynamics and heat content on seasonal timescales. Sathyendranath et al. (1991) were among the first to document the bio-modulation effect of chlorophyll on SST. They used a modelling experiment to show that the inclusion of chlorophyll altered the upper ocean mixed layer structure and enhanced the large thermal contrast between the surface and deep waters which drives the meridional overturning circulation. Only two studies have investigated the influence of chlorophyll on high frequency processes such as diurnal stratification (Dickey & Simpson, 1983 and Stramska & Dickey, 1993).

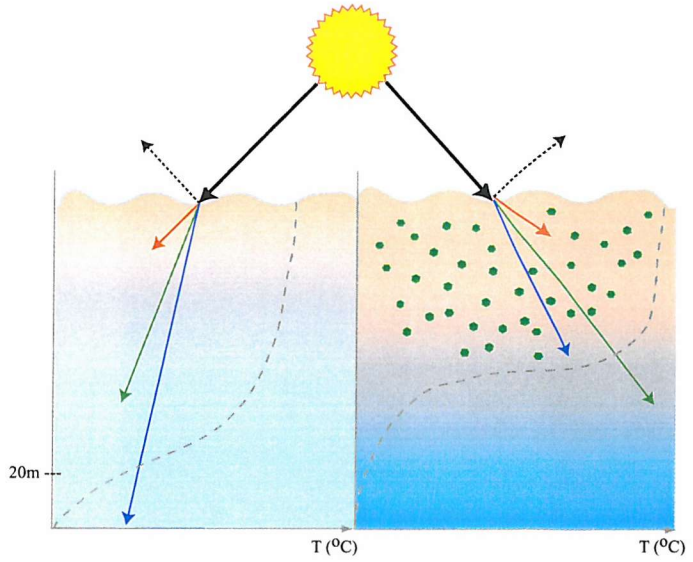

Figure 4.1: Schematic of influence of chlorophyll pigments on the transmission of solar irradiance through the water column under clear sky conditions.

Before these two studies are reviewed it is necessary to provide some additional background information. Any modelling study that wishes to investigate the relationship between chlorophyll and the upper ocean thermal field needs to consider what solar transmission parameterisation to use since this is how the influence of chlorophyll is implemented into a model. Several different parameterisations are available to predict the penetration of irradiance through the water column. A review of the main ones is given below. For diurnal warming applications it is important to use a full spectral parameterisation, which includes the infrared component, to accurately model the distribution of heat at and near the surface. The parameterisations are known as either solar transmission or absorption models. Both these naming conventions will be used in this chapter. There is no difference between transmission/absorption parameterisations: they are simply different ways to term the model.

4.1.1 Review of solar irradiance parameterisations

Parameterisations of downward irradiance have evolved considerably over the last thirty years. The effect of upward irradiance due to backscattering is neglected in solar irradiance parameterisations since the scattering effect is small (0.3-3%; Paulson & Simpson, 1977). The evolution of these models is briefly described here.

For optically homogenous water, the vertical distribution of downward irradiance is given by:

$$I_{(z)} = \int_{\lambda=0}^{\infty} I_{(\lambda,0^-)} e^{z/\zeta(\lambda)} d\lambda \tag{4.1}$$

where $I_{(z)}$ is the solar flux at depth, z (depth is negative); $\zeta_{(\lambda)}$ is the irradiance attenuation length for wavelength, λ.

One of the first and most frequently used approximations derived from the equation above (e.g. Denman, 1973), is:

$$I_{(z)} = I_{o-} e^{z/\zeta} \tag{4.2}$$

where I is the total (spectrally integrated) net flux of solar radiation at the base of the layer (depth, z), I_{o-} is total net solar flux just below the surface and ζ is the attenuation length.

This model assumes that light decays exponentially with depth at the same rate for all wavelengths and for light incident at any angle to the vertical. This assumption is a poor approximation (Paulson & Simpson, 1977) due to the preferential absorption of long- over short-wavelengths in the top metre of the water column and therefore is not suitable for the top 10m. Paulson and Simpson (1977) developed a two-band parameterisation, based on irradiance measurements between 400-1000 μm, that tried to resolve the downward irradiance in the top 10m, as well as below, by separating light into two distinct waveband groups (red light and visible blue/green light) to account for their different attenuation lengths:

$$I_{(z)} = I_o \left\{ R.e^{z/\zeta_1} + (1-R)e^{z/\zeta_2} \right\} \tag{4.3}$$

The first term characterises the rapid attenuation of light in the upper 5m due to absorption of the longwave (red) spectral components while the absorption of visible (blue-green) spectral components below a depth of 10m is characterised by the second term, where $\zeta_2 > \zeta_1$. The ultraviolet region is not included since its contribution is

relatively small compared to that in the red region of the spectrum. R represents the partition function between the two waveband groups.

Table 4.1: Coefficients for Paulson & Simpson (1977) bi-modal downward irradiance parameterisation

Jerlov Water Type	R	ζ_1 (m)	ζ_2 (m)
I	0.58	0.35	23
IA	0.62	0.60	20
IB	0.67	1.00	17
II	0.77	1.50	14
III	0.78	1.40	7.9

In recognition that the optical properties of the world's oceans are not uniform, Paulson and Simpson (1977) used data from Jerlov's (1968) water type classification study to determine R, ζ_1 and ζ_2 for each of the Jerlov water types (Table 4.1). Jerlov water types classify open ocean conditions from clear waters (Type I) to high chlorophyll waters (Type III).

A further development of this parameterisation was the spectral decomposition of the irradiance into several wavelength bands given by:

$$I_{(z)} = I_{o^-} \sum_{i=1}^{n} a_i e^{z/\zeta_i} \tag{4.4}$$

where n is the number of wavebands and a_i and ζ_i are analogous to R, ζ_1 and ζ_2 from [4.3]. Paulson & Simpson (1981) derived constants for nine waveband groups, using pure water data given by Defant (1961) (Table 4.2a). The waveband groups range from visible light through to the near and thermal infrared. Soloviev & Schlussel (1996) adapted this model and derived new attenuation lengths for the visible waveband group (i=1) for each of the Jerlov water types (Table 4.2b). This nine-band model covers the full spectral range, including the near and mid infrared energy which is a significant part of the solar irradiance.

Table 4.2a: Coefficients for Paulson & Simpson (1981) 9-band downward irradiance parameterisation

Wavelength (μm)	i	a_i	ζ_i (m)
0.2-0.6	1	0.237	34.849
0.6-0.9	2	0.360	2.2661
0.9-1.2	3	0.179	3.1486×10^{-2}
1.2-1.5	4	0.087	5.4831×10^{-3}
1.5-1.8	5	0.080	8.3170×10^{-4}
1.8-2.1	6	0.0246	1.2612×10^{-4}
2.1-2.4	7	0.025	3.1326×10^{-5}
2.4-2.7	8	0.007	7.8186×10^{-5}
2.7-3.0	9	0.0004	1.4427×10^{-5}

Table 4.2b: Coefficients for 1st band of Paulson & Simpson (1981) 9-band downward irradiance parameterisation, for different water types (Soloviev & Schlussel, 1986).

Jerlov Water Type	I	IA	IB	II	III
$\zeta_{i=1}$ (m)	15.15	13.16	11.36	7.58	2.62

The nine-band model was simplified to a three band model by Soloviev (1982). The coefficients for the three-band model were derived from cruise measurements, typical of water type IA (Table 4.3a). The range of the three waveband groups was not given in the paper, but it can be deduced from Table 4.3 that they range from visible light (i=1) through to thermal infrared (i=3). Different attenuation lengths, ζ, for the visible band (i=1) were taken from Jerlov (1968) to take into account different water types (Table 4.3b).

Table 4.3a: Coefficients for Soloviev (1982) 3-band downward irradiance parameterisation

i	a_i	ζ_i (m)
1	0.45	12.8
2	0.27	0.357
3	0.28	0.014

Table 4.3b: Coefficients for 1st band of Soloviev (1982) 3-band downward irradiance parameterisation, for different water types.

Jerlov Water Type	I	IA	IB
$\zeta_{i=1}$ (m)	14.08	12.82	10.0

Over the last ten years, coincident with the advent of ocean colour sensors in space such as CZCS and SeaWiFS, more sophisticated solar transmission parameterisations have been developed that rely on continuous, measurable physical and biological properties to determine the light attenuation coefficients (e.g. Morel, 1988; Morel & Antoine, 1994 and Ohlmann & Siegel, 2000). Morel & Antoine (1994) used profiles determined from a non-parameterised full spectral model to derive a new parameterisation dependent on

chlorophyll concentration and solar zenith angle. The irradiance is separated into two waveband groups: infrared and UV-visible. They acknowledge that the parameterisation is erroneous at the shallowest depths since they represent the infrared spectral region as a single exponential term. Ohlmann & Siegel (2000) developed a parameterisation from a set of irradiance profiles, generated from the HYDROLIGHT radiative transfer model (Ohlmann et al., 2000), to specifically resolve the distribution of irradiance in the top 10m of the water column. The parameterisation is based on chlorophyll concentration, solar zenith angle and cloud cover and is the first parameterisation that claims to resolve solar transmission within the top 2m. All other parameterisations acknowledge some degree of uncertainty near the surface.

The more recent parameterisations are expected to be more accurate for two main reasons. Firstly, they have been developed for all conditions using radiative transfer calculations. The older two-band, three-band and nine-band model coefficients are derived from sparse in situ data sets, with poor vertical resolution. Secondly, the recent models depend on continuous measurements to capture the exact oceanic conditions and do not categorise them into crude water types. Siegel & Dickey (1987) found that their measured vertical irradiance profiles did not compare favourably with the profiles predicted using the Jerlov classifications.

4.1.2 Review of relevant literature

It is crucial to correctly parameterise the penetration of irradiance when studying the upper ocean thermal structure. Simpson & Dickey (1981) were among the first to conclude this. They compared the difference between model runs using the one-band (e.g. Denman, 1973) and two-band (Paulson & Simpson, 1977) solar transmission parameterisations. They used a level 2.5 layer version of the Mellor-Yamada turbulence closure scheme 1-D mixed layer model (Mellor-Yamada, 1982) forced with constant wind stress and surface heating and ran the model with both parameterisations. They reported that at low to moderate winds (u<6m/s), the 2-band model showed sensitivity to wind speed which was not evident in the 1-band model. Under these conditions, the 2-band model produced warmer surface temperatures, shallower mixed layers and more intense thermoclines than the 1-band results. They concluded that it is crucial to properly parameterise downwelling irradiance to accurately predict upper ocean thermal structure.

Following these results, the same authors went on to examine the effects of water type on the diurnal evolution of the upper ocean (Dickey & Simpson, 1983). They used the same 1-D model as before, implemented with the Paulson & Simpson (1977) 2-band parameterisation to predict the penetration of radiant energy. The model was run for Type I and Type III waters, for a range of wind speeds. The Type I and Type III simulations were compared to assess the influence of chlorophyll on the upper ocean thermal structure. They reported contrasting effects for low winds (u<3 m/s) and moderate winds (3<u<6 m/s). At higher wind speeds the model was insensitive to the water type. For low winds, Type I water simulations had a larger diurnal SST amplitude, ΔT_{max}, than the Type III water, while for moderate winds, the Type III simulations had the larger ΔT_{max} amplitudes. They concluded that diurnal SST amplitudes and long term changes in heat content can be strongly influenced by water type and that optical properties of sea water should be considered when modelling the upper ocean structure and climate.

The study was developed further by Stramska & Dickey (1993) during the 1989 Marine Light Mixed Layer Experiment to examine the bio-physical feedbacks during the development of the seasonal thermocline and chlorophyll blooms just South of Iceland. The Mellor-Yamada model was used again but this time with a more detailed solar transmission parameterisation. The solar absorption model was broken down into 5nm wavelength groups. 50% of the light was absorbed in the top metre while the remaining energy, from the visible spectral range penetrated deeper. Morel's (1988) model was used to parameterise the vertical attenuation coefficient for visible wavebands as a function of chlorophyll. They compared model runs using the chlorophyll time series obtained during the field study against model runs using fixed phytoplankton concentrations. They reported that the presence of chlorophyll trapped heat nearer to the surface, creating stronger thermal stratification with increased heating near the surface and reduced heating at depth. The model was run for a range of chlorophyll concentrations and they reported SST changes as large as 2°C between chlorophyll concentrations of 0.2mg/m^3 to 20mg/m^3 in the top grid level of the model. In reality chlorophyll concentrations in the open ocean rarely exceed 3-4 mg/m^3. The differences caused by these concentrations (0 - 4mg/m^3) were reported to be no more than 0.5°C.

4.1.3 Research Aims

The studies described above highlight the importance of properly parameterising the downward penetration of irradiance through the water column when predicting the thermal structure of the upper ocean. It is important to use the most appropriate parameterisation and also to consider the optical properties of the water being investigated. The results presented in this chapter builds upon these studies. The work can be broken down into three parts. Firstly, chlorophyll measurements along with SST and meteorological data from a mooring in the Arabian Sea are analysed to try and identify evidence of the influence of chlorophyll on the diurnal warm layer. To investigate the relationship between chlorophyll and SST in more detail, a 1-D mixed layer model is used to examine how the thermal structure of the diurnal warm layer changes in response to increasing chlorophyll concentrations. The work focuses on realistic optical scenarios (chlorophyll concentrations between 0 to 5mg/m^{-3}) and does not look at the impact of very large chlorophyll concentrations since these are rarely found in open ocean conditions. Before, carrying out the modelling experiment, an intercomparison study is carried out for several different solar transmission parameterisations to assess which parameterisation should be used for the modelling work. Subsequently the observational results will be presented first, followed by the parameterisation intercomparison study and finally the modelling study.

4.2 DATA

Data from a Woods Hole Oceanographic Institution (WHOI) mooring deployed as part of the Arabian Sea Experiment during October 1994-1995 at 61.5°E and 15.5°N (Weller et al., 1998) is used in this study (Figure 4.2). The data was downloaded from the WHOI Upper Ocean Mooring Data Archive website (http://uop.whoi.edu/uopdata). The Arabian Sea is an excellent location in which to observe diurnal warming as the intermonsoon periods are characterised by low wind and clear skies (Dickey et al., 1998; Weller et al., 1998). The Arabian Sea Experiment was a multi-disciplinary project involving biological as well as physical measurements (Dickey et al., 1998). Meteorological measurements were obtained from a WHOI Improved METeorological (IMET) buoy and oceanographic instruments were deployed at a range of depths on a mooring line below the IMET buoy. The mooring had nine temperature measurements in the top 5m of the water column (at 0.17m, 0.5m, 1m, 1.5m, 2m, 2.5m, 3.5m, 4.5m,

5m) and a full suite of meteorological sensors. SST is provided at 15 minute resolution, and the meteorological variables, at 7.5 minute resolution. Several multi-variable moored systems (MVMSs), which included a fluorometer, were attached to the WHOI mooring. The fluorometer readings were converted to chlorophyll concentrations and for this study the uppermost chlorophyll measurements (10m) are used. Chlorophyll measurements are also available from water samples, taken at 10m depth, during several US Joint Global Ocean Flux Study (JGOFS) cruises (Kinkade et al., 1999) during the Arabian Sea Experiment.

The Arabian Sea is also an ideal region to investigate the relationship between chlorophyll concentrations and the upper ocean heat content. Sathyendranath et al. (1991), Dickey et al. (1998) and Nakamoto et al. (1999) report that chlorophyll levels play an important role in the evolution of SST. The Arabian Sea has large annual variations in SST and chlorophyll driven in part by the monsoon system and also by passing eddies (Fischer et al., 2002). In this region, the year can be divided into four seasons: the North East (NE) Monsoon (~November to February), the Spring Inter-Monsoon (SIM) (~February to May), the South West (SW) Monsoon (~June to September) and the Autumn Inter-Monsoon (AIM) (~September to October). Dickey et al. (1998) report the exact timings of the seasons for the experiment year as: NE monsoon (1/11/1994 – 15/2/1995), SIM (16/2/1995 – 31 May 1995), SW monsoon (1/6/1995 – 15/9/1995) and AIM (16/9/1995 – 15/10/1995).

The monsoon periods are associated with high winds while the inter-monsoon periods are associated with calm, clear sky conditions (Weller et al., 1998), ideal for diurnal warming. The SIM typically has larger diurnal warming events because insolation is at a maximum at that time of the year. The SW monsoon winds drive strong upwelling off the Somali coast which triggers a huge chlorophyll bloom in the area of the cold nutrient-rich water (Dickey et al., 1998). Chlorophyll blooms are also associated with the NE monsoon but on a smaller scale. During the field study, two other chlorophyll blooms were recorded which related to passing eddies (Dickey et al., 1998).

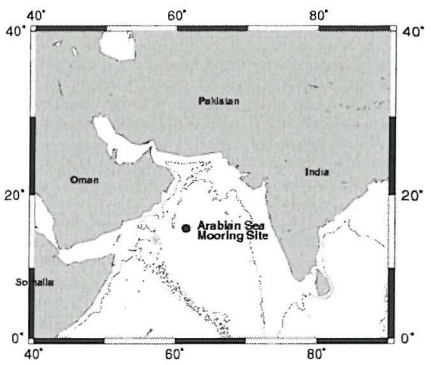

Figure 4.2: Location of WHOI Arabian Sea Mooring (from http://uop.whoi.edu/uopdata/arabiansea/images/arabian_sea_map.gif)

Figure 4.3 presents the mooring time series for SST, wind speed, downward shortwave radiation (insolation) and chlorophyll concentration. During the large monsoon-associated blooms, the fluorometer became badly biofouled and although the instrument was replaced mid-way through the experiment after the NE monsoon bloom, unfortunately there are few data available for the diurnal warming periods of interest. However, using a combination of cruise and mooring measurements a time series can be constructed and the data can still be used for the study (Figure 4.3d). The large chlorophyll blooms in December 1994 and late June 1995 are not related to the monsoons but are the result of passing eddies (Dickey et al., 1998). During the NE and SW monsoon bloom periods, the only chlorophyll information is provided by the JGOFS cruise measurements (represented as x).

Based on the time series shown in Figure 4.3, two six day periods of contrasting chlorophyll concentrations are selected to investigate the influence of chlorophyll concentrations on the formation of the diurnal warm layer. Ideally the two periods should have identical meteorological fields. However, it is impossible to select perfectly matching meteorological conditions and so two periods with the most similar meteorological conditions were chosen. The first period comes from the transition between the end of NE monsoon and the start of the SIM, when the NE monsoon bloom was still present, from 7th to 13th February 1995. The second period is from the end of the SIM, when chlorophyll levels are low, from 30th April to 6th May 1995. The first period is associated with moderately high concentrations of chlorophyll (~[1 mg/m^3]) remaining from the NE monsoon bloom while the second period is coincident with very low levels of chlorophyll (< 1mg/m^3) after the decay of this bloom. The first period is

termed as NEB (NE monsoon Bloom) and the second period, SIM (Spring Inter Monsoon). The two periods are overlaid in grey on Figure 4.3. Neither of these periods coincide with passing eddies and therefore the heat balance is expected to be local (1-D).

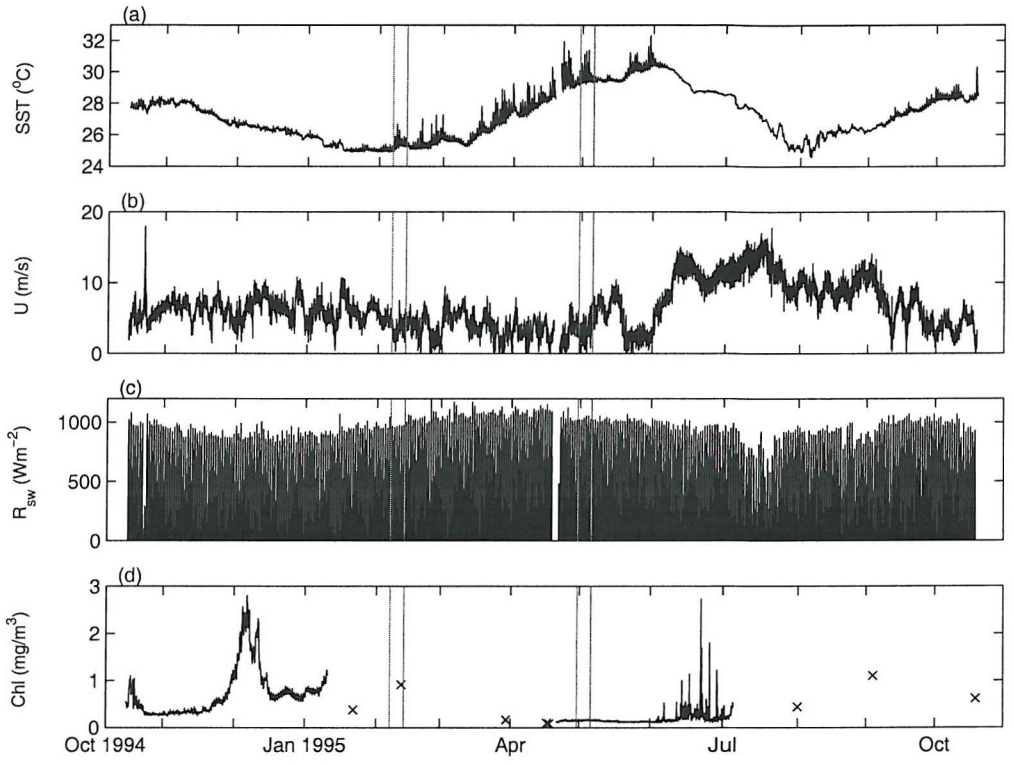

Figure 4.3: Time series (15 min. average) of (a) SST (0.17m), (b) wind speed, (c) downwelling shortwave radiation and (d) chlorophyll concentration. 'x' represent chlorophyll measurements obtained from US JGOFS cruises. The vertical lines mark the two six day periods used in this study.

4.3 METHOD

In this study the buoy and ship data described above are analysed to identify evidence that increasing chlorophyll concentration impacts the structure of the diurnal warm layer. The thermal structure of the top 5m of the water column, for the selected NEB and SIM periods, are compared against each other. To examine this relationship further, a numerical experiment is carried out to theoretically investigate the influence of increasing chlorophyll on the diurnal warm layer using the Price, Weller and Pinkel (1986) 1-D mixed layer model. Several different solar transmission parameterisations (Paulson & Simpson, 1977; Paulson & Simpson, 1981; Soloviev, 1982 and Ohlmann & Siegel, 2000) are tested in the model to assess the skill of each parameterisation. This is the first time a detailed optical parameterisation intercomparison has been carried out to

improve the simulation of the diurnal warm layer. The model runs are compared to the observed thermal fields and against each other. Having established the most accurate and appropriate parameterisation from the inter-comparison results, the PWP model is run with identical forcing conditions, taken from the buoy fluxes, for a range of different chlorophyll concentrations. The different model runs are compared to reveal whether chlorophyll can influence the evolution of the diurnal stratification.

4.3.1 PWP Model

The Price, Weller and Pinkel (1986; hereafter PWP) 1-D mixed layer model was developed to model the diurnal SST cycle. The PWP model was chosen over other 1-D mixed layer models for its simplicity and good record. A recent paper by Pritchard & Weller (2004) report that the PWP model performs better than the 2.5 layer turbulent closure scheme Mellor-Yamada model (Mellor & Yamada, 1982) and works well given its simple physics. Simpson & Dickey (1981) and Dickey & Simpson (1983) preferred to use a diffusive model rather than an integral model in order to distribute heat differentially through the water column. Bulk integral mixed layer models assume that the water temperature is well mixed within each grid level. The PWP model resolution is set to 0.25m which provides adequate detail of the radiant energy profile for this study.

The diurnal cycle is constrained in the model by vertical mixing and radiative heating processes driven solely by the local surface fluxes of heat and momentum:

$$\frac{\partial T}{\partial t} = \frac{-1}{\rho_o c}\frac{\partial F}{\partial z} \tag{4.5}$$

where $T_{(t,z)}$ is the temperature at time (t) and at depth (z), ρ_o is the density of sea water, c is the heat capacity of sea water and F is the heat flux.

The PWP approach is based on the dynamic instability model of Price et al. (1978) and differs from most other traditional bulk models by including mixing processes in the stratified fluid below the mixed layer to smooth the transition between the mixed layer and the water below it. There are three types of mixing process. The first simulates free convection caused by heat loss from the sea surface. The second and third are wind

driven and are the dominant mixing processes. The second mixing process replicates mixed layer entrainment by relaxation of an overall Richardson Number, R_b, and the third process simulates the effects of shear flow instability by relaxation of the Gradient Richardson Number, R_g. The Richardson numbers represent the ratio between buoyancy and shear. If the wind vanishes, both these processes are inactive and the only mixing is by free convection. Therefore diurnal warming can be categorised into two regimes: the radiative/free convection regime and the wind mixing regime. Given the simplicity of the model physics, vertical heat transport is purely driven by overturning created by momentum and/or static instability and does not include vertical transport processes created by turbulent convection, which can be important during diurnal warming conditions.

The solar irradiance absorbed over depth is modelled by the two-band parameterisation [4.3] of Paulson and Simpson (1977; hereafter PS77). Price et al. (1987) comment that the parameterisation could lead to considerable uncertainty in the radiation/convection regime because of the model's sensitivity to the optical properties, particularly for the long-waveband attenuation length, ζ_1. To investigate this uncertainty, the model is also run using the full spectral parameterisations of Paulson & Simpson (1981; hereafter PS81), Soloviev (1982; hereafter S82) and Ohlmann and Siegel (2000; hereafter OS00). PS77, PS81 and S82 have been discussed already in Section 4.1.1. A summary of the OS00 model is given below.

Ohlmann and Siegel solar transmission parameterisation

Ohlmann and Siegel (2000) developed a new solar transmission parameterisation based on results from HYDROLIGHT radiative transfer calculations (Ohlmann et al., 2000), and noted that the solar flux in the top few metres of the ocean can vary by $40 Wm^{-2}$. They reported that most of this variation could be explained by upper ocean chlorophyll concentrations, solar zenith angle and cloud amount. Chlorophyll is always important for predicting solar transmission whereas solar zenith angle and cloud amount are only considered for clear and cloudy conditions respectively.

OS00 developed an all-condition physically and biologically based solar transmission model that focuses on the heat distribution within the top 10m. It is the first parameterisation which attempts accurately to resolve the solar transmission in the top

few metres of the water column. The parameterisation is divided into two parts, with different models for clear sky (function of chlorophyll concentration, *chl*, and solar zenith angle, Θ) and cloudy sky conditions (function of chlorophyll concentration, *chl*, and cloud index, *CI*). The models were determined empirically by fitting curves, expressed as a sum of four exponential terms, to individual simulated irradiance profiles and takes the form:

$$I_{(z)} = I_{o+} \sum_{i=1}^{n=4} A_i e^{K_i z} \tag{4.6}$$

where A_i and K_i are determined from [4.7a] or [4.7b] for either clear sky or cloudy conditions respectively (where Y represents A_i and K_i):

$$Y = C_1.chl + C_3.\cos^{-1}\Theta + C_4 \qquad \text{(Clear Sky)} \tag{4.7a}$$

$$Y = C'_1.chl + C'_2.CI + C'_4 \qquad \text{(Cloudy Sky)} \tag{4.7b}$$

The choice of equation depends on the cloud conditions. The model estimates A_i and K_i using coefficients ($C_{1\text{-}4}$) which are read off from a table (Table 4.4). The coefficients are derived for cloudy and clear sky conditions. Only the clear sky model coefficients are tabulated here as the cloudy sky model is not applicable for this study. The parameterisation requires the downward irradiance just above the sea surface which differs from all the other parameterisations which require irradiance just below the surface. This allows varying albedo, associated with solar zenith angle and cloud, rather than relying on a fixed mean albedo which can introduce error.

Table 4.4: Linear regression coefficients for determination of the eight model parameters used in the clear sky solar transmission parameterisation (from Ohlmann & Siegel, 2000)

	C_1 (chl)	C_3 (zenith angle)	C_4
A_1	0.033	-0.025	0.419
A_2	-0.010	-0.007	0.231
A_3	-0.019	-0.003	0.195
A_4	-0.006	-0.004	0.154
K_1	0.066	0.006	0.066
K_2	0.396	-0.027	0.886
K_3	7.68	-2.49	17.81
K_4	51.27	13.14	665.19

4.3.2 Model Runs

Several model runs are performed using the PWP model. The model is forced using the surface fluxes calculated from the IMET meteorological measurements by the COARE bulk flux algorithm Version 3 (Fairall et al., 2003). The time step is set to 15 minutes and the depth interval is 0.25m. The model is initialised to the oceanic temperature and salinity profiles obtained from the WHOI mooring. To deal with cases of local advection at night and any concern of simplified model mixing in low winds, the model was run separately for each day using the temperature and salinity profiles from 6am local time to represent the most uniform conditions.

4.3.2.1 Optical model intercomparison runs

To carry out the solar transmission parameterisation intercomparison (with the aim to assess which parameterisation is most suitable to investigate the relationship between chlorophyll and SST), the model was run, for the NEB and SIM periods, using four different optical parameterisations:

- Paulson & Simpson (1997) - PS77
- Paulson & Simpson (1981) - PS81
- Soloviev (1982) - S82
- Ohlmann & Siegel (2000) - OS00

The parameterisations were run using either the observed chlorophyll concentration or with the attenuation coefficients selected for the appropriate water type, depending on the nature of the parameterisation. Morel (1988) developed a rough correspondence between chlorophyll concentration and Jerlov water type (Table 4.5) which was used to determine which set of coefficients should be used for the NEB and SIM periods. The NEB period was chosen to coincide closely with chlorophyll ship measurements taken on the 11th February, of approximately 1mg/m^3. For the SIM period, data from the mooring was available and a mean value over the six day period of 0.1 mg/m^3 is used. Referring to Table 4.5, the associated water types for the NEB and SIM period are II and IB respectively. For OS00, the chlorophyll value remains fixed over each 6 day period since there is not enough information to allow concentrations to vary with time.

Table 4.5: Approximate correspondence between Jerlov's Water Type classification and chlorophyll concentrations (from Morel (1988)).

Jerlov Water Type	I	IA	IB	II	III
[Chl] mg/m^3	0 - 0.01	~0.05	~0.1	~0.5	~1.5 - 2.0

4.3.2.2 Main model runs

Based on the results from the intercomparison study, the PWP model is run with the most appropriate optical parameterisation to investigate whether the presence of chlorophyll can influence the structure of the warm layer. The model is forced with the same fluxes for a range of different chlorophyll concentrations (0.1, 1, 2 & 5 mg/m^3). Carrying out the experiment in this way, allows the influence of chlorophyll to be isolated removing any additional influence due to meteorological variability, background oceanic state and advection.

Figure 4.4 shows how the irradiance profile, resulting from the OS00 parameterisation, varies over a range of chlorophyll values (setting cloud index to 0 and keeping solar zenith angle constant at 10°). This visualises how the amount of surface radiant energy absorbed over a given depth is expected to vary as a function of chlorophyll concentration. Assuming OS00 is physically based and theoretically sound, this figure serves as a helpful reference when interpreting the observations and model results. The figure shows that chlorophyll has little influence on the radiation absorbed in the top half metre but below 0.5m, it has a significant effect, absorbing and trapping more heat closer to the surface. A chlorophyll concentration of 3mg/m^3 can increase the absorption by approximately 10% at 2m and by 15% at 5m.

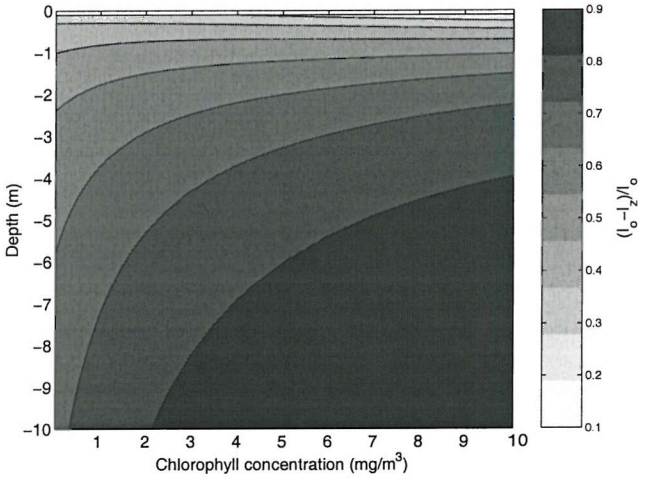

Figure 4.4: Percentage of cumulative irradiance absorbed over depth as a function of chlorophyll concentration ($[I_o - I_z]/I_o$). Irradiance profiles were modelled by the OS00 parameterisation.

4.4 RESULTS

4.4.1 Observations

Figure 4.5 shows the sea temperature measurements from the top 5m of the water column and the meteorological forcing (wind and insolation) during the two selected time periods (described in Section 4.2). Both are very clear periods with low to moderate winds. The SIM period has higher insolation than the NEB, which is explained by the different time of year. The SIM has slightly lower winds than the NEB period and therefore care must be taken not to confuse the meteorological forcing differences with the chlorophyll effect.

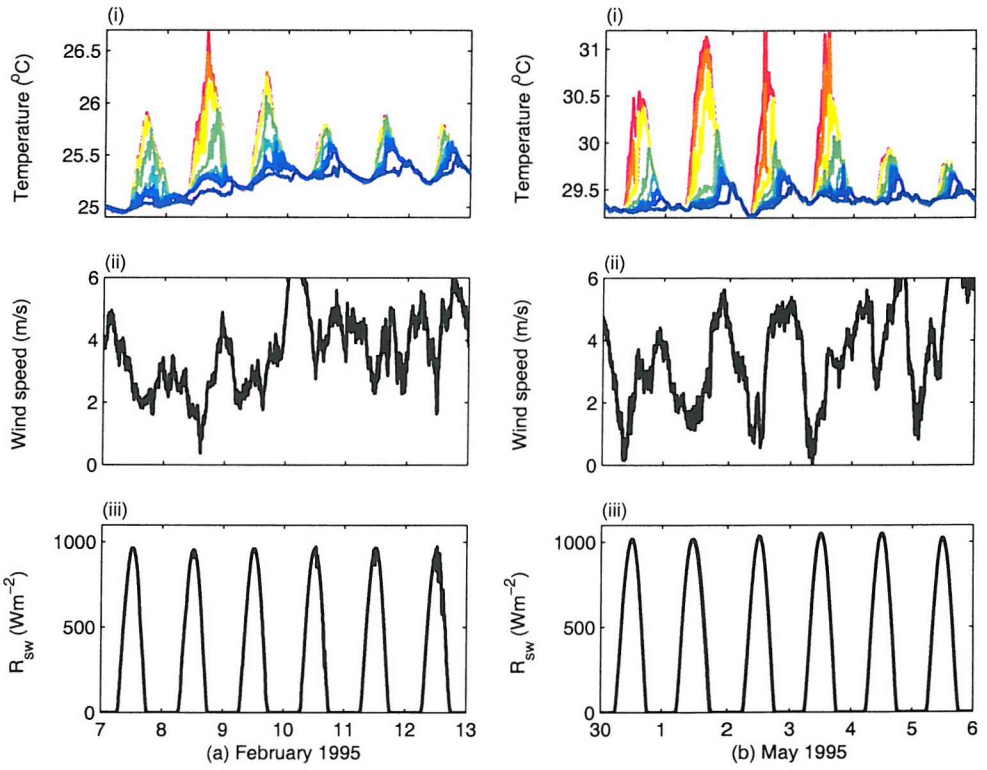

Figure 4.5: Time series of (i) temperature, (ii) wind speed and (iii) downwelling shortwave radiation for the (a) NEB period and (b) SIM period. The temperature plots show temperature at 0.17m (red), 1m (orange), 1.8m (yellow), 2.5m (green), 3.5m (light blue), 4.5m (royal blue), 5m (navy).

Figure 4.6 shows the temperature field in the top 5m of the water column measured by the WHOI mooring for the two 6 day periods. Despite the different SST values, the temperature range plotted is the same for both the SIM and NEB. There is quite a difference in the thermal structure between the two periods. Looking at the low chlorophyll period (SIM) first (Figure 4.6b), the diurnal thermocline is quite narrow with a sharp thermal contrast between the diurnal mixed layer and the cooler water below. In contrast, in the higher chlorophyll (NEB) case (Figure 4.6a), the shallow

diurnal warm layers have smoother gradients across the diurnal thermocline and weaker stratification. Even during the moderate wind periods (second half of each period) with deeper diurnal mixed layers, the two show quite contrasting structures with less heating evident during SIM. While these observations may appear to contradict what was discussed in relation to Figure 4.1, they actually tie in with what is theoretically expected to occur in the near surface for water with and without chlorophyll. It is important to note that we are now considering the influence of chlorophyll in the top few metres, not the top 20-30m.

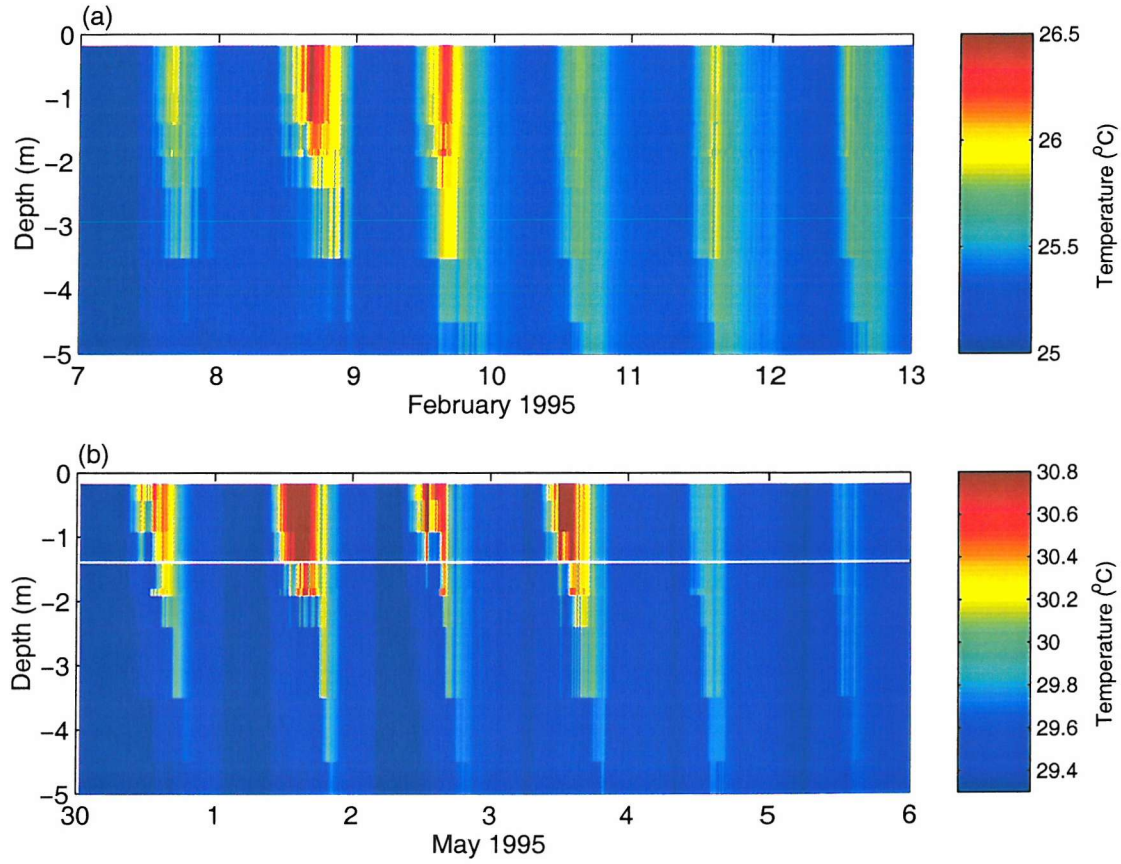

Figure 4.6: Thermal structure of upper 5m of the water column as measured by the WHOI mooring for (a) NEB period and (b) SIM period. Both figures have the same temperature range (1.5°C).

Low wind theory

During very low winds (< 3 m/s) , little/no mixing occurs and therefore the upper ocean becomes strongly stratified and the distribution of heat depends entirely on the distribution of the downward solar irradiance. Water with moderate or high chlorophyll concentrations will absorb more heat within the surface layers. In the top half metre, in the absence of mixing, chlorophyll will have little impact since the red light is absorbed rapidly near the surface. Below this depth, only blue-green light remains and in the

presence of chlorophyll pigments this is absorbed quickly, deepening the diurnal warm layer and smoothing the temperature gradients across the diurnal thermocline. This is visualised in the schematic shown in Figure 4.7. The influence of chlorophyll has a big impact on the erosion of the diurnal warm layer. In low chlorophyll conditions, due to the sharp contrast across the diurnal thermocline, the mixed layer will deepen quickly and the sea surface will cool. In the chlorophyll case, the increased heating below the diurnal mixed layer acts to moderate the cooling rate of the mixed layer by entraining relatively warm water.

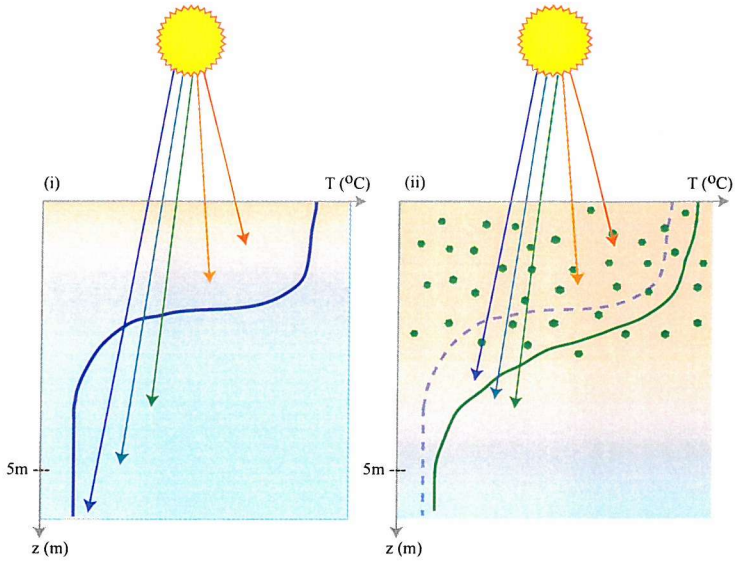

Figure 4.7: Schematic of absorption of heat in the diurnal mixed layer for (i) low chlorophyll and (ii) high chlorophyll conditions for low wind, clear sky conditions. The blue line represents the vertical profile of temperature for low chlorophyll conditions and the green line represents the temperature profile for high chlorophyll conditions.

Moderate wind theory

In the case of moderate winds (3 – 7 m/s), the top few metres will become well mixed and in the higher chlorophyll case, the overall temperature will be warmer since more heat is absorbed in the top few metres. In contrast to the low wind theory, the chlorophyll case for moderate winds may have a more marked diurnal thermocline.

Some of these results have been discussed before by Dickey and Simpson (1983) and Stramska and Dickey (1993) but this is the first time observations have been presented which appear to support the theory. Differences in meteorological forcing and ocean structure also contribute to the contrasts between the two periods. It is difficult to isolate the consequences of increasing chlorophyll concentration from those of varying

wind conditions and consequently a mixed layer model is used to isolate the influence of chlorophyll.

4.4.2 PWP model simulations

To separate the influence of meteorological forcing conditions from that of chlorophyll and to verify that the differences noted between the two periods reflect the chlorophyll influence to some extent, the bio-physical relationship is explored through the PWP 1-D mixed layer model. The model is forced with identical meteorological conditions, allowing only chlorophyll concentration to vary. Before this study is carried out it is important to assess the accuracy of the solar transmission parameterisations discussed in Section 4.3.2.1 so that the experiment can be performed using the most appropriate parameterisation.

4.4.2.1 Parameterisation intercomparison

Figure 4.8a presents the solar absorption profile of irradiance with depth (down to 5m) for the OS00, PS81, S82 and PS77 parameterisations for (i) low, (ii) moderate and (iii) high chlorophyll concentrations. There are quite large differences between the different parameterisations, particularly in the top metre. The profiles cross over each other at several depths.

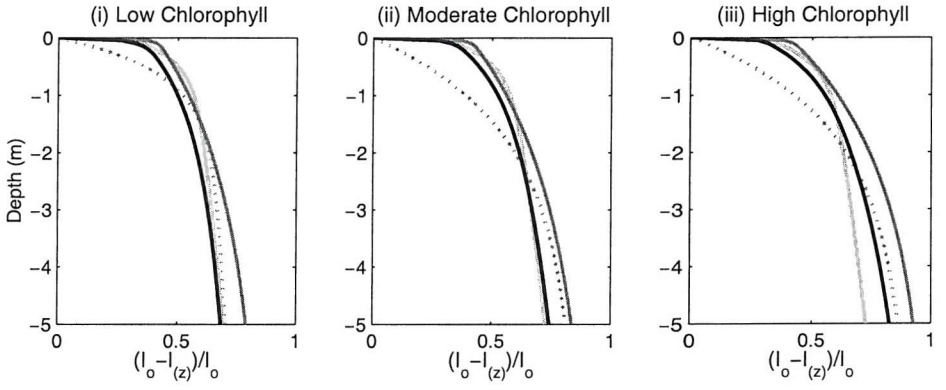

Figure 4.8a: Total irradiance absorbed (%) as a function of depth (to 5m) for four popular parameterisations. i) low chlorophyll (0.05 mg/m^3 / water type I), ii) moderate chlorophyll (1 mg/m^3 / water type II) and iii) high chlorophyll conditions (3mg/m^3 / water type III). Black: Ohlmann et al (2000), dark grey: 9-band Paulson & Simpson (1981), light grey: 3-band Soloviev (1982), dotted line: 2-band Paulson & Simpson (1977).

The presence of chlorophyll quickly increases (reduces) the absorption (transmission) compared to the clear water case. PS77 shows a much smoother absorption profile with less irradiance absorbed near the surface compared to the other models. The differences

between the models increase as chlorophyll concentrations increase. These differences are expected to affect the simulation of the diurnal warm layer in the absence of wind mixing.

Figure 4.8b shows a sub-sample of Figure 4.8a, focusing on the top 1m of the water column. PS81 absorbs more irradiance near the surface than the other models. PS77 profile is completely different from the other three parameterisations and is almost linear in comparison.

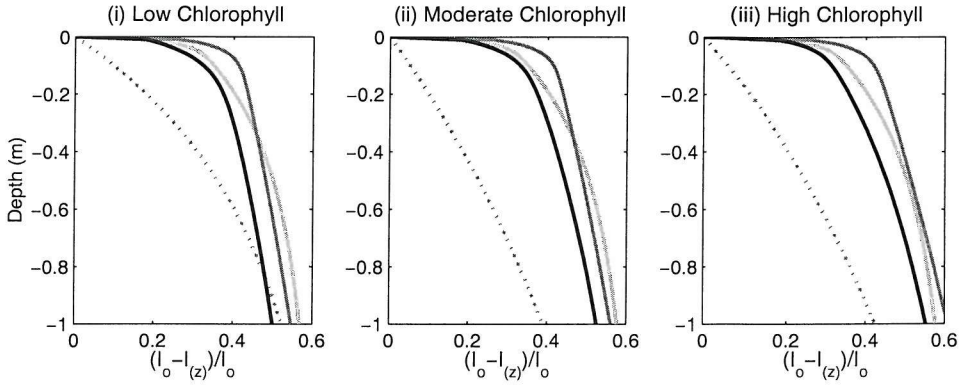

Figure 4.8b: Same as Figure 4.8a except for top 1m of the water column.

In Ohlmann & Siegel (2000), the OS00 model is compared against several of the other main parameterisations (Figure 4.9) in the literature. Transmission profiles were derived for each parameterisation and the root mean square error (rmse) profile from the HYDROLIGHT profiles were computed. The figure shows that all the parameterisations other than their own model had large rms errors in the top 1m. Based on this result, the OS00 parameterisation is expected to perform the best in this intercomparison study.

Figure 4.10 shows the model results for the NEB period. The top panel presents the observations (a) and the lower panels show the model runs using (b) OS00 and (c) PS77. Focusing on the red and yellow contours, the OS00 run captures the strength of the diurnal stratification well, clearly resolving the detail in the top 2m and predicting shallow mixed layers and evolution of the diurnal thermocline. It appears to slightly over-estimate the warming at the surface in the low wind cases (7^{th}-9^{th} February). In contrast the PS77 model clearly can not resolve the detailed structure of the warm layer. This is not unexpected after the earlier analysis of the absorption profiles (Figure 4.8).

In agreement with those profiles, the PS77 model absorbs less heat in the top 2m and as a result produces a deeper diurnal mixed layer, a smaller diurnal cycle and cooler SST.

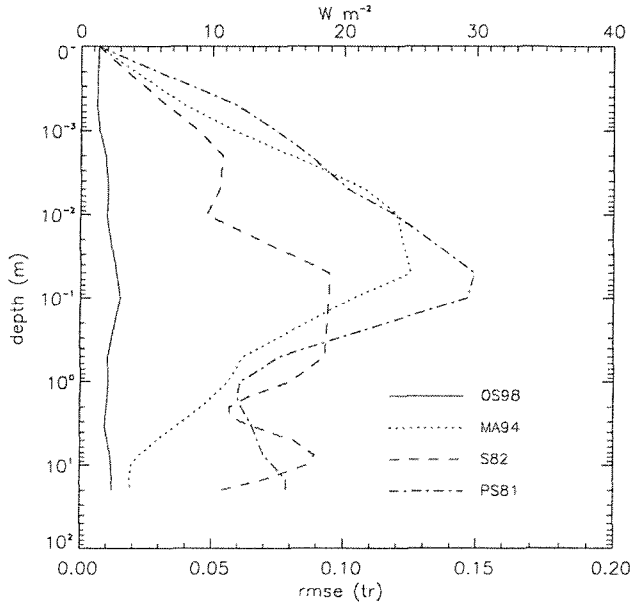

Figure 4.9: Taken from Ohlmann & Siegel (2000) Figure 7. Ensemble-average rmse profiled for the two-equation model Ohlmann & Siegel (2000) (solid line), the Morel & Antoine (1994: dotted line), the Soloviev (1982: dashed line), and the Paulson & Simpson (1981: dash-dot line) solar transmission parameterisations. The lower x-axis represents the rmse in the transmission and the upper x-axis represents the absolute solar flux (based on climatological surface irradiance of 200Wm^{-2}).

The same differences are observed for the SIM period (see Figure 4.11) although the PS77 model appears to predict more realistic warming in low wind conditions which may suggest that the IB coefficients are more reliable than the II coefficients. Both models capture the differences in the thermal gradients associated with the change in chlorophyll concentration. The chlorophyll effect is particularly obvious in the observations and model runs when comparing the moderate wind periods during NEB (10th-12th February) and SIM (4th & 5th April). Despite the SIM period having stronger insolation, it shows weaker warming during the moderate wind period in contrast to the NEB period. In the NEB, there is over 0.5°C of surface warming during moderate winds. This agrees with the moderate wind theoretical explanation discussed in 4.4.1.

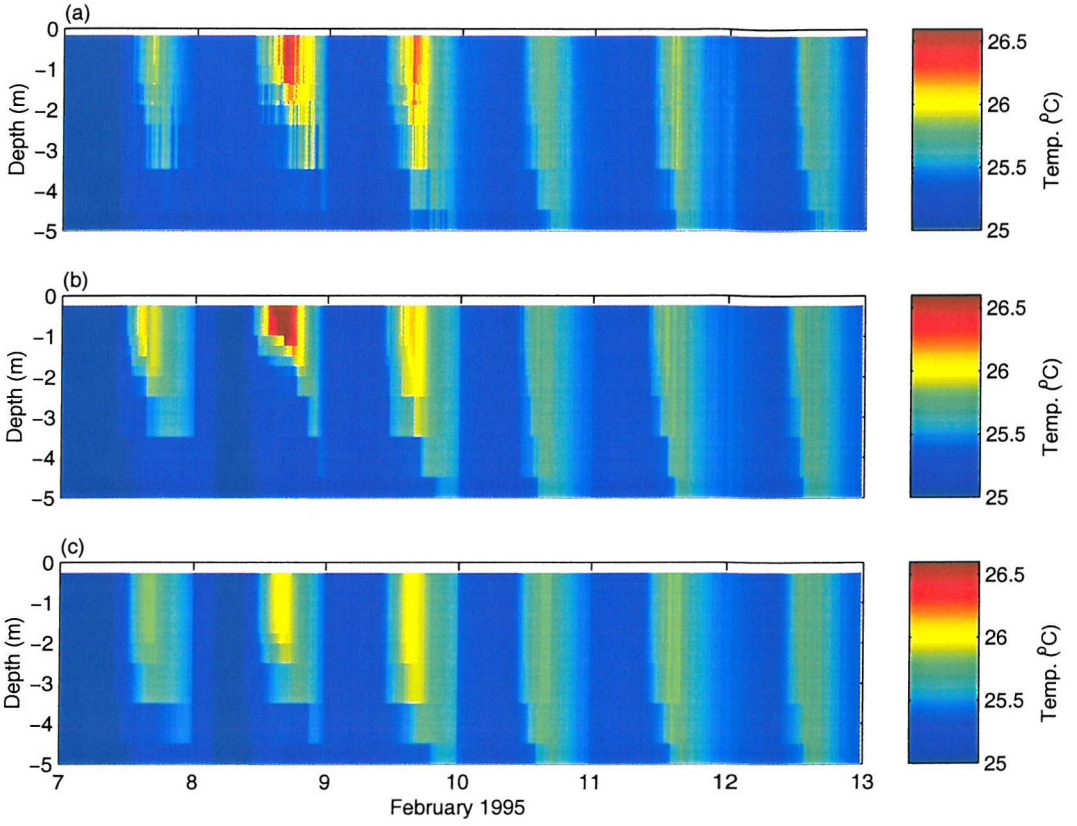

Figure 4.10: Thermal structure of top 5m during NEB (moderate chlorophyll) period. (a) observations, (b) PWP OS00 and (c) PWP PS77.

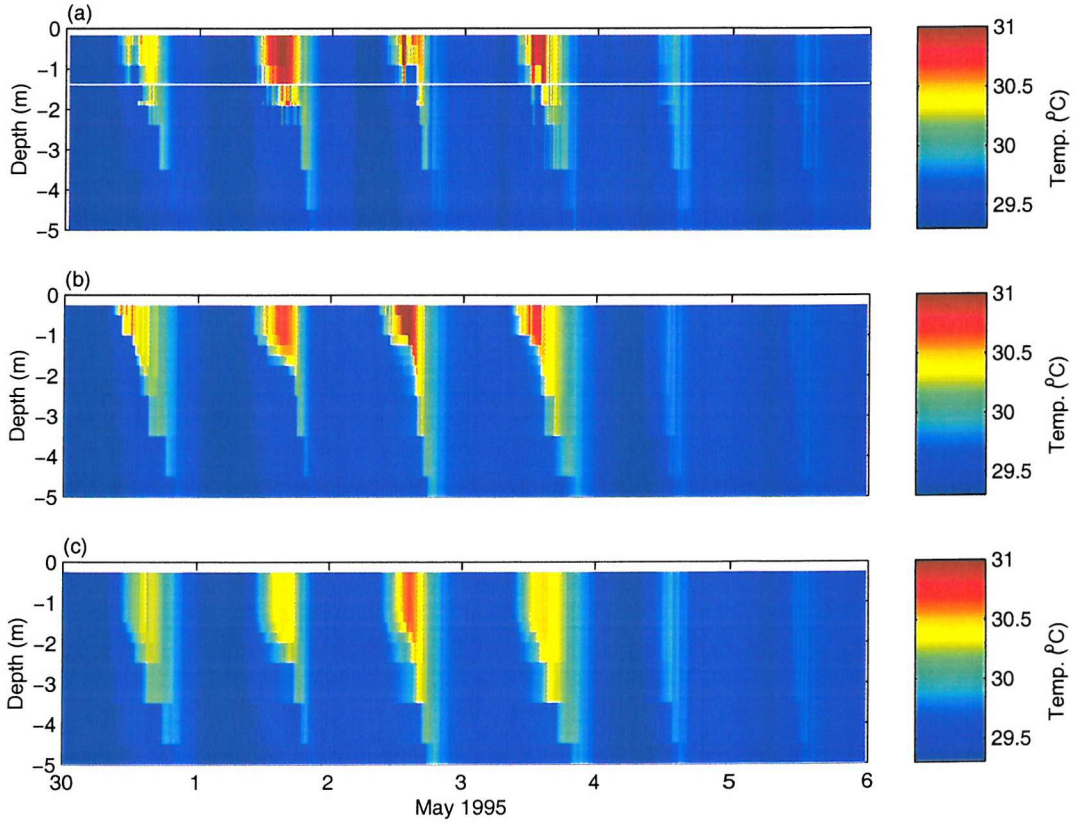

Figure 4.11: Thermal structure of top 5m during SIM (low chlorophyll) period. (a) observations, (b) PWP OS00 and (c) PWP PS77.

As part of this work, additional parameterisations (PS81 and S82) were tested and inter-compared. An example of the results is shown in Figure 4.12a for the 8th February from the NEB period (chl=1mg/m^3) and for 1st May (Figure 14.b) from the SIM period (chl=0.1mg/m^3). The upper panel (i) shows the observed field and the lower four panels present the model runs with the different parameterisations (ii) OS00, (iii) PS81, (iv) S82 and (v) PS77. The data are contoured to help identify the main differences between the different parameterisations. Looking at Figure 4.12a, the runs with full spectral parameterisations (Figure 4.12a ii, iii & iv) show good detail in the upper 2m of the water column in contrast to the 2-band parameterisation (Figure 4.12a v). There are differences between each of the runs which can be interpreted by referring back to the absorbance profiles of the different parameterisations (Figure 4.8a). The three full spectral parameterisation runs over-predict the maximum amount of heating at the surface. The largest bias is found in PS81 (which was also noted in Figure 4.8a to absorb the most energy near the surface). The OS00 and PS81 show good evolution of the diurnal mixed layer. The mixed layer produced by S82 is too shallow and the stratification across the thermocline is more intense than the other models and observations. In the second example (Figure 4.12b), OS00 and PS81 under-predict the surface heating while S82 captures the surface heat gain more accurately but again the mixed layer is too shallow. The varying success of the different parameterisations for the two days shown in Figure 4.12 suggests that the accuracy of the parameterisations may change for different chlorophyll concentrations or water types.

The OS00 parameterisation is chosen for the next stage of the study to investigate the influence of increasing chlorophyll concentration on the diurnal warm layer. It is the only full spectral model, which does not approximate the infrared absorption, that includes chlorophyll concentrations and is not based on crude water types which may limit the investigation. It is hard to conclude from the inter-comparison results whether OS00 is more accurate than PS81 and S82 but based on the results from OS00 and Figure 4.9, it is taken to be the most reliable. OS00 state that "*The primary strength of the parameterisation lies in its ability to accurately resolve solar transmission variations within the top few metres of the ocean. It is in this depth range that existing parameterisations are only approximate*".

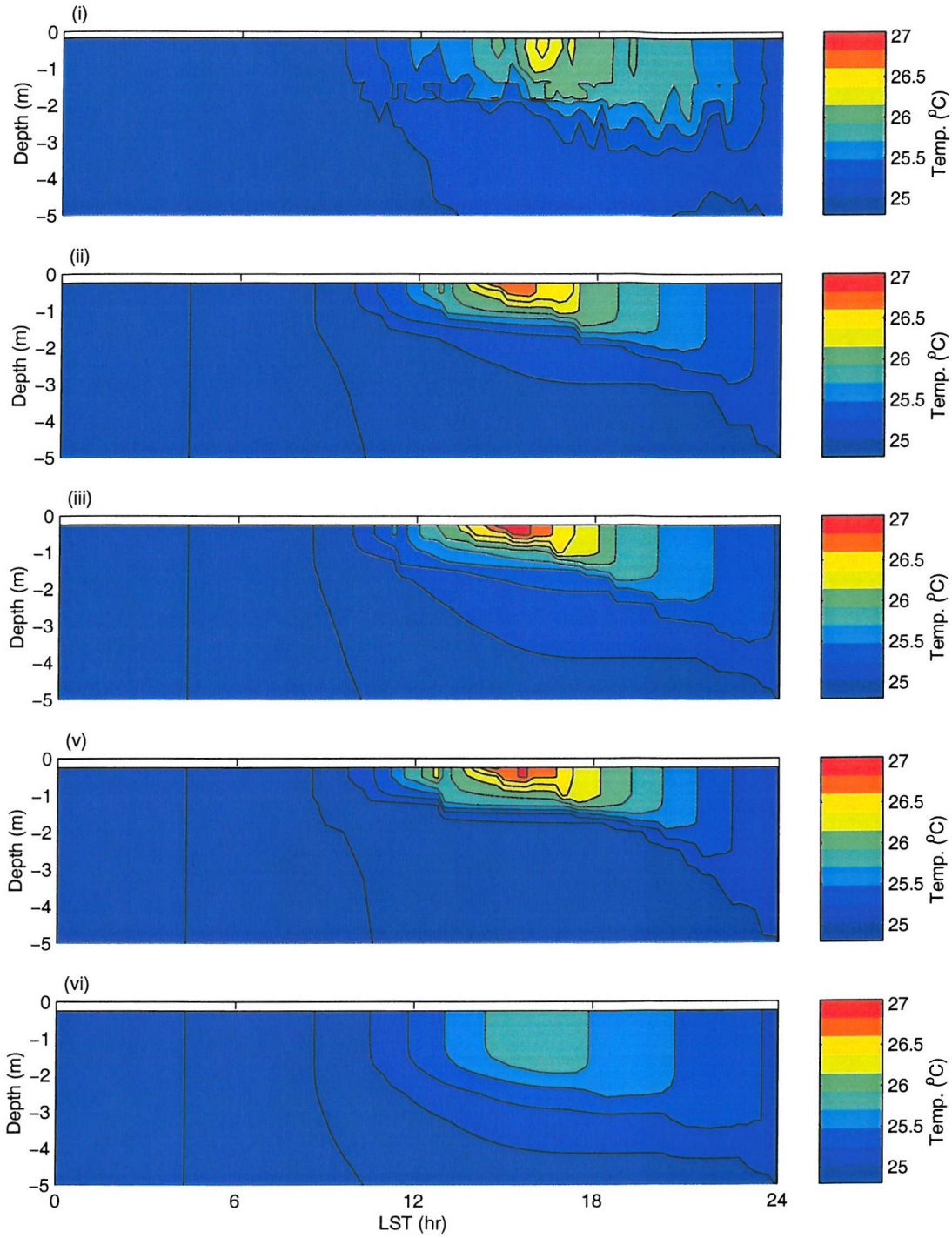

Figure 4.12a: Thermal structure of the top 5m of the water column for 8th February (chl = 1 mg/m^3). Solar transmission inter-comparison: (i) Observations, (ii) PWP OS00, (iii) PWP PS81, (iv) PWP S82 and (v) PWP PS77.

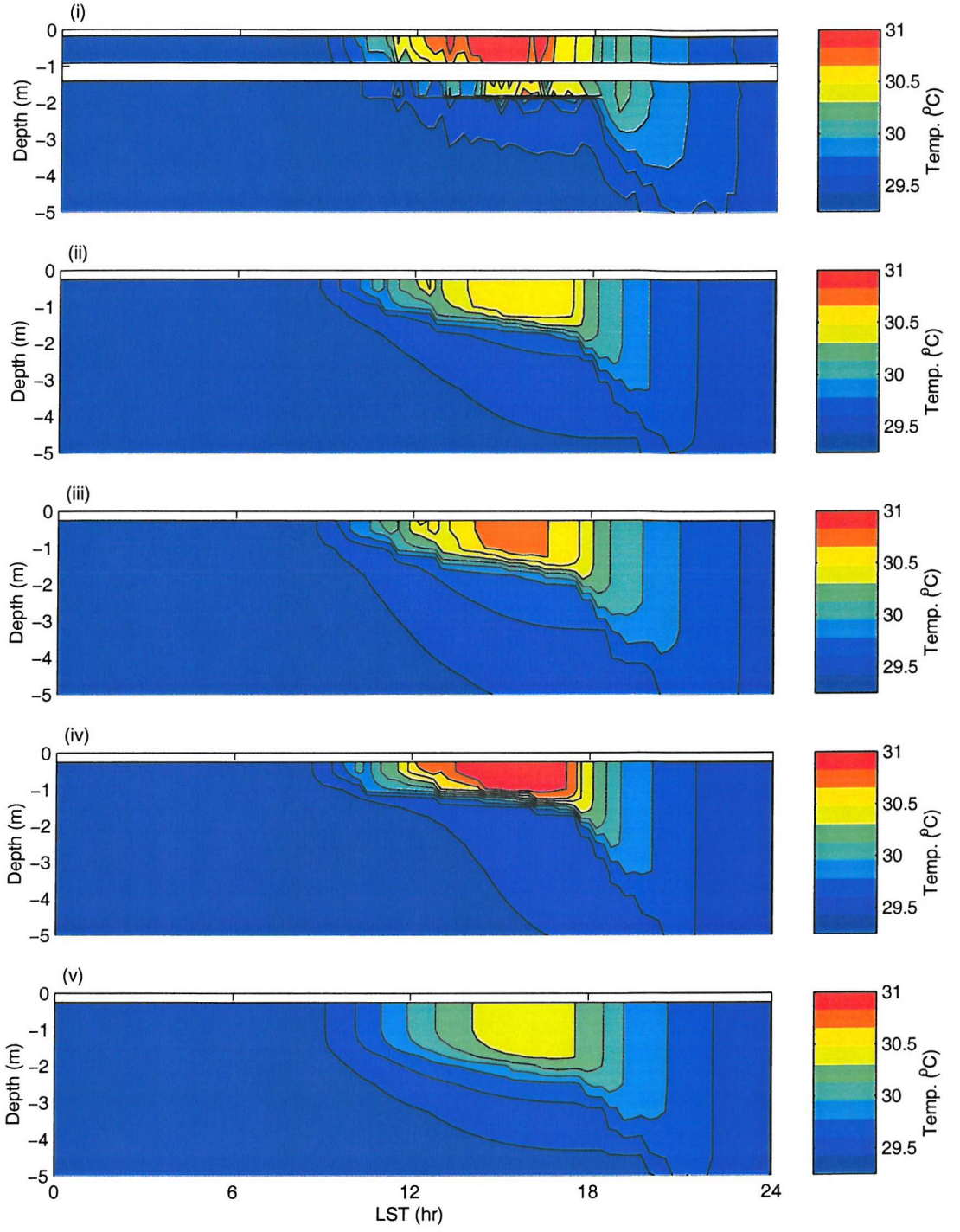

Figure 4.12b: Thermal structure of the top 5m of the water column for 1st May (chl = 0.1 mg/m^3). Solar transmission inter-comparison: (i) Observations, (ii) PWP OS00, (iii) PWP PS81, (iv) PWP S82 and (v) PWP PS77. The white band in (i) reflects the failure of one of the thermistors.

4.4.2.2 Impact of chlorophyll on the diurnal warm layer

As discussed in Sections 4.1.2 and 4.4.1, chlorophyll is expected to have different influences on the diurnal warm layer for low and moderate winds. At high winds, chlorophyll concentrations have little impact on diurnal stratification as the amplitudes are negligible. During low wind periods, chlorophyll increases the temperature below

the top half metre and appears to have little influence in the near surface layer. In moderate winds, the surface temperature is increased as chlorophyll concentrations increases. For both low and moderate winds, the presence of chlorophyll may alter the temporal evolution (shape) of the signal as the diurnal warm layer is broken down, since the temperature gradients across the diurnal thermocline are modified. This theory and the results are investigated further using the 1-D mixed layer PWP model. The model, implemented with OS00, is forced for a range of chlorophyll concentrations (0.1, 1, 2 & 5 mg/m^3) for two different forcing conditions: low wind (8th February) and moderate wind (11th February). The influence of chlorophyll has now been isolated and can be tested by changing the concentration used in the OS00 parameterisation.

Figure 4.13 displays the simulated diurnal cycle at several different depths for different chlorophyll concentrations for the low wind (Figure 4.13a) and moderate wind day (Figure 4.13b). The maximum diurnal amplitude does not increase at the surface for the low wind case, but increases at depth. The evening cooling rate is reduced at all depths as chlorophyll levels increase.

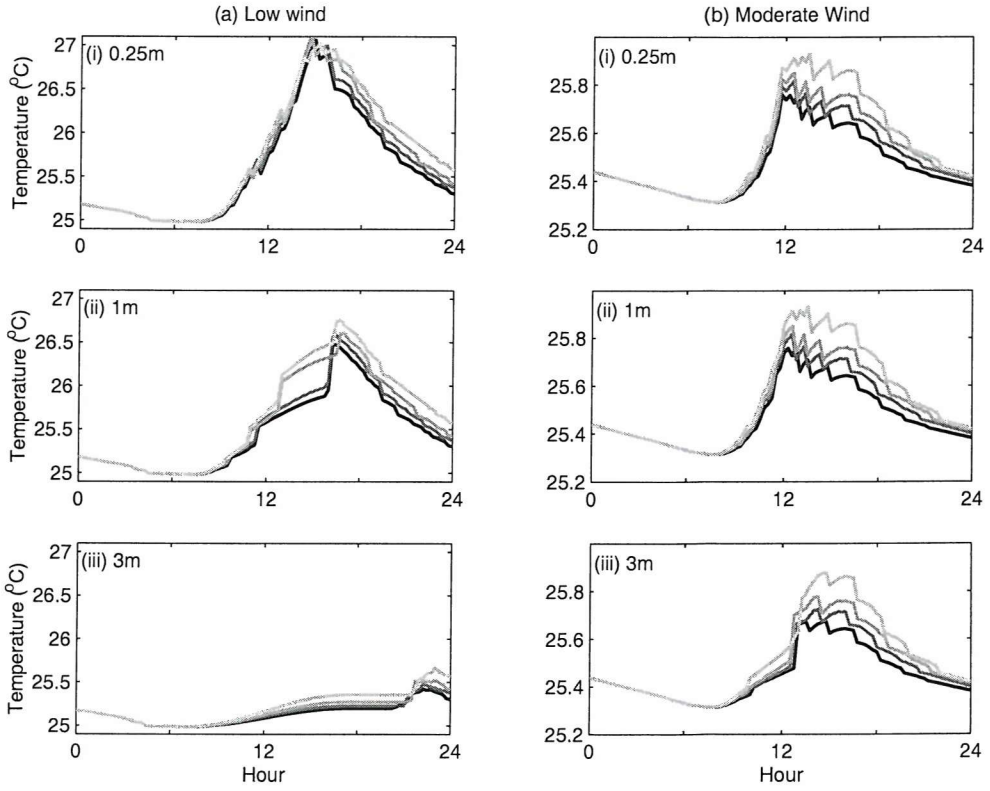

Figure 4.13: PWP OS00 temperature simulations for (a) a low wind day – 8th February & (b) a moderate wind day – 11th February. (i) 0.25m, (ii) 1m & (iii) 3m. The different colours represent different chlorophyll concentrations used in the parameterisation (light grey: 5mg/m^3, grey: 2 mg/m^3, dark grey: 1 mg/m^3, black: 0.1 mg/m^3).

Figure 4.14 displays the thermal structure of the diurnal warm layer for the same two days for different chlorophyll concentrations. In low winds, as chlorophyll concentrations increase, the diurnal mixed layer slightly deepens and the stratification becomes weaker due to broader thermal gradients. During moderate winds, SST increases and the stratification is slightly intensified.

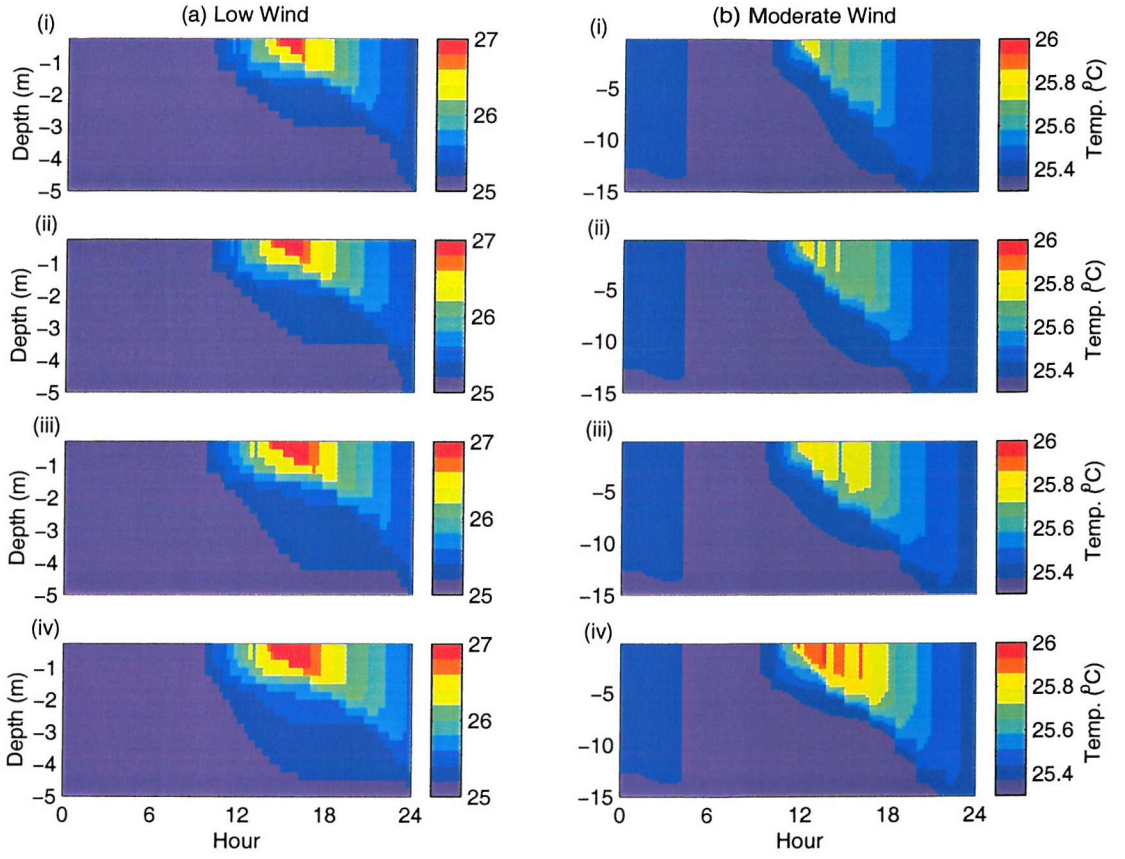

Figure 4.14: PWP OS00 temperature simulations for top 5m of the water column for different chlorophyll concentrations (i) 0.1mg/m^3, (ii) 1mg/m^3, (iii) 2mg/m^3 and (iv) 5mg/m^3. (a) Low wind day (8th February) & (b) Moderate wind day (11th February).

It may seem counter-intuitive that the surface temperature does not increase as a function of chlorophyll for the low wind case. Although red light is dominantly absorbed in the top 1m, it might be expected that the presence of chlorophyll should trap even more heat in this shallow surface layer. Morel & Antoine (1994) state that any additional absorption within the top 20-30cm remains negligible in comparison to that of pure water. To investigate this, the OS00 parameterisation is run alone for varying chlorophyll concentrations, setting cloud index to 0, solar zenith angle to 10°. The change in the fraction of energy, I', absorbed over a depth interval (Δz) of 0.01m for a chlorophyll concentration (chl), $A_{(i,chl)}$, was calculated for a range of chlorophyll

concentrations, from the surface (i=0) down to 1m (i=1/Δz). This is not a cumulative fraction of the total energy absorbed as shown in Figure 4.4 but is the fraction of energy absorbed across each 0.01m depth interval.

$$A_{(i,chl)} = I'_{(\Delta z(i-1),chl)} - I'_{(\Delta z(i),chl)} \tag{4.8}$$

$A_{(i,chl)}$ is referenced to the fraction of energy absorbed across Δz when chl=0, $A_{(i,chl=0)}$, and standardised as shown:

$$R_{(i,chl)} = \frac{A_{(i,chl)} - A_{(i,chl=0)}}{A_{(i,chl=0)}} \tag{4.9}$$

Figure 4.15 shows the results for the top 1m. As chlorophyll increases, slightly less heat is absorbed in the top 0.2m. Below this depth, more energy is absorbed as chlorophyll increases. This therefore explains why the surface temperature does not increase as a function of increasing chlorophyll in low wind conditions.

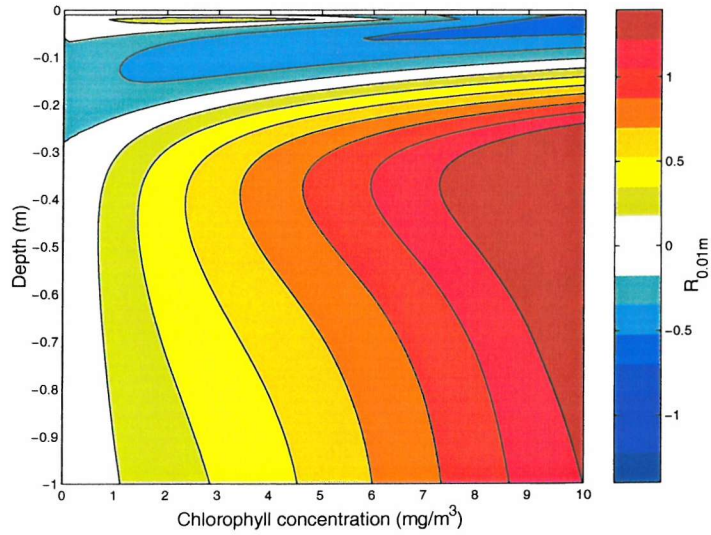

Figure 4.15: Change in fraction of energy absorbed across depth interval of 0.01m as a function of increasing chlorophyll concentration (referenced from [chl]=0), $R_{0.01m}$, for depth intervals down to 1m.

This relationship is not observed in PS81. In Figure 4.16, the calculation of R_i is repeated for OS00 and PS81, as function of water type/chlorophyll concentration up to the maximum water type limit of 1.5mg/m^3. PS81 does not show any surface cooling as a function of chlorophyll concentration. A similar test was carried out for PS77 (not

shown) and the results for this parameterisation showed a decrease in absorbance in the top 0.5m from Type I to Type III waters. This agrees with the results from Dickey & Simpson (1983; discussed in Section 4.1.2) where they reported that in low winds, Type I water had larger ΔT amplitudes than Type III.

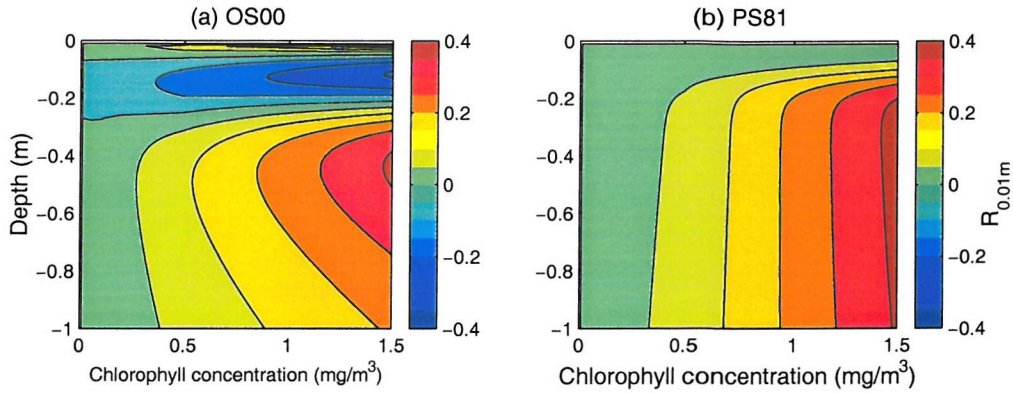

Figure 4.16: Change in fraction of energy absorbed across depth interval of 0.01m as a function of increasing chlorophyll concentration (referenced from $[chl]=0$), $R_{0.01m}$, for depth intervals down to 1m. (a) OS00, (b) PS81.

Ohlmann (personal communication) suggests the behaviour of the OS00 parameterisation is realistic and not an artefact of the curve fitting. For low to moderate chlorophyll concentrations, where there is increased absorbance in the top 5cm (Figure 4.16a), Ohlmann suggests that the extra absorption at the surface may completely absorb some wavelengths that would usually be absorbed in the top 20-30cm, resulting in less absorbance in this 20-30cm layer. However as chlorophyll concentrations continue to increase, the decrease in absorbance is noted at the surface. As it was discussed in the section describing the OS00 parameterisation (Section 4.3.1), the parameterisation includes albedo effects and as chlorophyll increases, the albedo effect also increases which suggests that scattering is included in the parameterisation. However, enhanced scattering at the surface would increase the path length of the photon and therefore should lead to an increase in absorption. Therefore the results suggest that the problem is more likely to be an artefact of the curve fitting and not physical. I am waiting further comments from Ohlmann to confirm the reason for the decreased absorbance. The results indicate that more detailed in situ observations are needed to help assess the influence of chlorophyll concentration on the upper 0.5m and determine whether OS00 is realistic.

4.5 IMPLICATIONS

The presence of chlorophyll can influence the temperature at the surface and below and will alter the thermal structure of the water column. In low winds, the presence of chlorophyll reduces the thermal contrast across the diurnal mixed layer. According to OS00 the water at the surface is not affected by the presence of chlorophyll but below 0.3m, the temperature will increase as more heat is absorbed and the radiant heating rate rises. The presence of chlorophyll is not only important for the heating stage of the diurnal cycle but it also plays an important role at night. In low chlorophyll conditions, there will be a sharp thermal contrast between the diurnal mixed layer and the water below. As the stratification breaks down through convective overturning, the nocturnal mixing will penetrate to greater depths, redistributing the daytime heat gain over a greater depth and will reduce the temperature of the mixed layer. In the presence of chlorophyll, the mixing depth will be reduced and the daily mean SST will increase.

This is demonstrated in Figure 4.17 where the mixed layer depth is plotted for the NEB period for PWP runs for a range of chlorophyll concentrations. Increasing chlorophyll results in a shallower mixed layer depth. The effect is more noticeable for moderate winds where the mixed layer depths are greater.

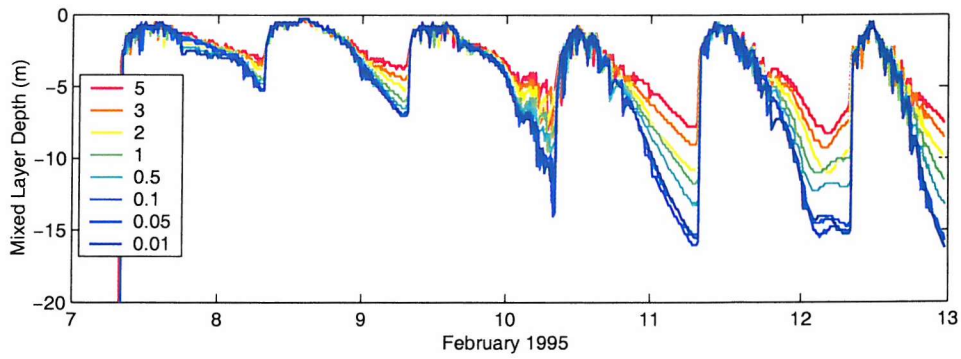

Figure 4.17: Time series of mixed layer depth from PWP model runs, using OS00 parameterisation, for NEB. Model is run for a range of different chlorophyll concentrations from 0.01 mg/m^3 to 5mg/m^3.

In absolute terms, the chlorophyll effect on the diurnal variation of SST is quite small and high chlorophyll concentrations are required to have a noticeable impact. The impact on the maximum diurnal amplitude occurs below the top 20-30 cm, with differences as large as 0.5°C noted over chlorophyll ranges from 0.01 – 5mg/m^3. In

moderate winds, since the top few metres of the water column are well mixed, the influence of chlorophyll is evident in the surface SST. In this case, the maximum diurnal surface SST amplitude increased by 40% but the absolute amplitude was relatively small. The influence of water clarity plays a secondary role in determining the heating rate and depth of the warm layer compared to the dominant wind and heating forces. Salinity gradients at the surface can also play a role in the evolution of diurnal warming by helping to stabilize the water column and suppress turbulent mixing but it will not alter the distribution of irradiance through the water column. In open ocean, chlorophyll concentrations are not expected to exceed much above 5mg/m^3 and therefore will only have quite a small impact on the evolution of the diurnal warm layer and SST. Towards the coast where chlorophyll concentrations are much higher, the impact can be more dramatic and cause more significant changes in the thermal structure and heating rate of the diurnal warm layer.

Comparing the climatological ΔT maps presented in Chapter 3 against a chlorophyll climatology from SeaWiFS for February and July (Figure 4.18), high chlorophyll areas can coincide with diurnal warming hotspots, particularly in the tropics (see Appendix C for plots for all 12 months). It may be possible that the stabilising conditions promoted by diurnal warming, provide favourable conditions for primary production, which in turn will further enhance the stratification by trapping more heat near the surface, creating a positive feedback. This type of feedback suggests that it would not be unusual to have chlorophyll blooms coincident with diurnal warming hotspots. Naturally other factors such as nutrient availability are also important which is why there is no coincidence of high chlorophyll in the oligotrophic sub-tropical gyre regions. Monthly mean chlorophyll concentrations do not give an indication of daily concentrations but they suggest chlorophyll levels could be quite high. The influence of water clarity will be greater near the coasts where chlorophyll concentrations are much higher but the effect will be more complex due to the influence of suspended particles associated with riverine discharge.

The results stress the importance of the optical properties of the water column when modelling the fine detail of the diurnal warm layer and its evolution. The presence of chlorophyll must be considered and the choice of solar transmission parameterisation

used in a modelling study is crucial. A full spectral model should be used and not the commonly used PS77, since it is unable to resolve the detail near the surface. There are subtle differences between each of the full spectral parameterisations but the advantage of OS00 is that it has been derived from a wide range of conditions and implicitly includes chlorophyll concentration and does not base its coefficients on crude water types. Morel (1988) suggested that Type III waters refer to concentrations between 1.5-2 mg/m^{-3}. At these concentrations and above, chlorophyll has a major influence and it is important to distinguish between increasing concentrations, which is not possible with the other parameterisations.

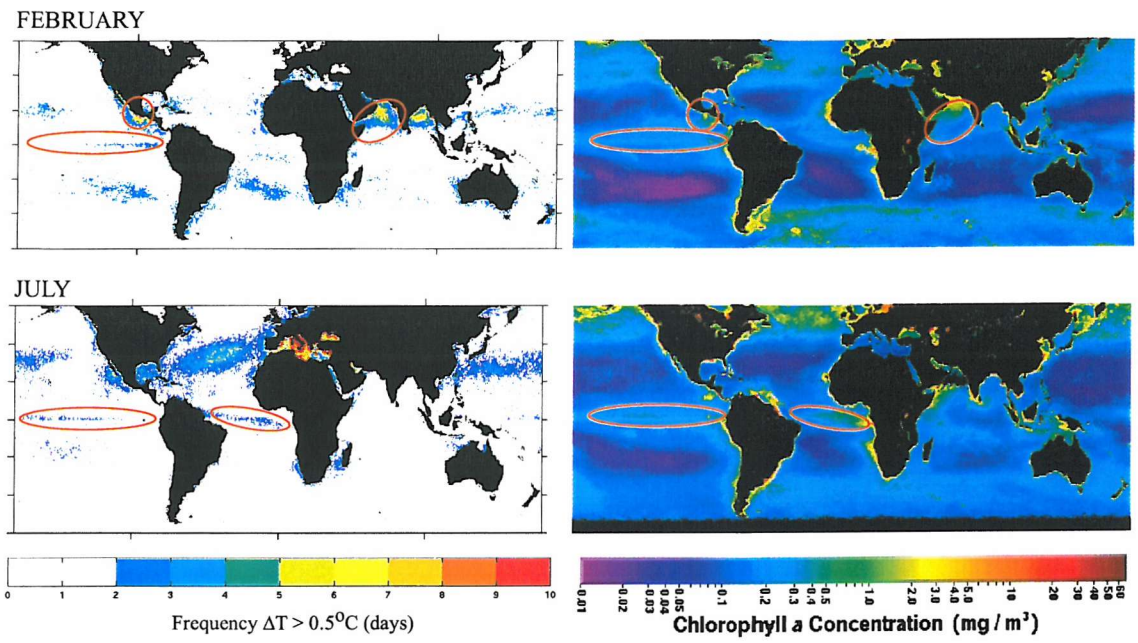

Figure 4.18: Monthly climatological diurnal warming frequency fields from Stuart-Menteth et al. (2003) and climatological SeaWiFS chlorophyll maps for February and July. (SeaWiFS images from http://seawifs.gsfc.nasa.gov/cgi/monthly_climatologies.pl) Red rings highlight regions of coincident high chlorophyll and frequent diurnal warming. In the diurnal warming frequency maps, colour is only given to frequency values of greater than 2 days. (See Appendix C for all 12 months.)

4.6 SUMMARY

This chapter has discussed the relationship between chlorophyll and SST in the context of diurnal warming using observations and model simulations. The main achievements and findings are:

- This is the first time that in situ observations have been analysed to identify the relationship between chlorophyll and the structure of the diurnal warm layer.

The PWP model simulations have been used to investigate the relationship in more detail, removing additional influences of meteorological variability and the background oceanic state.

- The implications of the biological modulation for SST measurements have been discussed. Chlorophyll will impact both the rate of heating and cooling at the surface and at depth. OS00 suggests the rate of heating is increased below 0.3m and not at the surface. Consequently in very low winds, the influence of chlorophyll is not obvious at the surface. The increased heating near the surface will decrease the thermal contrast across the diurnal mixed layer which may affect the true mixed layer temperature through limiting the depth of nocturnal convection.

- The choice of solar transmission parameterisation used to model the vertical profile of irradiance through the water column has been investigated for the first time. Many studies in the past have discussed this issue but this is the first time it has been systematically addressed. Full spectral models out-perform the popular PS77 2-band parameterisation, reproducing the detailed thermal structure in the top 2m which the PS77 is unable to resolve. More recent parameterisations implicitly include the influence of chlorophyll (e.g. OS00) and do not rely on a crude water type classification. There are differences among the parameterisations, which vary as chlorophyll concentration increases or water type changes, which clearly should be investigated in more detail with optical measurements to fully assess their skill.

CHAPTER 5: SENSITIVITY OF THE DIURNAL CYCLE TO METEOROLOGICAL VARIABILITY

5.1 BACKGROUND

In this chapter, the sensitivity of the diurnal cycle to meteorological variability is investigated. Part of the motivation for this work follows from the results discussed in Chapter 3 where the southern hemisphere showed larger satellite ΔT amplitudes when the satellite overpass time became later in the afternoon while no significant differences were noted in other regions. It raised the questions: does the phase of the diurnal cycle vary and if so, what influences any change in phase? Although the different patterns presented in Chapter 3 are most likely due to a combination of factors, the question about the phase is still interesting and has not been properly addressed before.

Most of the literature and studies on diurnal warming have focused on the amplitude of the diurnal signal (Stramma et al., 1986; Cornillon & Stramma, 1985; Price et al., 1986 & 1987; Webster et al., 1996). The time of the daily SST peak, t_{max}, is reported to occur a couple of hours after midday. Dickey & Simpson (1983) reported that the SST peak lagged the insolation peak by 3.5 hours, agreeing with earlier studies by Shonting (1964) and Ostapoff & Worthem (1974). However, other studies report the mean to be 2 to 3 hours after midday (Price et al., 1987; Yokohama et al., 1995; Flament et al., 1994). Price et al. (1987) reported a mean t_{max} of 14:30 local time but commented on the considerable scatter around this mean value with values ranging between 11:00 to 18:00, particularly during low winds.

There has, as yet, not been a detailed study into the shape and phase of the diurnal cycle. While the amplitude of the diurnal signal is important, it cannot be applied without having some information about the shape and phase of the signal. The scientific community is becoming more aware of the diurnal signal in SST and its possible implications for producing accurate climate SST data sets from satellite and in situ data. It is important to distinguish between the phase and shape of the diurnal signal at the surface and depth in order to interpret the diurnal variations detected by satellite and in situ techniques. Work is underway to remove the diurnal signal from satellite SST data sets (Donlon, 2004b; Gentemann et al., 2003; Kawai & Kawamura, 2002; 2003) and

therefore knowledge about the phase of the cycle will help to estimate the magnitude of the diurnal stratification at the time and depth of the measurement.

This study aims to analyse the variability of the shape and phase of the diurnal sea temperature signal at the surface and at depth using oceanographic and meteorological buoy data. The importance of the time variability in the forcing fields has been raised in several studies (e.g. Price et al., 1987), although only one study has investigated this in the past. Dickey & Simpson (1983) investigated the impact of the time varying wind variability on the magnitude of the diurnal cycle in an idealised modeling study. They created a diurnal signal in the wind field and compared the modelled ΔT output at different phase lags/lead of the wind cycle. They reported that the maximum diurnal cycle occurred when winds were low during the daytime, in particular around midday.

This work will build upon the results of Dickey & Simpson (1983) and will use field data to look at the sensitivity of the diurnal mixed layer to meteorological variability in more detail. Several hundred diurnal cycles are analysed in conjunction with their associated meteorological fields, namely wind speed and incoming shortwave radiation, to understand the sensitivity of the diurnal cycle to meteorological variability during the day and to investigate their impact at the surface and at depth.

5.2 DATA

In order to investigate the sensitivity of the diurnal cycle to small fluctuations in wind and insolation during the day, high temporal resolution SST and meteorological data is required. Data from several Woods Hole Oceanographic Institution (WHOI) Improved METeorological (IMET) buoys are used in this study. IMET measurements are ideal for diurnal warming studies as they provide SST at 15 minute resolution, wind and downward shortwave radiation (insolation), among other meteorological variables, at 7.5 minute resolution and in some cases have several temperature measurements in the upper 5m of the water column on a mooring line below the buoy. The IMET buoys have been deployed for a number of different experiments, at a range of latitudes and seasons, over the last twenty years by the Upper Ocean Processes (UOP) Group at WHOI. Data from three experiments, selected for their susceptibility to diurnal warming (Stuart-Menteth et al., 2003), are examined for this study (Table 5.1). Each of

the buoy locations (Figure 5.1) represents different oceanic and climatic conditions to provide a quasi-global perspective to the study.

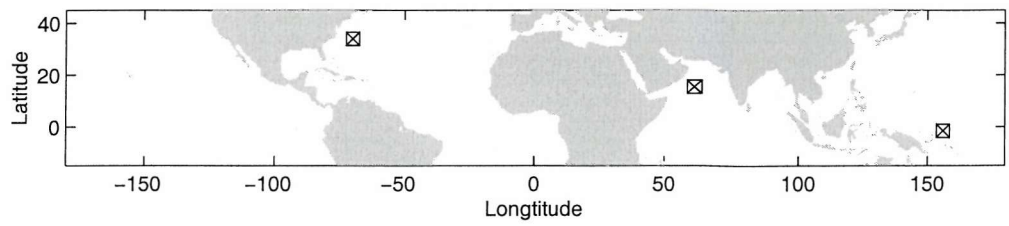

Figure 5.1: Location of the WHOI IMET buoys

The first data set is from the Arabian Sea Experiment which was introduced in the previous chapter. The Arabian Sea is an excellent location for observing diurnal warming as the inter-monsoon periods are characterised by low wind and clear sky periods (Dickey et al., 1998; Weller et al., 1998). The mooring had nine temperature measurements in the upper 5m of the water column along with a full suite of meteorological sensors, allowing the computation of the air-sea fluxes. The second data set is taken from the Tropical Ocean Global Atmosphere (TOGA) Coupled Ocean-Atmosphere Response Experiment (COARE) experiment in the Western Equatorial Pacific Warm Pool (Webster & Lukas, 1992). An IMET buoy was deployed as part of the observational programme (Anderson et al., 1996) during October 1992 to March 1993 at 156E, 1.5S. This region is another excellent location for diurnal warming as reported by Anderson et al. (1996), Fairall et al. (1996b), Webster et al. (1996) and Pritchard & Weller (2004). The buoy recorded a full time series of meteorological measurements along with five temperature measurements in the upper 5m of the water column. The final data set used in this study is from the Long Term Upper Ocean Study (LOTUS) experiment, carried out in the Sargasso Sea (70W, 34N) from spring 1982 to spring 1984 (Price et al., 1987). The WHOI meteorological buoy was only attached to the LOTUS mooring during the spring and summer months. This data set also has an excellent record of frequent diurnal warming events and has been used in past diurnal warming studies by Stramma et al. (1986) and Price et al. (1987). For this field study, the mooring had only one temperature sensor in the top 5m at a depth of 0.6m and did not measure the full set of meteorological variables.

Table 5.1: Details of buoy data sets

	Location	Time	Depth of SST sensors	U	Q_{sw}	Full Met. Time series	Skin & sub-skin computed
Arabian Sea	61.5E, 15.5N	Oct 1994 - Oct 95	0.17m, 0.5m, 1m, 1.5m, 2m, 2.5m, 3.5m, 4.5m, 5m	x	x	x	x
Warm Pool	156E, 1.5S	Oct 1992 – Mar 93	0.5m, 1m, 1.5m, 2m, 2.5m, 7m	x	x	x	x
Sargasso Sea	70W, 34N	Spring/ Summer 1982-84	0.6m, 5m	x	x		

5.3 METHOD

5.3.1 Estimating the diurnal cycle at the sea surface

Since one of the primary aims of this thesis is to focus on the variability of the diurnal warming signal detected by SST platforms (mainly satellite and buoys), it is necessary to derive surface SST values so that differences between the surface and at depth can be understood. During very low wind conditions, the diurnal cycle at the surface can be much greater than at 1m as the diurnal mixed layer (DML) rapidly shoals and even vanishes. Yokohama et al. (1995) reported a 4.5°C difference in the top 2m of the water column during an extremely low wind period in Mutsu Bay. Very few true surface temperature measurements exist coincident with diurnal warming conditions and no surface measurements were available with the buoy data. Therefore the surface temperature must be determined from a model. The skin and sub-skin temperatures are derived by applying the Fairall et al. (1996b; hereafter F96) warm layer and cool skin models to the buoy SST measurements using the Coare bulk flux algorithm version 3 (Fairall et al., 2003). The algorithm, based upon the Liu et al. (1979) bulk flux parameterisation, uses similarity theory to obtain turbulent air-sea heat fluxes from bulk meteorological variables. It has been thoroughly tested and validated (Fairall et al., 2003) and has been widely applied in air-sea heat flux studies and other ocean-atmosphere interaction studies. The model requires a full meteorological time series to compute the fluxes and determine the warm layer and cool skin temperature corrections. The F96 corrections are applied only to the Arabian Sea and TOGA COARE datasets as the LOTUS data does not have a complete meteorological time series. While certain variables could be estimated to compute the fluxes for the LOTUS buoy (Price et al., 1987), this could lead to unrealistic surface temperatures which are not suitable when

the aim of the study is to assess the sensitivity of the diurnal cycle to time variability in the forcing conditions.

5.3.2 Fairall et al. (1996) cool skin and warm layer models

The Fairall et al. (1996b) cool skin and warm layer models were developed in response to results from the TOGA COARE experiment where it was found that to estimate air-sea fluxes and the heat balance to an accuracy of $10 Wm^{-2}$ required SST to be accurate to ± 0.2°C (Fairall et al., 1996a). Under these strict requirements, in situ SST measurements are therefore not appropriate and the skin temperature should be used. Skin measurements are still sparse in relation to in situ measurements and therefore the F96-derived warm layer and cool skin corrections (ΔT_w and ΔT_c) permit the skin temperature to be estimated from an in situ SST measurement at depth, z, where:

$$T_{skin} = T_{(z)} - \Delta T_c + \Delta T_{w(z)} \tag{5.1}$$

By deriving a warm layer correction, as well as a cool skin correction, F96 acknowledged that the temperature across the top couple of metres of the water column can vary greatly under low wind conditions.

5.3.2.1 Fairall et al. (1996b) cool skin correction

The cool skin model is based on Saunder's (1967) model, predicting the depth of the ocean skin layer and the temperature difference across it. There have been many studies on cool skin parameterisations (e.g. Wick et al., 1996, Horrocks et al., 2003b, Donlon et al., 2002b) and overall the F96 model is consistently reported to perform well (Horrocks et al., 2003b). In low wind regimes, the behaviour of the skin effect is less well understood. The F96 skin model often predicts warm skin layers during diurnal warming conditions. Few true observations of the skin temperature difference exist under low wind conditions to validate this result. The cool skin effect is measured as the difference between a skin SST (recorded by infrared sensors) and a 'bulk' in situ measurement (from buoy/ship). Under low winds, the in situ SST should ideally be measured just below the skin, in the top few mm's, because of the strong diurnal stratification. Only highly specialized instruments can measure SST just below the skin,

and consequently very few precise cool skin temperature differences have been measured in diurnal warming conditions.

In low wind conditions, cool skin parameterisations are very sensitive to the assumed solar radiation absorption profiles which have not been examined in detail until recently (Wick et al., 2004). Wick et al. (2004) discuss the uncertainties in the cool skin model due to the choice of solar absorption scheme. F96 base their solar absorption scheme on the 9-band Paulson & Simpson (1981) parameterisation but approximate it to describe the absorption across the skin layer by summing the different waveband groups. Wick et al. (2004) conclude that the adapted Paulson & Simpson (1981) model overestimates the amount of heating in the skin layer and can often produce warm skins during low wind periods. By replacing the absorption scheme with that of Ohlmann and Siegel (2000), the cool skin correction is improved by reducing the amount of heat absorbed in the skin layer. Their results suggest that even less heat is absorbed than that predicted by either parameterisation. This is an active field of research and further analysis is required to have more confidence in cool skin corrections under strong diurnal heating conditions.

For this reason, the derived skin SST will not be used in this study and only the warm layer corrections will be applied to the buoy data to give a sub-skin SST. The F96-derived sub-skin will represent the diurnal warming signal detected from space by both passive microwave and infrared sensors. Since the difference between the skin and sub-skin temperature is effectively the cool skin difference, it is assumed that the diurnal heating cycle will be almost identical for the skin and sub-skin. The skin may heat up more than the sub-skin under low winds but there is not enough detailed information and understanding in these small differences and the competing effects of heating and cooling at the surface to justify investigating skin and sub-skin diurnal cycles. Results from Ohlmann & Siegel (2000) and Wick et al. (2004) suggest that the cool skin temperature difference may not vary during daytime diurnal warming conditions, which supports the assumption that the diurnal heating cycle at the skin and sub-skin can be treated as identical.

5.3.2.2 Fairall et al. (1996) warm layer correction

The warm layer model is based on a single layer scaling version of the Price, Weller and Pinkel (1986; hereafter PWP) 1-D mixed layer model which assumes that once solar heating exceeds the cooling at the surface, the main body of the mixed layer becomes cut off from turbulence. At this point, the surface heat and momentum fluxes are confined to a depth, D_T. The F96 model was chosen over the PWP model and other mixed layer models since results suggest that the F96 model works equally well as full mixed layer models for simulating the surface temperature. Results from Wick (personal communication) show that the F96 model compares well to his adapted Mellor-Yamada turbulence scheme model. Each mixed layer model has its own inadequacies (Pritchard & Weller, 2004). In contrast to full 1-D models, the F96 warm layer correction is applied to the measured SST value and therefore removes the concern of model deficiencies affecting the underlying true mixed layer temperature. Therefore it appears that there is little advantage to be gained from using a full 1-D model to predict the surface temperature.

The warm layer correction, ΔT_w, is given as:

$$\Delta T_w = \frac{2\int(f_w.R_{sw} - Q_{out})dt}{\rho.c_p.D_T} = \frac{2I_s}{\rho.c_p.D_T} \tag{5.2}$$

where ρ is sea water density, c_p specific heat of sea water, R_{sw} downward shortwave radiation, Q_{out} total outgoing heat flux and f_w represents the fraction of radiation absorbed in the trapping layer, D_T:

$$D_T = (2R_{ic})^{1/2} \frac{I_\tau}{(\alpha.g.I_s / \rho.c_p)^{1/2}} \tag{5.3}$$

where

$$I_\tau = u_{*w}^2 (t - t_0) \tag{5.4}$$

$$I_s = \frac{f(D_T)}{2\rho c_p}\frac{\partial R_{sw}}{\partial t}(t-t_0)^2 \tag{5.5}$$

$$f_w = f(D_T) = 1 - \left\{\sum_{i=1}^{N} F_i \zeta_i [1 - e^{-D_T/\zeta_i}]/D_T\right\} \tag{5.6}$$

where t_0 is time of warm layer onset ($R_{sw} > Q_{out}$), u^2_{*w} is friction velocity for water, F and ζ are the absorption coefficients from Soloviev (1982) (Table 4.3). D_T and f_w are solved iteratively before calculating ΔT_w.

Having computed the temperature correction across the entire warm layer (ΔT_w), the temperature correction must be determined for the depth of the measurement (z). The model assumes linear profiles of temperature within the warm layer and therefore the warm layer correction at the depth of the measurement is determined as

$$\Delta T_{w(z)} = \Delta T_w \frac{z}{D_T} \qquad (\text{if } z < D_T) \tag{5.5}$$

If the depth of the measurement is greater than or equal to D_T, the full ΔT_w is applied to the measurement.

Under low winds, the linear profile assumed by the model may not be realistic. The absorbance profiles discussed in the previous chapter (Figure 4.8) do not suggest a linear profile. A sensitivity test was carried out to assess the impact of using different measurement depths (z) using the Arabian Sea dataset. The warm layer model was applied to a range of depths and the sub-skin surface temperature values ($T_{(z)} + \Delta T_{w(z)}$) were compared. Figure 5.2 shows some examples of the results and reveals a sensitivity to the measurement depth, z. Using a depth typically below D_T (e.g. 5m) often results in an under-estimation during low wind periods. The results suggest that the model may underestimate ΔT_w and therefore applying the model to a depth of 5m will result in an under-prediction. Applying the model to shallower depths, can sometimes produce large differences in the modelled surface temperatures. On the basis that the shallower the measurement, the smaller the correction ($\Delta T_{w(z)}$), the model was applied to the

shallowest measurement depth possible, which corresponded to 0.17m for the Arabian Sea data and 0.45m for the TOGA COARE buoy.

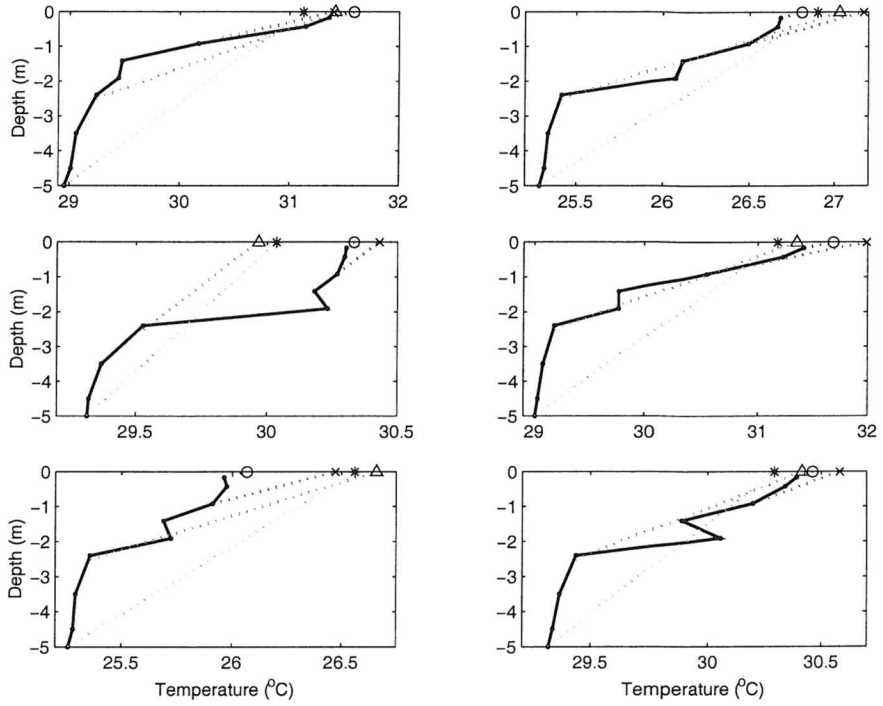

Figure 5.2: Observed temperature profiles from Arabian Sea mooring and surface temperature values (sub-skin) determined from F96 warm layer model applied to different depths. Black dot: observed $SST_{0.17m}$, light grey *: F96 sub-skin (z=5m), grey triangle: F96 sub-skin (z=2m), dark grey x: F96 sub-skin (z=1m), circle: F96 sub-skin (z=0.17m).

A comparison was also carried out to compare the F96 warm layer model output using the Soloviev (1982) and Ohlmann & Siegel (2000) solar absorption parameterizations, based on the results from Section 4.4.2.1. The Ohlmann & Siegel (2000) parameterisation was run using the chlorophyll time series presented in the previous chapter. The differences between the two parameterisations were quite small and much smaller than the errors found from using different z (discussed above) as demonstrated in Figure 5.3. Since there is not a high resolution time series of chlorophyll for the datasets and given the differences between the Ohlmann & Siegel (2000) and Soloviev (1982) parameterisations are small, the model is run in its standard configuration using Soloviev (1982).

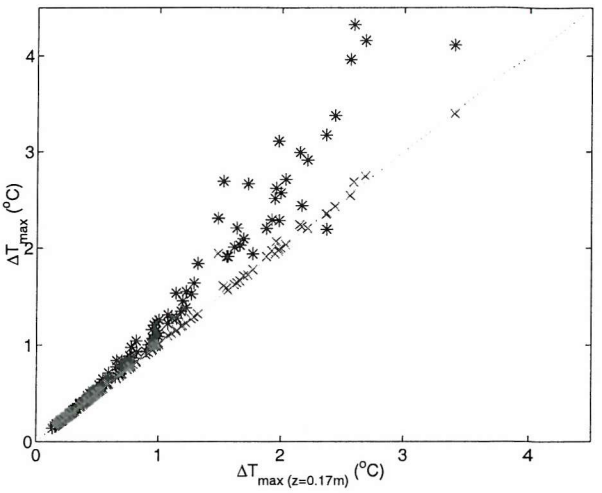

Figure 5.3: Comparison of daily maximum diurnal sub-skin temperature variation, ΔT_{max}, derived from the F96 warm layer model. X-axis shows sub-skin ΔT_{max} derived from F96 using S82 solar transmission parameterisation and depth of measurement z=0.17m. Y-axis shows sub-skin ΔT_{max} derived using (grey x) OS00 parameterisation and z=0.17m and (black *) S82 parameterisation and z=1m.

5.3.3 Data Filtering

Before the data were analysed, the data sets were filtered to remove any non-local processes. The purpose of this study is to analyse the diurnal warming signal which is assumed to be a 1-D process, controlled by the local balance of heat and momentum fluxes. Consequently other processes such as advection of heat or internal waves can influence the diurnal signal and provide misleading noisy results. These processes should not be included in the data analysis. Advective effects can not be removed explicitly and therefore periods of apparent advection are removed from the dataset before analysis. This is not a trivial process as discussed by Price et al. (1987). The following filtering steps were carried out:

1. As a starting point, the data sets were subsetted to include only the seasons or periods favourable for diurnal warming. For example, the south-west monsoon period was omitted from the Arabian Sea data set and westerly wind burst periods and short-lived squalls, identified by Anderson et al. (1996), were omitted from the TOGA COARE data.

2. In the case of the LOTUS data set, where the buoy SST is at 0.6m and not 1m, days when the daytime winds fell below 3m/s are omitted from the analysis as in these conditions, the top metre is likely to be stratified and will not reflect the

1m temperature. Large differences were detected between the 0.5m and 1m measurements from the Arabian Sea and TOGA COARE data. Figure 5.4 presents an example of this surface stratification in low winds. Figure 5.4a shows the time series of temperature at 0.17m, 0.5m and 1m and Figure 5.4b reveals the difference between the 0.5m and 1m temperatures. The differences exceed 1°C. For this reason, LOTUS 0.6m measurements are excluded from the analysis under low winds.

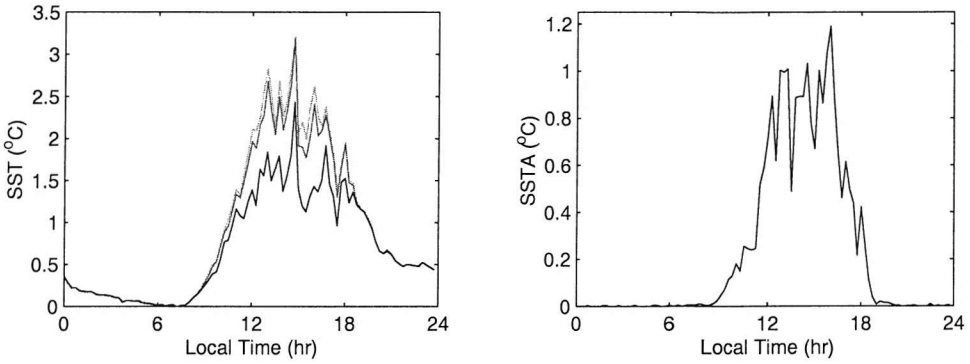

Figure 5.4: (a) Example of diurnal temperature cycle under low wind conditions (u<3 m/s) from the Arabian Sea mooring. Light grey: 0.17m, dark grey: 0.5m and black: 1m. (b) Difference between 0.5m and 1m temperatures.

3. Next, in a similar way to Price et al. (1987), the data were subjectively analysed to identify advective effects visible to the eye. Each diurnal cycle was visually analysed. For the Arabian Sea and COARE data, all the available temperature measurements at different depths were analysed to help detect non-local processes. In both the Arabian Sea and COARE datasets, there is evidence of internal wave activity that did sometimes penetrate into the diurnal warm layer and cases of advection. An example of this technique is demonstrated in Figure 5.5 in which a time series of the 0.17m temperature over 10 days is shown. Days marked with an 'X' were not included in the analysis because they revealed variations in SST not associated with the diurnal heating cycle and were consequently assumed to reflect non-local processes.

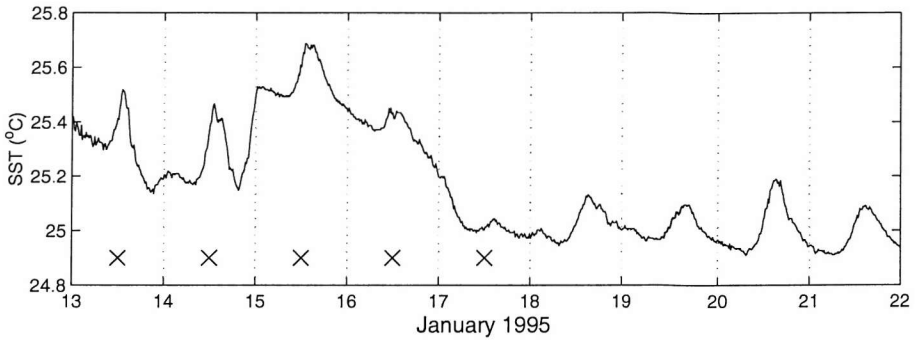

Figure 5.5: Time series of 0.17m temperature from the Arabian Sea mooring. Non-local effects are identified in the first five days (marked with X) and consequently these days are removed from the analysis.

4. As a final check the maximum daily SST amplitude, ΔT_{max}, was plotted against the daily mean wind speed where ΔT_{max} should increase as wind decreases. This extra test highlighted any 'noisy' periods that had been missed in the previous filtering steps. Any points which did not match the general trend were easily identified. A few extreme points were revealed where a high ΔT_{max} was reported in a high wind period. The visual analysis was repeated and confirmed the day had non-local processes and the day was removed from the dataset.

Figure 5.6 shows the final SST time series for each of the data sets after filtering. The outcome is 345 days of good quasi-pure diurnal warming signals. Out of these days, 270 days had a full meteorological time series which allowed the sub-skin SST to be computed.

5.3.4 Data Analysis

The buoy temperature, wind and downward shortwave radiation data have been analysed in detail. The evolution of each diurnal cycle and the corresponding wind and insolation fields have been visually studied, focusing on the shape of the signal and primarily its phase. The wind and insolation time series for each diurnal period are referred to in order to investigate the cause of the phase variations and where possible, the structure of the upper 5m is analysed to observe the stratification in the top few metres of the water column. However the main focus is on the temperature at 1m and the surface since these are the two depths most routinely measured by SST platforms (buoys and satellites). The 1m depth represents the typical depth attributed to in situ 'bulk' SST measurements, measured by buoys. The maximum diurnal SST amplitude,

ΔT_{max}, and the time of the SST peak, t_{max}, were calculated for the sub-skin and 1m data (Table 5.2). Any reference to time refers to the local solar time.

Table 5.2: List of diurnal warming variables derived from the buoy dataset used in this chapter.

Variable	Definition	Calculation	Units
ΔT_{max}	Maximum daily SST amplitude	T_{max}(10h-18h) – T_{min}(5h-9h)	°C
t_{max}	Time of maximum SST		Hours

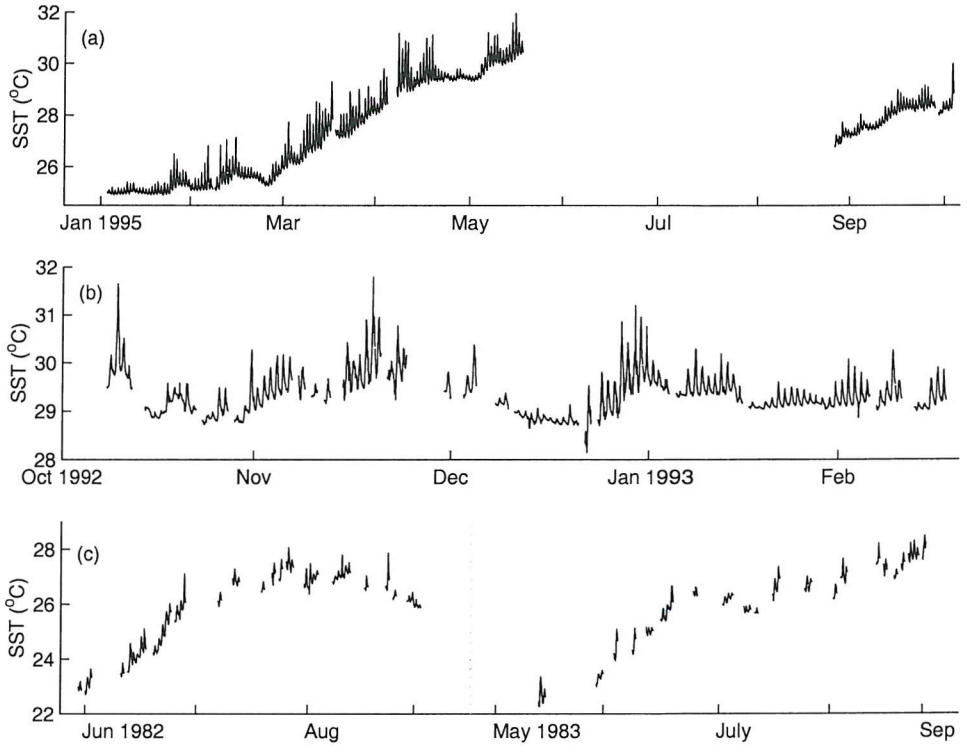

Figure 5.6: Time series of IMET SST data used in sensitivity study after data filtering. a) Arabian Sea - 1m, b) Equatorial Pacific Western Warm Pool (Coare) – 1m & c) Sargasso Sea (LOTUS) – 0.6m.

5.4 RESULTS

5.4.1 Differences between the diurnal signal at the surface and at 1m

In low winds (u<3m/s), large differences exist between the sub-skin and 1m diurnal signals (Figure 5.7a). The sub-skin ΔT amplitudes are much larger than the 1m ΔT amplitudes and are associated with phase differences between the two depths (Figure 5.7b). The time of the daily maximum SST, t_{max}, at 1m is later than sub-skin t_{max} during low wind periods (Table 5.3). In moderate and high winds, the 1m and sub-skin SST diurnal cycles should be identical since the top metre is well mixed. In some cases, the

maximum is not identical. The F96 model may sometimes apply a very small ΔT_w at high winds which has a negligible effect on ΔT_{max} between 1m and the sub-skin, but can create differences in t_{max} due to subtle variations in the surface fluxes used to derive the sub-skin values.

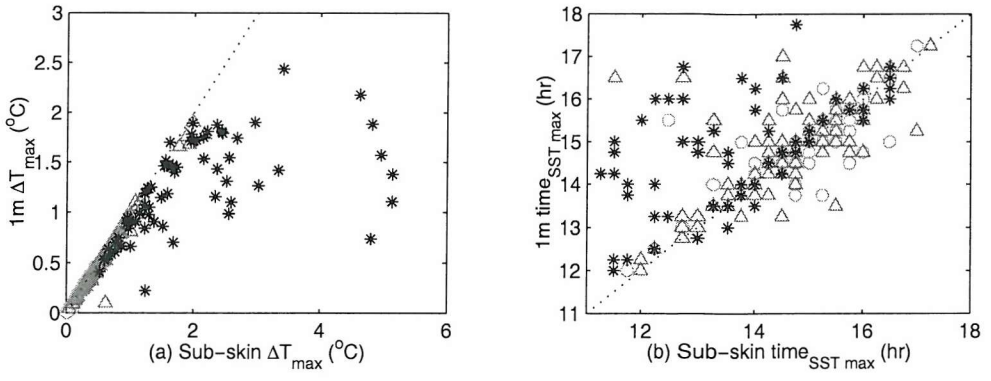

Figure 5.7: Comparison of diurnal warming variables at the sub-skin (x) and 1m (y). (a) shows the daily maximum ΔT and (b) shows the time of daily maximum SST, t_{max}. Black star: wind speed <3m/s, dark grey triangle: wind speed 3-6 m/s and light grey circle: wind speed >6m/s.

Table 5.3: Differences between sub-skin and 1m ΔT_{max} and $Time_{SSTmax}$ (sub-skin – 1m).

	ΔT_{max} (°C)	$Time_{SSTmax}$ (hr)	n (day)
$u < 3$ m/s	0.80 ± 1.20	-1.2 ± 1.3	62
$3 < u < 6$ m/s	0.04 ± 0.07	-0.25 ± 0.93	142
$u > 6$ m/s	0 ± 0.01	-0.07 ± 0.71	66

The large sub-skin ΔT_{max} may appear unrealistically high but these amplitudes are observed in the field. Figure 5.8 shows an example of observed skin measurements obtained during the TOGA COARE experiment aboard R/V Franklin and the F96-derived sub-skin determined from the IMET buoy. The ship was not at the exact location of the buoy, so the comparison cannot be quantitative. The observations show large diurnal skin variations of over 4°C which are also predicted by the model.

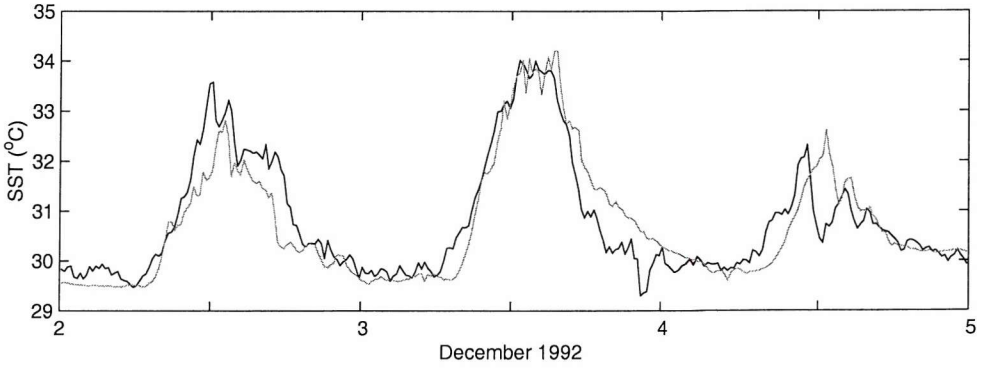

Figure 5.8: Observed skin and F96-derived sub-skin SST. Black line: observed skin from R/V Franklin, grey line: F96-derived sub-skin from IMET.

5.4.2 Sensitivity of the diurnal cycle to wind and insolation variability

Each diurnal SST cycle is visually analysed along with the corresponding wind and insolation fields to assess the variability in the shape of the diurnal cycle. The analysis reveals that the diurnal cycle can have a variable shape, particularly at the surface. The diurnal warm layer is highly sensitive to wind and insolation fluctuations with wind the dominant controlling force out of the two. Heating can still occur during quite cloudy conditions if the wind is low. However, if the wind is high, the stratification will be weak regardless of the insolation. Wind fluctuations can have an immediate impact on the diurnal warm layer and influence both the phase and magnitude of the diurnal cycle. Changes in insolation have a more gradual impact and mainly affect the magnitude of the diurnal signal. For example, high wind/cloud can exist in the morning, but if the afternoon develops into low wind, clear sky conditions, then diurnal stratification can still occur (Figure 5.9.a). Low winds in the morning followed by increased winds can rapidly break down the diurnal cycle and can result in t_{max} occurring just after or even before midday (Figure 5.9.b). Figure 5.7b confirms this sensitivity as t_{max} is noted to have large scatter, ranging between 11am to 6pm. Since the system is so sensitive to wind variability, it results in rapid changes in the phase of the diurnal signal, causing a wide scatter in the range of t_{max}.

It is during very low wind conditions (u<3 m/s) that the diurnal signal becomes most sensitive to meteorological fluctuations. With little or no wind mixing and high insolation, the upper few metres of the water column rapidly stratify and the diurnal mixed layer (DML) vanishes as the strong buoyancy effect suppresses any weak wind mixing. The heat distribution is explained by the exponential absorption of radiation with depth through the water column, with half the irradiance absorbed within the top 1m. Around 18% of the surface downwelling irradiance is absorbed over the top 1cm ($[I_o - I_{0.01}] / I_o$) compared to 0.1% over 1cm at a depth of 1m ($[I_{1.01} - I_{1.00}] / I_o$), creating strong surface stratification and a disappearing DML under very low winds. In low winds, the distribution of heat will be determined by the optical properties of the water, as discussed in the previous chapter.

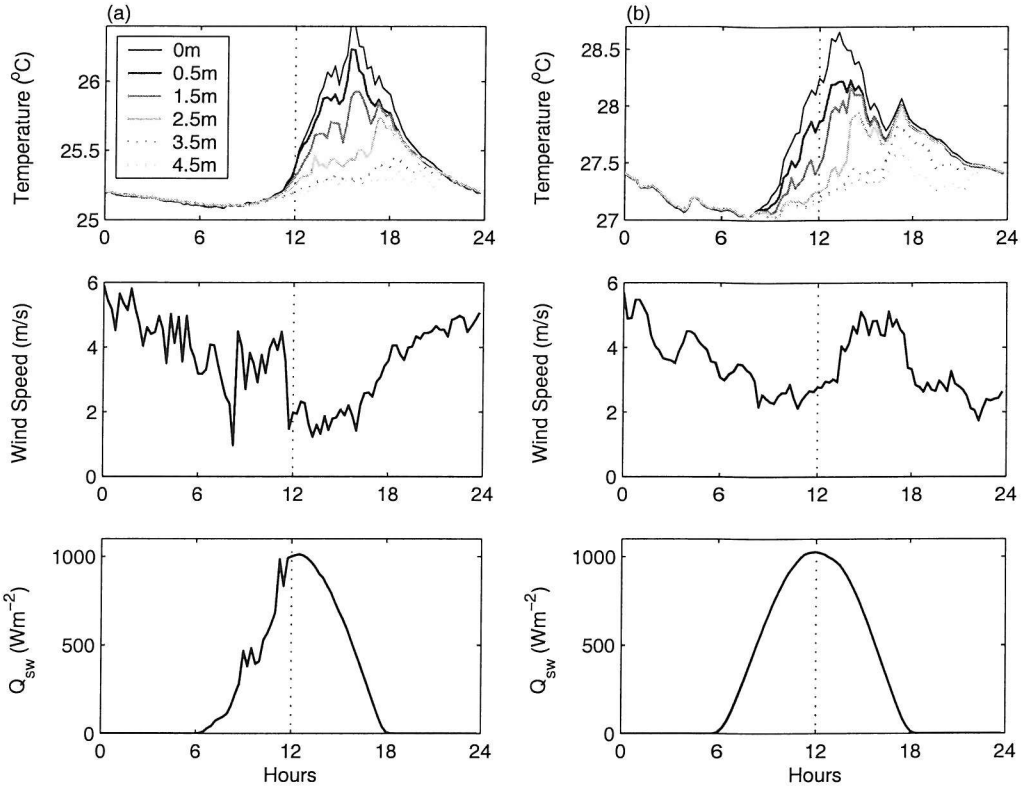

Figure 5.9: Two examples of the sensitivity of the diurnal mixed layer to wind fluctuations from the Arabian Sea mooring. Top panel shows temperature at 1m intervals ranging from sub-skin to 4.5m. The second row shows wind speed and bottom panel presents the downward shortwave radiation.

Depending on the degree of stratification (strength of buoyancy against turbulence), an increase in wind of only 1 m/s, even if wind speed is still less than 3m/s, is enough to break down the stratification near the surface. The breakdown of stratification in the top metre can have opposing consequences on the sub-skin and 1m temperatures. Surface temperatures will drop immediately as the water is mixed into cooler water below. In contrast, if the increase in wind speed is quite small, the 1m temperature will increase as the warmer water from above is mixed down. These conditions create highly variable diurnal warming shapes. The time of the daily maximum temperature at the surface will depend on the exact time of the change in wind speed. Figure 5.10 presents an example of a diurnal cycle where the time of the maximum SST at the surface and at 1m is marked by the sudden timing of a wind burst. The wind burst mixes the top metre of water deeper into the water column, reducing its temperature. In moderate winds, the top few metres are well mixed and therefore are less sensitive to sudden changes in the meteorological forcing and react more gradually.

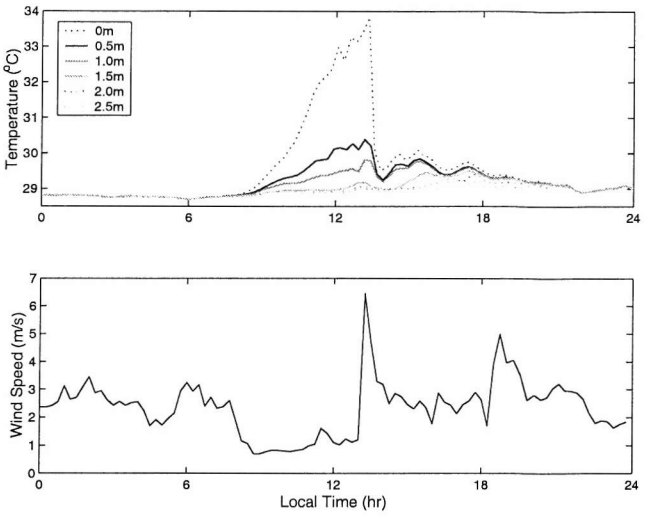

Figure 5.10: Example of a diurnal cycle of temperature (upper panel) and associated wind variability (lower panel) from the TOGA COARE mooring. The warm layer breaks down instantaneously as the wind suddenly increases.

The diurnal cycle shows greatest sensitivity to the morning wind conditions, with low winds in the morning having greater impact than identical forcing conditions in the afternoon. This is demonstrated in Figure 5.11 where the morning heating rate is higher than the afternoon heating rate despite the uniform clear sky, low wind conditions. At dawn, the mixed layer is uniform and stable and therefore is highly sensitive to changes in the buoyancy flux.

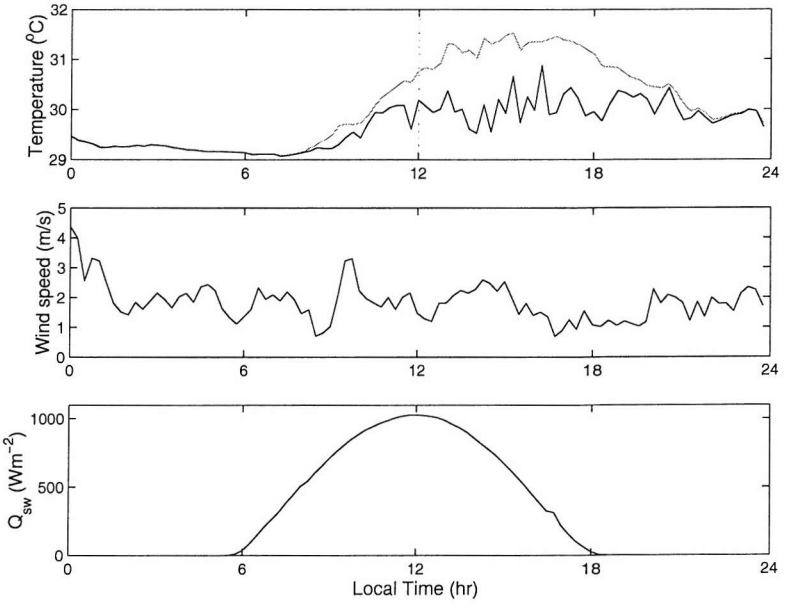

Figure 5.11: Example of a diurnal temperature cycle (top panel) from the Arabian Sea mooring. Grey represents the sub-skin and black the 1m temperature. The middle and lower panels show the wind and insolation variability over the same period.

5.4.2.1 Diurnal Shape Classification

Based on the extensive visual analysis of over 300 diurnal cycles, the diurnal signal has been grouped into four categories related to wind and insolation fluctuations to help classify the shape of the diurnal signal. Figure 5.12 presents examples of different diurnal warming cycles, from the buoy dataset, for each shape category. The shapes for each classification can vary between the surface and 1m under stratified low wind conditions. The categories are described and discussed below.

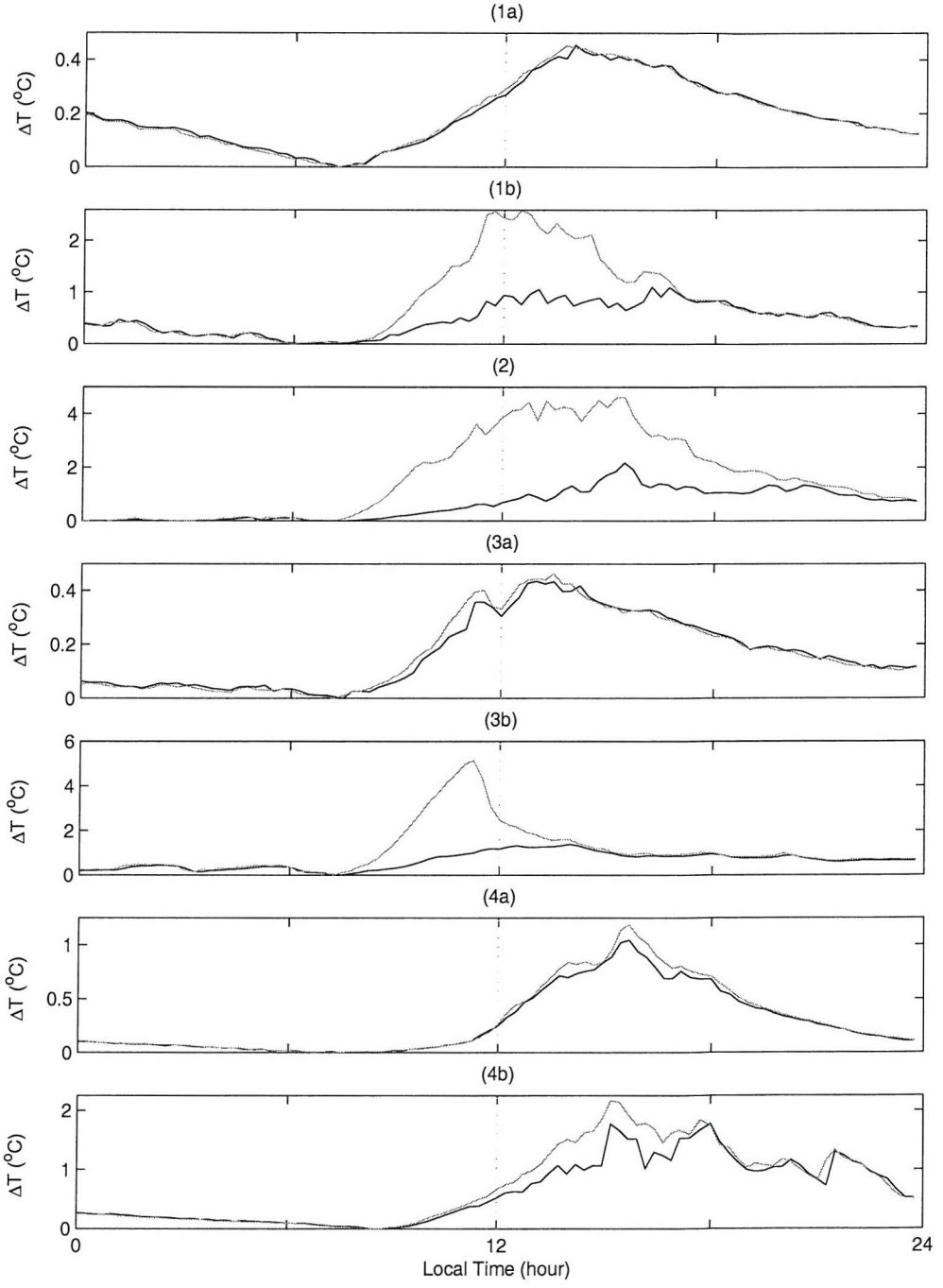

Figure 5.12 Observed examples of classified diurnal shapes from IMET buoy data set for 1m (black) and sub-skin (grey).

1. Classic Shape - Constant wind and insolation

In this situation, the wind speed is fairly constant throughout the day and the diurnal signal has a smooth shape. This is the classical shape that is normally used to describe the diurnal cycle. In reality this shape is only observed in moderate wind conditions where the upper few metres are well mixed and therefore less sensitive to changes in wind speed or in rare situations where the wind speed remains low throughout the day.

1a) Moderate winds (3<u<7m/s).

The upper 1m is well mixed and the sub-skin and 1m SST have the same phase and magnitude, typically peaking around 15:00. The amplitude of the signal will depend on the amount of insolation and wind speed, but the maximum ΔT is unlikely to exceed 1°C.

1b) Low winds (u<3 m/s)

In very low winds, stratification will occur within the top metre of the water column and the heating rate near the surface will be much greater than that at 1m. The 1m and sub-skin SST will peak at different times and with differing magnitudes. Sub-skin SST can peak as late as 4-5pm assuming the wind remains low and there are moderately clear skies. The 1m SST will peak later depending on when the stratification above it collapses and mixes down the warmer water. The 1m ΔT amplitude will not be as high as the sub-skin. The sub-skin ΔT can be over 4-5°C while the 1m ΔT amplitude is unlikely to exceed 2°C.

2. Low winds all day and night (u<3 m/s)

From the buoy analysis, it appears quite rare for winds to remain low all day but there are examples when the wind does remain low throughout the day and night or afternoon and night. The diurnal cycle builds up in the same way as described above with strong stratification occurring in the upper metre and below. If the low wind persists through the night then the DML will not be fully broken down. The stratification near the surface is likely to break down through convective overturning as the ocean loses heat to the atmosphere but in some cases stratification can still exist lower down within the top few metres of the water column. Temperature differences of 0.5°C across the top 5m were still observed at midnight.

3. Wind burst or cloud in the afternoon

In this scenario, we assume approximately constant moderate to low winds in the morning and moderately clear skies followed by a sharp wind burst/persistent cloud in the afternoon. In the case of the wind, depending on the severity of the wind burst and the stratification in the morning, the warm layer may be completely destroyed before dusk. Wind speeds need only increase by 1-2m/s for the warm layer to deepen and the surface SST to cool. In the case of thick cloud and a dramatic decrease in insolation during the afternoon, there will not be a sudden break down of the diurnal cycle. The diurnal warm layer will begin to gradually break down as the net heat flux changes sign.

3a) Moderate winds (3<u<7m/s) in the morning

Assuming that the upper metre(s) of the water column is well mixed, a sudden increase in wind speed will mix the DML deeper and reduce the heating in top few metres. The time of the maximum SST is likely to occur around the increase in wind speed. In the case of increased cloud and therefore decreased insolation, the changes will be more gradual.

3b) Low winds (u<3 m/s) in the morning

In this scenario, the surface will heat up quickly and the top few metres of the water column will become strongly stratified as the DML vanishes, causing the 1m SST to heat up at a slower rate. Due to the strong stratification near the surface, any fluctuations in wind speed and therefore, upper ocean mixing, can cause the diurnal shape at the surface to change dramatically. The change in wind speed does not need to be large: an increase of 1-2m/s, even if the actual wind speed is still less than 3m/s can break down the stratification and stop further temperature increases at the surface. The sub-skin SST will peak at the time of the wind burst, while the 1m SST will peak slightly later when the warmer water above it has been mixed down. The sub-skin maximum ΔT can still be large just from the morning heating and can exceed 2-3°C though the 1m ΔT amplitude will never be as large. If the wind increases very gently over the afternoon and there is not a sudden increase in wind, the water in the upper few metres will gradually heat up as the warm water gets mixed deeper as the wind gently increases.

In the case of a drop in insolation in the afternoon while winds are still low/moderate, the diurnal cycle may plateau off until the cooling at the surfaces mixes the warmer water deeper. There may be an abrupt change in the sub-skin SST but it will not break down the stratification within the top metre immediately.

4. Wind burst or cloud in the morning

In this case we assume that there is a strong wind burst in the morning and then approximately constant moderate or low winds and moderately/clear skies in the afternoon. Regardless of the wind speed in the morning, if the wind drops to less than 3m/s in the afternoon then stratification can still occur. There will be very little/no heating in the morning but as the wind drops/clouds disappear, stratification will develop and depending on the wind speed and insolation, the top 1m may stratify.

4a) Moderate winds (3<u<7 m/s) in the afternoon

The top metre of the water column will be well mixed and the temperature will peak late in the afternoon around 4-5pm. The maximum ΔT will not exceed 1°C.

4b) Low winds (u<3 m/s) in the afternoon

In this case, the sub-skin will deviate away from the 1m SST as the upper few metres stratify but the deviation will be much smaller than if the low wind occurred during the morning. In this case, both the 1m and sub-skin temperature will peak late in the afternoon, with the SST at 1m peaking just after the sub-skin when the stratification in the top metre has been broken down. If the low wind persists into the night, the stratification may not be fully broken down.

Figure 5.13 reports the frequency of each of the classifications for the entire buoy dataset. The classification was carried out objectively assigning thresholds of wind speed in the morning and afternoon to categorise the different shapes (Table 5.4). Random checks were carried out to verify that the threshold classification separated the diurnal shapes correctly and matched the shapes presented in Figure 5.12 and described above. Very low winds (stratification in top 1m) occur just under a third of the time. The most common shape is the classical moderate wind shape (Type 1a).

Table 5.4: Wind speed thresholds used to categorise diurnal warming shapes into groups described in Section 5.4.2.1.

SHAPE	1a	1b	2	3a	3b	4a	4b
U_{am} (m/s)	> 3	< 3	< 3	> 3 & < 4.5	< 3	> 4	> 3
U_{pm} (m/s)	> 3	< 3	< 3	> 4	> 3	> 3 & < 4.5	< 3
U_{nght} (m/s)		> 3	< 3				

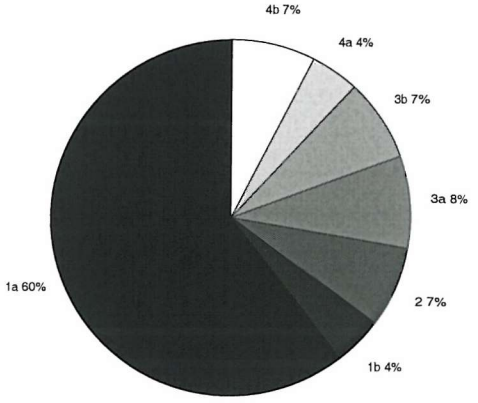

Figure 5.13: Frequency of classified diurnal SST shapes observed in IMET dataset

5.5 IMPLICATIONS

This chapter has investigated the sensitivity of the diurnal warm layer evolution to variations in wind speed and insolation during the day. The majority of diurnal warming studies have focused on discussing the maximum amplitude of the diurnal heating and rise in SST with only a few comments related to the timing of the SST peak. To be able to apply information about the maximum diurnal amplitude, some information about the phase is required. The timing of the peak SST can vary from pre-noon to late afternoon and the phase will change with depth, with a lag in the time of the maximum SST, depending on the depth of the diurnal warm layer. The shallower the warm layer, the greater its sensitivity. The Fairall et al. (1996b) warm layer model was applied to buoy data to investigate the variability of the diurnal cycle at the surface. Large differences between the surface and 1m were noted at low winds. The surface SST often responded instantaneously to changes in wind speed which resulted in more variable timing in the peak SST at the surface than at depth. Changes in insolation, due to cloud cover, had a delayed effect.

The results highlight the variability in the shape of the diurnal warm layer and also draw attention to the large differences in SST that can occur between the surface and 1m. This is very important for air-sea heat and gas exchange as the diurnal temperature variations at the surface, under low winds, can be much larger that what has been

presented in the past with in situ observations. It also highlights the complexity and uncertainty in SST as values can vary by over 1-2°C over the top 1m.

5.6 SUMMARY

The main results from this chapter are summarized below:

- Large temperature differences exist between the surface and 1m during clear sky periods with low winds (u<3m/s). The results stress the importance of resolving the differences in the diurnal SST amplitude at the surface and at depth to help understand the diurnal signal in satellite and in situ measurements.

- The diurnal cycle is sensitive to time variability in the meteorological forcing fields. Wind variability has a larger and more immediate impact on the diurnal warm layer than changes in insolation. The system becomes more sensitive as winds decrease, in particular if low winds (u<3m/s) persist in the morning. The wind variability induces an abrupt time shift in the diurnal signal, creating highly variable diurnal signals.

- A simple classification has been developed to describe the different possible shapes of the diurnal cycle related to time variability in the forcing fields. The classification helps to identify days when the diurnal cycle has a more asymmetric shape compared to the classic mean signal.

- The F96 warm layer model is sensitive to the depth of the measurement it is applied to. Either very shallow or deep sea 'surface' temperatures should be used to avoid the complications caused by the assumption of a linear temperature profile within the diurnal warm layer.

These results are discussed in more detail in the next chapter where they are applied to derive a new parameterisation of the diurnal cycle, which takes into consideration the time variability of the forcing fields.

CHAPTER 6: A NEW PARAMETERISATION FOR DIURNAL WARMING

6.1 BACKGROUND

Chapter 3 presented the global temporal and spatial distribution of diurnal warming patterns and revealed strong seasonal signals with large areas frequently susceptible to strong surface heating under low wind conditions. With very few SST platforms regularly measuring SST through the day, especially at a global scale, it has been desirable for some SST users to estimate the magnitude of the diurnal SST cycle using a parameterisation to apply or remove the diurnal signal. Three main parameterisations exist in the literature: Webster et al. (1996), Kawai & Kawamura (2002 & 2003) and Gentemann et al. (2003). Parameterisations were first developed to estimate the amplitude of the diurnal signal at the surface (skin) and investigate the implications for air-sea interaction (Webster et al., 1996). More recently diurnal warming parameterisations have been developed to help identify and remove the diurnal signal in satellite SST measurements (Kawai & Kawamura, 2002; Gentemann et al., 2003). All three parameterisations require wind speed and insolation as their main inputs, based on the theory that turbulent mixing (wind) and radiative heating (insolation) are the dominant influences for the evolution of diurnal stratification.

Based on the results from Chapter 5, these parameterisations can be built upon and improved by taking into consideration the temporal variability of the meteorological forcing during the day. This chapter describes the development and validation of a new diurnal warming parameterisation that estimates the shape of the diurnal cycle throughout the day at the sea surface and at 1m. Before introducing the new parameterisation, the existing models are discussed below.

6.1.1 Summary of diurnal warming parameterisations

Webster et al. (1996)

Webster et al. (1996; hereafter W96) developed a parameterisation for the maximum diurnal skin SST amplitude, ΔT_{max}, based on a combination of meteorological observations from the R/V Moana Wave during the TOGA COARE Intensive Observing Period in the tropical western Pacific warm pool and model-derived skin

data. ΔT_{max} is described as a function of daily peak insolation, Q_{sw_max} (Wm^{-2}), daily averaged wind speed, U (m/s), and daily averaged precipitation, P (mm/hr):

$$\Delta T_{max} = a + bQ_{sw\_max} + cP + dln(U) + eQ_{sw\_max}ln(U) + fU \quad (6.1)$$

U, Q_{sw_max} and P were regressed against model estimates of the maximum diurnal skin SST amplitude, ΔT_{max}, derived from the Kantha-Clayson 1-D diffusion model (Kantha & Clayson, 1994), since no skin measurements were available. The model was forced using the ship's surface flux measurements, and the transmission of solar irradiance through the water column was modelled by Morel and Antoine's (1994) parameterisation. Two sets of coefficients were derived for daily mean wind speeds above and below 2m/s (Table 6.1) to account for the differences between the radiative/convective regime (where no wind is present) and the wind mixing regime (Price et al., 1987).

Precipitation was included in the parameterisation. Fresh water acts as an additional stabilising force in the surface layer, reinforcing the thermal stratification and therefore minimising mixing (Price, 1979; Lukas & Soloviev, 1997). While rainfall is not normally associated with diurnal warming conditions, the warm pool region has highly variable weather including sudden short periods of heavy rainfall. Results from the TOGA COARE experiment revealed that local convection and precipitation typically peaked at 2-3am each day, so that there was a regular input of freshwater buoyancy at night that complemented the daytime thermal stratification the following day (R. Weller, personal communication). According to the parameterisation, strong precipitation can increase ΔT_{max} by a few tenths of a degree. At very low winds, the rain has negligible influence on the diurnal warm layer as it has already reached its limit in terms of stratification due to the lack of wind mixing and therefore any increased stabilisation becomes irrelevant.

Table 6.1: Coefficients for determination of ΔT_{max} from [6.1]

Coefficient	$U > 2$m/s	$U \leq 2$m/s
a	2.62×10^{-1}	3.28×10^{-1}
b	2.65×10^{-3}	2.00×10^{-3}
c	2.80×10^{-2}	4.10×10^{-2}
d	-8.38×10^{-1}	2.12×10^{-1}
e	-1.05×10^{-3}	-1.85×10^{-4}
f	1.58×10^{-1}	-3.29×10^{-1}

Kawai and Kawamura (2002 & 2003)

Based on the work by W96, Kawai & Kawamura (2002; hereafter KK02) adapted the simple parameterisation for ΔT_{max}, to apply it to the air-sea interface and at 1m, using a combination of in situ data and model output. The meteorological data were obtained from a selection of Japan Meteorological Agency (JMA), TRITON and drifting buoys in the western Pacific (40°S – 40°N, 90°E – 160°W). No skin measurements were available so the diurnal skin SST amplitude, ΔT_{max}, was estimated using the Kondo-Sasano-Ishii 1-D model (described in KK02) and by applying the Fairall et al. (1996b) cool skin model. The solar absorption profile was parameterised using the Kondo et al. (1979) empirical formula. The 1m ΔT_{max} parameterisation was also derived from model output and not the observations to avoid including any data influenced by non-local processes.

ΔT_{max} is described as a function of daily peak insolation, Q_{sw_max}, and daily or day-time mean wind speed, U. Precipitation was not included in this parameterisation because of a lack of data.

$$\Delta T_{max} = a + bQ_{sw\_max}^{2} + cln(U) + dQ_{sw\_max}^{2}ln(U) \tag{6.2}$$

The parameterisation was developed to consider only wind speeds during the daytime, $U_{9\text{-}15h}$, in recognition that this time period is most critical in the evolution of the diurnal warm layer. However since in practice a daily mean wind speed is often easier and more practical to obtain, the model was also developed to use a daily mean wind speed, U. In a similar way to W96, two sets of coefficients were derived for when the mean wind speed was above and below 2.5m/s (Table 6.2) to reflect the radiative and mixing regimes.

Table 6.2: Coefficients for determination of ΔT_{max} from [6.2]

	Coefficient	$U_{9\text{-}15h} > 2.5$m/s	$U_{9\text{-}15h} \leq 2.5$m/s	$U_{0\text{-}24h} > 2.5$m/s	$U_{0\text{-}24h} \leq 2.5$m/s
SKIN	*a*	-2.5893×10^{-2}	-2.0216×10^{-1}	-7.3287×10^{-2}	-3.6700×10^{-1}
	b	3.0494×10^{-6}	5.0109×10^{-6}	3.2708×10^{-6}	5.6814×10^{-6}
	c	-2.8258×10^{-2}	2.2063×10^{-1}	-7.9982×10^{-2}	4.0052×10^{-1}
	d	-1.1987×10^{-6}	-3.3394×10^{-6}	-1.3329×10^{-6}	-3.9637×10^{-6}
1m	*a*	-1.8838×10^{-1}	-5.8428×10^{-2}	-1.4236×10^{-1}	-1.0322×10^{-1}
	b	2.4069×10^{-6}	1.8265×10^{-6}	2.3989×10^{-6}	1.9361×10^{-6}
	c	7.5810×10^{-2}	-6.6016×10^{-2}	5.7289×10^{-2}	1.4576×10^{-2}
	d	-9.2014×10^{-7}	-2.8672×10^{-7}	-9.2463×10^{-7}	-4.1966×10^{-7}

An evaluation of this parameterisation (Kawai & Kawamura, 2003; hereafter KK03) reported biases of 0.1-0.2°C in the tropics which the authors related to the difference between latent heat fluxes in the tropics and extra-tropics. They revised their 1m model to include a daily mean latent heat flux variable, Q_l (where Q_l is negative), based on the theory that a greater air-sea latent heat flux cools the sea surface and suppresses the rise of SST. To keep in line with the new Q_l variable, they also adapted their parameterisation to use a daily mean shortwave flux, Q_{sw}, instead of a daily maximum. The coefficients are listed in Table 6.3.

$$\Delta T_{max} = a + b(Q_{sw} + Q_l + 300)^2 + c\ln(U) + d(Q_{sw} + Q_l + 300)^2\ln(U) \qquad (6.3)$$

Table 6.3: Coefficients for determination of ΔT_{max} from [6.3]

	Coefficient	$U_{0\text{-}24h} > 2.5$m/s	$U_{0\text{-}24h} \leq 2.5$m/s
1m	a	-3.7498×10^{-1}	-1.8850×10^{-1}
	b	7.8326×10^{-6}	5.8608×10^{-6}
	c	1.3847×10^{-1}	-6.5047×10^{-2}
	d	-2.8923×10^{-6}	-7.4042×10^{-7}

Gentemann et al. (2003)

Gentemann et al. (2003) derived empirical models of the diurnal SST cycle tailored to two of the main satellite SST datasets: the Pathfinder AVHRR pseudo-bulk 1m SST and the TMI sub-skin SST. The diurnal SST signal was determined by subtracting the weekly Reynolds 'bulk' SST product (Reynolds & Smith, 1994) from the global satellite SST measurements, noting the time of the satellite overpass. The Reynolds SST is assumed to represent the true mixed layer temperature. Only TMI measures SST over the full diurnal period. AVHRR has two overpasses a day which are fixed to around 2:00 and 14:00. TMI is also limited to two overpasses a day but they are not fixed in time and vary each day. The diurnal cycle shape for the TMI and Pathfinder is expected to be identical and consequently the TMI is used to model the shape of the diurnal cycle for both the TMI and Pathfinder data. The amplitudes of each dataset are modelled onto the TMI shape and referenced to 2am where the diurnal amplitude is set to zero. More recently a further model has been developed for 1m using NBDC buoys (Gentemann, personal communication). For the satellite parameterisations, the model is

derived from daily mean clear sky incoming shortwave radiation, Q, calculated following Liou (1980) and daily mean wind speed, U, derived from global SSM/I and TRMM-TMI wind fields. The 1m model is derived using the buoy wind speeds and modelled Q (as described above). The TMI model has been recently updated (Gentemann, personal communication; hereafter G04) and this version is presented below rather than the published model.

$$\Delta T_{pf} = 0.344f(t)[(Q - Q^{p}_{o}) - 1.444 \times 10^{-3}(Q - Q^{p}_{o})^{2}]e^{-0.29U} \quad (6.4a)$$

$$\Delta T_{tmi} = 77.704f(t)[(2.129\times10^{-2}(Q - Q^{t}_{o}) - 3.075\times10^{-5}(Q - Q^{t}_{o})^{2}]e^{-0.53U} \quad (6.4b)$$

$$\Delta T_{buoy} = f_{b}(t)[9.767\times10^{-1}(Q - Q^{b}_{o}) - 4.813\times10^{-4}(Q - Q^{b}_{o})^{2}]e^{-0.28U} \quad (6.4c)$$

where t = time (hours), Q^{p}_{o} = 24 (Wm^{-2}), Q^{t}_{o} = 132(Wm^{-2}), Q^{b}_{o} = 88 (Wm^{-2}). Each parameterisation is only valid when Q is greater than Q_o (e.g. for Pathfinder $Q>Q^{p}_{o}$).

$f(t) = [4.118 - 4.13\cos(\omega t) - 5.039\sin(\omega t) + 0.8746\cos(2\omega t) + 2.583\sin(2\omega t) - 0.246\cos(3\omega t) - 0.5143\sin(3\omega t) + 0.2762\cos(4\omega t) - 0.3355\sin(4\omega t) - 0.0609\cos(5\omega t) + 0.2669\sin(5\omega t)]10^{-3}$

$f_b(t) = [3.7 - 2.1\cos(\omega t) - 3.8\sin(\omega t) + 0.1044\cos(2\omega t) + 1.2\sin(2\omega t) - 0.0759\cos(3\omega t) - 0.1471\sin(3\omega t) + 0.0141\cos(4\omega t) - 0.0159\sin(4\omega t) + 0.0278\cos(5\omega t) - 0.026\sin(5\omega t)]10^{-3}$

where ω is 0.2618 (hr^{-1}).

The parameterisations described above are discussed in more detail in Sections 6.5.2 & 6.5.3, where they are analysed and compared to observations and the new parameterisation presented in this chapter.

6.1.2 A new parameterisation

The empirical models described above use a daily mean wind speed, daily mean/maximum insolation and in some cases, extra variables such as daily mean precipitation or latent heat flux to predict the diurnal SST amplitude. The results from

Chapter 5 suggest that to estimate the diurnal cycle with more confidence and precision, diurnal fluctuations in the wind and insolation should be considered. Wind is never constant and a sudden wind burst in the afternoon of 9 m/s while the rest of the day is around 3 m/s will bring the daily mean wind speed to 4-5 m/s and therefore a model is likely to underestimate the diurnal amplitude. The same applies to the insolation, in particular if the daily maximum insolation is used. Cloud cover can vary through-out the day and the only clear patch in a day could be around noon and therefore a model would over-estimate the amplitude of the diurnal cycle.

Current modelling efforts have been built upon to derive a more complex model of the diurnal cycle. A new parameterisation has been developed which estimates the shape (phase and amplitude) of the diurnal cycle for 1m and the sub-skin, based only on wind and insolation measurements at several times of the day. The parameterisation follows on from Gentemann et al. (2003) by estimating the amplitude of the diurnal signal at any time of day and is not restricted to only defining ΔT_{max}. No diurnal skin model is produced since the nature of the skin effect during strong diurnal warming is still not properly observed or understood. It is assumed that the difference in diurnal heating between the skin and sub-skin is almost negligible and therefore the sub-skin diurnal warming parameterisation should be able to be applied to all satellite measurements. An additional cool skin model would need to be applied to the sub-skin model to include all skin effects.

This chapter describes the development of the new parameterisation. The model derivation is described in detail in Sections 6.3 and 6.4 and the results of applying the model and performing independent validation tests are reported in Section 6.5. Potential applications of the new parameterisation are discussed in Section 6.6.

6.2 DATA

The new diurnal warming parameterisation is derived from the WHOI IMET buoy dataset (Section 5.2) and the F96-derived sub-skin temperatures analysed in the previous two chapters. Additional meteorological buoy data along with cruise data are used to create independent datasets to validate the parameterisation (Table 6.4, Figure 6.1). While the sub-skin model is derived using modelled values, it is preferable to test

the parameterisation using observations. To validate the parameterisation, wind, downward shortwave radiation and SST are needed. Wind and downward shortwave radiation measurements are required as inputs for the parameterisation and SST provides validation of the model output. The validation datasets are not filtered to remove non-local effects as was carried out for the regression dataset (Section 5.3.3) due to the large volume of data. The implications of this are discussed in Section 6.5.2.

6.2.1 Sub-skin validation dataset

Almost no in situ sub-skin measurements exist since the depth required to measure the true sub-skin temperature during strong diurnal warming is in the top millimetre of the ocean and therefore requires a highly specialised instrument. Shipboard infrared radiometers have been deployed on several research cruises over the past decade and provide the only source of in situ skin measurements. Since the magnitude of diurnal heating of the skin and sub-skin is assumed to be identical, skin measurements are used to validate the sub-skin model. While several cruise skin SST datasets exist, very few coincide with strong diurnal warming conditions which are required to validate the parameterisation. A small skin SST data set is collected from two cruises from the R/V Franklin during the TOGA COARE experiment (Webster & Lukas, 1992) and the RRS Charles Darwin during an ATSR-2 validation cruise in the Indian Ocean in October/November 2001 (Pascal et al., 2002). The skin measurements were taken by two different infrared radiometers: a Commonwealth Scientific and Industrial Research Organisation (CSIRO) radiometer (Coppin et al., 1991) was used onboard RV Franklin and the Rutherford Appleton Laboratory (RAL) SISTeR radiometer was used onboard RRS Charles Darwin. To increase the number of validation points, some data are also obtained from the Mutsu Bay experiment (Yokoyama et al., 1995). A special instrument was developed and deployed on several buoys to measure SST at 0.02m, 0.3m, 0.5m, 1m and 2m (Yokoyama et al., 1995). The 0.02m measurements are used to validate the sub-skin model. $SST_{0.02m}$ does not represent a skin or sub-skin measurement but the differences between temperatures at 0.02m and the sub-skin are expected to be small and therefore, since it provides an extra source of data very close to the surface, $SST_{0.02m}$ is used in the validation.

6.2.2 1m validation dataset

The 1m validation dataset is made up of measurements from the Pilot Research Moored Array in the Tropical Atlantic (PIRATA), the Tropical Atmosphere Ocean (TAO) / Triangle Trans-Ocean Buoy Network (TRITON) Autonomous Temperature Line Acquisition Systems (ATLAS) in the tropical Pacific Ocean and two IMET buoys from mid-latitude locations.

The TAO/TRITON mooring array and the more recent PIRATA mooring array provide long term time series of the tropical oceanic and atmospheric variability. Data are taken from the high-resolution New Generation ATLAS moorings, which have replaced the standard ATLAS moorings over the last five years. All the ATLAS moorings record wind speed and SST at 1m but only a few moorings measure downward radiation, which restricts the number of locations that can be used in the validation study.

Two additional WHOI IMET buoys are also used in the validation study to provide validation tests outside the tropics. These buoys were not used in the derivation of the model and are an independent dataset like the TAO/TRITON and PIRATA data. The first dataset is from the Subduction Experiment in the eastern Atlantic off the West Coast of Africa (33N, 22W) during October 1992 to June 1993. The second dataset is from the Marine Light Mixed Layer Experiment (MLML91) in the North Atlantic (59.5N, 20.8W) during April to September 1991. Both these datasets provide wind speed, downward shortwave radiation and SST at 1m.

Table 6.4: Details of data used in the validation dataset

	Location	**Time**	**Depth of SST measurement**	U	Q_{sw}
TAO/TRITON Tropical Pacific	140W,0N; 95W, 0N; 95W, 5S; 165E, 2N; 165E, 5N; 165E, 8S	Jan 1998 to Jan 2003	1m	x	x
PIRATA Tropical Atlantic	10W, 0N 10W, 10S 35W, 0N	Jan 1998 to Jan 2003	1m	x	x
NE Atlantic (Subduction exp)	22W, 33N	Oct 1992 to Jun 1993	1m	x	x
N Atlantic (MLML91 exp)	21W, 60N	Apr – Sep 1991	1m	x	x
Mutsu Bay	141E, 40N	Summer 1996 & 97	0.02m	x	x
R/V Franklin West Warm Pool	156W, 1.5S	Nov 1992	Skin	x	x
RRS Ch. Darwin Trop. Indian Ocean	61W, ±4N/S	Oct/Nov 2001	Skin	x	x

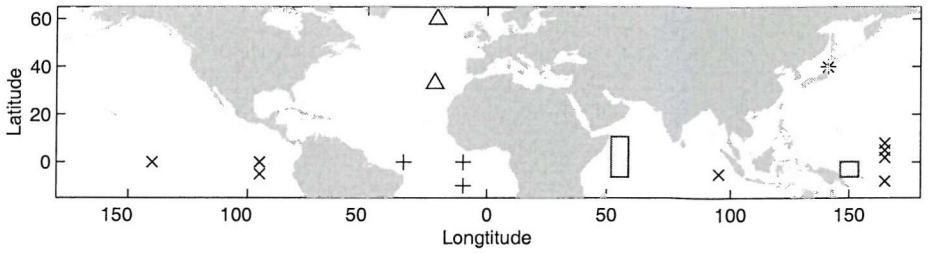

Figure 6.1 Location of buoys used in validation data set. x – TAO/TRITON buoys, + PIRATA buoys, Δ IMET buoys, * Mutsu Bay buoy and the boxes highlight the two cruise regions.

6.3 DESCRIPTION OF THE PARAMETERISATION

The parameterisation is developed as a single parameterisation which computes both the sub-skin and 1m diurnal temperature variations. The 1m diurnal shape is the primary output from the parameterisation. In moderate winds, the 1m and sub-skin output are identical as the top few metres will be well mixed. Under low winds, when the top metre is stratified, the sub-skin shape is based upon the 1m curve and for this reason the 1m parameterisation is required when computing the sub-skin diurnal temperature variations. The parameterisation is developed from the work presented in the previous chapter and aims to capture the different diurnal warming shapes discussed in the classification. The structure of the parameterisation is documented in this section. A coded version of the parameterisation is provided in Appendix D, along with a schematic flow diagram which summarises the steps of the model.

The day is divided into four parts to consider the time variability of the forcing fields:

Period 1: morning cooling	0:00 – time of daily minimum SST (t_{min})
Period 2: morning heating	t_{min} – 12:00
Period 3: afternoon heating/cooling	12:00 – t_{pm}
Period 4: evening cooling	t_{pm} – 24:00

where t_{pm} is set to 17:00, except for certain meteorological conditions (described in detail further on) when t_{pm} is set to $t_{max\ 1m}$+($t_{max\ 1m}$-12:00), where t_{max} is the time of the daily maximum SST. (Time always refers to local solar time.) The day is not separated any further to keep the parameterisation as simple and practical as possible for users. For each segment of the day, a quadratic curve is derived to describe the diurnal

variation of temperature, ΔT, referenced from the daily minimum SST, SST_{min}, as a function of time, t.

To define the characteristics of the 1m and sub-skin curves, eight parameters are required:

(i)	Cooling rate in the morning	$cgrad$
(ii)	Time of minimum SST	t_{min}
(iii)	Maximum morning SST deviation	$\Delta T_{(12h\text{-}tmin)}$
(iv)	Maximum afternoon SST deviation	$\Delta T_{(tmax\text{-}12)}$
(v)	Time of daily maximum SST	t_{max}
(vi)	SST deviation at midnight	$\Delta T_{(24h\text{-}tmin)}$
(vii)	End (start) time of period 3 (4)	t_{pm}
(viii)	Diurnal temperature variation at t_{pm}	ΔT_{tpm}

The last two parameters are implicit to the model as they are taken from the parameterisation. The other six parameters must be derived explicitly from ancillary data. Individual empirical models have been developed to compute the explicit parameters, as a function of four wind speed and two insolation values averaged over different periods of the day. The models were derived by regression using highly accurate buoy measurements from three Woods Hole Oceanographic Institution (WHOI) Improved Meteorological (IMET) buoys at different locations (Arabian Sea, western Pacific warm Pool & Sargasso Sea) presented in Chapter 5. No direct sub-skin measurements are available so these have been derived from the Fairall et al. (1996b) warm layer model described in Section 5.3.2. The details of the parameter modelling are described in detail in the next section (6.4).

Chlorophyll concentration and precipitation are not included in the parameterisation. Although they contribute to the surface stratification when they coincide with the right diurnal warming conditions, the effect is small compared to the dominant influence of wind and insolation and they are not expected to add much value to a simple parameterisation. Precipitation is only important for some tropical regions such as the western Pacific warm pool and does not occur during diurnal warming conditions outside these localised regions. As Chapter 4 discussed, large chlorophyll

concentrations (>2-3 mg/m^3) are required to have a noticeable influence on the thermal structure of the diurnal warm layer. These high concentrations are again infrequent compared to the frequency of diurnal warming events. Chlorophyll and fresh water effects should certainly be considered by 1-D mixed layer models, which have more detail and sensitivity but they are unlikely to significantly contribute to the accuracy of a diurnal warming parameterisation for open ocean. In coastal areas, associated with fresh water discharge from rivers and high chlorophyll concentrations, a parameterisation would benefit from including these two variables. However, this work is concerned with global open ocean conditions.

Figure 6.2 demonstrates how the diurnal variation of temperature is represented by the four curves and the six explicit parameters required to model them. Table 6.5 lists and defines the explicit parameters and the required wind and insolation variables. To run the parameterisation, all that is required are the wind and insolation variables. The time step of the parameterisation is flexible to suit user's needs. The output is the diurnal temperature variation referenced from the daily minimum SST which is assumed to represent the true mixed layer temperature.

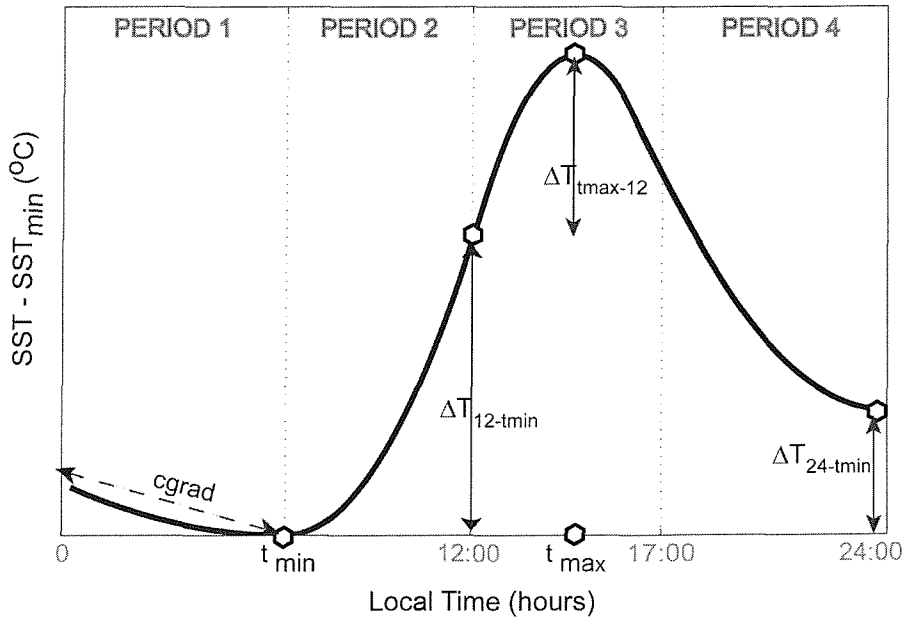

Figure 6.2: Schematic of the diurnal SST cycle parameterisation. The day is divided into four parts and six models define the shape of the four curves: *cgrad*, t_{min}, $\Delta T_{12\text{-}tmin}$, t_{max}, $\Delta T_{tmax\text{-}12}$, $\Delta T_{24\text{-}tmin}$. The predicted diurnal warm layer temperature deviation, ΔT, is referenced from the daily minimum SST where $\Delta T_{(t=tmin)} = 0$.

Table 6.5: List and definition of diurnal warming parameters & variables

Model Parameter	Definition	Calculation	Units	Variables required
cgrad	Cooling gradient in morning	$(SST_{6h} - SST_0) / 6$	°C /hr	$U_{0\text{-}6h}$
t_{min}	Time of daily minimum SST	Time of min. SST observed between 5-9am	Hours	$U_{8\text{-}12h}$, $Q_{sw\ 6\text{-}12h}$
$\Delta T_{(12h\text{-}tmin)}$	Maximum morning SST deviation	SST_{min}(5h-9h) – SST_{12h}	°C	$U_{8\text{-}12h}$, $Q_{sw\ 6\text{-}12h}$
$\Delta T_{(tmax\ -\ 12h)}$	Maximum afternoon SST deviation	SST_{max}(10h-18h) – SST_{12h}	°C	$U_{12\text{-}15h}$, $Q_{sw\ 12\text{-}18h}$
t_{max}	Time of daily maximum SST	Time of max. SST observed between 10am & 6pm	Hours	$U_{8\text{-}12h}$, $Q_{sw\ 6\text{-}12h}$ $U_{12\text{-}15h}$, $Q_{sw\ 12\text{-}18h}$
$\Delta T_{(24h\ -\ tmin)}$	SST deviation at 24:00	SST_{24h} – SST_{min}(5h-9h)	°C	$U_{16\text{-}24}$, ΔT_{max}
Variable				
$U_{0\text{-}6h}$	Mean wind speed over midnight to 6am		m/s	
$U_{8\text{-}12h}$	Mean wind speed over 8am to noon		m/s	
$U_{12\text{-}15h}$	Mean wind speed over noon to 3pm		m/s	
$U_{16\text{-}24}$	Mean wind speed over 4pm to midnight		m/s	
$Q_{6\text{-}12h}$	Mean downward Q_{sw} over 6am to noon		Wm^{-2}	
$Q_{12\text{-}18h}$	Mean downward Q_{sw} over noon to 6pm		Wm^{-2}	

The curves are defined as:

Period 1 (t = 0:00 – t_{min})

$$\Delta T_t = cgrad.t_{\min}\left(\frac{(t - t_{\min})^2}{(0 - t_{\min})^2}\right) \tag{6.5a}$$

Period 2 ($t = t_{min}$ – 12:00)

$$\Delta T_t = \Delta T_{(12h - t\ \min)}\left(\frac{(t - t_{\min})^2}{(12 - t_{\min})^2}\right) \tag{6.5b}$$

Period 3 (t = 12:00 – t_{pm})

$$\Delta T_t = \Delta T_{(t\ \max - t\ \min)} - \left(\frac{\Delta T_{(t\ \max - 12h)}(t - t_{\max})^2}{(12 - t_{\max})^2}\right) \tag{6.5c}$$

Period 4 ($t = t_{pm}$ – 24:00)

$$\Delta T_t = \Delta T_{(24h-t\,\min)} + \left(\frac{\left(\Delta T_{(t_{pm})} - \Delta T_{(24h-t\,\min)}\right)(t-24)^2}{(24-t_{pm})^2} \right) \tag{6.5d}$$

There are two adaptations of this shape for the afternoon heating/cooling period (Period 3) based on the extensive examination of many diurnal SST signals carried out in Chapter 5, particularly of Type 3a and 3b (diurnal shape classification, Section 5.4.2.1). The other types of diurnal warming shapes can be modelled using the main curve equations and do not require special treatment.

1. The first case is for the 1m afternoon heating/cooling curve during moderate winds. If the time of the peak SST, t_{max}, at 1m is earlier than 14h30 then the length of time of period 3 is reduced from 17h00 to [$t_{max\ 1m}$+($t_{max\ 1m}$-12h00)], to make the third curve symmetric about the peak of the diurnal cycle. This produces a more realistic cooling shape at 1m during moderate wind conditions.

2. The second adaptation is for the sub-skin. An additional curve is derived for the afternoon heating/cooling period of the sub-skin to represent cases where there is an abrupt break down in the diurnal stratification. The top metre can become strongly stratified during the morning so that even a small increase in wind can break down the stratification in the top layer and cause the sub-skin SST to drop rapidly (Figure 5.10). In this situation, the temperature cools from the time of the sub-skin peak SST to the time of the 1m maximum SST and then follows the 1m curve for the rest of the day. For this case, the new curve is computed in addition to the original curve [6.5c]. The time period for this curve becomes $t_{max\ sub\text{-}skin}$ - $t_{max\ 1m}$.

$$\Delta T_t = \Delta T_{\max 1m} + \left(\Delta T_{\max sub} - \Delta T_{\max 1m}\right)\left(\frac{(t - t_{\max 1m})^2}{(t_{\max 1m} - t_{\max sub})^2} \right) \tag{6.6}$$

where

$$\Delta T_{\max} = \Delta T_{(12h-t\,\min)} + \Delta T_{(t\,\max-12h)} \tag{6.7}$$

An example of this different curve definition is demonstrated in Figure 6.3. The first plot shows the results using the principal curve equations [6.5] for the sub-skin (grey) and 1m (black). The second plot shows the altered curve for the sub-skin to represent the sudden drop in sub-skin SST as water is mixed downwards by an increase in wind speed. The threshold, which determines whether this curve is used, is estimated from the modelled sub-skin and buoy data.

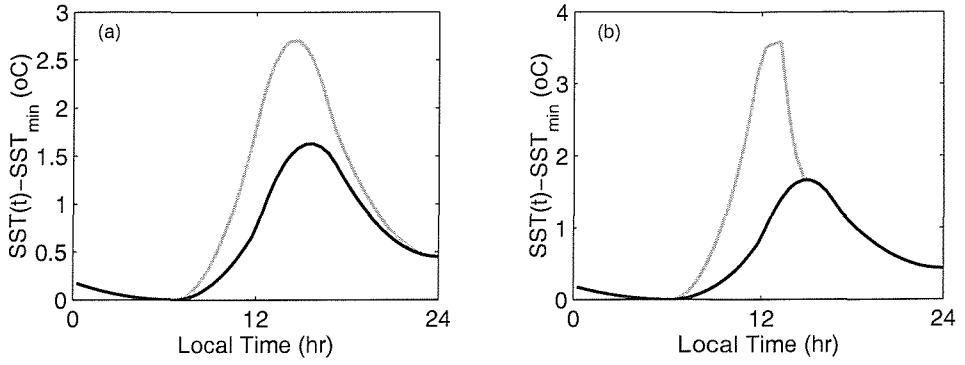

Figure 6.3: Example of the diurnal cycle parameterisation for 1m (black) and sub-skin (grey) during low wind conditions. In the second plot, wind speed has increased at mid-day after low winds in the morning and the surface water gets mixed down resulting in a sudden drop in sub-skin SST. A different curve is applied to the afternoon time period to represent this.

6.4 DERIVATION OF THE DIURNAL WARMING PARAMETER MODELS

6.4.1 Regression data set

To derive the models for the six explicit parameters, the wind and insolation variables were computed, along with the parameters for the regression, from the buoy measurements as described in Table 6.5. The search for the time of the daily minimum and maximum SST is restricted to 5am to 9am for the minimum SST and 10am to 6pm for the maximum SST. The time of the minimum SST is very sensitive to subtle non-local effects since the changes in temperature are very small on the order of milli-degrees to a tenth of a degree, which makes it difficult to be confident of the exact time of the true minimum SST due to cooling. The time of the maximum SST is easier to locate as the changes in temperature around the maximum are larger.

6.4.2 Derivation of models and coefficients

Each of the models was derived empirically by regression against the IMET buoy data. In general, the same model and coefficients are applicable for the 1m and sub-skin

diurnal cycle parameterisation. However, for low winds, when the water between the surface and 1m becomes stratified, different coefficients should be applied to the 1m t_{max} model, and extra terms applied to the 1m $\Delta T_{12h\text{-}tmin}$. The changes are applied to the 1m parameterisation based on the premise that, at very low winds, the 1m response is dampened since less heat is mixed to that depth. Figure 6.4 shows the observed ΔT_{max}, derived from the IMET buoy data plotted against $U_{8\text{-}12h}$ for different ranges of $Q_{6\text{-}12}$ (Figure 6.4a) and against $Q_{6\text{-}12h}$ for different ranges of $U_{8\text{-}12h}$ (Figure 6.4b). Grey represents the sub-skin ΔT_{max} and black, the 1m value. The different symbols represent different insolation or wind speed ranges. The combination of these figures demonstrates the deviation of the sub-skin and 1m values under low wind and high insolation conditions. Under very low winds, the 1m ΔT_{max} does not continue to increase like the sub-skin. This result was also found in KK02's comprehensive buoy analysis.

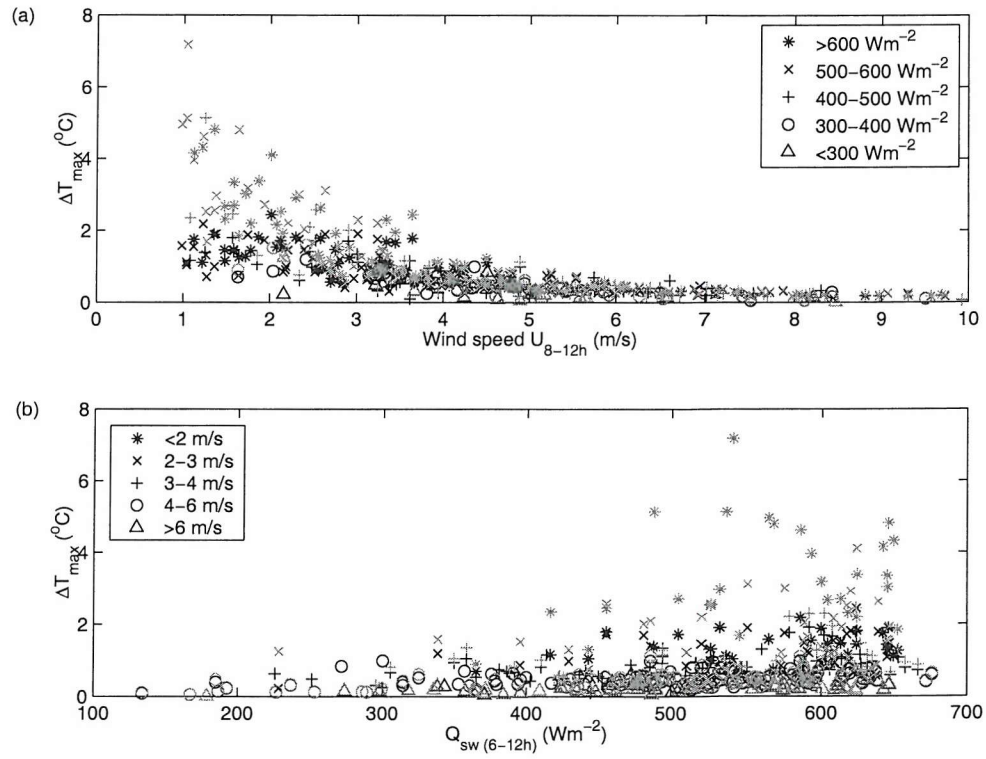

Figure 6.4: a) ΔT_{max} against morning mean wind speed, $U_{8\text{-}12h}$, for different ranges of mean morning insolation values, $Q_{6\text{-}12h}$. b) ΔT_{max} against morning mean insolation, $Q_{6\text{-}12h}$, for different ranges of mean morning wind, $U_{8\text{-}12h}$. Grey represents sub-skin values and black are 1m values.

Additional 1m models are derived for $\Delta T_{(12\text{-}tmin)}$ and t_{max}. The surface layer is most sensitive to wind and insolation during the morning period rather than during the

afternoon. In the morning, the stratification between the surface and 1m is due to the combination of wind speed and insolation. The lower the insolation, the lower the wind required for stratification in the top metre to occur. Figure 6.5a shows an example of this. $\Delta T_{(12\text{-}tmin)}$ is plotted against morning wind speed for $Q_{6\text{-}12h}$ greater than 600Wm^{-2} (grey) and for $Q_{6\text{-}12h}$ between 350 and 450Wm^{-2} (black). The dots represent the 1m $\Delta T_{(12\text{-}tmin)}$ and the crosses represent the sub-skin values. The lines are the model results (solid: sub-skin and dotted: 1m). The figure highlights how the sub-skin and 1m $\Delta T_{(12\text{-}tmin)}$ deviate at different wind speeds depending on the amount of heating. For this reason a more complex threshold is used rather than just using a wind value (as used by W96, KK02 & KK03). In the afternoon, changes in temperature become more dependent on the mixing processes (mixing downwards warmer water from above) than just the radiative heating, making it problematic to accurately predict with simple wind and insolation variables. This can be seen in Figure 6.5b where the deviation between the sub-skin and 1m $\Delta T_{(tmax\text{-}12)}$ is almost negligible. Therefore the same model is applied to the sub-skin and 1m, although if afternoon wind speeds drop below 2m/s, the 1m $\Delta T_{(tmax\text{-}12)}$ is prevented from increasing and is kept constant below this wind speed threshold.

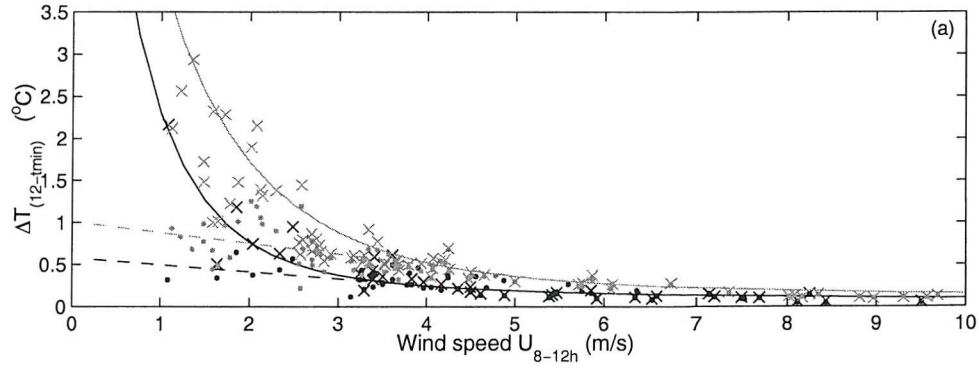

Figure 6.5a: $\Delta T_{(12\text{-}tmin)}$ against morning wind speed, $U_{8\text{-}12h}$, for $Q_{6\text{-}12h}$ greater than 600Wm^{-2} (grey) and for $Q_{6\text{-}12h}$ between 350 and 450Wm^{-2} (black). The dots represent 1m $\Delta T_{(12\text{-}tmin)}$ and the crosses represent the sub-skin values. The lines are the model predictions for $Q_{6\text{-}12h}$ 650Wm^{-2} (grey) and 400Wm^{-2} (black). The solid line represents the sub-skin and the dotted line 1m.

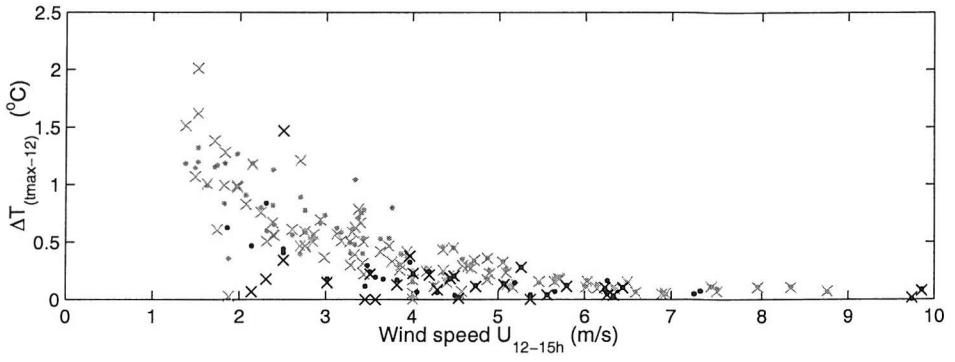

Figure 6.5b: $\Delta T_{(tmax\text{-}12)}$ against afternoon wind speed, $U_{12\text{-}15h}$, for $Q_{12\text{-}18h}$ greater than 600Wm^{-2} (grey) and for $Q_{6\text{-}12h}$ between 350 and 450Wm^{-2} (black). The dots represent 1m $\Delta T_{(12\text{-}tmin)}$ and the crosses represent the sub-skin values.

The relationship between each of the model parameters, calculated from the buoy data, and the wind speed and insolation variables required to predict it are shown in Figure 6.6. Figures 6.6c-e show both the 1m (black dots) and sub-skin (grey dots) values. The ΔT amplitudes show the clearest relationship with their wind and insolation variables. For $\Delta T_{(24h\text{-}tmin)}$, ΔT_{max} is used in the regression as well as the wind speed at night to summarise the history of diurnal warming conditions during the day time. Low winds at night can occur regardless of the wind conditions during the day and therefore some history is needed to identify whether stratification may still exist during the evening. t_{min} and t_{max} do not show a strong correlation with their variables. For t_{max}, under low wind and high insolation conditions, the 1m t_{max} lags the sub-skin peak as expected (Figure 6.6c). The scatterplots also show differences between the sub-skin and 1m t_{max} even at higher winds. In these conditions the diurnal signal is quite small, and in the same way as for t_{min}, very small SST variations at 1m or at the sub-skin can cause different t_{max} values.

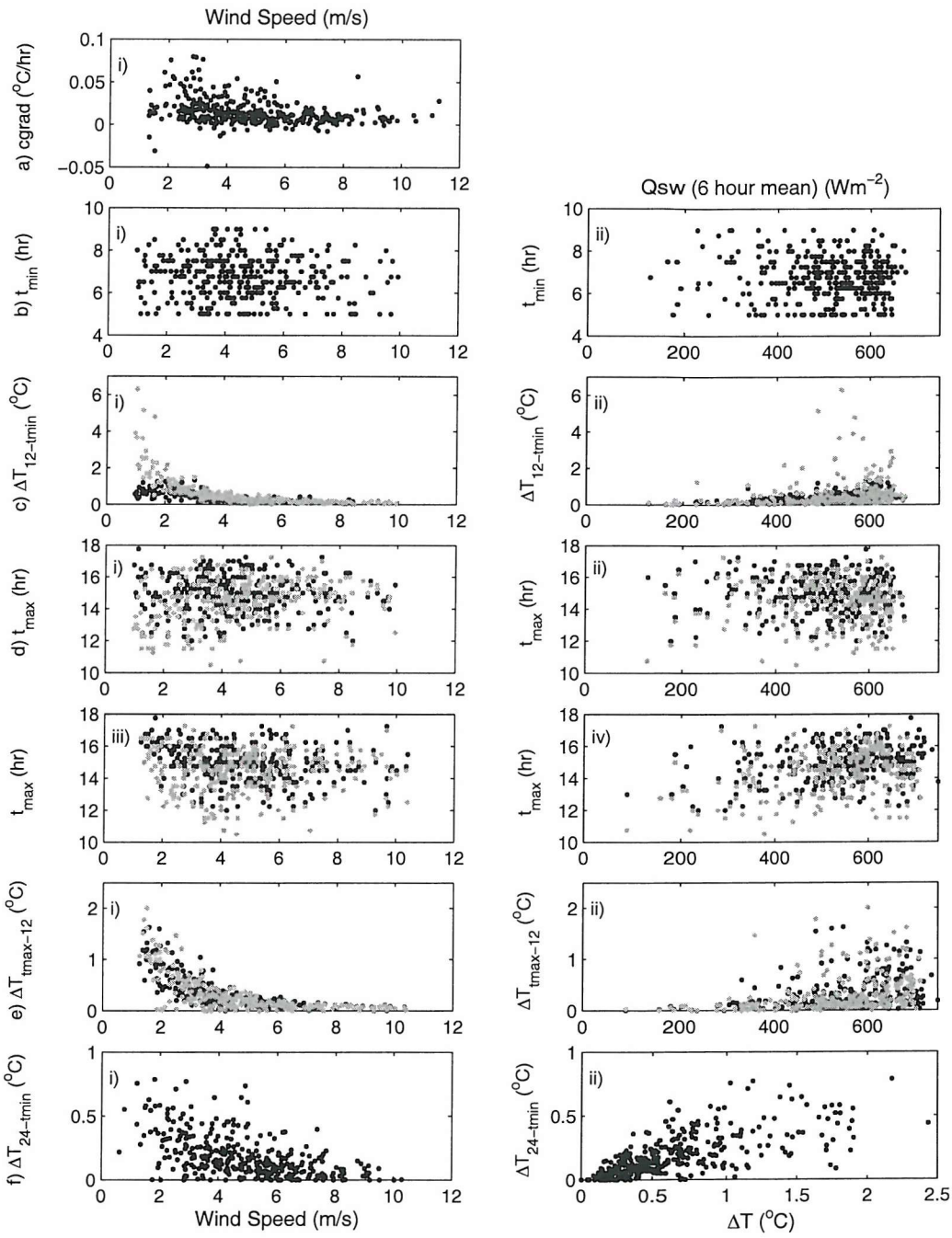

Figure 6.6: Model variables against wind and insolation values. All values are calculated from the regression dataset. a) Cooling gradient, *cgrad*, against $U_{0\text{-}6h}$. b) Time of daily minimum SST, t_{min}, against (i) $U_{8\text{-}12h}$ and (ii) $Q_{6\text{-}12h}$. c) Morning diurnal heating amplitude, $\Delta T_{(12\text{-}tmin)}$, against (i) $U_{8\text{-}12h}$ and (ii) $Q_{6\text{-}12h}$. d) Time of daily maximum SST, t_{max}, against (i) $U_{8\text{-}12h}$, (ii) $Q_{6\text{-}12h}$, (iii) $U_{12\text{-}15h}$ and (iv) $Q_{12\text{-}18h}$. e) Afternoon diurnal heating amplitude, $\Delta T_{(tmax\text{-}12h)}$, against (i) $U_{12\text{-}15h}$ and (ii) $Q_{12\text{-}18h}$. f) Residual stratification at midnight, $\Delta T_{(24h\text{-}tmin)}$, against (i) $U_{16\text{-}24h}$ and (ii) ΔT_{max}.

The form of the models is presented in Equations [6.8] to [6.13] and their coefficients are listed in Table 6.6. The functional dependence of the models is based upon existing parameterisations. Due to the lack of data for very low winds (u<0.5 m/s), both the

$\Delta T_{12h\text{-}tmin}$ and $\Delta T_{tmax\text{-}12h}$ models are limited to wind speeds greater or equal to 0.5 m/s. More observations are required for these extreme low winds conditions to extend the parameterisation below wind speeds of 0.5m/s and consequently, any mean wind values below this threshold should be fixed to 0.5 m/s. To reflect the sudden breakdown of stratification in the top 1m, if there is an increase in wind speed during the afternoon, the sub-skin $\Delta T_{tmax\text{-}12h}$ is set to 0.1°C. When different $\Delta T_{12h\text{-}tmin}$ and t_{max} models are required for the 1m parameterisation, the threshold conditions, determined from the buoy data analysis, are described.

$$cgrad = a + be^{(-0.3U_{0-6h})} \tag{6.8}$$

$$t_{\min} = a + b\ln(U_{8-12h}) \tag{6.9}$$

$$\Delta T_{12h-t\min} = a + be^{(-600/Qsw_{6-12h})U_{8-12h}} + c\left(Qsw_{6-12h}/U_{8-12h}\right) \tag{6.10a}$$

If $U_{8\text{-}12h} < us$, where $us=(0.0064Qsw_{6\text{-}12h})+1.2$

$$\Delta T_{12h-t\min} = a + be^{(-600/Qsw_{6-12h})us} + c\left(Qsw_{6-12h}/us\right) + \left(\left(d.Qsw_{6-12h}\right) + f\right)\left(us - U_{8-12h}\right) \tag{6.10b}$$

$$t_{\max} = a + b\ln(U_{8-12h}) + cQsw_{6-12h} + d\ln(U_{12-15h}) + fQsw_{12-18h} \tag{6.11a}$$

If $U_{8\text{-}12h} < us$, where $us=(0.0064Qsw_{6\text{-}12h})+1.2$

$$t_{\max} = a' + b'\ln(U_{8-12h}) + c'Qsw_{6-12h} + d'\ln(U_{12-15h}) + f'Qsw_{12-18h} \tag{6.11b}$$

$$\Delta T_{t\max-12h} = a + be^{(-600/Qsw_{12-18h})U_{12-15h}} + c\left(Qsw_{12-18h}/U_{12-15h}\right) \tag{6.12a}$$

(If $U_{12\text{-}15h} < 2$ m/s: $U_{12\text{-}15h} = 2$ m/s)

If $U_{8\text{-}12h} < 2.5$ m/s & $(U_{12\text{-}15h}\text{-}U_{8\text{-}12h}) > 0.7$ m/s:

$$\Delta T_{t\max-12h} = 0.1 \tag{6.12b}$$

$$\Delta T_{24h-t\min} = a + b\Delta T_{\max 1m} + cU_{16-24h} \tag{6.13}$$

Table 6.6: Coefficients for the regression models listed above. Coefficients in grey represent the different coefficients that are applied to the 1m diurnal model under certain low wind conditions.

Coeff.	*cgrad*	t_{min}	$\Delta T_{12h\text{-}tmin}$	t_{max}	t_{max} 1m	$\Delta T_{tmax\text{-}12h}$	$\Delta T_{24h\text{-}tmin}$
a	0.0034	6.4724	0.009	13.0157	15.75	-0.0541	0.1365
b	0.0486	0.1766	6.3071	2.2835	0.8754	2.057	0.209
c			0.0022	-0.002	-0.0027	0.002	-0.017
d			$1.8\text{x}10^{-4}$	-1.9736	-1.9109		
f			0.0114	0.0042	0.0035		

6.5 RESULTS

6.5.1 Comparison against regression dataset

Table 6.7 summarises the statistics of the model estimation against the observed variables used in the regression. Bias represents observed – model. The 1m results are in black while the sub-skin statistics are shown in grey. The ΔT models have the highest skill. Due to the extreme sensitivity of the diurnal cycle to wind and insolation fluctuations, the phase of the surface signal responds almost instantaneously to wind variations and therefore to be able to accurately predict the time of the maximum SST, t_{max}, a high resolution time series is required. The model described here provides a best estimate of the phase and it is the first time the phase of the diurnal signal has ever been parameterised. The model does reasonably well and captures the main variations in the timing of the peak of the signal due to changes in wind or insolation conditions. Figure 6.7 compares the observed and modelled values for $\Delta T_{(12\text{-}tmin)}$, $\Delta T_{(tmax\text{-}12)}$ and t_{max}. As the ΔT values increase, the agreement between the model and observations becomes poorer due to the extreme sensitivity of the diurnal cycle under these low wind conditions. Under low winds, the sub-skin and 1m ΔT will be sensitive to any increase in wind speed. At the surface, an increase in wind will act only to lower the SST. However, at 1m, ΔT is more unpredictable since an increase in wind can either increase or decrease the SST depending on the balance between the stratification and turbulent mixing. For this reason, the sub-skin ΔT models have better skill than the 1m models. The time of minimum SST, t_{min}, has the poorest correlation. At this time of day, the changes in SST are very small and any slight variation in SST will influence the time of the minimum SST. Consequently the observed t_{min} from which the model was derived may not be precise. An alternative method may be to assume that t_{min} occurs an hour after sunrise. This resulted in a correlation of 0.064 between the observed and predicted t_{min} (where t_{min} is one hour after dawn).

Table 6.7: Statistics of derived models against IMET buoy data. Bias = observation – model. Black: 1m model, grey: sub-skin model.

Models	Correlation	Bias ± std. dev.
cgrad	0.34	0 ± 0.014 °C/hr
t_{min}	0.05	0.02 ± 1 hr
$\Delta T_{(12h - tmin)}$	0.83 0.86	0.002 ± 0.14 °C 0.01 ± 0.41 °C
t_{max}	0.53 0.64	0.1 ± 1hr 0 ± 1hr
$\Delta T_{(tmax - 12h)}$	0.88 0.88	0.02 ± 0.15 °C 0.001 ± 0.16 °C
$\Delta T_{(24h - tmin)}$	0.61	0 ± 0.13 °C

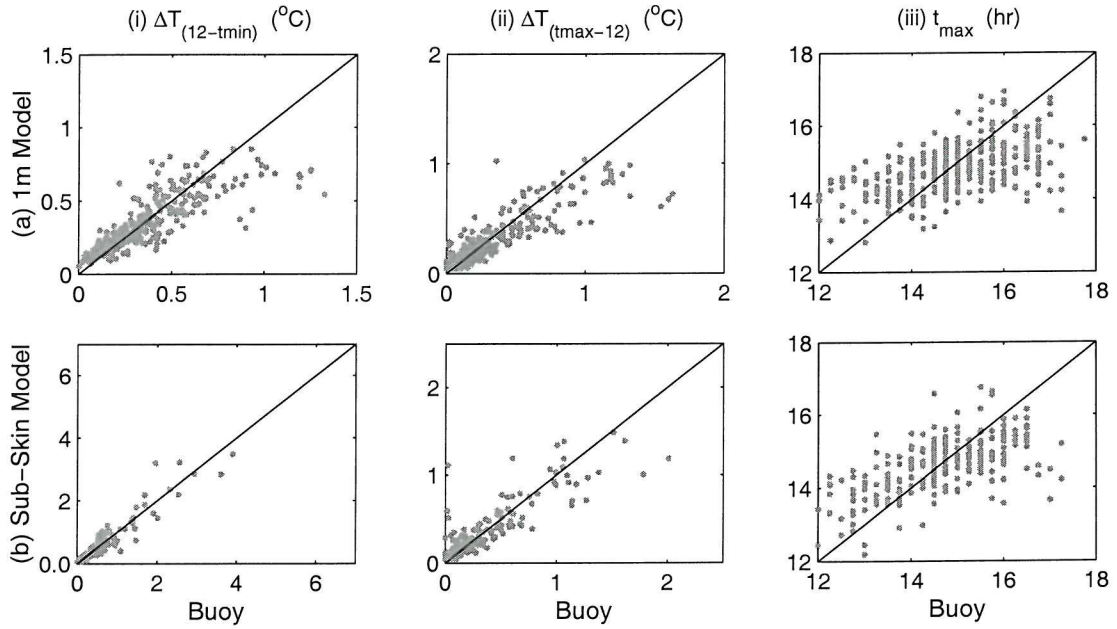

Figure 6.7: Diurnal warming variables derived from regression dataset against the modelled parameter values for (a) 1m, (b) sub-skin. (i) $\Delta T_{(12\text{-}tmin)}$, (ii) $\Delta T_{(tmax\text{-}12)}$, (iii) t_{max}.

Examples of the parameterisation output are shown in Figure 6.8. The modelled diurnal variations are plotted against the regression buoy data. The first example shows moderate wind conditions when the diurnal variation is the same at 1m and the sub-skin, corresponding to the Type 1a diurnal shape (Section 5.4.2.1). The second example shows low winds throughout the daytime where the top metre is stratified until dusk, corresponding to a Type 1b diurnal shape. The third example shows a case with low winds in the morning followed by an increase in wind and a sudden break down in stratification in the afternoon (Type 3b). The parameterisation captures these different

shapes well. The bias and standard deviation is –0.02 ± 0.02°C for the first example, -0.02 ± 0.08°C (sub-skin) and 0.08 ± 0.1°C (1m) for the second example and –0.12 ± 0.36°C (sub-skin) and –0.05 ± 0.27°C for the final case. Many more examples are shown in the next section where the parameterisation is validated against independent data sets.

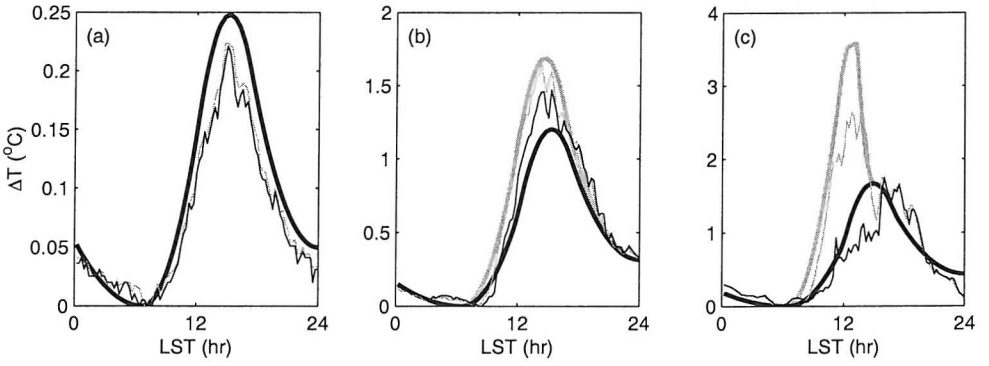

Figure 6.8: Example of the parameterisation (ΔT = diurnal variation from daily minimum SST). Bold lines represent the parameterisation and thin lines represent observations. Grey lines represent sub-skin and black lines represent 1m.

6.5.2 Parameterisation Intercomparison

In addition to validating the parameterisation against independent data, it will also be compared against the existing parameterisations. The up-dated KK03 parameterisation requires a daily mean latent heat flux value which is not available in the validation dataset and therefore before the independent validation, an intercomparison is carried out between the two 1m Kawai & Kawamura models (KK02 & KK03), the 1m Gentemann (G04) and the new (SM) 1m parameterisation using the regression buoy dataset. These data are independent for all parameterisations except for SM.

Figure 6.9 shows the 1m model intercomparison for 20 consecutive days from the Arabian Sea dataset. The observed diurnal cycles are often quite variable demonstrating the difficulty of precisely parameterising the evolution of the diurnal heating. Since the Kawai & Kawamura parameterisations only predict the maximum diurnal amplitude, they are plotted as a straight line over the day. The G04 and new parameterisation match the buoy data well though the G04 parameterisation fails to predict the large ΔT amplitudes at low winds. The new parameterisation captures the variability in the phase of the signal, for example re-producing the early heating, as can been seen for the last

few days in the figure. The KK03 ΔT_{max} agrees reasonably well with the buoy ΔT_{max}. However in very low wind cases, the predicted amplitude is close to zero and in some cases negative and therefore not visible in the plot (e.g. 6th day, counting across). The KK02 ΔT_{max} are consistently higher than KK03 and show better agreement at low winds that at moderate to high winds. In moderate winds the KK02 model overestimates ΔT_{max}.

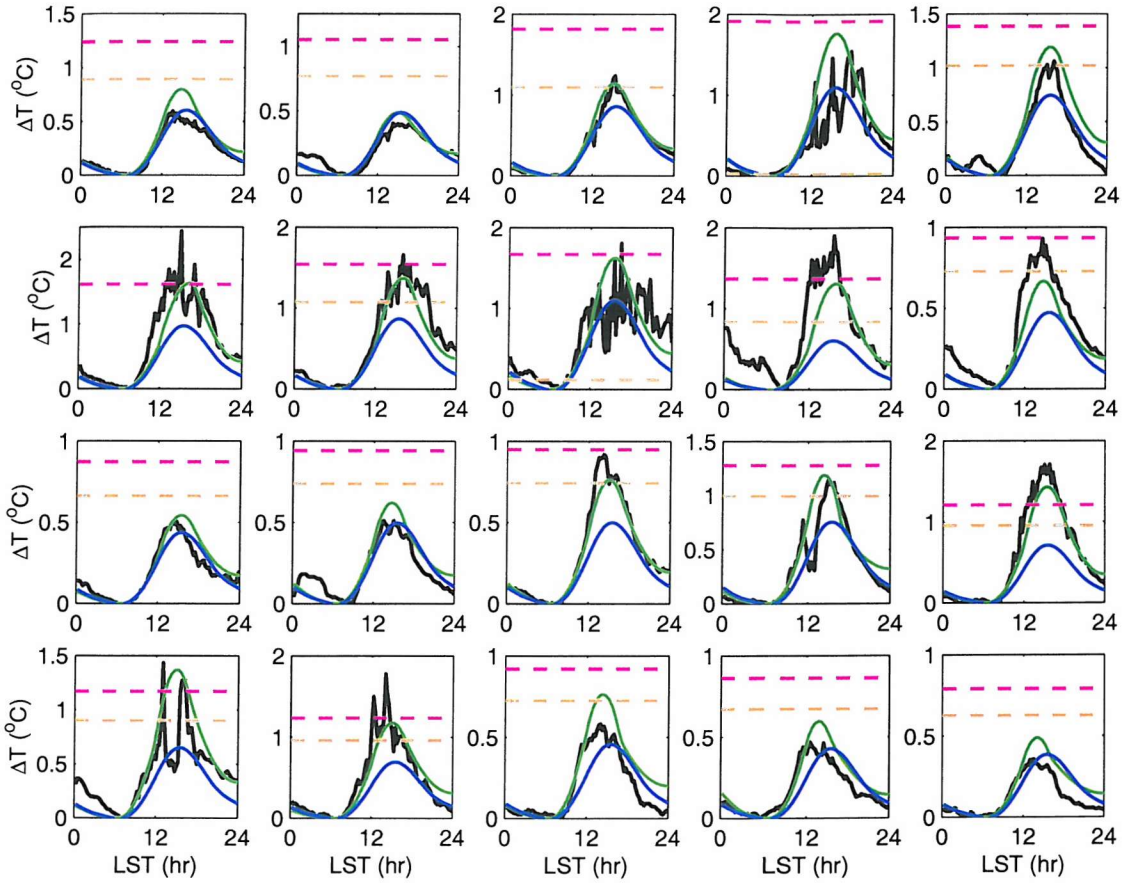

Figure 6.9: Example of the ΔT parameterisation intercomparison results using the Arabian Sea IMET data. Black line: observed 1m ΔT, green line: SM (new) ΔT, blue line: G04 ΔT, pink dotted line: KK02 ΔT_{max} and orange dotted line: KK03 ΔT_{max}.

The reason for the low KK03 ΔT_{max} during low winds was investigated by plotting ΔT_{max} as a function of daily mean wind speed (Figure 6.10a). This was also carried out for the KK02 and G04 parameterisations to identify any differences. The KK02 & KK03 parameterisations use a different set of coefficients for daily mean wind speeds below and above 2.5 m/s and it appears that there is a problem with the KK03 low wind coefficients. The parameterisation shows a sudden drop with negative ΔT_{max} which then rapidly rises. The same curve was plotted for a range of Q_l and Q_{sw} and the same

problem was observed. The authors were asked to comment on Figure 6.10a and they replied just before this thesis was submitted, reporting that there was an error in the published coefficients which had not been picked up. Reproducing Figure 6.10a with the corrected coefficients (Figure 6.10b), confirms that the problem is resolved. (The corrected coefficients were listed in Table 6.3.)

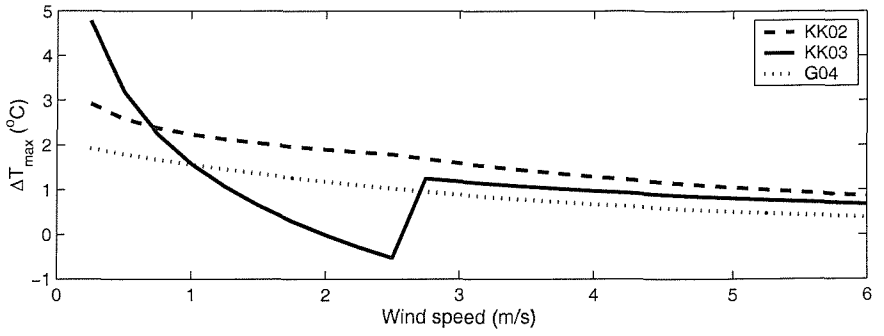

Figure 6.10a: KK02, KK03 and G04 1m ΔT_{max} as a function of increasing daily mean wind speed. The parameterisations were run with same values for Q_{sw_max}, Q_{sw} and Q_{lat}. Q_{sw_max} = 1100Wm^{-2}, Q_{sw} = 350Wm^{-2} and Q_{lat} = -100Wm^{-2}.

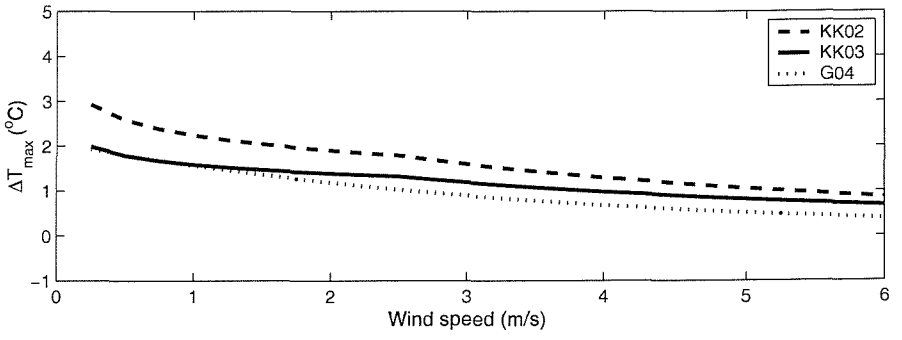

Figure 6.10b: Same as Figure 6.10a using the corrected low wind coefficients for KK03.

ΔT_{max} values for all of the parameterisations are compared against the observed ΔT_{max} (Figure 6.11, Table 6.8). In the case of KK03, the corrected values are used. The results show that KK02 ΔT_{max} are biased high by 0.3°C and improvement is noted with the updated KK03. The G04, KK03 and SM parameterisations do well but as already observed, at lower winds, the G04 parameterisation underestimates the ΔT_{max}, which results in a cool bias of 0.22°C. The KK03 parameterisation also underestimates the large ΔT_{max} values under low wind conditions. The new SM parameterisation agrees best with no bias and a small scatter (0 ± 0.18°C). However, this is not an independent validation for the new parameterisation. Independent validation and intercomparison

results are shown in the next section using the SM, G04 and KK02 parameterisations. Initially the KK03 parameterisation was not included in the next stage since it was believed to have an error. Despite resolving the problem with KK03, the parameterisation is not used since it requires the extra Q_l term which is not available in the validation dataset collected. Furthermore the corrected KK03 parameterisation has only been derived for 1m and not the skin, and both models are inter-compared and validated in the next section.

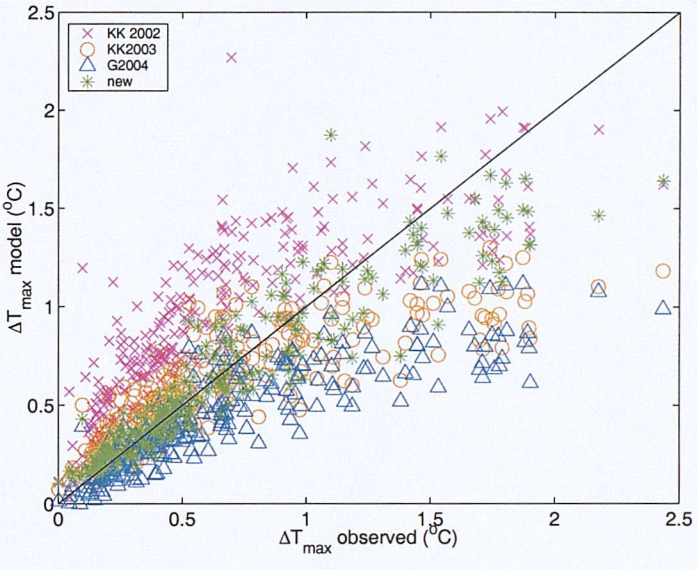

Figure 6.11: Comparison of model ΔT_{max} for Toga Coare and Arabian Sea IMET datasets. Negative KK03 ΔT_{max} values have been set to zero. Green *: SM (new), blue Δ: G04, pink x: KK02 and orange o: KK03 (corrected).

Table 6.8: Statistics from ΔT_{max} intercomparison using Arabian Sea and Toga Coare IMET data. Bias = observations – model.

	SM	G04	KK02	KK03 (cor.)
r^2	0.93	0.86	0.82	0.83
bias ± std. dev (°C)	0.00 ± 0.18	0.22 ± 0.3	-0.3 ± 0.28	0.06± 0.30
Root mean square error (°C)	0.18	0.37	0.41	0.31

6.5.3 Validating the parameterisation

To validate the parameterisation and assess its accuracy, the parameterisation is tested on new datasets that are independent of the data used in the regression. The sub-skin model is tested less thoroughly than the 1m model since very few in situ surface measurements exist in low wind conditions.

6.5.3.1 1m parameterisation validation

The 1m parameterisation is applied to wind and insolation data from PIRATA, TAO/TRITON and IMET buoys which cover a range of latitudes and climatic regions (Table 6.1). As well as comparing the observed diurnal cycle against the new parameterisation, the other parameterisations discussed in the section above are also included to continue the intercomparison effort.

Figure 6.12 presents examples of the fully independent validation and parameterisation intercomparison results using the datasets described in Section 6.2. The statistics of the intercomparison are listed in Table 6.9 and are discussed after the following summary. Many different examples are shown for several of the validation datasets. Each figure shows a period of 9 or 20 consecutive days so as not to present the best examples. As the figures show, the new parameterisation appears to work well on the independent data. Given the complexity of the diurnal cycle and its non-linear behaviour, it is a great challenge to parameterise the signal with more accuracy. Out of the two diurnal shape parameterisations (G04 & SM), the new parameterisation captures some of the variability of the shape and phase of the diurnal signal that G04 is unable to achieve using a fixed phase. The agreement is weakest for the IMET buoy at 60°N (Figure 6.12a) where the diurnal signal is contaminated by non-local effects.

The KK02 model frequently overestimates the magnitude of ΔT_{max}. Some of the explanation of this probably lies in the way the model was derived using the peak insolation and not a mean value. Using the peak value can miss out important information about the cloud. Cloud is often variable and a clear patch can occur around mid-day when other parts of the day are cloudier. Given that the SM and G04 models work well for these contrasting mid-latitude and tropical conditions without including a latent heat flux variable suggests that Q_l term used in KK03 is not a crucial variable. The improvement of the KK03 model (Table 6.8) is perhaps more influenced by the inclusion of the daily mean Q_{sw} which gives a better representation of the day's heating. Since Q_l is not easy to determine globally and operationally, it is encouraging that the G04 and SM models, which rely only on wind and insolation, work well for both mid-latitudes and tropical regions.

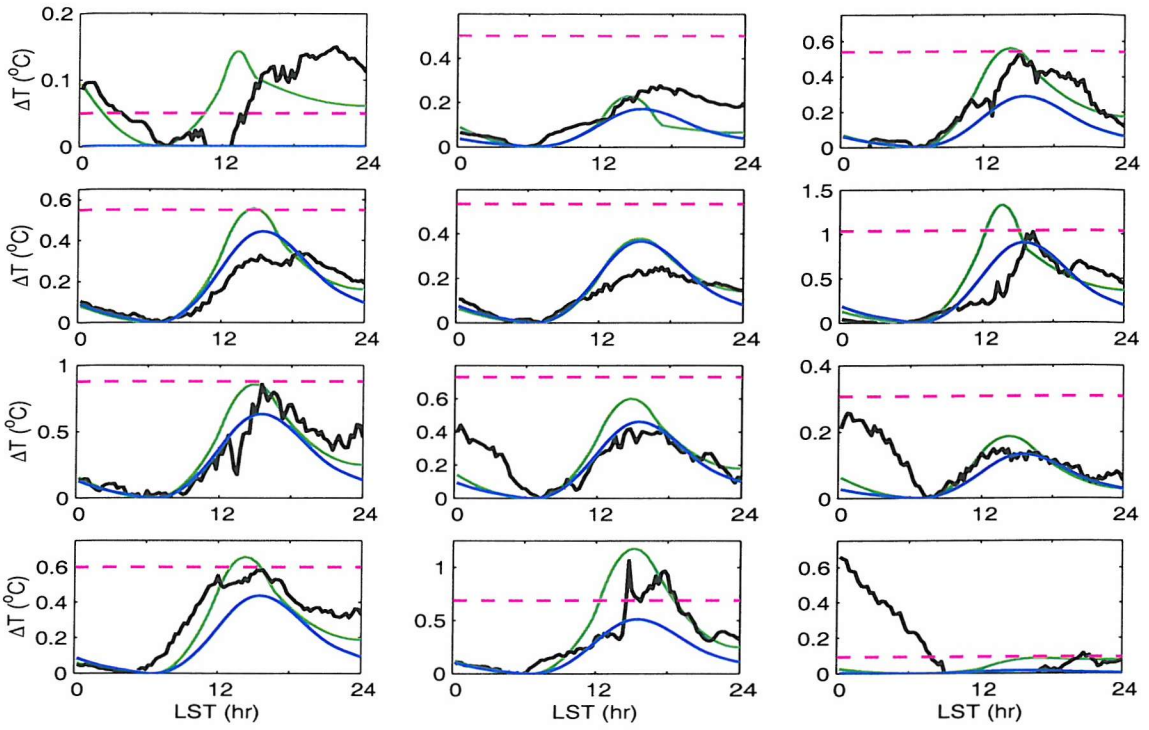

Figure 6.12a: Validation of 1m diurnal variation parameterisation from MLML91 data (33W, 60N). Nine consecutive days are shown where non-local affects did not dominate the diurnal cycle. Black line: observed 1m SST, green line: new Stuart-Menteth (SM) parameterisation, blue line: Gentemann G04 1m parameterisation and pink dotted line: KK02 1m ΔT_{max}.

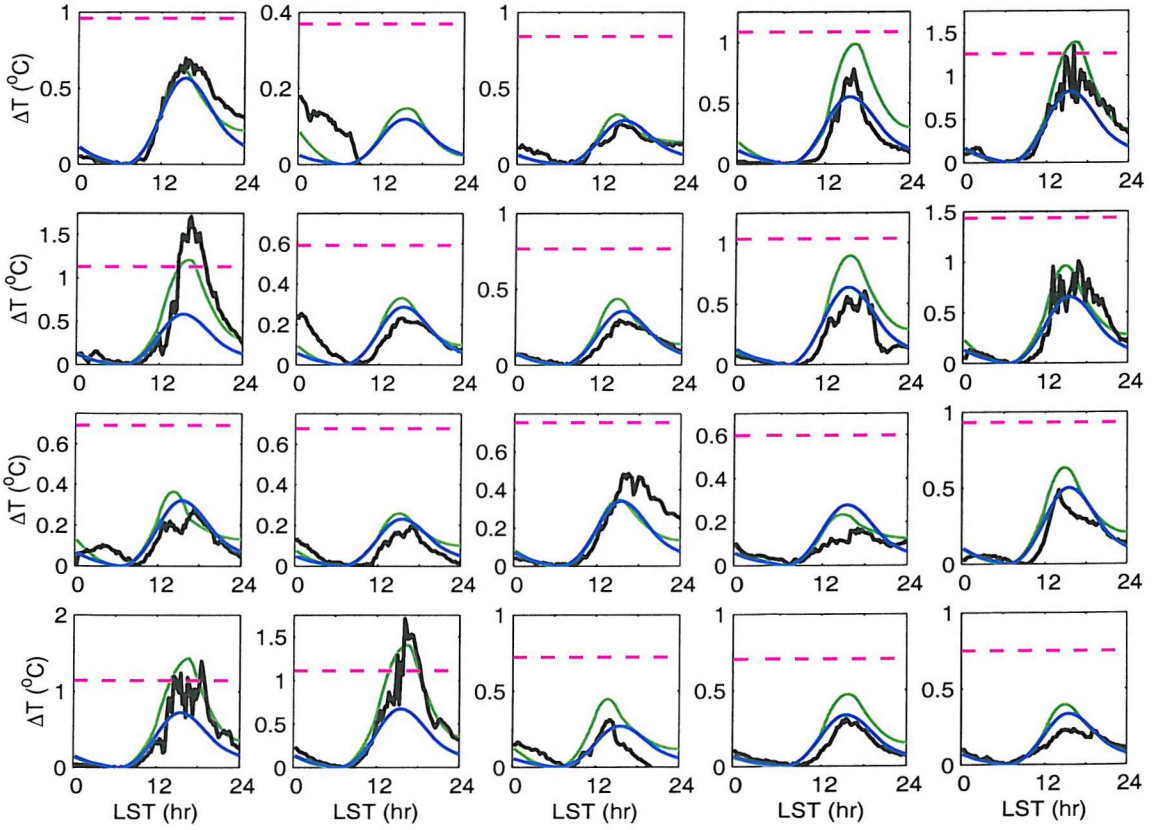

Figure 6.12b: Same as Figure 6.12a, except validation data for 20 days from Subduction IMET buoy (22W, 33N). Twenty consecutive days are shown here.

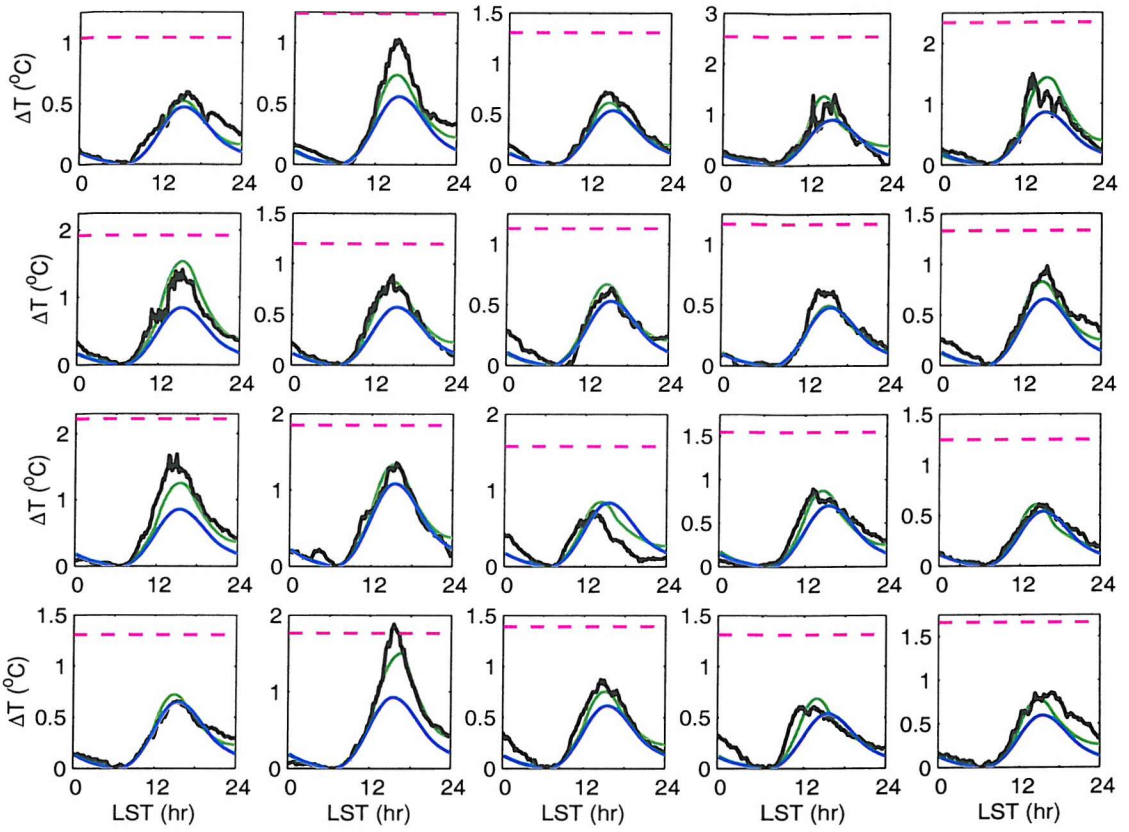

Figure 6.12c: Same as Figure 6.12a, except validation data for 20 days from TAO/TRITON buoy at 140W, 0N. Twenty consecutive days are shown here.

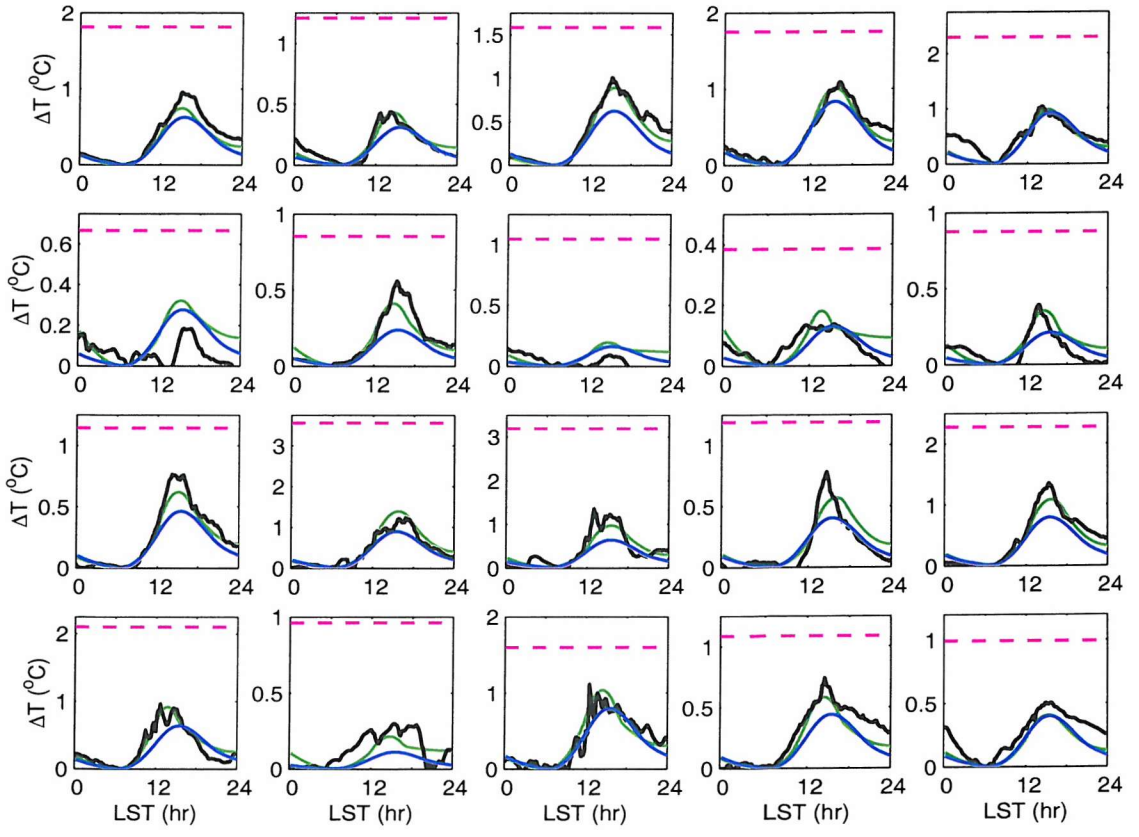

Figure 6.12d: Same as Figure 6.12a, except validation data for 20 days from TAO/TRITON buoy at 95W, 5S. Twenty consecutive days are shown here.

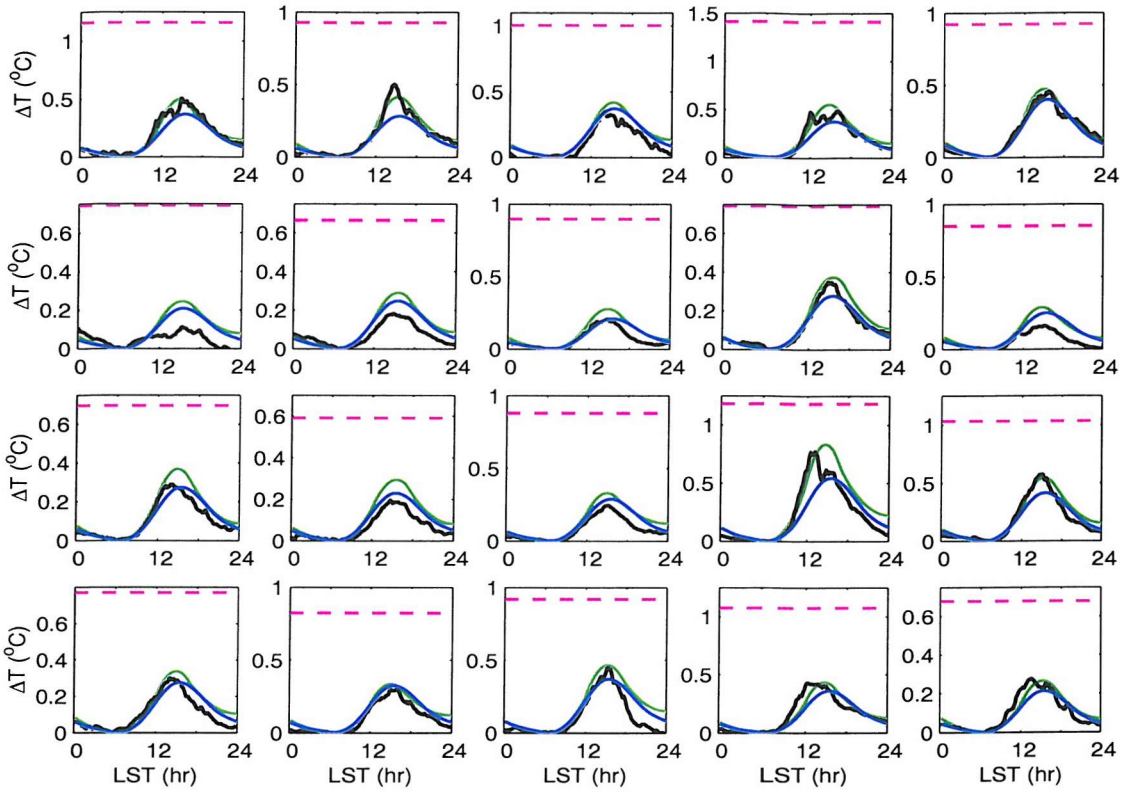

Figure 6.12e: Same as Figure 6.12a, except validation data for 20 days from PIRATA buoy at 10W, 10S. Twenty consecutive days are shown here.

To evaluate the results more objectively, some statistical tests were carried out on each buoy dataset to determine the correlation (r^2), bias, standard deviation and root mean square error (rmse). The results are presented in Table 6.9. The overall result for each parameterisation is listed at the end of the table under Total, where the bias and standard deviation of the individual bias and standard deviations for each buoy have been computed. The results are very good for the new parameterisation (-0.01 ± 0.11 °C). It has a bias not significantly different from zero and a very small scatter. KK02 has the largest bias (-0.5°C) and scatter (± 0.26°C), with the model biased high as noted in previous section (Table 6.8). The large bias and scatter of KK02 is persistently high as shown by the low scatter in the total bias (± 0.06°C) and standard deviation (± 0.05°C). The G04 parameterisation shows good agreement and is slightly biased low, which is likely to reflect its inability to predict the larger diurnal warming events. The intercomparison results are nicely demonstrated in Figure 6.13, which shows the observed ΔT_{max} against the modelled value for the three different parameterisations, for three of the buoy datasets. These datasets are selected to represent contrasting climatic conditions. The new parameterisation shows the best skill, estimating the magnitude of

the diurnal cycle for low wind conditions as well as moderate wind conditions, reflected by its good agreement for both $\Delta T_{max} < 1°C$ and $\Delta T_{max} \geq 1°C$.

Table 6.9: Statistics of parameterisation validation and inter-comparison against independent buoy data sets. Bias = observed – model. Units for bias, standard deviation and rmse are °C.

Buoy	**Bias ± Std. Dev.** Stuart-Menteth	**Bias ± Std. Dev.** Kawai & Kawamura	**Bias ± Std. Dev.** Gentemann	**No. of days**
TAO/TRITON 140W, 0N	0.08 ± 0.16 r^2 = 0.85 rmse = 0.17	-0.40 ± 0.21 r^2 = 0.78 rmse = 0.25	0.16 ± 0.19 r^2 = 0.81 rmse = 0.24	616
TAO/TRITON 95W, 0N	0.20 ± 0.30 r^2 = 0.80 rmse = 0.36	-0.40 ± 0.38 r^2 = 0.68 rmse = 0.62	0.34 ± 0.35 r^2 = 0.78 rmse = 0.17	178
TAO/TRITON 95W, 5S	0.02 ± 0.10 r^2 = 0.95 rmse = 0.1	-0.47 ± 0.26 r^2 = 0.82 rmse = 0.54	0.10 ± 0.15 r^2 = 0.91 rmse = 0.17	262
TAO/TRITON 165E, 2N	-0.04 ± 0.12 r^2 = 0.92 rmse = 0.13	-0.56 ± 0.28 r^2 = 0.68 rmse = 0.62	0.08 ± 0.17 r^2 = 0.82 rmse = 0.20	530
TAO/TRITON 165E, 5N	-0.07 ± 0.11 r^2 = 0.94 rmse = 0.14	-0.58 ± 0.31 r^2 = 0.76 rmse = 0.66	0.05 ± 0.18 r^2 = 0.85 rmse = 0.17	400
TAO/TRITON 165E, 8S	-0.06 ± 0.12 r^2 = 0.93 rmse = 0.14	-0.58 ± 0.32 r^2 = 0.78 rmse = 0.66	0.07 ± 0.16 r^2 = 0.89 rmse = 0.17	265
PIRATA 10W, 0N	0.06 ± 0.12 r^2 = 0.88 rmse = 0.13	-0.46 ± 0.22 r^2 = 0.70 rmse = 0.51	0.14 ± 0.15 r^2 = 0.82 rmse = 0.20	149
PIRATA 10W, 10S	-0.05 ± 0.05 r^2 = 0.92 rmse = 0.07	-0.51 ± 0.18 r^2 = 0.72 rmse = 0.54	0.01 ± 0.06 r^2 = 0.87 rmse = 0.06	312
PIRATA 35W, 0N	-0.04 ± 0.08 r^2 = 0.94 rmse = 0.09	-0.52 ± 0.27 r^2 = 0.69 rmse = 0.58	0.05 ± 0.12 r^2 = 0.86 rmse = 0.14	143
Total Bias	-0.01 ± 0.06	-0.50 ± 0.06	0.08 ± 0.05	
Total Std. dev (excluding 95W, 0N)	0.11 ± 0.03	0.26 ± 0.05	0.15 ± 0.04	

The advantages and limitations of the statistical analysis of these results were carefully considered before these tests were carried out. The data used in the derivation of the model was methodically screened to remove any non-local effects which involved a thorough visual comparison which is not possible with the very large quantity of data included in the validation dataset. For each buoy, ΔT_{max} was computed and plotted as a function of wind speed. If a strong relationship existed between the two (as shown in Figure 6.4a and 6.6 c & e), this was taken as confirmation that non-local processes were small in comparison to the number of diurnal warming signals. The two IMET buoys at mid-latitudes contained frequent advective and other non-local processes and therefore

they were omitted from the statistical analysis. The TAO/TRITON and PIRATA buoys all show a good wind speed/ΔT_{max} relationship, except for the buoy at 95W, 0N which often revealed rapid changes in SST associated with passing fronts. This is evident in the statistics (Table 6.9) as the standard deviation, bias and root mean square error are much higher for this buoy than any of the others. When computing the overall result for each parameterisation, listed at the end of Table 6.9, this buoy was excluded.

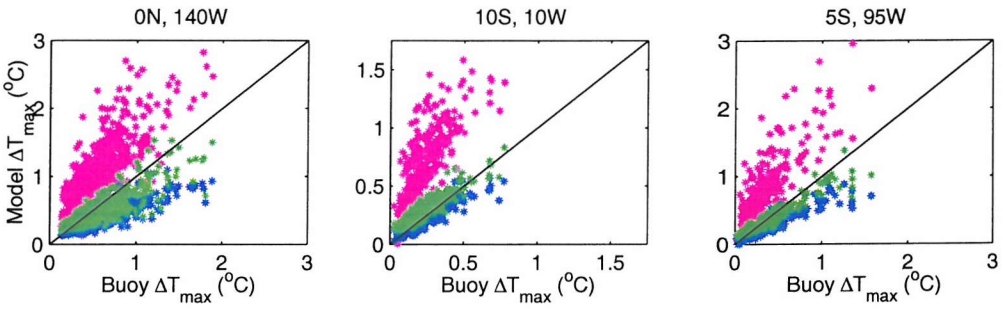

Figure 6.13: Scatter plots of observed 1m ΔT_{max} against modelled ΔT_{max} for new (SM) parameterisation (green), KK02 (pink) and G04 (blue) for a range of different oceanic regions. The first buoy (0N, 140W) is located east of the cold tongue along the central Pacific equator. The second buoy (10S, 10W) is located in the tropical East Atlantic and the third buoy (5S, 95W) is in the equatorial Pacific cold tongue.

6.5.3.2 Sub-skin parameterisation validation

Figure 6.14 presents the sub-skin validation results for the R/V Franklin and RRS Charles Darwin skin measurements and the Mutsu Bay 0.02m data. The existing parameterisations are also included as an intercomparison for the skin/sub-skin models. In this case, the G04 TMI sub-skin model, the KK02 and W96 skin models and the new (SM) sub-skin parameterisation are used. The statistics of the intercomparison are listed in Table 6.10 and are discussed after the following summary.

All datasets have days with large diurnal amplitudes, some with rapid changes in temperature correlated with the variability in the forcing fields. The new model shows mixed skill in accurately capturing these changes and reflects the difficulty in parameterising such a sensitive process. The full history of the time variability is required to precisely predict the fluctuations in the diurnal temperature cycle at the sea surface. The different models show varying degrees of skill. W96 ΔT_{max} is always smaller than KK02 and underestimates ΔT_{max} at low winds. G04 model also underestimates the size of the diurnal amplitude at low winds. While the G04 TMI model has been designed specifically for the TMI dataset, it should detect the same

large diurnal warming amplitudes that are revealed by the in situ data. The new model correctly identifies strong diurnal heating conditions but can over/under-estimate the absolute amplitude since it lacks the full time history of the wind and insolation variability. The results show the benefit of allowing the phase of the diurnal signal to vary (SM) rather than remaining fixed (G04). In low winds, the new parameterisation captures the rapid heating in the morning and is often successful at capturing the sudden break down in stratification. In these conditions, the surface layer responds rapidly to wind variations, and consequently the parameterisation can under or over-estimate the magnitude of the diurnal warming and miss the exact timing of the break down of the stratification. However, it is an encouraging achievement that this simple parameterisation can capture some of this variability and it is the only parameterisation that is sensitive to such variations.

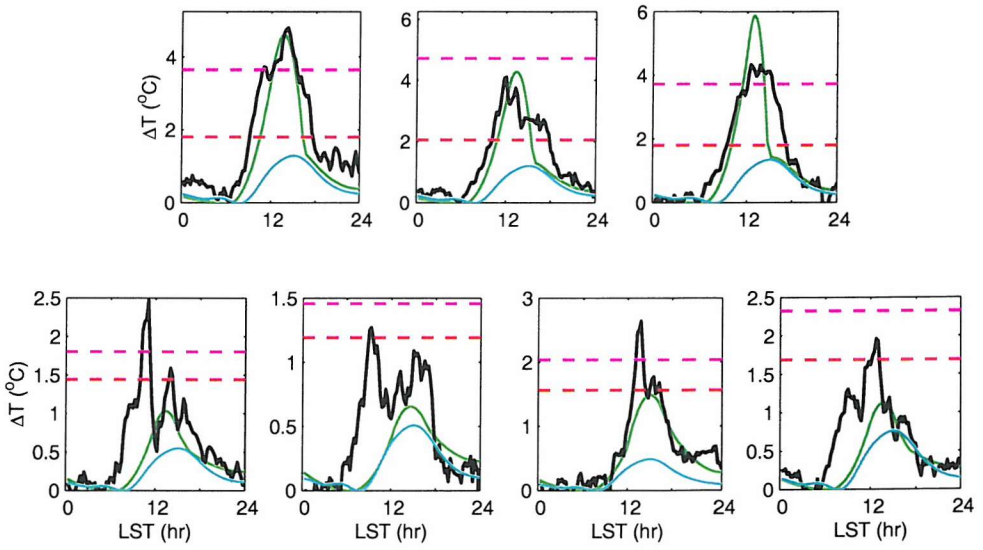

Figure 6.14a: Validation of sub-skin diurnal variation parameterisation using the RV Franklin data. Black line: observed skin SST, green line: new Stuart-Menteth (SM) parameterisation, blue line: Gentemann G04 TMI parameterisation, pink dotted line: KK02 skin ΔT_{max} and the red dotted line: W96 ΔT_{max}.

In the RRS Charles Darwin data validation (Figure 6.14b), there is an unusual example where the new model greatly underestimates the diurnal SST amplitude (4th example, counting across). Referring to the time series of the forcing fields (Figure 6.15), three large wind bursts are evident. These large wind bursts should have eroded any diurnal stratification but since the diurnal signal still exists in the data, it suggests there may have been a problem with the anemometer.

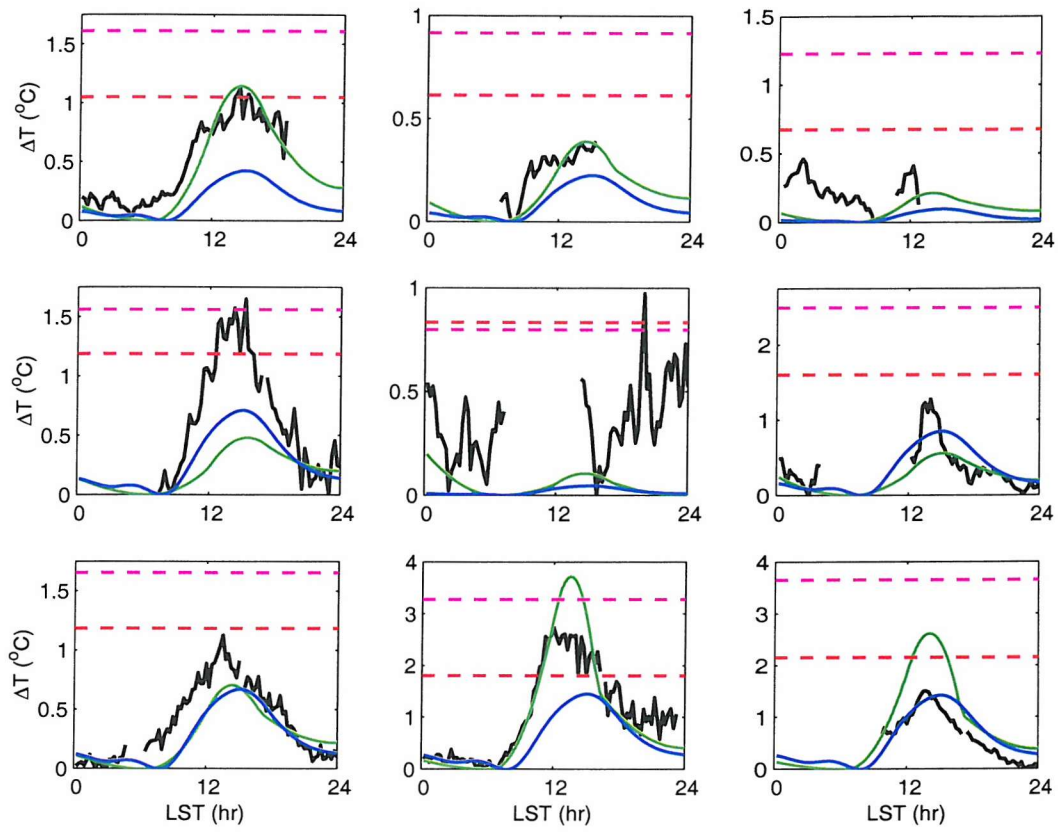

Figure 6.14b: Same as Figure 6.14a except using the RRS Charles Darwin skin data.

Figure 6.16 compares the ΔT_{max} amplitudes for all the sub-skin validation points. The agreement is not as good as for the 1m validation which most likely reflects the sensitivity of the surface to changes in the local forcing and the low number of validation points used. All parameterisations have quite large scatter (Table 6.10) which can be explained in part by the large observed amplitudes. The new model shows almost no bias (-0.02 °C) and has the highest correlation, although KK02 shows a slightly better overall root mean square error. The KK02 skin parameterisation also agrees well with the observations and works better than its 1m counterpart. The G04 TMI model is biased low by over 1°C, reflecting its inability to predict the large ΔT_{max} at low winds.

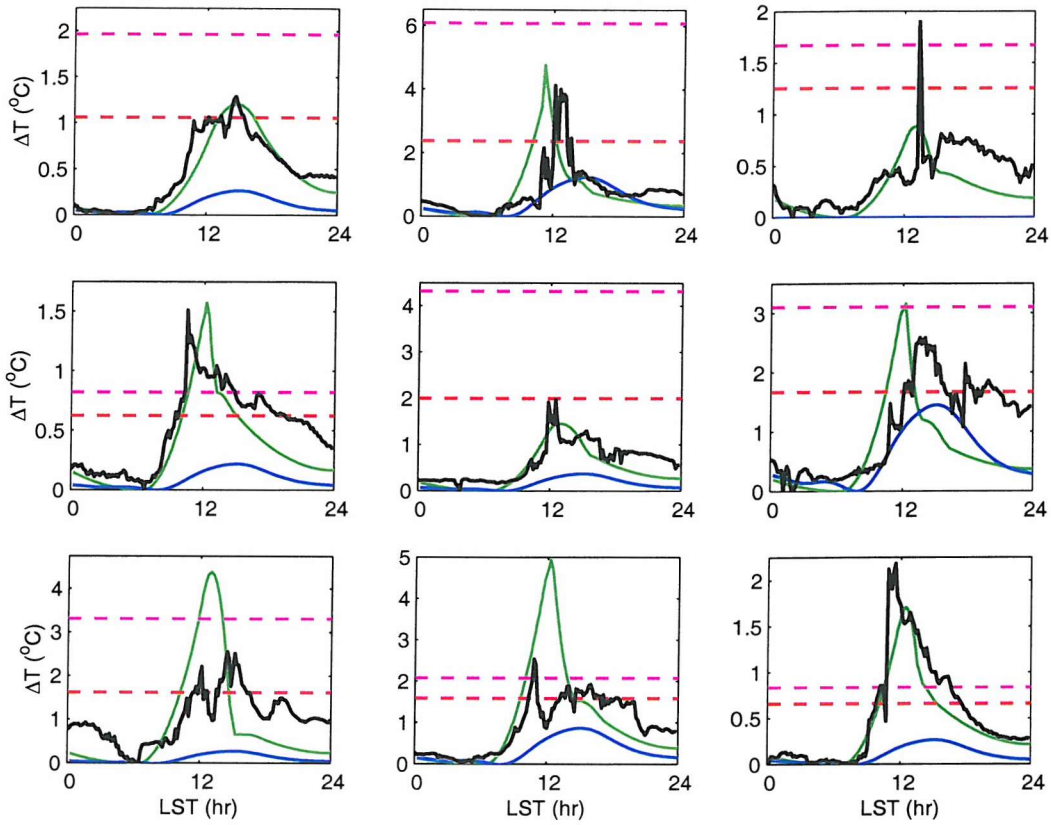

Figure 6.14c: Same as Figure 6.14a except using the Mutsu Bay 0.02m data.

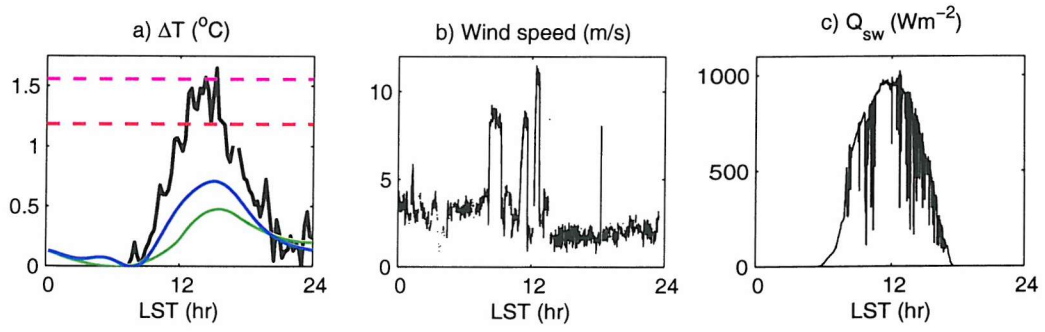

Figure 6.15: a) Model validation for 4th day of RRS Charles Darwin (Figure 6.14b) and the associated time series of b) wind speed and c) downward shortwave radiation (Wm^{-2}).

Table 6.10: Statistics from sub-skin ΔT_{max} intercomparison. Units for bias, standard deviation and rmse are °C.

Bias ± Std. Dev. Stuart-Menteth	**Bias ± Std. Dev.** Gentemann	**Bias ± Std. Dev.** Kawai & Kawamura	**Bias ± Std. Dev.** Webster et al.	**No. of days**
-0.02 ± 0.99 r^2 = 0.86 rmse = 0.99	1.51 ± 0.93 r^2 = 0.75 rmse = 1.77	-0.23 ± 0.91 r^2 = 0.77 rmse = 0.94	0.78 ± 0.90 r^2 = 0.78 rmse = 1.19	25

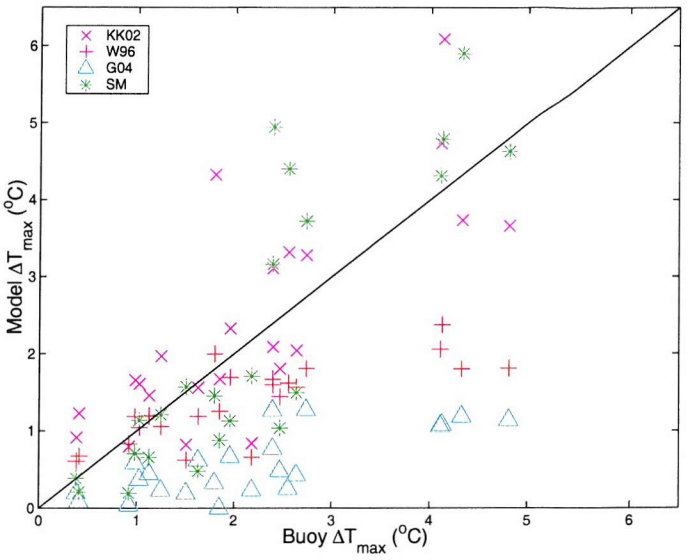

Figure 6.16: Scatter plots of observed sub-skin ΔT_{max} against modelled ΔT_{max} for new (SM) parameterisation (green *), KK02 (pink x), W96 (red +) and G04 (blue Δ) for a range of different oceanic regions.

6.6 POTENTIAL APPLICATIONS OF PARAMETERISATION

There are two main potential applications for this parameterisation. The first is to allow the diurnal cycle to be derived either at 1m or the surface using ancillary wind and insolation information. This may be important for NWP models which just use a daily or weekly bulk SST measurement. When large diurnal warming occurs it is likely to impact the local air-sea interaction. Webster et al. (1996) discuss the importance of the diurnal cycle for tropical air-sea processes. As their work and also the results presented in Chapter 3 & 5 have shown, the tropics are highly susceptible to large diurnal warming amplitudes. In the western Pacific tropical warm pool, El Nino brings about a change in SST of around 1°C. During diurnal warming events, the changes in skin and 1m SST can be much larger. Since the temperature is already so high in this region, any further increases have an important impact on air-sea interactions. More recently further studies have analysed the diurnal cycle in the tropics to better understand its role in tropical air-sea variability (e.g. Yang & Slingo, 2001; Dai & Trenberth, 2004). Dai & Trenberth (2004) evaluated the performance of the coupled Climate Community System Model (CCSM2) in simulating the diurnal cycle and reported deficiencies in diurnal cycles over ocean areas (e.g. in air, precipitation, cloud) which they attributed to the absence of diurnal variations of SST. One of the biggest errors was the weak simulation of the diurnal cycle in convective precipitation, linked to the weak diurnal

cycle in surface air temperature, which in turn was related to the lack of diurnal variability in SST. They report that the absence of a diurnal cycle in SST is a significant deficiency in the model. Running a full 1-D mixed layer model can be computationally expensive and therefore, the application of a simple parameterisation would address this issue and would permit the diurnal SST cycle to be included in a simpler and quicker way. Dai & Trenberth (2004) concluded that the implementation of an empirical parameterisation of the diurnal cycle of the ocean skin temperature could provide an effective way to include the air-sea interaction. The diurnal warming parameterisation could also be applied and used as the lower boundary condition for regional or global atmospheric models. Most AGCMs use a 'bulk' SST and as the results from Chapter 5 have shown, the difference between the surface and 1m can be large. Furthermore many AGCMs use monthly mean SSTs as their lower boundary condition and do not include any diurnal variability. The application of the sub-skin diurnal warming parameterisation could improve studies focused on air-sea interaction.

The second application is to use the parameterisation to remove the diurnal signal from a measurement and obtain the true mixed layer temperature. Through to the GODAE High Resolution Sea Surface Temperature - Pilot Project (GHRSST-PP), much research has been carried out recently to assess the user requirements of SST. For climate studies, it is desirable to have the true mixed layer temperature with no high frequency variability. In response to the user feedbacks, the GHRSST-PP will produce, as one of its products, a daily mixed layer temperature free from cool skin or warm layer effects (Donlon, 2004a). Therefore the diurnal signal must be removed from the satellite measurements used in the dataset. The large sub-skin ΔT_{max} amplitudes observed through this thesis confirm that satellites will measure a much stronger diurnal amplitude than in situ measurements during low winds and supports the need for the diurnal signal to be identified in satellite data.

In recognition of this, the parameterisation presented here has been incorporated into the European GHRSST-PP (Medspiration) data processing scheme (Version 1) as an initial method to remove the diurnal signal from satellite data (Donlon, 2004b). The Medspiration project has been funded by the European Space Agency to provide the European contribution to GHRSST-PP, producing merged and analysed skin and foundation temperature (Section 2.4) products for the Mediterranean Sea and North

Atlantic Ocean. Caution should be applied when considering to remove the diurnal variation predicted by the parameterisation from the satellite data, during periods of very low wind since the shape of the diurnal cycle can change dramatically in immediate response to changes in wind speed. In these situations the model is unlikely to predict the exact timing of the mixing and consequent sudden drop in the surface temperature. Therefore, in some cases the parameterisation could add more errors than it removes. However, this would be a common problem with all parameterisations. Alternatively the parameterisation could be used to simply flag measurements likely to have a large diurnal influence and estimate the error rather than attempt to remove the signal. The same process could also be extended to buoy data using the 1m parameterisation.

Tests were carried out to assess the impact of applying the model corrections on the overall bias and standard deviation of the data. The bias and standard deviation of SST at a particular time of day, referenced to the daily minimum SST (assumed to represent the true mixed layer temperature), were estimated at three times of day (10:30, 13:30 & 14:30), corresponding to some of the most common satellite overpass times. Using wind and insolation data from the IMET buoys, the parameterisation was run on the regression data set. The diurnal variations predicted by the parameterisation at each of the three times of day were then used to 'remove' the diurnal signal from the SST measurement to produce a corrected SST, SST_c. In addition to this, the diurnal variation was re-estimated from the parameterisation, this time using only an instantaneous wind measurement at the time of the satellite overpass rather than a mean morning or afternoon value, with the aim to assess the impact of using a single measurement compared with using an averaged measurement. The estimated diurnal variation was again removed from the original SST measurement to determine the corrected SST, SST_{cu}.

The results (Table 6.11) show that both the bias and the standard deviation are significantly reduced when the parameterisation is applied. In all three cases, the standard deviation is reduced by at least a third and the bias is reduced by an order of magnitude. This provides confidence that the parameterisation could be used to remove the diurnal signal without incurring worrying additional errors. The difference of using a point measurement of wind speed at the time of the SST measurement over a mean

value appears to have little effect on the bias of the dataset but the scatter is much larger and provides no improvement to the uncorrected data, except in the 10h30 case. Clearly the time of the wind measurement is important, as discussed in Chapter 5, and a single instantaneous wind measurement may not accurately summarise the morning or afternoon wind activity.

Table 6.11: Bias and standard deviation of satellite-measured SST and the foundation temperature with & without the sub-skin model diurnal variations (DV) corrections. SST(t): satellite SST at overpass time (t), SST_{min}: daily SST minimum, SST_c: corrected SST (SST-DV), SST_{cu}: corrected SST with point wind measurement at time (t) used for $U_{8\text{-}12h}$ & $U_{12\text{-}15h}$ instead of a mean value. (Number of data points used, n=270.)

	t = 10h30 (~AMSR/AATSR)	t = 13h30 (~AMSR/AATSR)	t = 14h30 (~AVHRR)
SST(t) - SST_{min}	0.33 ± 0.54	0.68 ± 0.77	0.68 ± 0.62
$SST_c(t)$ - SST_{min}	0.03 ± 0.33	-0.07 ± 0.49	-0.07 ± 0.29
$SST_{cu}(t)$ - SST_{min}	-0.002 ± 0.35	-0.08 ± 0.67	-0.16 ± 0.72

6.7 LIMITATIONS OF PARAMETERISATION

1. While the development of this new parameterisation is based on the requirement of wind and insolation variability information, it may be hard in practice for several wind and insolation measurements to be obtained. The parameterisation has been developed with the GHRSST-PP needs in mind, where it is expected that several wind and insolation measurements will be available from satellites or, alternatively, from NWP models. In situations where this is not possible, the same value would have to be used for all model wind variables and a daily mean insolation value could be doubled to give each model insolation variable. The consequences of this will particularly affect the skill of the model in low winds where it is sensitive to wind variability.

2. Following on from the point above, while a single measurement could be substituted for a mean wind speed value (though at the risk of reducing the model's accuracy), the same is not true for insolation. Insolation must be made up of a six hourly mean value. Given the shape of the solar cycle, regular insolation measurements are required to provide an accurate value since this is what the parameterisation is based upon. For example, assuming, Q_{7am}=100Wm^{-2}, Q_{8am}=300Wm^{-2}, Q_{9am}=600Wm^{-2}, Q_{10am}=750Wm^{-2}, Q_{11am}=900Wm^{-2}, Q_{12pm}=1000Wm^{-2}:

$Q_{6\text{-}12h} = (Q_{7am} + Q_{8am} + Q_{9am} + Q_{10am} + Q_{11am} + Q_{12pm})/6 \quad = 608 \text{ Wm}^{-2}$

$Q_{6\text{-}12h} = (Q_{8am} + Q_{10am} + Q_{12pm})/3 \quad = 683 \text{ Wm}^{-2}$

$Q_{6\text{-}12h} = (Q_{7am} + Q_{8am} + Q_{10am})/3 \quad = 383 \text{ Wm}^{-2}$

Therefore it will probably be necessary to interpolate between insolation measurements to determine the mean insolation or calculate the averaged value another way. The following method provides one way of determining the mean value. Assuming the time of day of an insolation measurement is known (e.g. 10am) along with the date, latitude and longitude of the measurement, the six hourly mean insolation could be derived by:

$$Q_{sw(6-12h)} = \frac{Q_{sw(t)}}{Q_{sw\_\mathrm{mod}(t)}} Q_{sw\_\mathrm{mod}(6-12h)} \tag{6.14}$$

where

t	time of measurement
$Q_{sw\ (6\text{-}12)}$	estimated $Q_{sw\ 6\text{-}12}$
$Q_{sw\ (t)}$	observed Q_{sw} at time (t)
$Q_{sw\_mod\ (t)}$	clear sky model Q_{sw} at time (t)
$Q_{sw\_mod\ (6\text{-}12)}$	clear sky modelled mean $Q_{sw\ (6\text{-}12h)}$

A common insolation model (e.g. Liou, 1980) could be used to calculate clear sky radiation, Q_{sw_mod}, given the time, day, year, latitude and longitude of the measurement. Alternatively, the clear sky model could be used alone and give a clear sky value if no measurements were available. Clear sky models tend to give the top of the atmosphere radiation which should be converted to a top of the ocean value. The typical percentage of transmission through the atmosphere ranges from 70-80%.

3. The sub-skin model has been derived from model data and not observations. Due to the highly nonlinear behaviour of the diurnal cycle, no model is able to perfectly replicate the diurnal cycle and therefore using model values may affect the skill of the model. However, the errors in the warm layer correction used here are likely to be small compared to the size of the diurnal signal and the parameterisation appears to work well when compared to in situ measurements (Figure 6.14).

4. This parameterisation is more complex than existing models and is not as simple to apply as the KK02/03 or the G04 parameterisations. However, the complication is rewarded by a more accurate parameterisation, in particular for the sub-skin, where the diurnal temperature variability is highly sensitive to the time variability of the forcing fields. Several small intricacies exist within the overall coding of the parameterisation based on extensive analysis of the diurnal warming shapes in Chapter 5. Therefore anyone wishing to apply the parameterisation is advised to refer to the code to set up the parameterisation in the correct way (Appendix D).

6.8 SUMMARY

This chapter has described the development of a new parameterisation to estimate the shape of the diurnal SST cycle at the surface and at 1m. The parameterisation only requires wind and insolation averaged over four parts of the day as input and produces the diurnal variation of temperature during the day, referenced to the daily minimum SST, which is assumed to represent the true mixed layer temperature. Given the non-linear nature of the diurnal cycle, it is a challenge to parameterise the diurnal cycle with great accuracy. This new parameterisation builds upon previous models by including the time variability of the wind and insolation fields, which control the evolution of the warm layer, and shows a marked improvement compared to the other models when validated against independent datasets. The applications of the parameterisation have been discussed and the model is being incorporated into the data processing scheme of the European contribution to the GHRSST-PP (Medspiration) as the initial method to remove or flag the diurnal signal in satellite SST. This will be a major test for the parameterisation and it is hoped the work can be developed through the testing stage.

CHAPTER 7: DISCUSSION

The introduction to this thesis presented the potential impacts of diurnal warming in two main contexts: the interpretation and application of SST and its role in high frequency air-sea interaction. The importance of diurnal warming has often been ignored in the past because it was not considered to occur very often and was not expected to have any significant impact. The observational studies discussed in Chapter 1 already provide evidence of large diurnal warming events in several different locations but they were limited in time and space and their implications were not fully appreciated. The results presented in this thesis have revealed the importance of diurnal warming. Satellite data have been analysed to provide a global view of diurnal warming patterns and in situ buoy and model data have been used to investigate the magnitude and variability of the diurnal cycle at the surface and at depth.

In terms of the interpretation of SST, the results clearly demonstrate that diurnal warming complicates the definition of SST. It will be a major source of noise for mixed layer SST measurements, masking the temperature of interest. Referring to Chapter 3, the results have shown that diurnal warming can potentially lead to large seasonal biases in the mixed layer temperature, which have been underestimated or ignored in the past, and demonstrates the benefit of identifying diurnal warming conditions to help interpret SST. Under diurnal warming conditions almost no SST instruments will record the true mixed layer temperature. These diurnal amplitudes can easily be aliased into the climate signal and should not be ignored.

The global diurnal warming maps were presented to the GHRSST science team at the 2nd GHRSST-PP workshop in Japan (May 2001) and based on this and other similar work, the science team agreed to resolve the diurnal cycle of SST as a step to produce the most accurate true mixed layer and skin temperatures. Satellite observations are likely to have much larger diurnal signals than buoy measurements and since GHRSST will use a combination of in situ and satellite data to produce the new generation SST products, they must recognise that in low winds, the diurnal variations in satellite and in situ measurements should not be treated as the same. The parameterisation presented in Chapter 6 provides a method to deal with the diurnal signal in satellite and buoy

measurements. The parameterisation can be used to predict the diurnal variation in temperature at the time of the measurement which can then be subtracted from the measurement as a correction to give the best-estimate of the true mixed layer temperature. The parameterisation was presented at the 4th GHRSST-PP workshop in September 2003 and is now being incorporated into the Medspiration SST project (the European contribution to GHRSST-PP, funded by the European Space Agency). Work is currently underway to implement this parameterisation into the data processing scheme and the full potential of the parameterisation will soon be investigated.

One of the concerns about diurnal warming contamination in the past has been its masking effect over fronts and eddies, as reported by Katsaros et al. (1983), Deschamps & Frouin (1984) and Bohm et al. (1991). The influence of chlorophyll near coastal regions may contribute to the phenomenon of front masking. In regions with sharp horizontal SST gradients, the gradients are often reduced during diurnal warming conditions. Recently Katsaros & Soloviev (2004) and Katsaros et al. (2004) suggested that this effect was driven by the heat and momentum fluxes over water of two different temperatures; where for identical atmospheric conditions, cooler water will heat more rapidly than warmer water. However, in association with coastal fronts there is usually a strong gradient of chlorophyll as well as temperature, with cooler water usually associated with higher chlorophyll concentrations. Variability in the optical properties of the water column was not considered in these studies. The results presented in Chapter 4 revealed that the diurnal heating rate will increase as a function of increasing chlorophyll. The effect is more important below the surface but in the presence of a little mixing, the surface diurnal amplitude (detected by satellites) will increase. In coastal regions associated with large fronts, chlorophyll concentrations can be very high and the surface layer can become strongly heated by the additional heat absorbed by the phytoplankton near the surface. Therefore it may be that a combination of the effects described by Katsaros & Soloviev (2004) and Katsaros et al. (2004) and the increased heating rate caused by the presence of chlorophyll may better explain the phenomenon. This has not been investigated in this thesis but it poses an interesting question for future work. The masking of fronts and eddies is a big problem for some SST applications, particularly commercial applications (e.g. fishing industry) which require information on the position of fronts.

The diurnal variability of SST can also impact on the accuracy of other types of measurements. The potential errors introduced by excluding the diurnal cycle can be considered in the context of NWP models. NWP models rely on an accurate estimate of the skin SST to assimilate satellite sounder radiances. The models compare their first guess state with observed radiances and use the difference to adjust the models to better fit the observations. For most models, the first guess skin temperature is taken from the model's SST analysis without considering whether a diurnal thermocline exists and consequently could be out by several degrees during the day. If diurnal warming is occurring, then during the assimilation, the offset between the cooler first guess radiances and the warmer measured radiances could be misinterpreted as an atmospheric signal.

There are other important implications for diurnal warming. Given the frequency and variability of the seasonal patterns, it suggests implications for upper ocean processes and air-sea interaction on diurnal and intraseasonal time scales.

Several studies have investigated the impact of the diurnal cycle on longer term oceanic timescales. Price et al. (1986) concluded that the process of diurnal cycling plays an important role in shaping the long term response of the upper ocean to atmospheric forcing. Zhang (1996) investigated the coherence between SST and atmospheric forcing for the tropical western Pacific warm pool and reported that diurnal heating was an inherent component of long term SST fluctuations. Bernie et al. (2003) report that the diurnal cycle of SST contributes to a third of the intraseasonal SST variability in the western tropical Pacific. Recent studies by Shinoda & Hendon (1998) and McCreary et al. (2001), comparing model solutions with and without the diurnal cycle for the tropical Western Pacific and Indian Ocean and the Arabian Sea respectively, concluded that the inclusion of diurnal forcing plays an important role in the mixed-layer dynamics. Most models do not include diurnal variations of SST and furthermore do not have adequate vertical resolution near the surface to include it without modification.

Other studies have discussed the importance of diurnal SST variability for air-sea heat exchange. Webster et al. (1996) estimated the changes in the surface heat fluxes associated with a 1°C change in SST for average conditions during the TOGA COARE

Intense Observing Period (IOP). Substantial differences were reported with all changes being of the same sign. The upwelling longwave increased by 6.3 Wm^{-2} (a 1.3% change), the sensible heat flux by 2.4 Wm^{-2} (23.2% change) and the latent heat by 18.7 Wm^{-2} (16.2% change). Similar results have also been reported by Zeng & Dickinson (1998) and Cornillon & Stramma (1985). The tropics are expected to be more sensitive to diurnal SST variations due to their higher temperatures. These studies highlight the potential deficiencies in current boundary conditions employed by many atmospheric general circulation models (AGCMs) and numerical weather prediction (NWP) models. Models use weekly or monthly mean fixed bulk SST which eliminate any diurnal SST variability and underestimate the enhanced temperatures observed in the skin layer during light wind conditions, which can lead to errors in the modelled surface fluxes. Research is currently underway to investigate whether the inclusion of the diurnal cycle of skin SST will improve simulations of the diurnal cycle of convection in the tropics in an AGCM (Woolnough & Inness, personal communication). Results from Dai & Trenberth (2004) highlight the importance of the diurnal cycle of SST. They report deficiencies in diurnal variability in a coupled ocean-atmosphere model over ocean areas which they attribute to the absence of a diurnal cycle of SST.

In the same way that omitting the diurnal cycle of SST has implications for air-sea heat exchange, it also has implications for gas exchange across the air-sea interface since the dissolution of gases is dependent on the skin temperature. This could be particularly important for the carbon budget. Takahashi et al. (1993) reported that the change in pCO_2 (partial pressure of CO_2) as a function of temperature was 4.23% $°C^{-1}$. The cool skin effect is already accounted for in air-sea gas flux calculations (Robertson & Watson, 1993) but the effect of the diurnal warm layer has not been considered seriously. The cool skin temperature difference is very small in comparison to the large diurnal warming variations and in the light of the results presented in Chapter 3, the large seasonal patterns in diurnal warming suggest that they could have an impact on gas fluxes. McNeil and Merlivat (1996) carried out a simple study to investigate the impact of the warm skin effect on CO_2 fluxes and commented that the diurnal warming cycle produced asymmetry in the net diurnal ocean to air CO_2 transfer. Equatorial/tropical regions (large source areas of CO_2), susceptible to diurnal warming, will have increased sea to air fluxes. In sink regions, an increase in SST will result in

less CO_2 being taken up by the ocean. The substantial regional and seasonal variations in diurnal warming need to be considered to understand the true influence of diurnal warm layers on the exchange of CO_2 and other gases. Collaborative work is in progress with Dr Olsen from the University of Bergen to investigate and quantify the influence of the diurnal variations of wind speed and SST on global CO_2 fluxes.

For many of the implications raised and discussed above, the parameterisation developed as part of this thesis could be used to include the diurnal temperature variation at the surface and allow the impact of diurnal variability to be properly addressed. Most general circulation models use a 'bulk' SST which does not include any diurnal temperature variations. For atmospheric models, the diurnal variation parameterisation can be applied to the 'bulk' measurement and used as a lower boundary condition for atmospheric models. In the case of coupled air-sea models, running a full 1-D ocean mixed layer model to determine the diurnal SST variations can be computationally expensive and therefore the application of a simple parameterisation could address this issue and would permit the diurnal cycle to be included in a simpler and quicker way. Dai & Trenberth (2004), who reported that the absence of the diurnal cycle of SST reduced the skill of the Community Climate System Model, suggest that a diurnal warming parameterisation may be an effective way to include diurnal skin SST variability in models.

Any detailed modelling study of the evolution of the diurnal warm layer needs to select the most appropriate solar transmission parameterisation to model the vertical profile of irradiance. Most 1-D models use the Paulson and Simpson (1977) 2-band parameterisation which does not consider the full spectral range of irradiance and excludes the important infrared end of the spectrum which contributes to the heat in the top metre. Most modelling studies of diurnal warming in the past have used the 2-band Paulson & Simpson (1977) parameterisation, which therefore reduces their ability to fully predict and understand the thermal structure of the top few metres under low winds, and brings into question the accuracy of the results. Only the Fairall et al. (1996b) warm layer model uses a more detailed parameterisation (Soloviev, 1982) and over the last couple of years, diurnal warm layer modelling work using the General Ocean Turbulence Model (GOTM) has also used a full spectral model (Hallsworth, personal communication).

Finally, it is also important to consider whether these diurnal warming amplitudes have an impact in the climate context. Diurnal SST amplitudes could be considered as a climatically significant variable in their own right. Diurnal warming has a regular seasonal cycle dictated by meteorological conditions which has been observed across ten years of data. With evidence of interannual variability reflected in the dataset, diurnal warming could therefore be a useful climate indicator for interannual and longer term climate variability. Recently, climate change is becoming associated with more extreme climatic variations (Easterling et al., 2000) and measurements of diurnal warming may provide a way to assess the trend in extreme changes.

CHAPTER 8: CONCLUSIONS & FUTURE WORK

This thesis has presented a detailed study of the diurnal variability of SST using a variety of data from satellites, buoys and a 1-D mixed layer model. The overall context of this work has been discussed in detail throughout the thesis and, in particular, in the previous chapter. This chapter summarises the main conclusions from this work and presents ideas for new research which lead on directly from this work.

The results presented in Chapter 3 provide the first long-term global assessment of diurnal warming patterns. Ten years of daily day and night-time satellite SST have revealed a detailed picture of the strong seasonal patterns of diurnal warming associated with large-scale meteorological variability. The long time series builds up a climatological view of the diurnal warming patterns providing concrete proof of the regularity of these seasonal warming patterns. There is evidence of interannual variability with indication of ENSO patterns and variability related to the monsoon. There is also evidence of large scale variability in the austral summer mid-latitudes though the interpretation of this pattern has been complicated by concerns related to the satellite orbit drift.

Numerical model results from the Price, Weller & Pinkel (1986) 1-D mixed layer model have revealed the sensitivity of the evolution of the diurnal warm layer to the presence of chlorophyll. Under very low wind conditions, the presence of chlorophyll has little impact on the heating rate at the surface since this is dominated by the absorption of red light. The impact on the maximum diurnal amplitude is only noted below the surface. In moderate winds, since the top few metres of the water column are well mixed, the influence of chlorophyll is evident in the surface SST. The presence of chlorophyll has an important effect for the break down of the diurnal stratification. As the warm layer breaks down through turbulent mixing, the erosion is weakened since the water below the diurnal mixed layer is warmer due to the extra heat absorbed by the chlorophyll pigments. During the day, the presence of chlorophyll plays a negligible role in the depth of the diurnal mixed layer but at night, large differences were noted. In open ocean, chlorophyll concentrations are not expected to exceed much above 5mg/m^3 and therefore only have quite a small impact on the evolution of the diurnal warm layer and

SST. Towards the coast where chlorophyll concentrations are much higher, the impact is expected to be more dramatic and cause more significant changes in the thermal structure and heating rate of the diurnal warm layer.

Part of the modelling work has highlighted the importance of selecting the most appropriate solar transmission parameterisation to estimate the vertical irradiance profile. PWP, like many other mixed layer models, implements the Paulson & Simpson (1977) 2-band parameterisation. An intercomparison of several parameterisations revealed the weakness of this parameterisation in simulating the distribution of heat in the upper 2-3m of the water column. This parameterisation does not consider the full spectral range of irradiance and excludes the important infrared end of the spectrum which contributes to the heat in the top metre. A full spectral parameterisation should be used for all modelling studies concerned with diurnal warming.

The analysis of a few hundred diurnal cycles of SST, insolation and wind speed, obtained from high resolution buoy data, has revealed that the evolution of the warm layer, and therefore the phase of the signal, is largely dependent on the time variability of the forcing fields (wind and heating). The shallower the warm layer, the greater its sensitivity to the forcing fluctuations. The timing of the peak SST can vary from pre-noon to late afternoon and the phase will change with depth, with SST peaking later with depth. The results highlight the variability in the shape of the diurnal SST cycle and also draw attention to the large differences in SST that can occur between the surface and 1m.

A new parameterisation has been developed to estimate the diurnal variation of SST at the surface and at 1m. The parameterisation requires only wind and insolation averaged over four parts of the day as input and produces the diurnal variation of temperature during the day, referenced to the daily minimum SST, which is assumed to represent the true mixed layer/foundation temperature. The parameterisation follows on from previous studies and aims to capture some of the variability in the diurnal signal as it responds to changes in the forcing conditions which have been ignored in past models. The parameterisation has been carefully validated using independent data not used in the derivation of the models and shows good agreement with the data and an improvement over existing parameterisations.

FUTURE WORK

There are several areas for future work which lead directly on from the implications of the results discussed in Chapter 7. Some of this work is currently underway. During the course of this study, the diurnal cycle of SST has become a 'hot' topic and there have been many interesting and new results over the last couple of years and more interesting research is in progress.

The most exciting progression for the work presented in this thesis, is to see the implementation of the diurnal warming parameterisation into the ESA Medspiration SST project. Work has begun to implement the parameterisation into the data processing scheme and careful testing and validation will be required to assess how well the parameterisation works when applied to the satellite data. The parameterisation has great potential to contribute to better SST records for the broad range of SST applications.

The parameterisation could be used to fill in the gaps in the global diurnal warming maps presented in Chapter 3. Very little information was revealed for the tropics due to the cloudiness of this region. Applying wind and insolation data from satellites, buoys or models to the parameterisation would give an estimate of the diurnal variability. Alternatively, the full time series of TAO/TRITON and PIRATA SST data could be analysed to provide a long-term view of the diurnal variability in the tropical Pacific and Atlantic.

There are also additional applications for the parameterisation. For example, the parameterisation could be used in air-sea interaction studies as a boundary condition for atmospheric models, as suggested by Dai & Trenberth (2004). The Centre for Global Atmospheric Modelling at Reading is looking at the importance of diurnal variability in the tropics and has expressed interest in using the parameterisation to assess the impact of diurnal SST variations on atmospheric variability. This is a very interesting and rapidly evolving field of research. The parameterisation could also be used to investigate the influence of diurnal SST variability on the transfer of CO_2 and other gases across the air-sea interface. The global diurnal warming maps, presented in Chapter 3, are being used in a study to investigate the impact of the diurnal SST

variations on global CO_2 fluxes. In the future the parameterisation could be applied to biogeochemical models which investigate gas fluxes across the air-sea interface.

In reality, the variability associated with diurnal warming is not purely driven by wind and insolation and more detailed modelling and observational work is required to understand the intricacies of the diurnal cycle and how the diurnal stratification interacts with other processes occurring locally in the upper ocean and atmosphere. One area of interest to arise from this thesis, is to investigate whether the influence of large chlorophyll gradients across fronts contributes to the masking effect observed during diurnal warming conditions (e.g. Katsaros et al., 1983; Bohm et al., 1991). Previous studies have shown that diurnal warming can reduce sharp thermal contrasts which are often important to detect for some SST applications. If the atmospheric forcing is the same across the front, what causes the uneven heating at the surface and the masking of the thermal gradient? One suggestion has been the change in heat and momentum fluxes due to the differences in the air-sea temperature differences across the two water masses (Katsaros & Soloviev, 2004). However, high chlorophyll concentrations could also contribute to this.

This work has revealed a particular weakness for the new parameterisation and all other parameterisations and 1-D mixed layer models: very few surface and near-surface measurements exist to validate the output. The thermal structure in the top 1m has rarely been observed in detail and of the few measurements that exist, a very limited amount coincide with diurnal warming conditions. For the work presented in Chapters 5 & 6, the Fairall et al. (1996b) warm layer model was applied to get a surface estimate of SST. Our main understanding of the thermal structure of the diurnal warm layer under low winds comes from model results. Since satellites are becoming the major source of SST measurements, it is important to be confident in the amplitude of the diurnal variations that the satellite will detect from space.

With recent advances in SST measurement techniques over the last few years and the large pool of different satellite data that exists, the diurnal temperature variability at the sea surface can be studied in more detail. The Skin Depth Experiment Profiler (SkinDeEP) instrument developed by Brian Ward (Ward et al., 2004) provides one of the only current opportunities to look at the fine thermal structure of the water column

during strong diurnal warming conditions. The profiler samples temperature rapidly as it sinks and rises through the top 10m of the water column. The instrument has fortunately been deployed in some strong diurnal warming conditions and provides a unique and exciting dataset to finally validate the models. The SkinDeEP measurements are also important to fully understand the cool skin effect during diurnal warming conditions as discussed in Section 5.3.2.1 as they provide the only source of the true skin to sub-skin temperature difference during very strong diurnal warming events. Geostationary satellites can be used to monitor the evolution of the diurnal changes in surface SST. The global satellite diurnal warming maps can be used to identify and select a suitable time and location to investigate the surface heating. The next GHRSST-PP workshop, this summer, will have a specialised diurnal warming session where some of these exciting measurements will be presented and compared against a variety of mixed-layer models and diurnal warming parameterisations.

The new results and literature presented and discussed in this thesis have demonstrated the importance of the diurnal SST cycle and its implications for air-sea interaction and the interpretation of SST measurements. Finally the diurnal cycle of SST is now being fully recognised and it is an exciting time to be involved in the field.

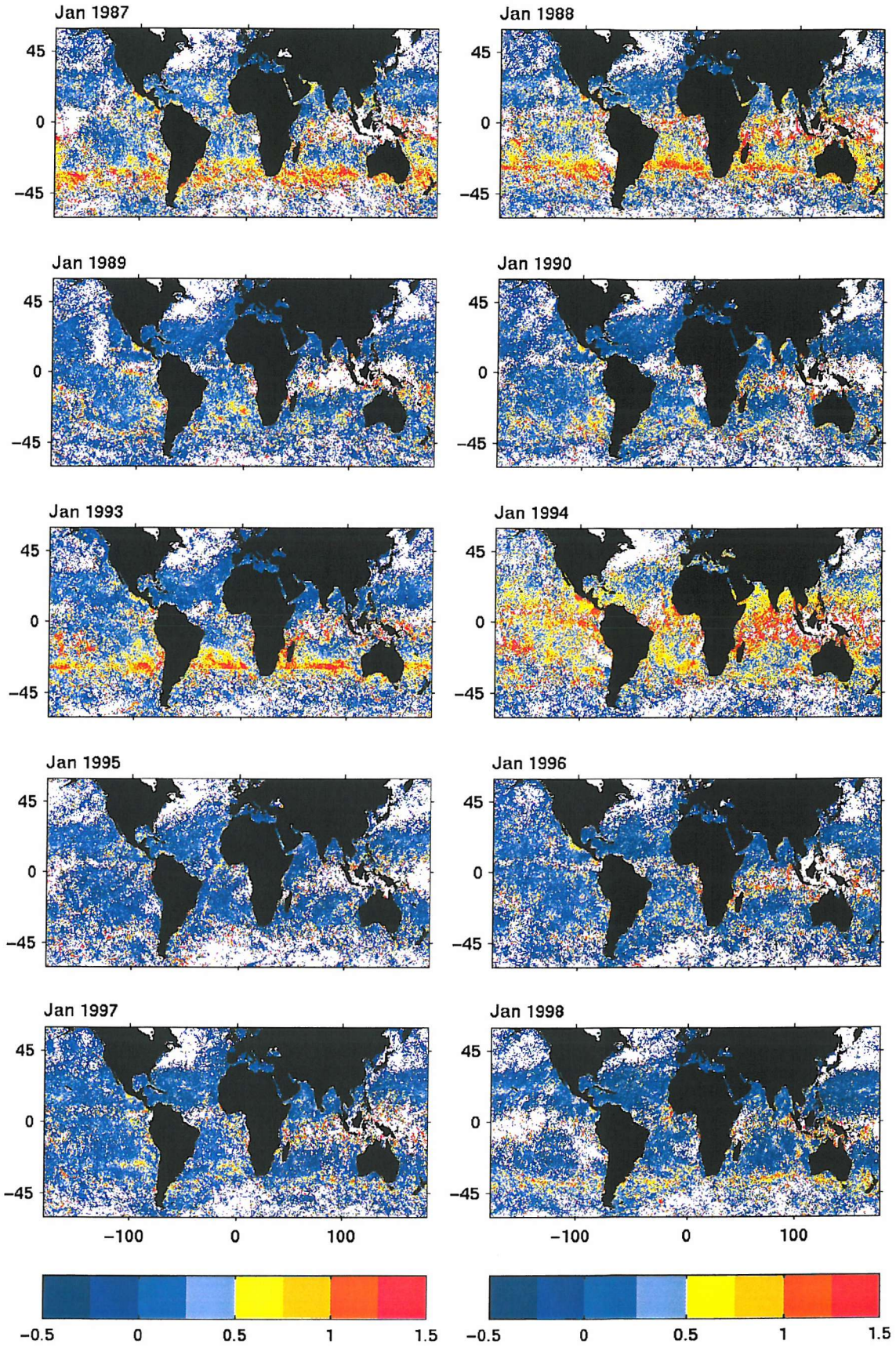

Figure A.1: Monthly mean ΔT for January computed from daily AVHRR SST data (Chapter 3).

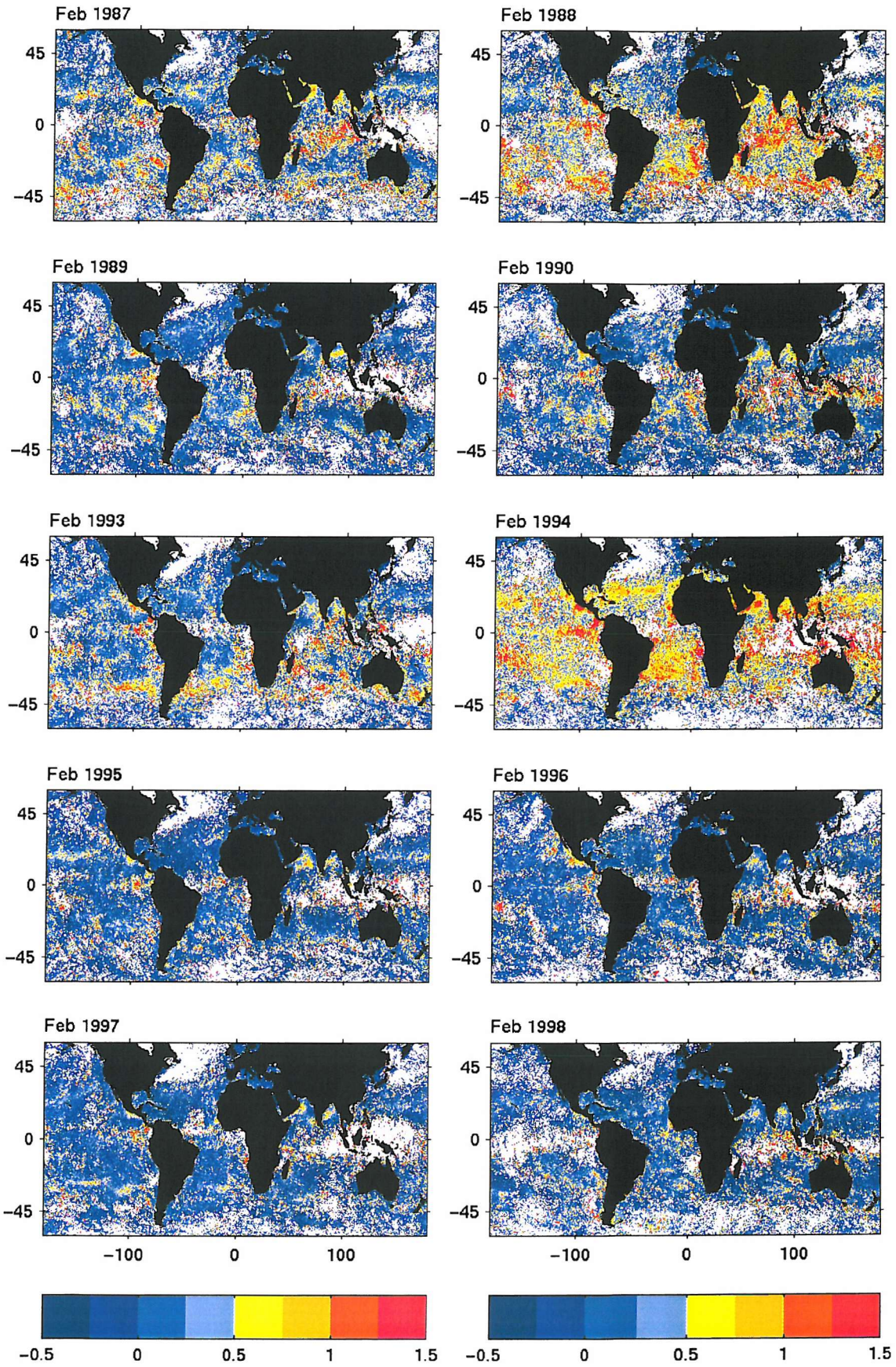

Figure A.2: Monthly mean ΔT for February computed from daily AVHRR SST data (Chapter 3).

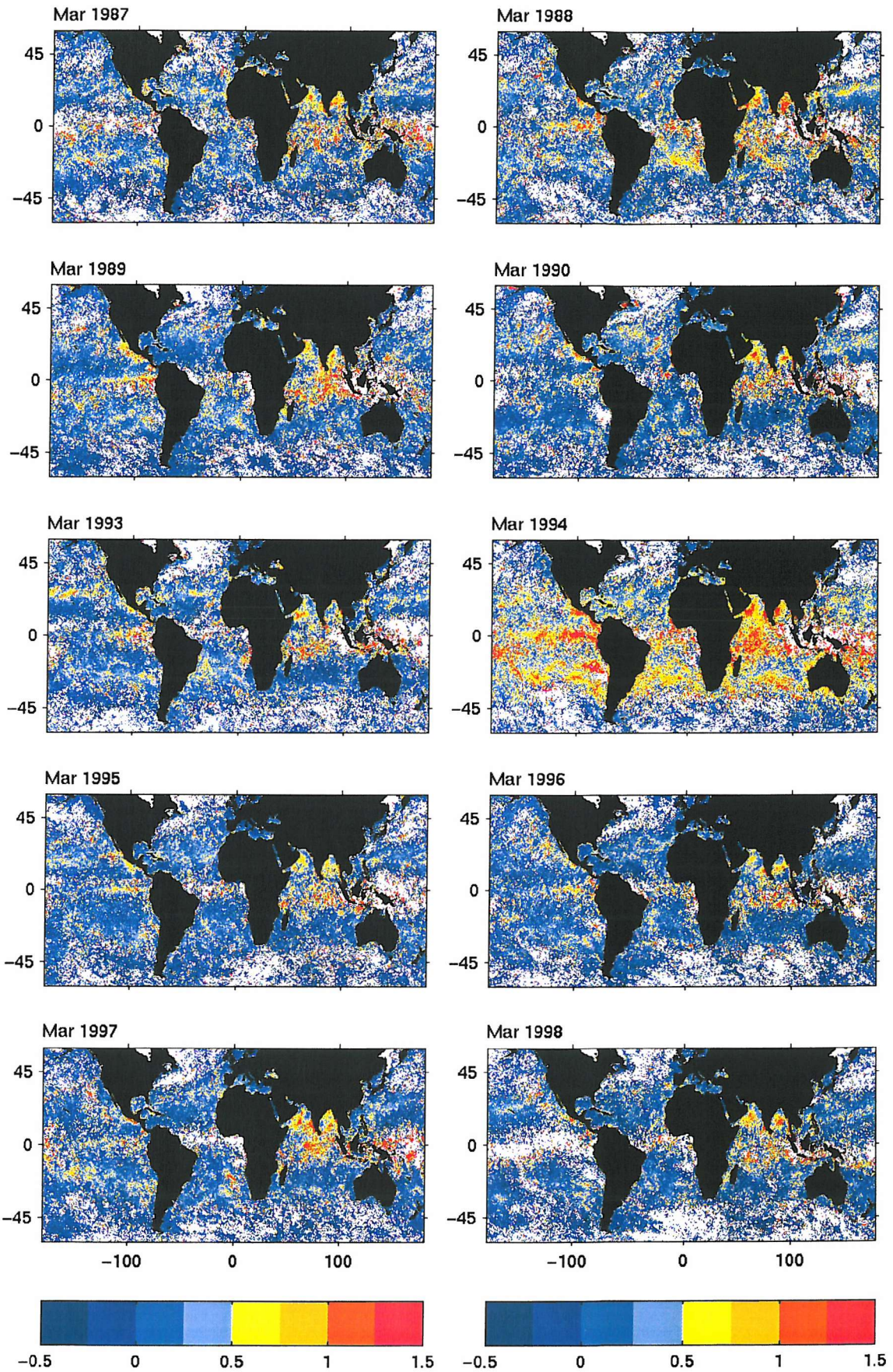

Figure A.3: Monthly mean ΔT for March computed from daily AVHRR SST data (Chapter 3).

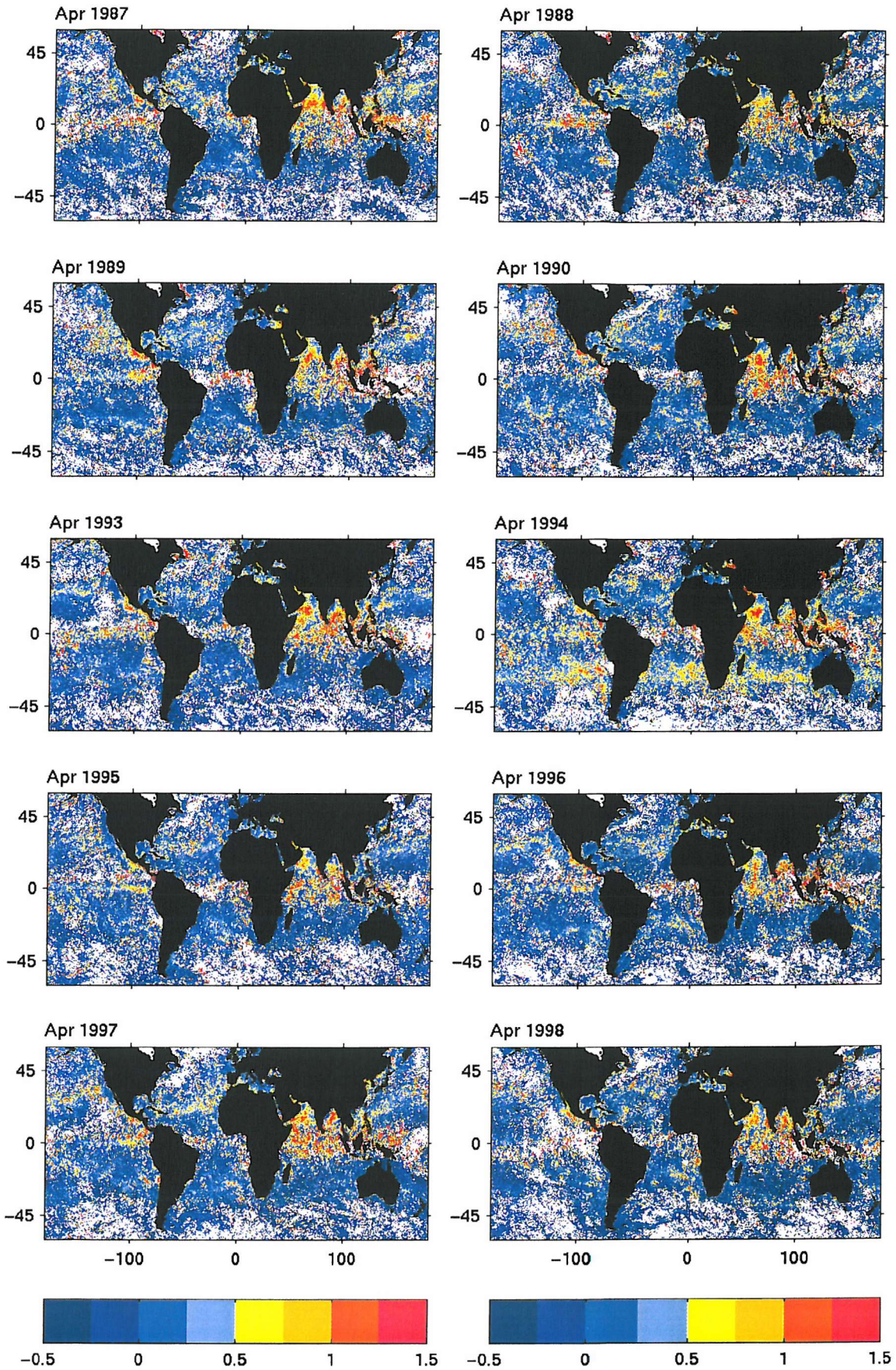

Figure A.4: Monthly mean ΔT for April computed from daily AVHRR SST data (Chapter 3).

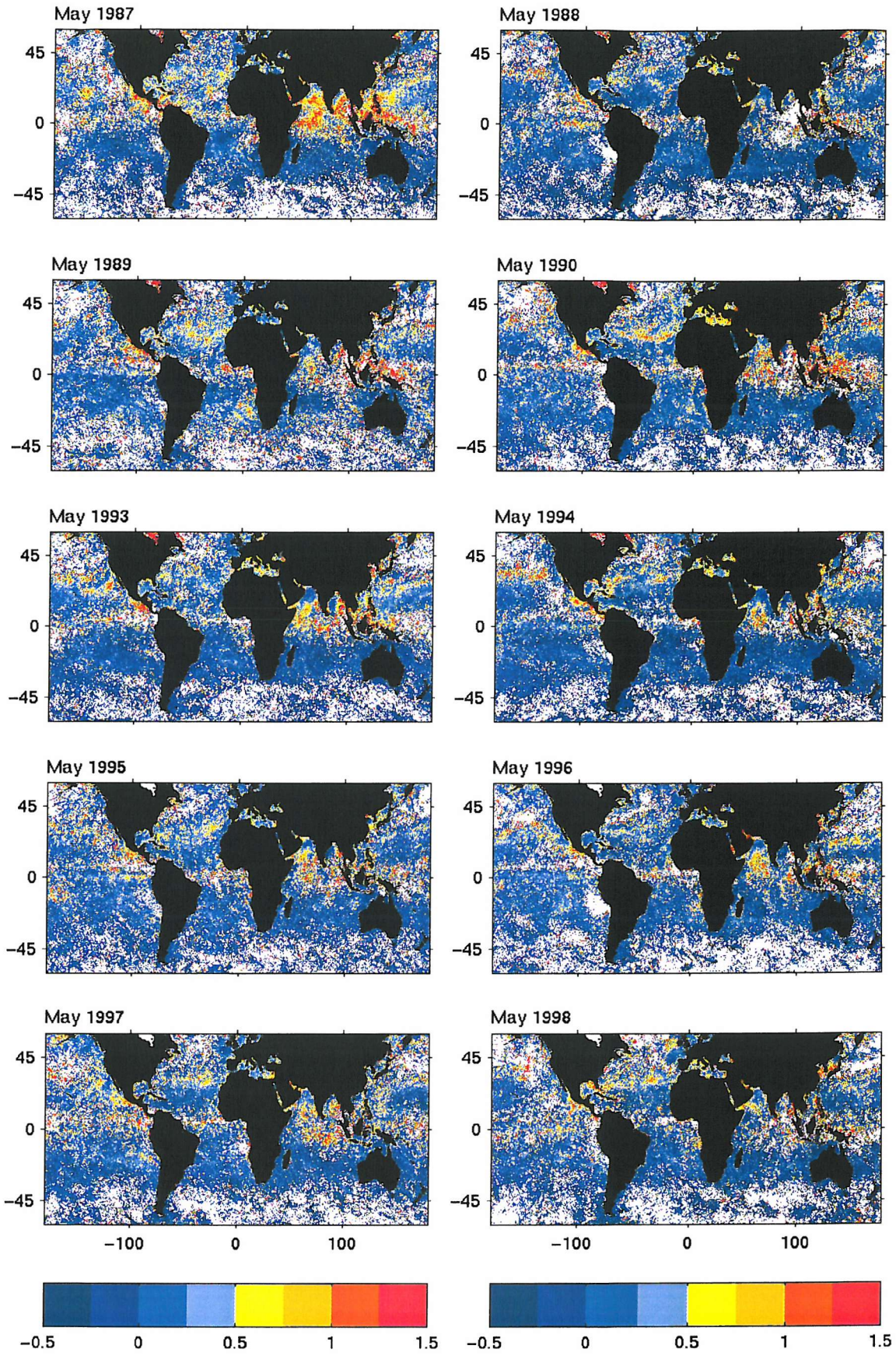

Figure A.5: Monthly mean ΔT for May computed from daily AVHRR SST data (Chapter 3).

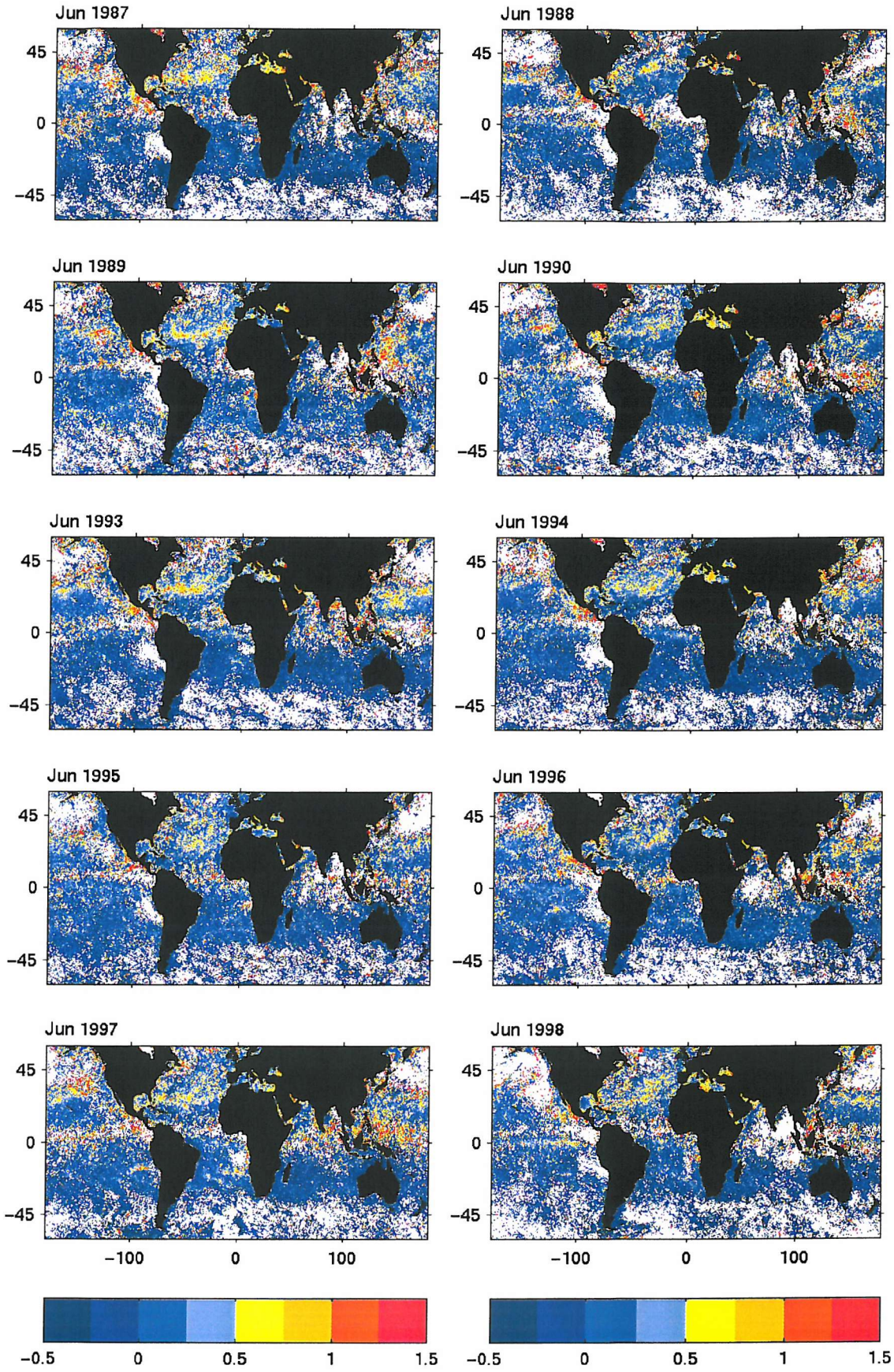

Figure A.6: Monthly mean ΔT for June computed from daily AVHRR SST data (Chapter 3).

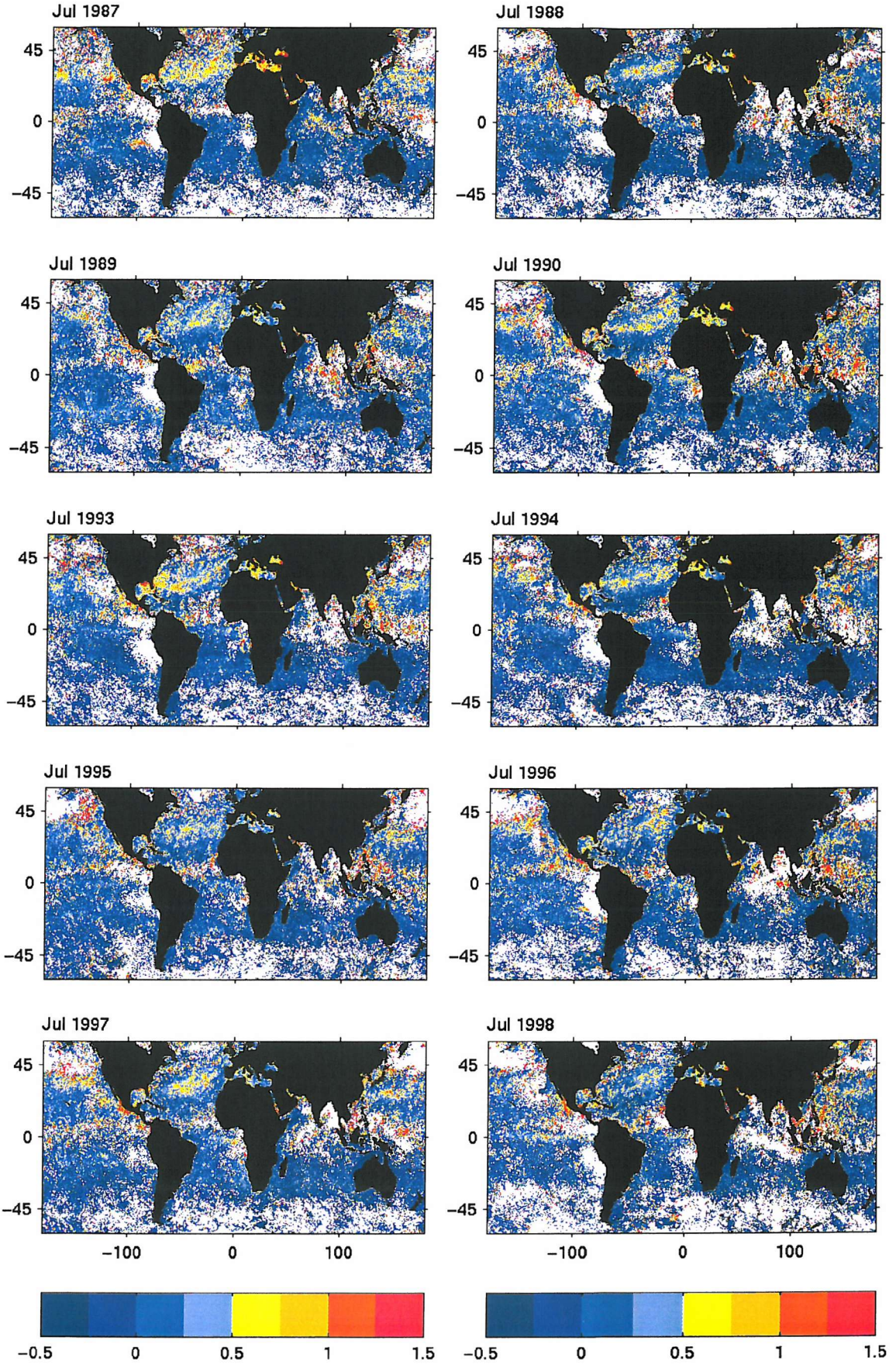

Figure A.7: Monthly mean ΔT for July computed from daily AVHRR SST data (Chapter 3).

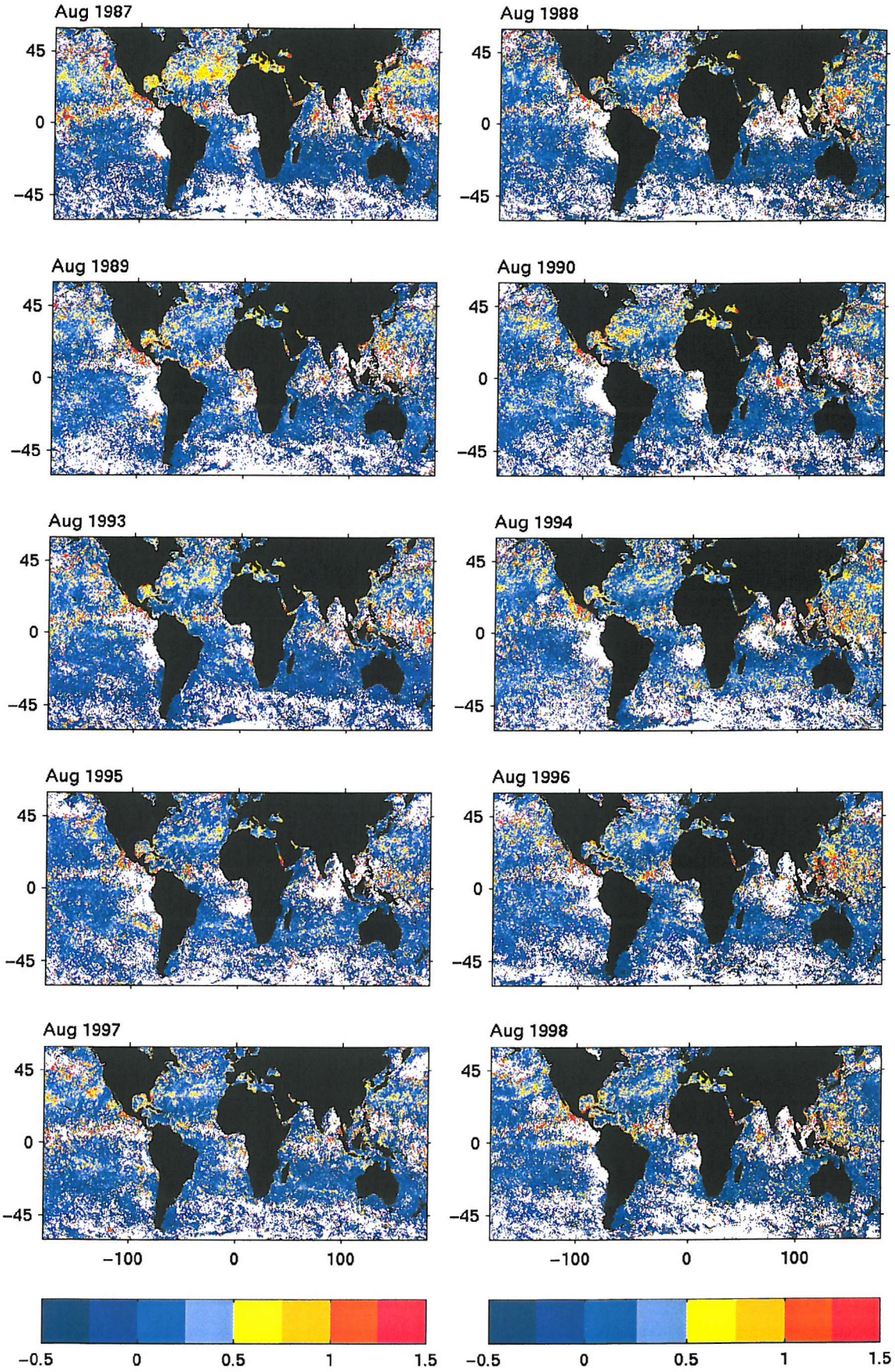

Figure A.8: Monthly mean ΔT for August computed from daily AVHRR SST data (Chapter 3).

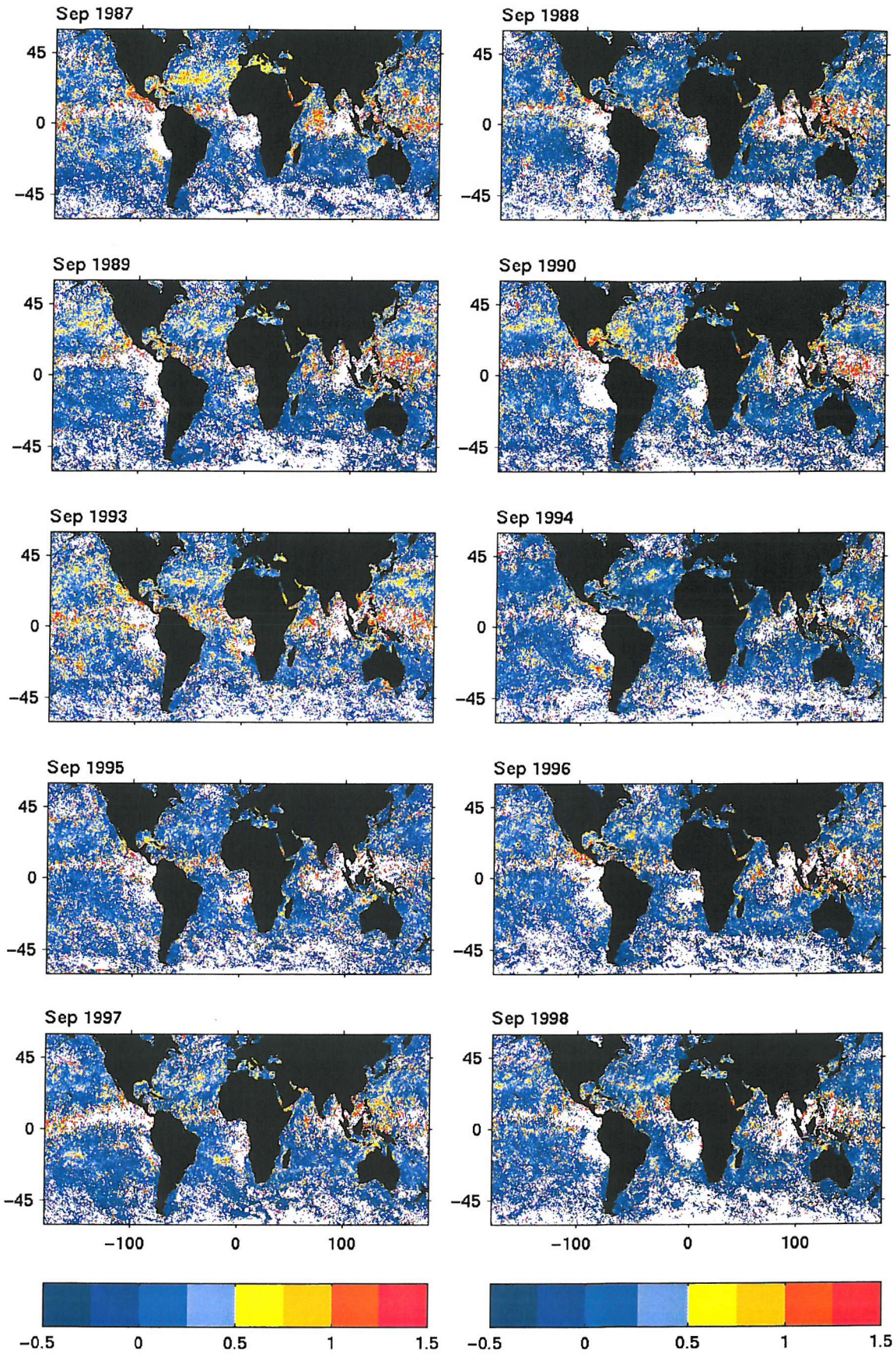

Figure A.9: Monthly mean ΔT for September computed from daily AVHRR SST data (Chapter 3).

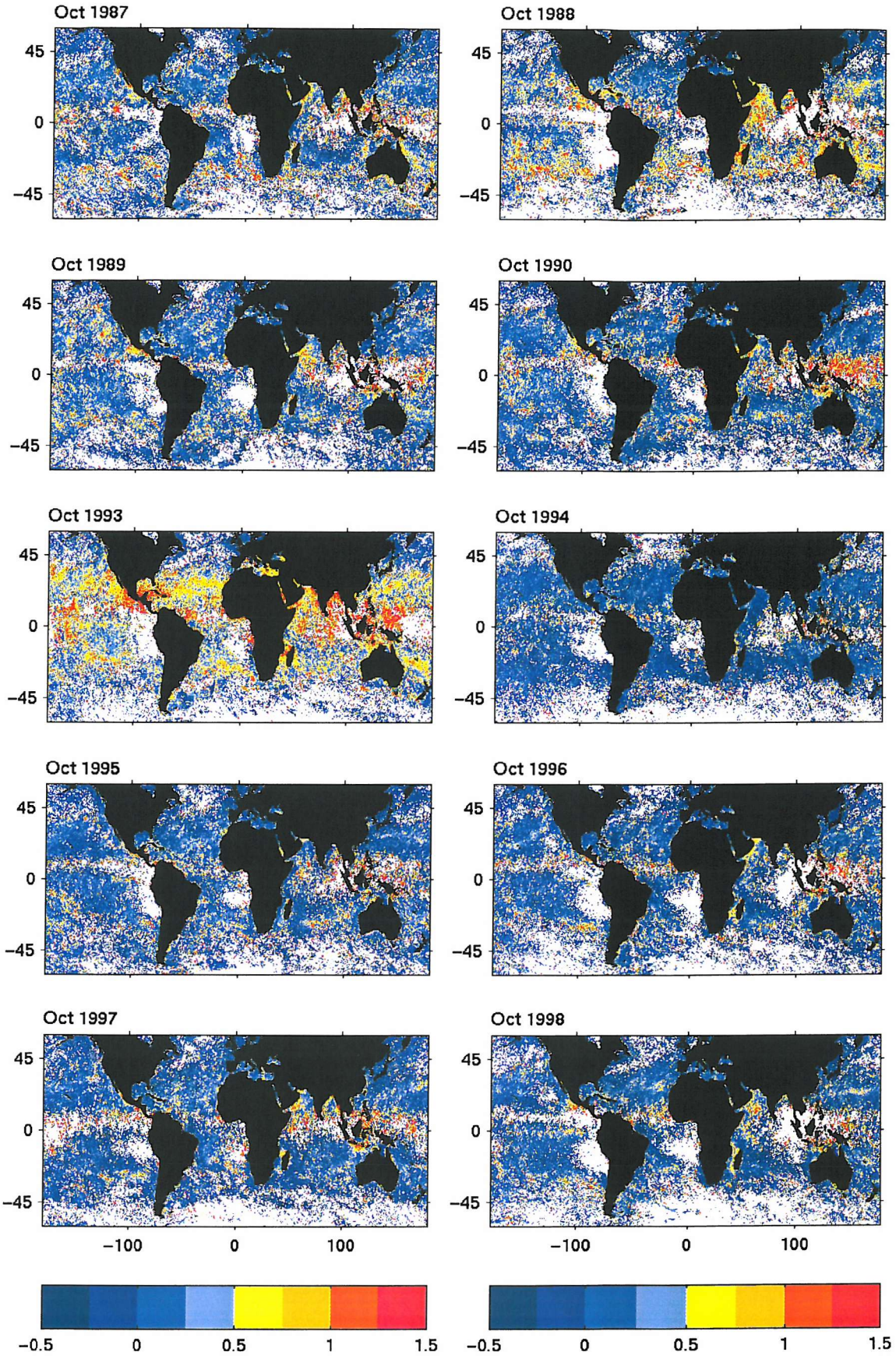

Figure A.10: Monthly mean ΔT for October computed from daily AVHRR SST data (Chapter 3).

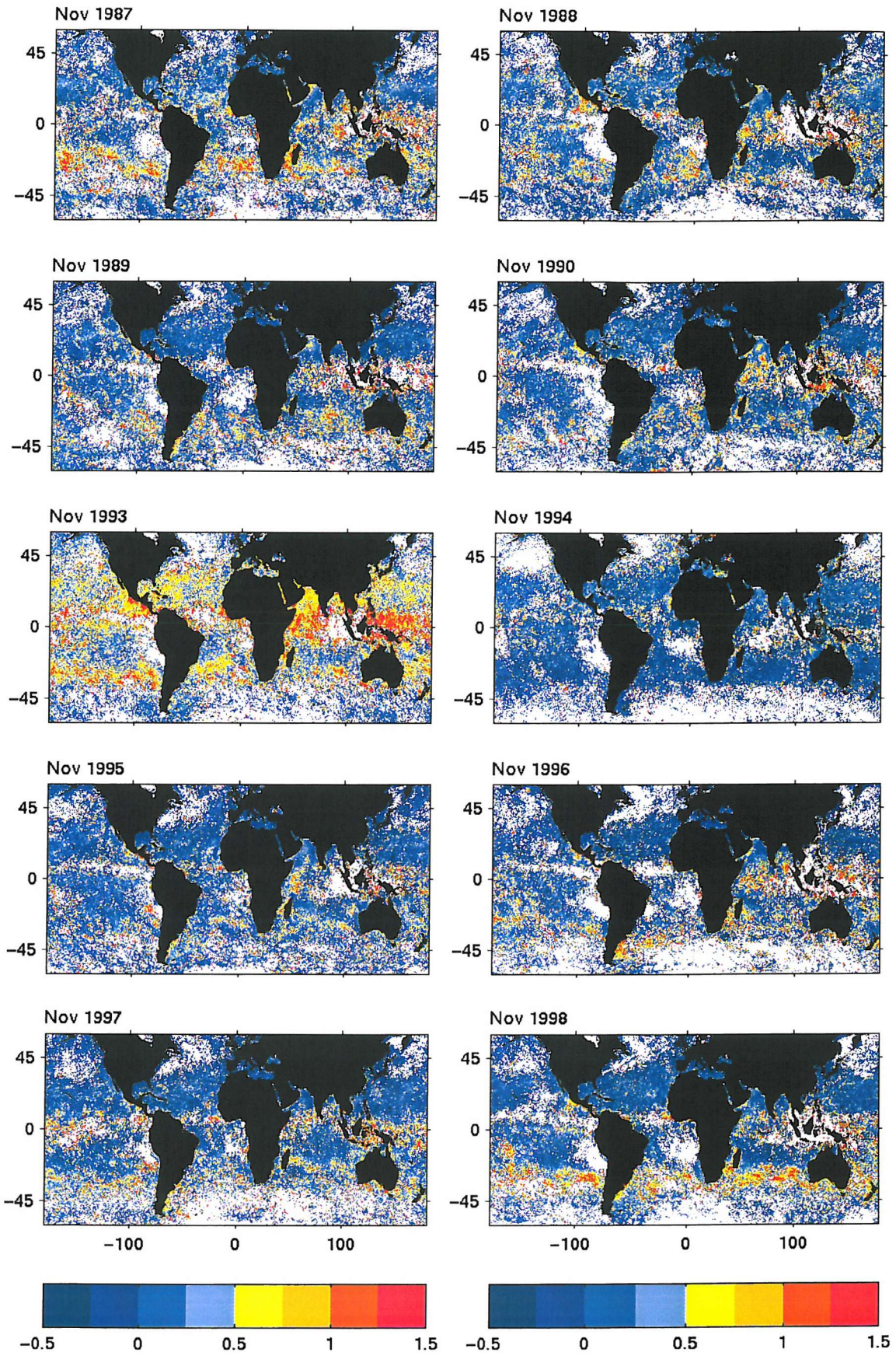

Figure A.11: Monthly mean ΔT for November computed from daily AVHRR SST data (Chapter 3).

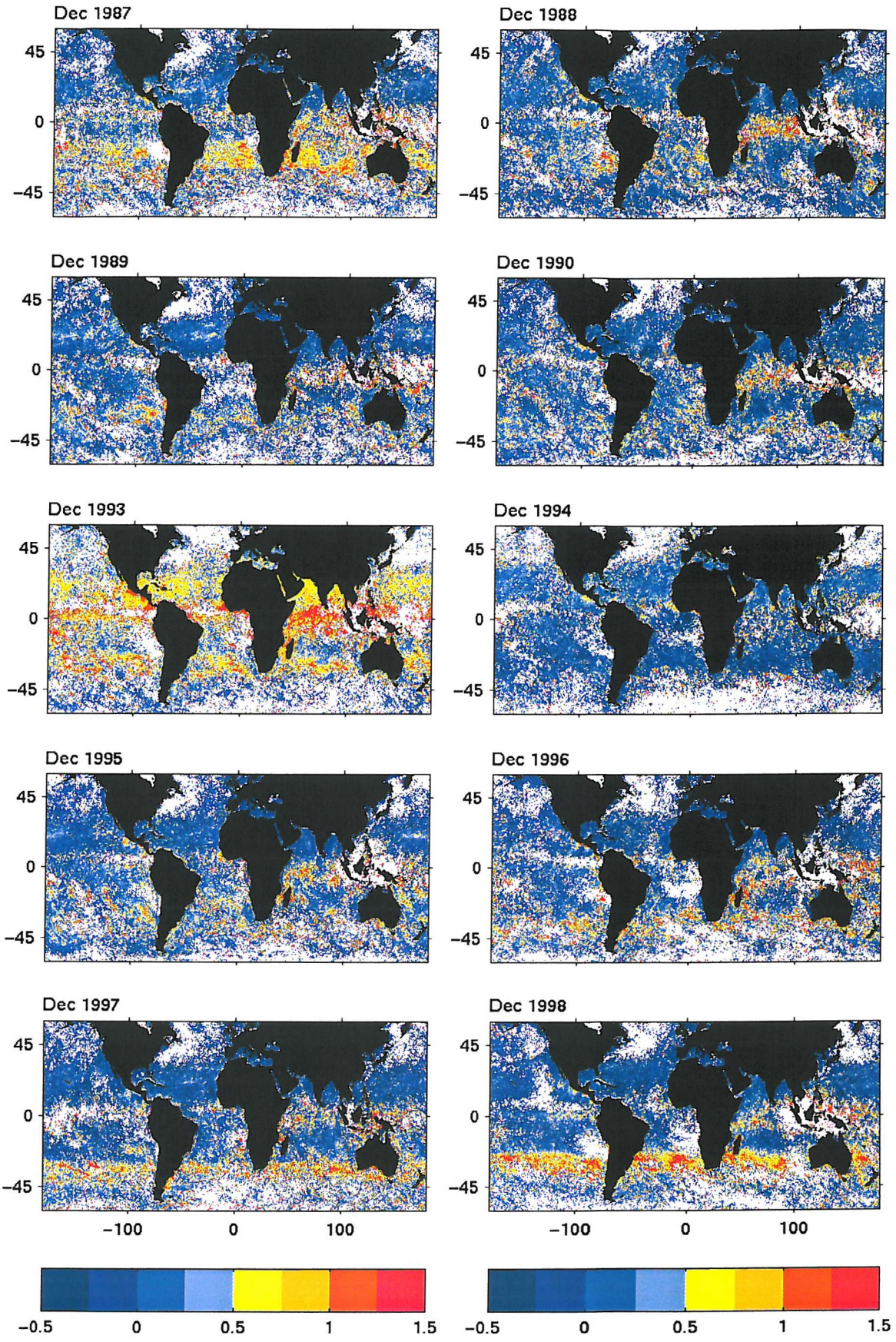

Figure A.12: Monthly mean ΔT for December computed from daily AVHRR SST data (Chapter 3).

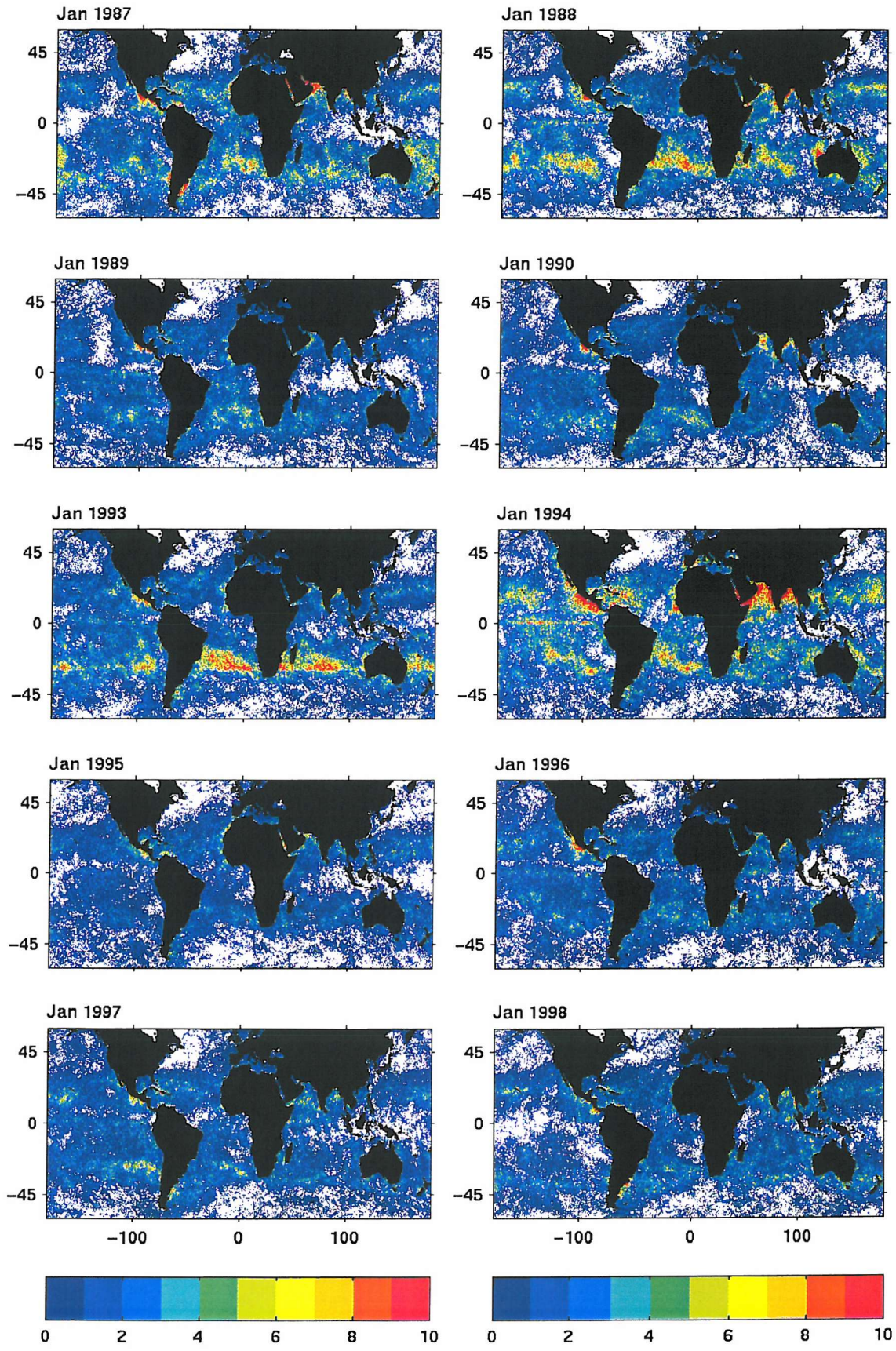

Figure A.13: Number of occurrences (days)/month when $\Delta T \geq 0.5$°C for January, computed from daily AVHRR SST data (Chapter 3).

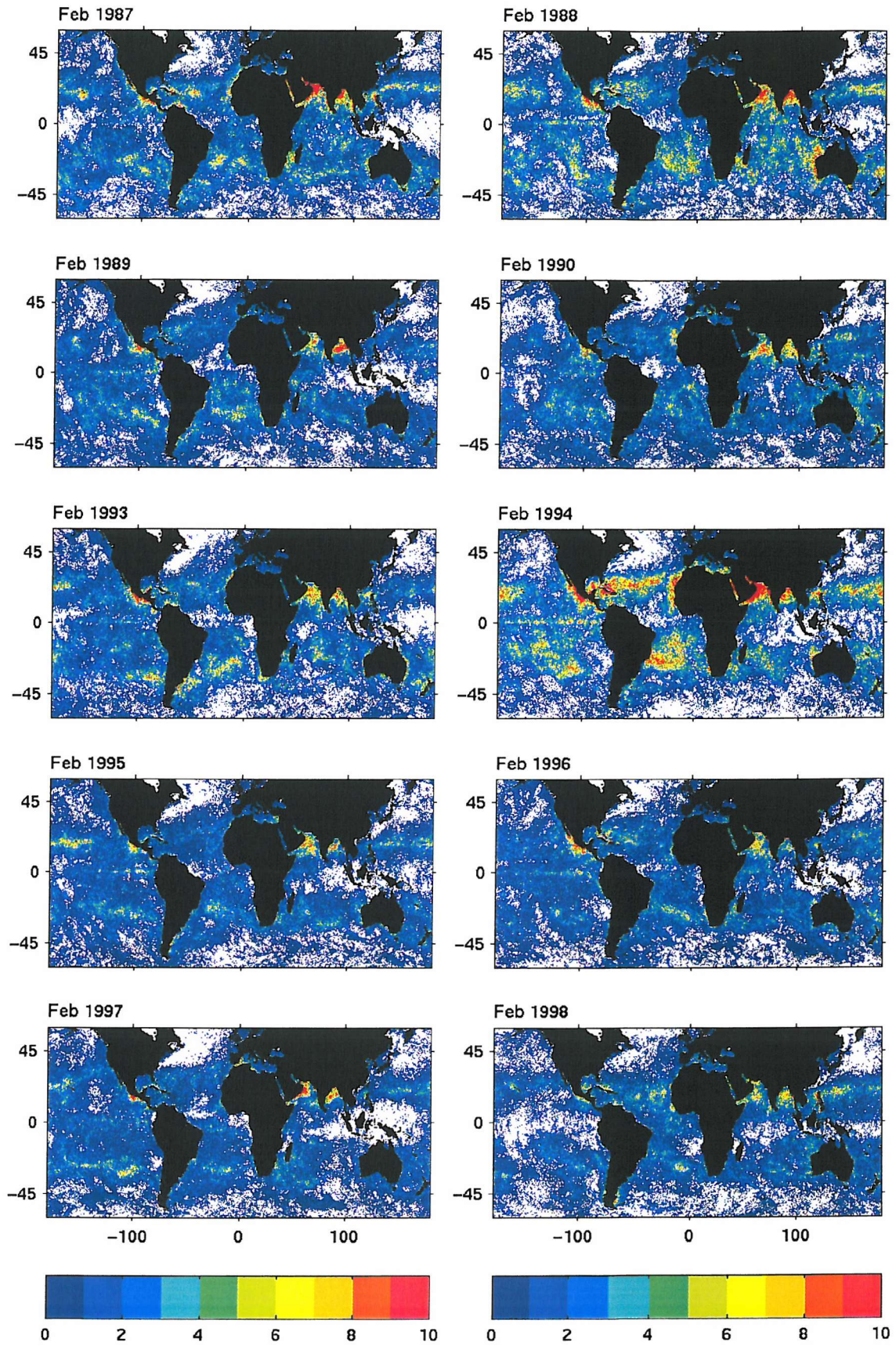

Figure A.14: Number of occurrences (days)/month when $\Delta T \geq 0.5$°C for February, computed from daily AVHRR SST data (Chapter 3).

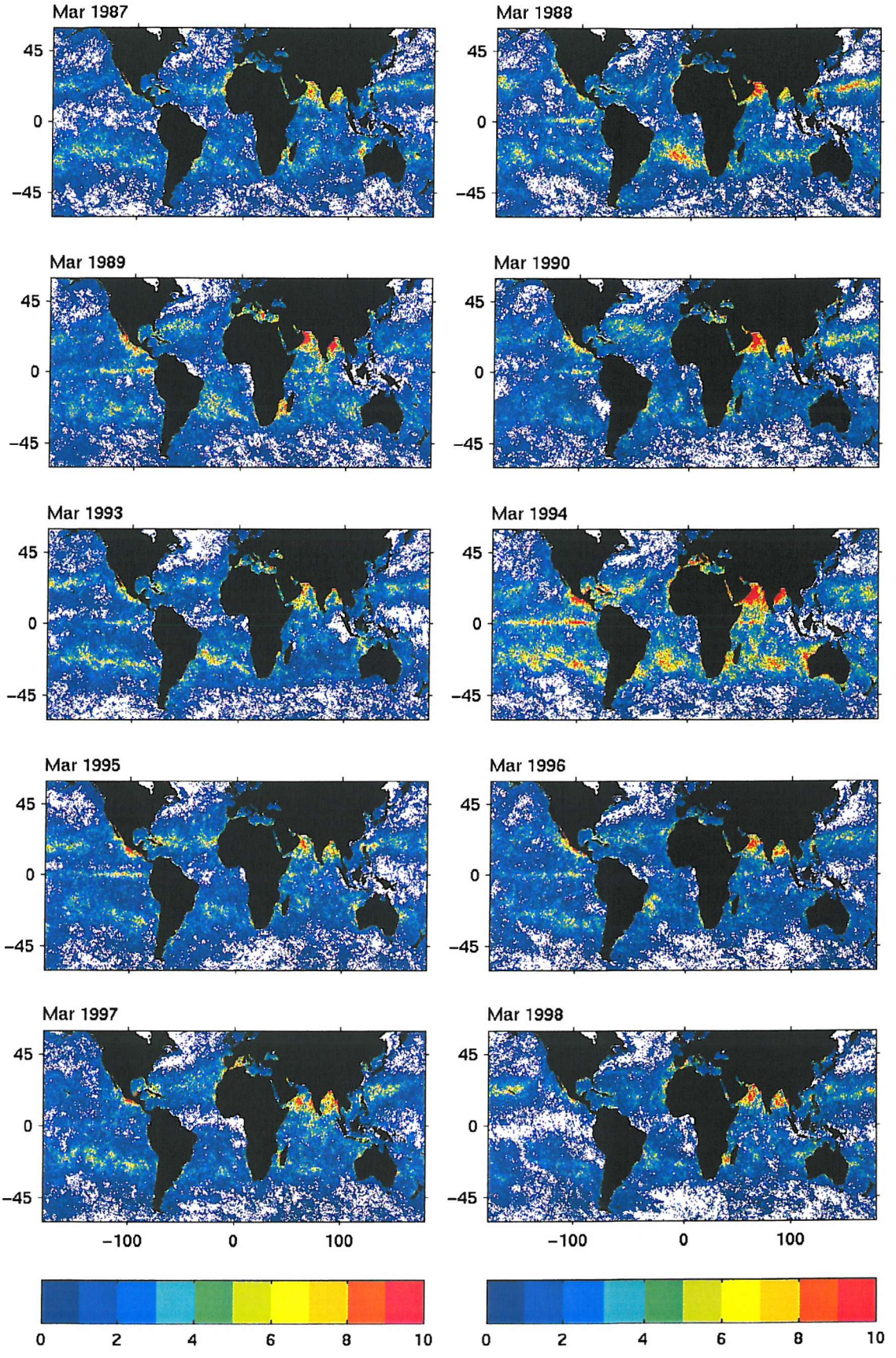

Figure A.15: Number of occurrences (days)/month when $\Delta T \geq 0.5$°C for March, computed from daily AVHRR SST data (Chapter 3).

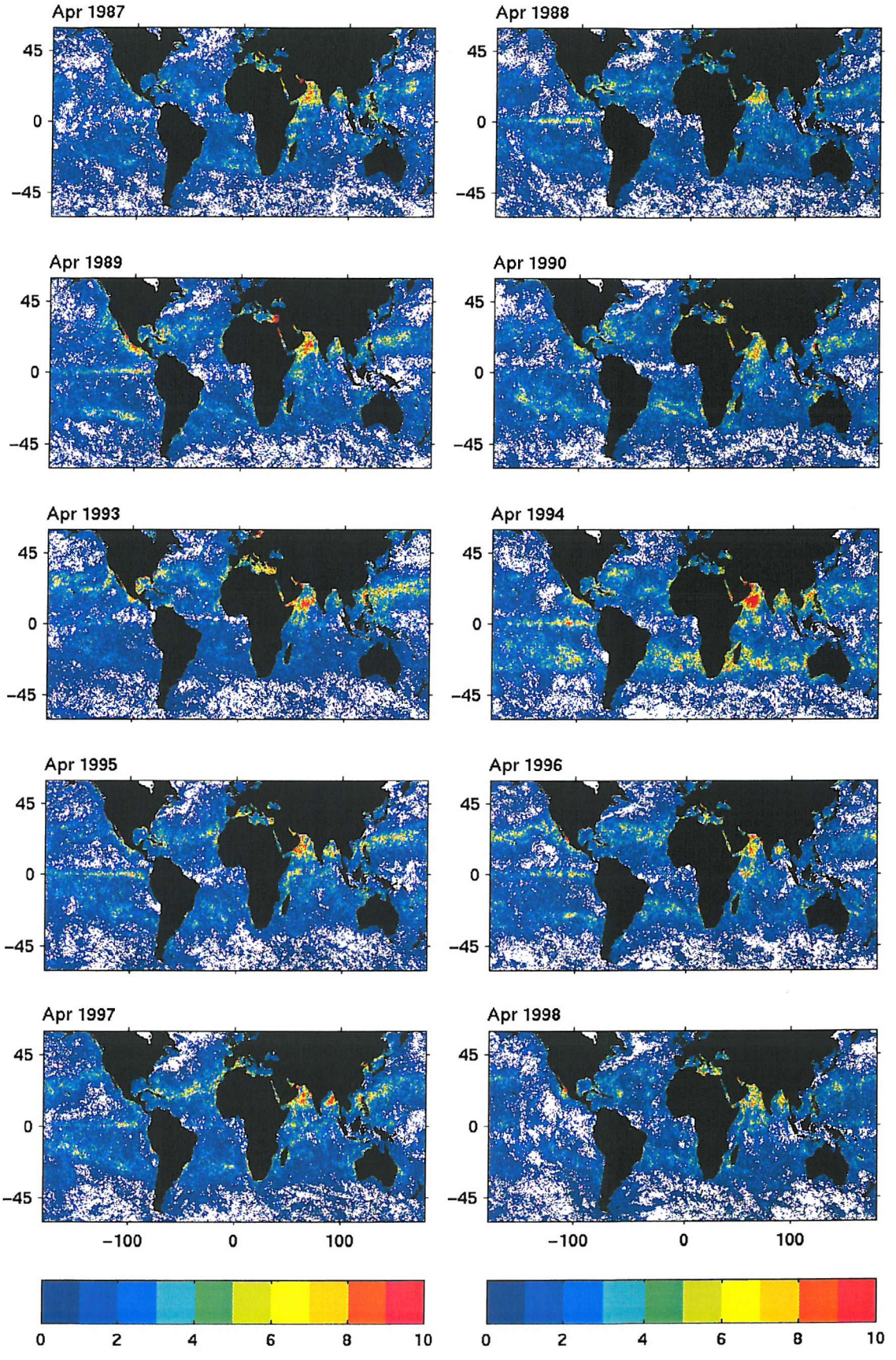

Figure A.16: Number of occurrences (days)/month when $\Delta T \geq 0.5$°C for April, computed from daily AVHRR SST data (Chapter 3).

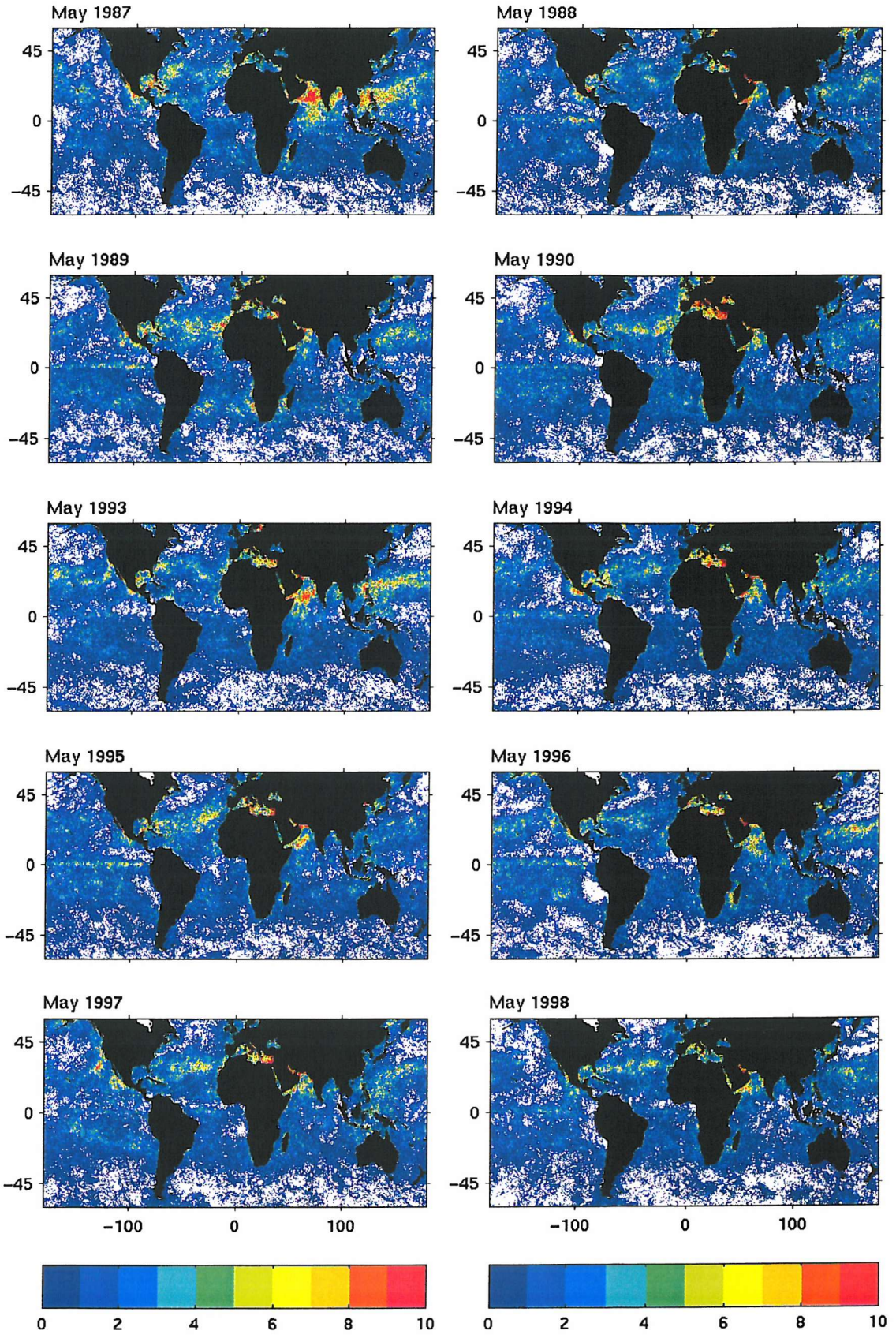

Figure A.17: Number of occurrences (days)/month when $\Delta T \geq 0.5$°C for May, computed from daily AVHRR SST data (Chapter 3).

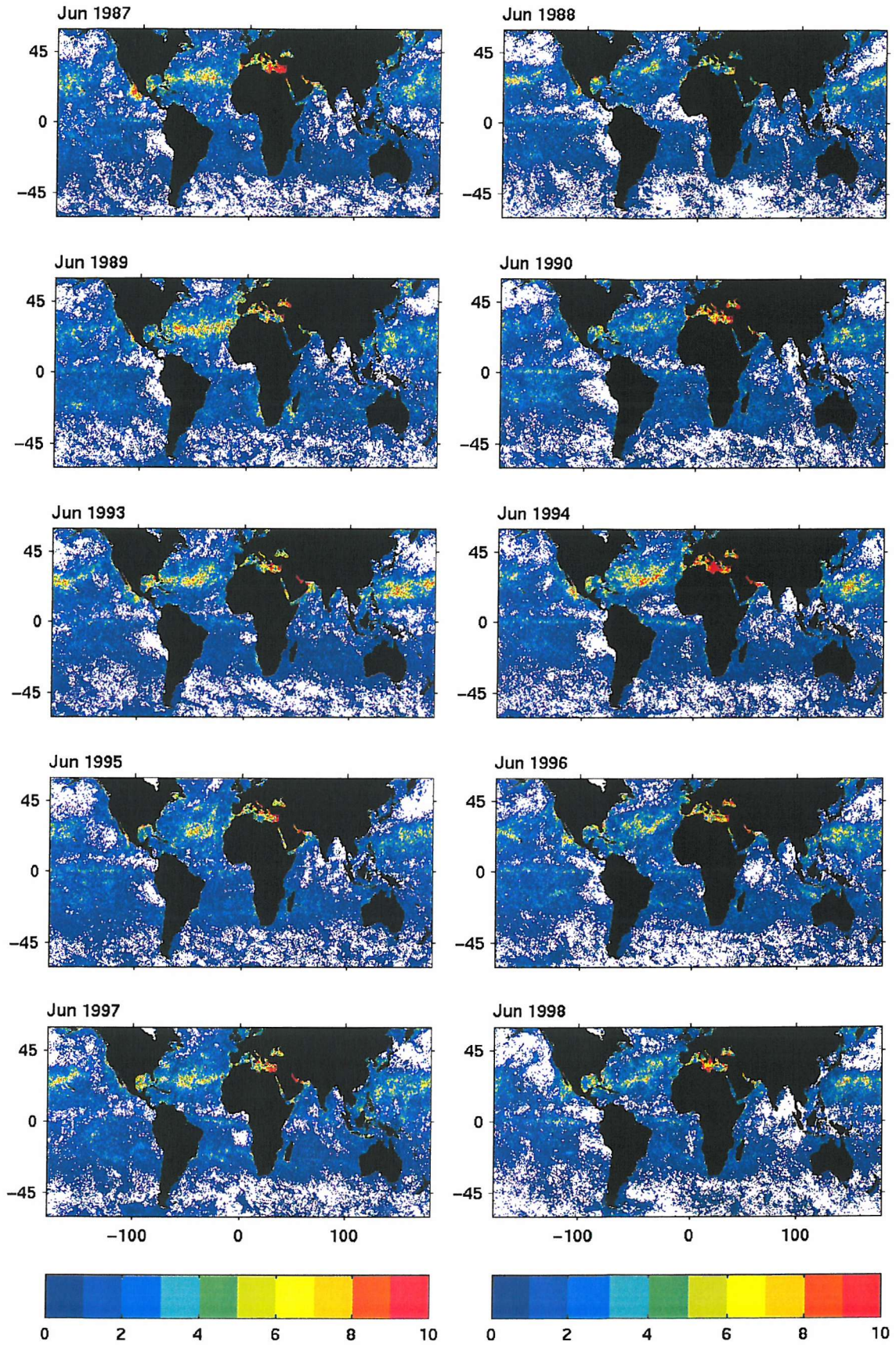

Figure A.18: Number of occurrences (days)/month when $\Delta T \geq 0.5°C$ for June, computed from daily AVHRR SST data (Chapter 3).

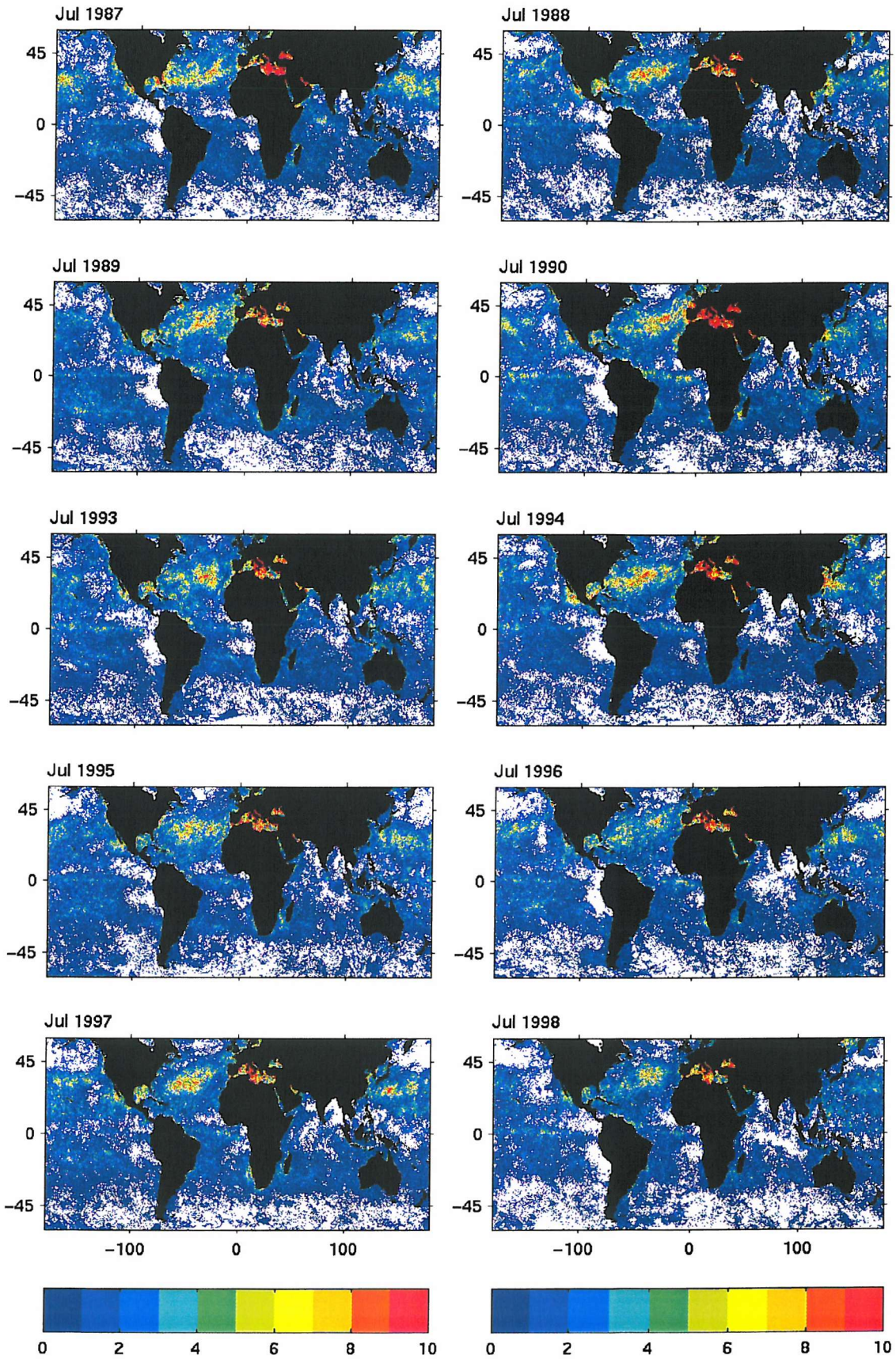

Figure A.19: Number of occurrences (days)/month when $\Delta T \geq 0.5°C$ for July, computed from daily AVHRR SST data (Chapter 3).

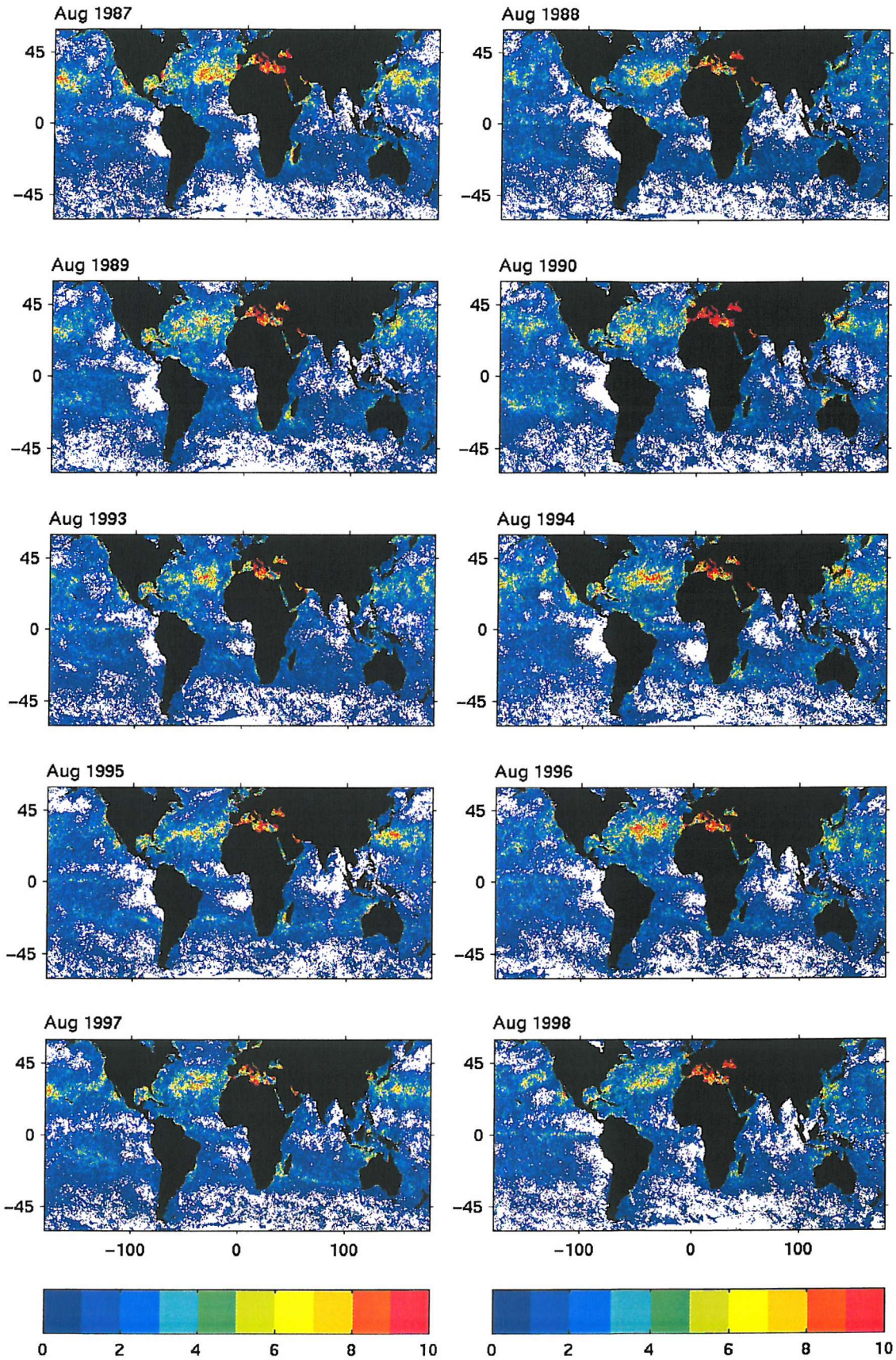

Figure A.20: Number of occurrences (days)/month when $\Delta T \geq 0.5°C$ for August, computed from daily AVHRR SST data (Chapter 3).

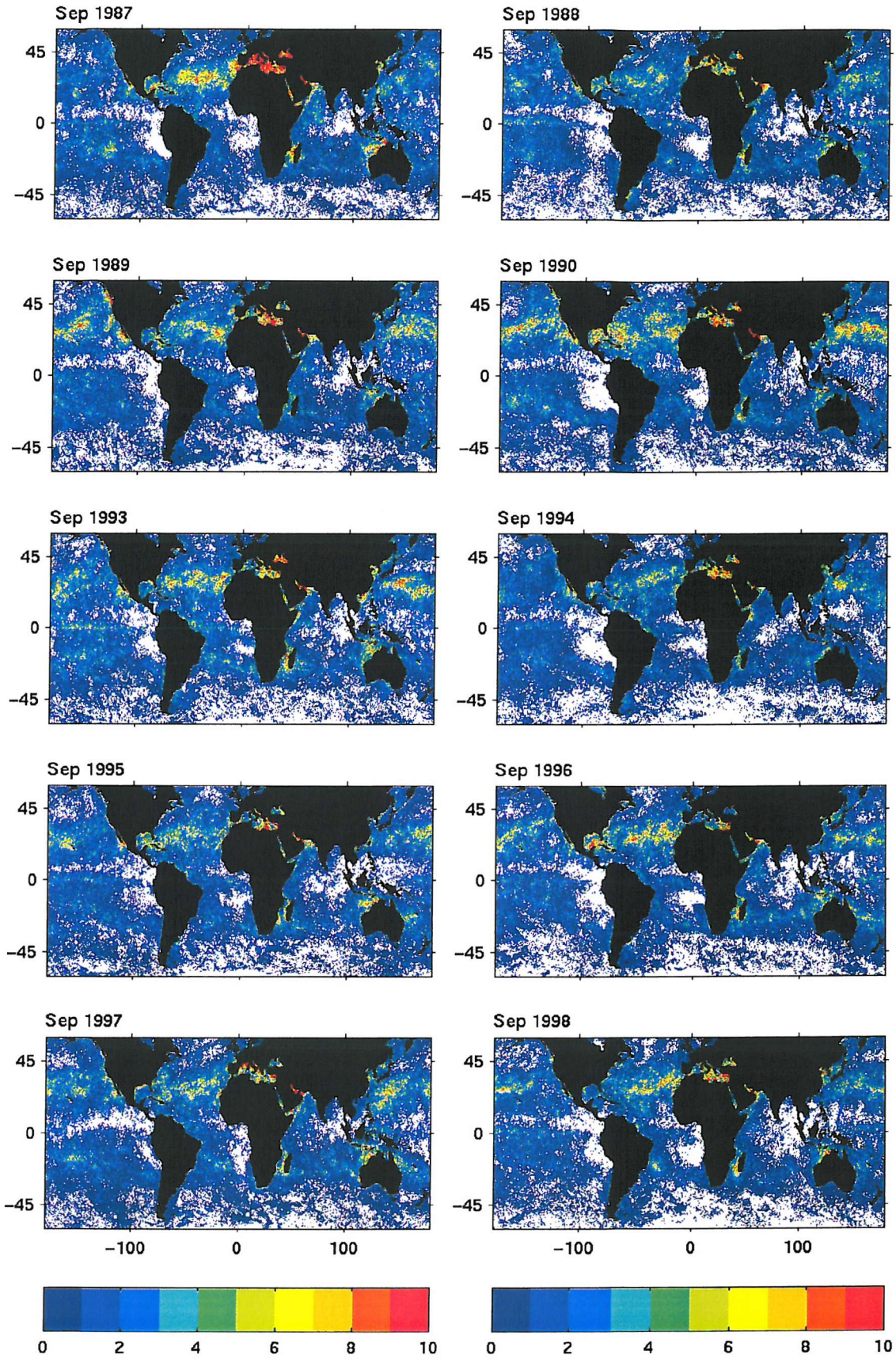

Figure A.21: Number of occurrences (days)/month when $\Delta T \geq 0.5$°C for September, computed from daily AVHRR SST data (Chapter 3).

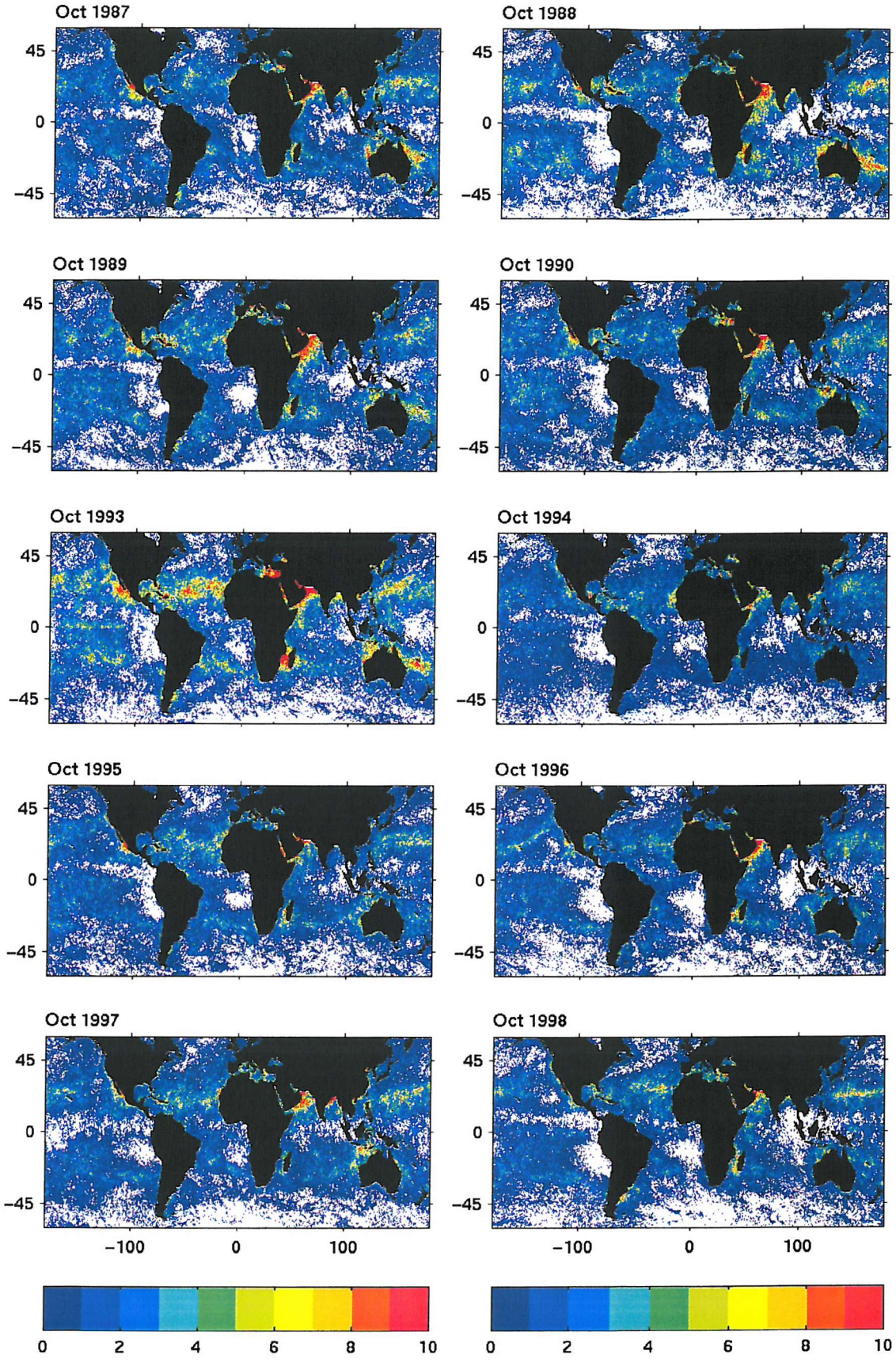

Figure A.22: Number of occurrences (days)/month when $\Delta T \geq 0.5$°C for October, computed from daily AVHRR SST data (Chapter 3).

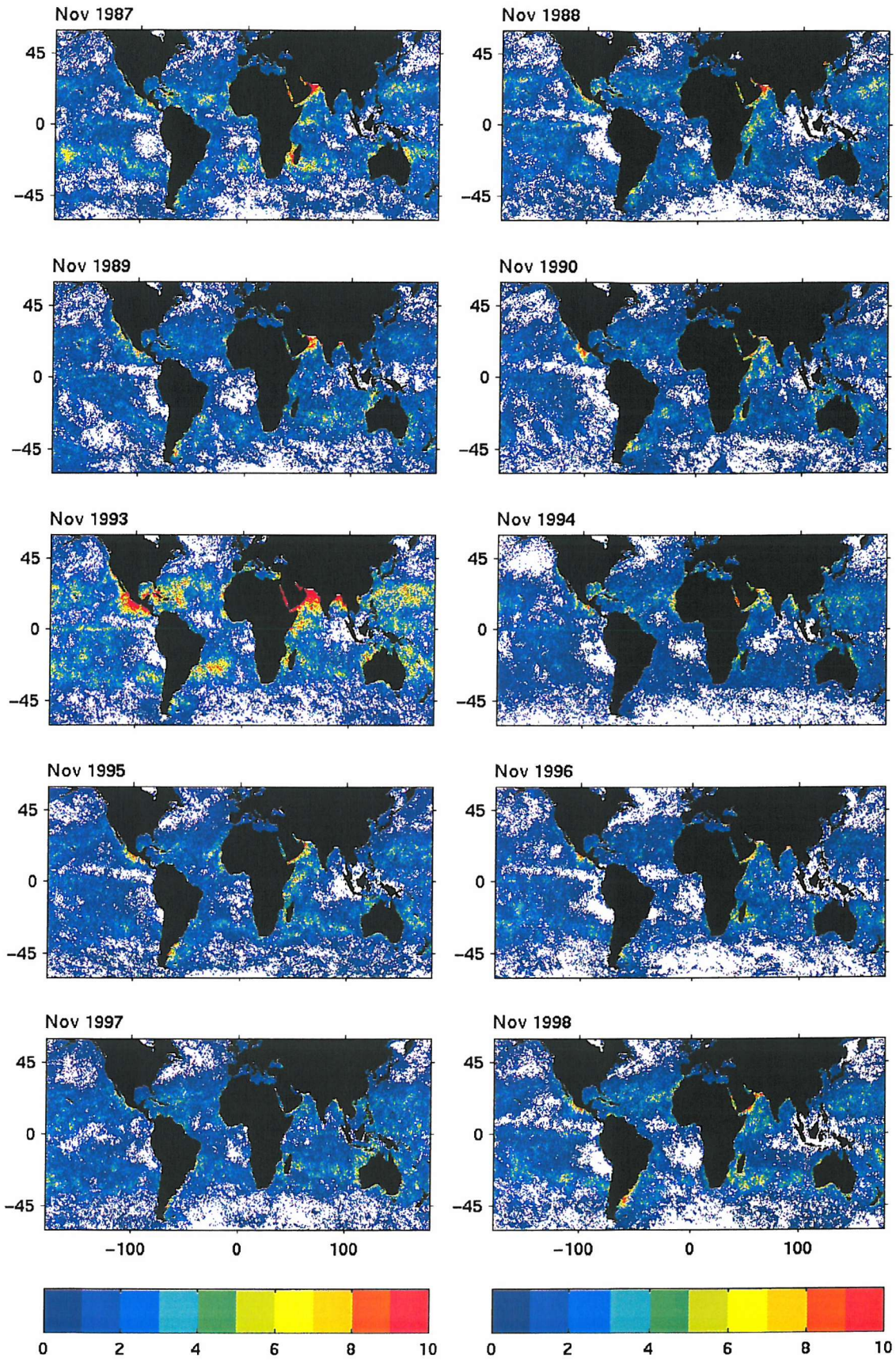

Figure A.23: Number of occurrences (days)/month when $\Delta T \geq 0.5$°C for November, computed from daily AVHRR SST data (Chapter 3).

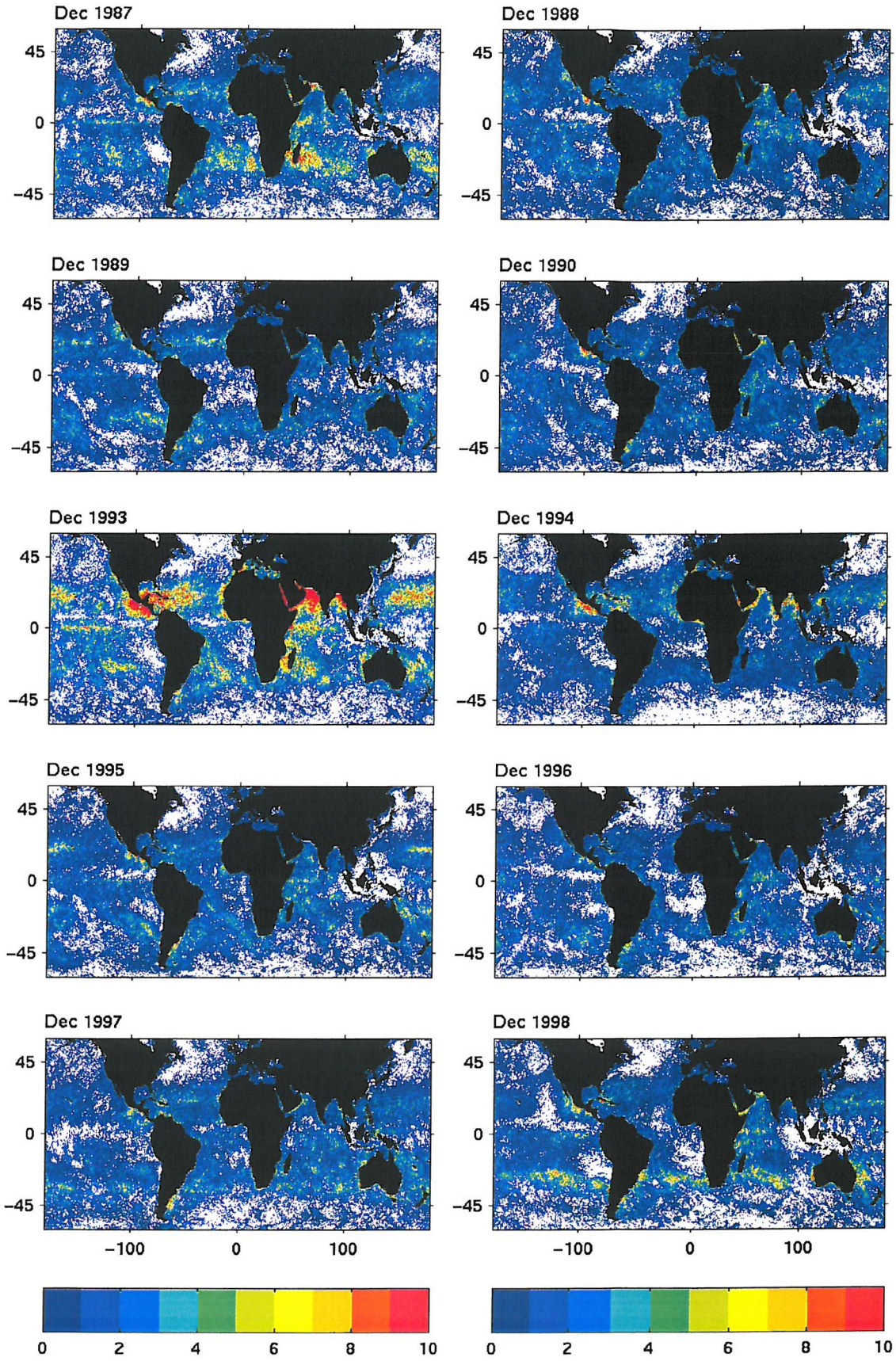

Figure A.24: Number of occurrences (days)/month when $\Delta T \geq 0.5°C$ for December, computed from daily AVHRR SST data (Chapter 3).

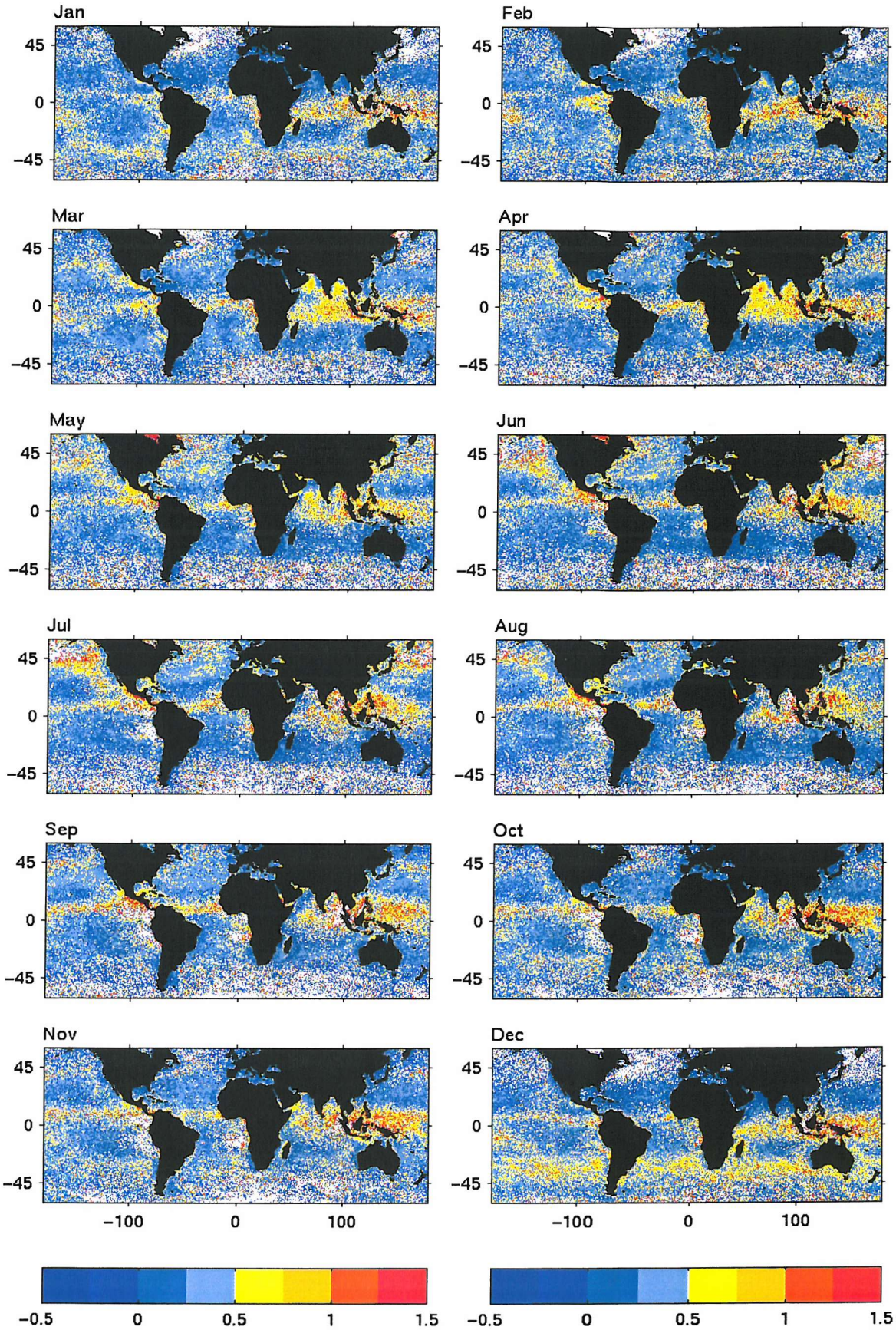

Figure B.1: Climatological ΔT maps from 6 years of AVHRR Pathfinder data.

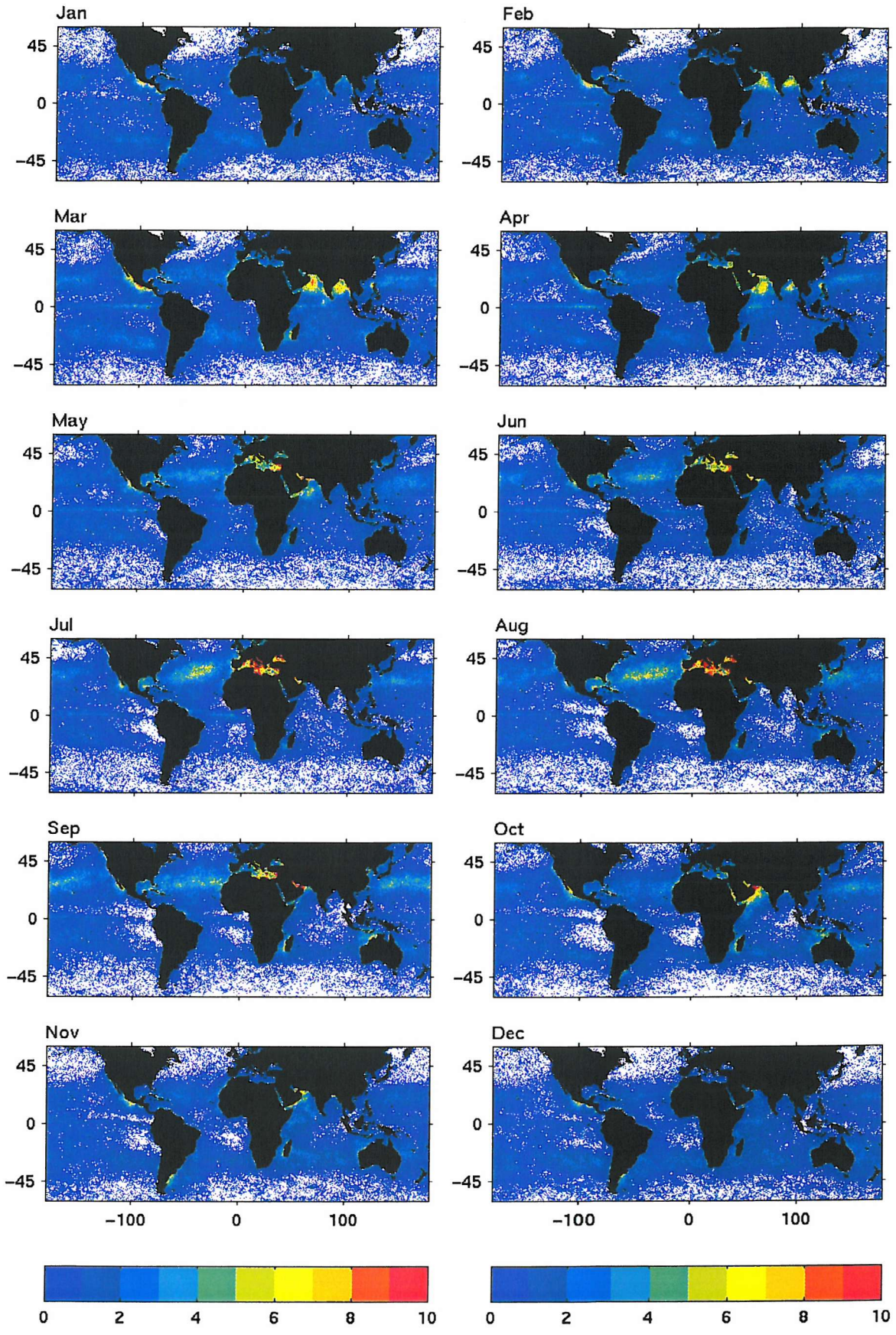

Figure B.2: Climatological diurnal warming frequency maps from 6 years of AVHRR Pathfinder data. Frequency = no. days / month $\Delta T \geq 0.5°C$.

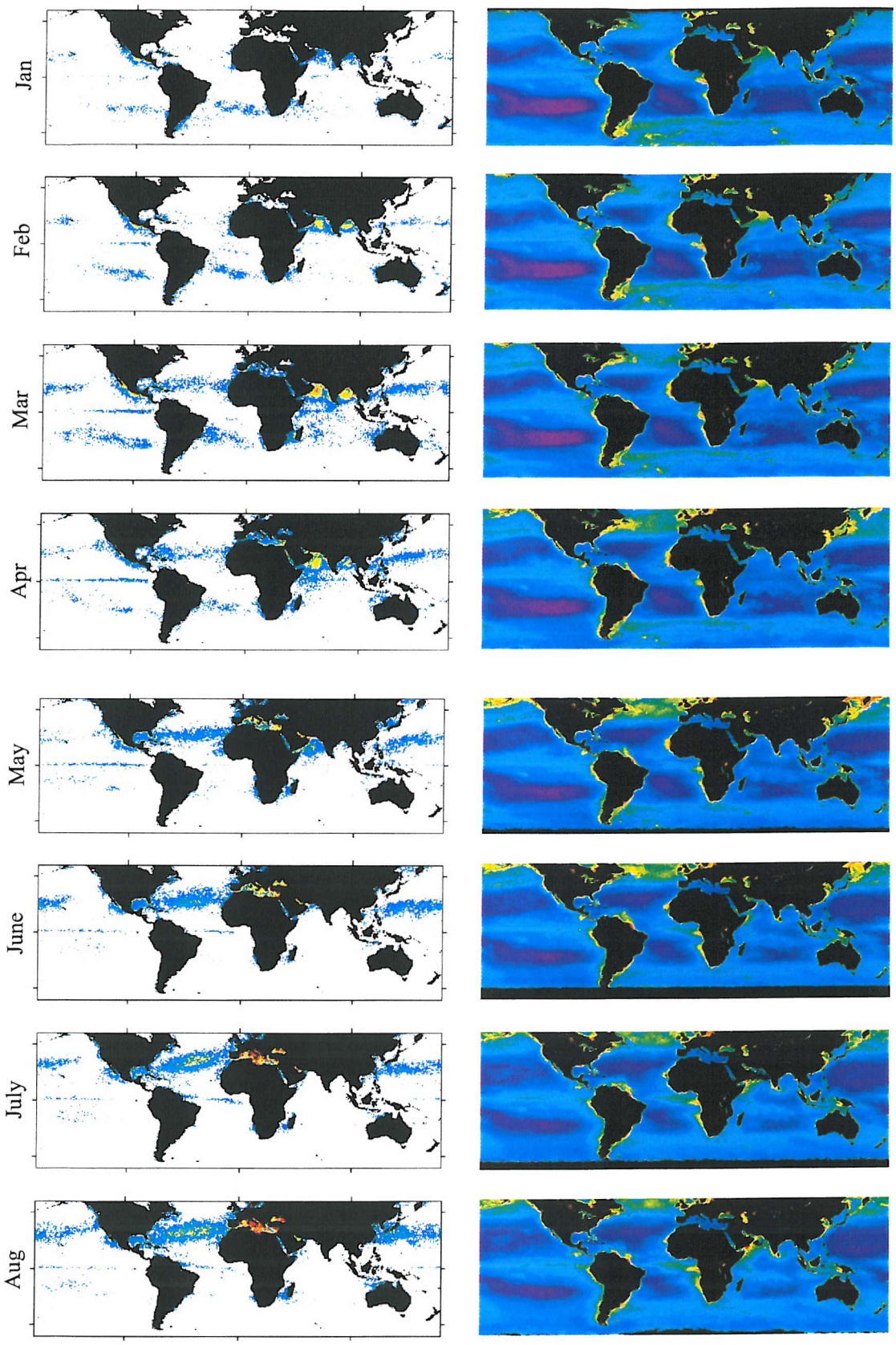

Figure C: Monthly climatological $\Delta T_{(day\text{-}night)}$ from Stuart-Menteth et al. (2003) and climatological SeaWiFS chlorophyll maps (http://seawifs.gsfc.nasa.gov/cgi/monthly_climatologies.pl)

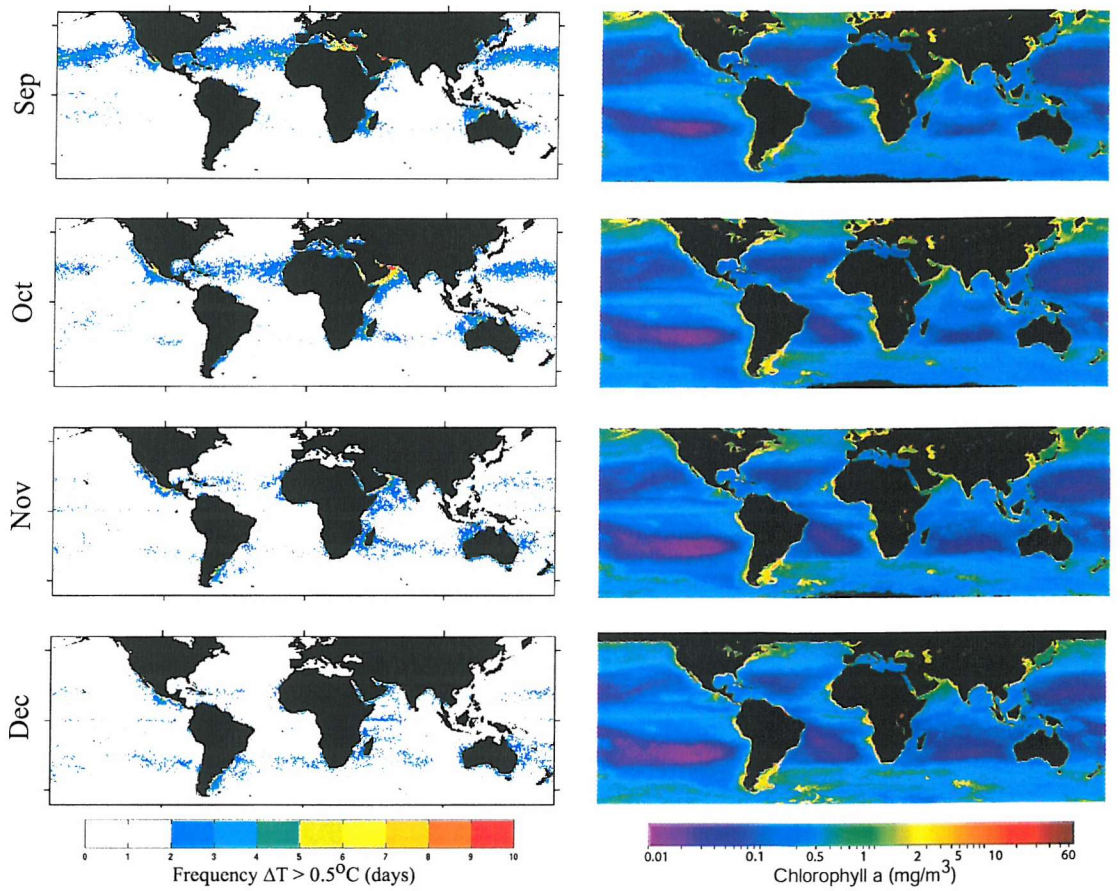

Figure C continued: Monthly climatological $\Delta T_{(day\text{-}night)}$ from Stuart-Menteth et al. (2003) and climatological SeaWiFS chlorophyll maps (http://seawifs.gsfc.nasa.gov/cgi/monthly_climatologies.pl)

```
%%%%%%%%%%%%%%%%%%%%%%%%%%%%%%%%%%%%%%%%%%%%%%%%%%%%%%%%%%%%%%%%%%%%%%%%%%%%%%%
%%%%%%%%%%%%%%%%%%%%%%%%
% Stuartmenteth_paramv2.m
% Version 2 (19/2/2004)
%
% Matlab code written by Alice Stuart-Menteth
%****
%
% This routine estimates the shape (phase and magnitude) of the
% diurnal SST cycle for 1m and subskin using only wind and insolation
% measurements from different times of the day.
%
% Required INPUTS:
% dt = time step of parameterisation (hrs)
% wind and insolation measurements to compute
%
% 1. tu06: mean(wind 0-6h) or point measurement in time period
% 2. tu812: mean(wind 8-12h) or point measurement in time period
% 3. tu1215: mean(wind 12-15h) or point measurement in time period
% 4. tu1624: mean(wind 16h-24h) or point measurement in time period
% 5. tq612: mean(qsw 6h-12h)
% 6. tq1218: mean(qsw 12h-18h)
%
% 6 models derived:
%  i)   cgrad (morning cooling gradient K/hr)
%  ii)  tmin (time of daily min SST DV=0)
%  iii) dt1s & dt11m (SST12h-SSTmin for sub-skin and 1m)
%  iv)  tmaxs & tmax1m (time of daily maximum SST for sub-skin and 1m)
%  v)   dt2s & dt21m (SSTmax-SST12 for sub-skin and 1m)
%  vi)  dt3 (SST24-SSTmin)
%
% OUTPUT:
% msub - sub-skin model of diurnal SST variation referenced from time
% of minimum SST where msub=0;
% m1m  - 1m model of diurnal SST variation referenced from time of
% minimum SST where m1m=msub=0;
%
%%%%%%%%%%%%%%%%%%%%%%%%%%%%%%%%%%%%%%%%%%%%%%%%%%%%%%%%%%%%%%%%%%%%%%%%%%%%%%%
%%%%%%%%%%%%%%%%%%%%%%%%%%%%


%%%%%%%%%%%%%%%%%%%%%%%%%%%%%%%%%%%
%**INPUTS to be defined
% Time step of model (hrs) - can be altered to suit user requirements
dts=.25;

% wind and insolation (tu06, tu812, tu1216, tu1624, tq612, tq1218)
% insert files
%%%%%%%%%%%%%%%%%%%%%%%%%%%%%%%%%%%


%%% START OF MODEL
%%%%%%%%%%%%%%%%%%%%%%%%%%%%%%%%%%%%%%%%%%%%%%%%%%%%%%%%%%%%%%%%%%%%%%%%%%%%%%%
% Defining key constants
time=0.25:dts:24;
ii=length(time); %no. times steps over 24 hrs
jj=length(tu812);%no. days in data set

h24=ii; %Time step at 24hrs
h12=ii/2; %Time step at 12hrs
h17=17/24*ii; %Time step at 17hrs
```

```
m1m=NaN*ones(jj,ii);
msub=NaN*ones(jj,ii);


%*** TIME 1 - 00:00 to Tmin (morning cooling)
*****************************

%------- computing cgrad (morning cooling gradient)
c1=[0.0034 0.0486];
cgrad=c1(1)+c1(2).*exp(-0.3.*tu06);
neg=find(cgrad<0); cgrad(neg)=0; neg=[];
%-----------------------------------------------------------------

%------- computing tmin (time of daily minimum SST)
c2=[6.4724 0.1766];
tmin=c2(1)+c2(2).*log(tu812);

%finding nearest time point to tmin
tt=floor(tmin*h24/24); %tmin=tt*dt;
%-----------------------------------------------------------------

%------- computing curve 1
for i=1:jj;
    t=tt(i);pmt1=time(1:t);
    m1m(i,1:t)=(cgrad(i).*tmin(i)).*((pmt1-tmin(i)).^2)./
               (((0-tmin(i)).^2));
    msub(i,1:t)=m1m(i,1:t);pmt1=[];
end
%-----------------------------------------------------------------
%*** End of Time 1
*********************************************************



%*** TIME 2 (morning heating)
*********************************************

%------- computing dt1 (computing morning heating)
limit=find(tu812<0.5);tu812(limit)=0.5;
c3=[0.009 6.3071 0.0022 0.00018 0.0114];
dt1s=c3(1)+c3(2).*exp(-(600./tq612).*tu812)+c3(3).*tq612./tu812;
dt11m=dt1s;

% if top metre stratified in morning
%(1m different from sub-skin, re-compute 1m)
strat_am=find(tu812<((tq612.*0.0064)+1.2));

if(isempty(strat_am)==0)
    ustr=(tq612(strat_am).*0.0064)+1.2;
    dt11m(strat_am)=c3(1)+c3(2).*exp(-ustr.*(600./tq612(strat_am)))
      +c3(3).*(tq612(strat_am)./ustr)+(((c3(4).*tq612(strat_am))+
      c3(5)).*(ustr-tu812(strat_am)));
end
%-----------------------------------------------------------------

%------- computing curve 2
for i=1:jj; pmt2=time(tt(i):h12);
    msub(i,tt(i):h12)=(dt1s(i)./((12-tmin(i)).^2)).*((pmt2-
    tmin(i)).^2);
    m1m(i,tt(i):h12)=(dt11m(i)./((12-tmin(i)).^2)).*((pmt2-
    tmin(i)).^2);
```

```
end
%-----------------------------------------------------------------
%*** End of Time 2
*********************************************************



%*** TIME 3 - 12:00 to 17:00 (afternoon heating)
*****************************

%------- computing tmax (time of daily maximum SST)
c4=[13.0157 -1.9736 2.2835 0.0042 -0.002];
tmaxs=c4(1)+c4(2).*log(tu1215)+c4(3).*log(tu812)+c4(4).*tq1218+c4(5).*
tq612;
tmax1m=tmaxs;

% if top metre stratified in morning
%(1m different from sub-skin, re-compute 1m)
if(isempty(strat_am)==0)
 c4b=[15.75 -1.9109 .8754 0.0035 -0.0027];
 tmax1m(strat_am)=c4b(1)+c4b(2).*log(tu1215(strat_am))+c4b(3).*
log(tu812(strat_am))+c4b(4).*tq1218(strat_am)+c4b(5).*tq612(strat_am);
end

mxt=floor(tmaxs*h24/24); % time step at sub-skin tmax
mxt1=floor(tmax1m*h24/24); % time step at 1m tmax
%-----------------------------------------------------------------


%------- computing dt2 & dt
%(afternoon heating and total diurnal SST amplitude)
limit=find(tu1215<0.5);tu1215(limit)=0.5;
c5=[-0.0541 2.057 0.002];

dt2s=c5(1)+c5(2).*exp(-(600./tq1218).*tu1215) +c5(3).*tq1218./tu1215;
dt21m=dt2s;

% if top metre stratified in afternoon
%(1m different from sub-skin, re-compute 1m)
strat_pm=find(tu1215<2);
if(isempty(strat_pm)==0)
    dt21m(strat_pm)=c5(1)+c5(2).*exp(-(600./tq1218(strat_pm)).*2)
    +c5(3).*tq1218(strat_pm)./2;
end

% if wind in afternoon breaks down strong morning stratification
break_strat=find(tu812<2.5 & (tu1215-tu812)>.7);dt2s(break_strat)=0.1;

%to keep realistic shape (rarely needed)
neg=find(dt2s<0.05);  dt2s(neg)=0.05; neg=[];
neg=find(dt21m<0.05);  dt21m(neg)=0.05; neg=[];

%computing daily maximum diurnal warming amplitude
dts=dt1s+dt2s;
dt1m=dt11m+dt21m;
%-----------------------------------------------------------------
```

```
%------- computing curve 3
 h17=h17*ones(1,jj);
 nn=find(tmax1m<14.5); h17(nn)=(round((tmax1m(nn)./24*96))-
      (h12+1))+(round((tmax1m(nn)./24*96)))+1;

 for i=1:jj;
    pmt3=time(h12+1:h17(i));
    m1m(i,h12+1:h17(i))=dt1m(i)-(dt21m(i)./((12-tmax1m(i)).^2)).*
            ((pmt3-tmax1m(i)).^2);
    msub(i,h12+1:h17(i))=dts(i)-(dt2s(i)./((12-tmaxs(i)).^2)).*
            ((pmt3-tmaxs(i)).^2);

    %to keep realistic shape (rarely needed)
    negs=find(m1m(i,h12+1:h17(i))<0); m1m(i,negs+h12)=0;
    negs=find(msub(i,h12+1:h17(i))<0); msub(i,negs+h12)=0;
end


% considering days with slight increase in wind in pm
%(reduces sub-skin and increases 1m)
if(isempty(break_strat)==0)
  for i=1:length(break_strat);

     if (tu812(break_strat(i))<2 & tq612(break_strat(i))>400)
      pmt3=time(mxt(break_strat(i))+1:mxt1(break_strat(i)));
      msub(break_strat(i),mxt(break_strat(i))+1:mxt1(break_strat(i)))=
      dt1m(break_strat(i))+((dts(break_strat(i))-
      dt1m(break_strat(i))).(tmax1m(break_strat(i))-
      tmaxs(break_strat(i))).^2.*(pmt3-tmax1m(break_strat(i))).^2);

      msub(break_strat(i),mxt1(break_strat(i))+1:h17(break_strat(i)))=
      m1m(break_strat(i),mxt1(break_strat(i))+1:h17(break_strat(i)));
     end

  end
end
%-----------------------------------------------------------------

%-----------------------------------------------------------------
%** making sub-skin join 1m curve during afternoon cooling
%** if sub-skin DV < 1m DV, sub-skin = 1m
for j=1:jj; k=0;ty=mxt((j));join(j)=0;
    for i=ty:h17(j); g=msub((j),i)-m1m((j),i);
        if g<0; k=k+1; if(k==1); join(j)=i;end;end;
    end;

    if(join(j)>0 & join(j)<68)
      msub(j,join(j):h17(j))=m1m(j,join(j):h17(j));
      dg=(msub(j,join(j)-1)-msub(j,join(j)+1))./2;
      msub(j,join(j))=msub(j,join(j)-1)-dg;
    end
end
%-----------------------------------------------------------
%*** End of Time
3*********************************************************
```

```
%*** TIME 4 - 17:00 to 24:00 (night-time cooling)
*************************

%------- computing dt3 (dt(24hr-tmin))
c6=[0.1365 0.209 -0.017];
dt31m=c6(1)+c6(2).*(dt1m)+c6(3).*tu1624;
neg=find(dt31m<0); dt31m(neg)=0;
dt3s=dt31m;
%-------------------------------------------------------------

%------- computing curve 4
for i=1:jj;
   pmt4=time(h17(i):h24);

   coamp(i)=m1m(i,h17(i))-dt31m(i)'; %1m
   % to keep realistic shape at high winds
   if(coamp(i)<0); coamp(i)=m1m(i,h17(i));dt31m(i)=0; dt3s(i)=0;end

   scoamp(i)=msub(i,h17(i))-dt3s(i)'; %sub-skin
   % to keep realistic shape at high winds
   if(scoamp<0); ;scoamp(i)=msub(i,h17(i));dt3s(i)=0; end

   m1m(i,h17(i):h24)=dt31m(i)+coamp(i)'./(((24-time(h17(i))).^2)).*
            ((pmt4-24).^2);
   msub(i,h17(i):h24)=dt3s(i)+scoamp(i)'./(((24-time(h17(i))).^2)).*
            ((pmt4-24).^2);

end
%-------------------------------------------------------------------
%*******************************************************************
*******


%********** optional tidying up
% smoothing joins between curves 2 & 3 and curves 3 & 4
dg=(m1m(:,h12+1)-m1m(:,h12-1))./2;
m1m(:,h12)=m1m(:,h12+1)-dg;
m1m(:,h12-1)=m1m(:,h12+1)-dg.*2;dg=[];
dg=(msub(:,h12+1)-msub(:,h12-1))./2;
msub(:,h12)=msub(:,h12+1)-dg;
msub(:,h12-1)=msub(:,h12+1)-dg.*2;

dg=[];dg=(m1m(:,h17-1)-m1m(:,h17+1))./2;
m1m(:,h17)=m1m(:,h17-1)-dg;
m1m(:,h17+1)=m1m(:,h17-1)-dg*2;
dg=[];dg=(msub(:,h17-1)-msub(:,h17+1))./2;
msub(:,h17)=msub(:,h17-1)-dg;
msub(:,h17+1)=msub(:,h17-1)-dg*2;
%*****************************


%%%%%%%%% END OF MODEL
%%%%%%%%%%%%%%%%%%%%%%%%%%%%%%%%%%%%%%%%%%%%%%%%%%%%%%%%%%%%%%%%%
```

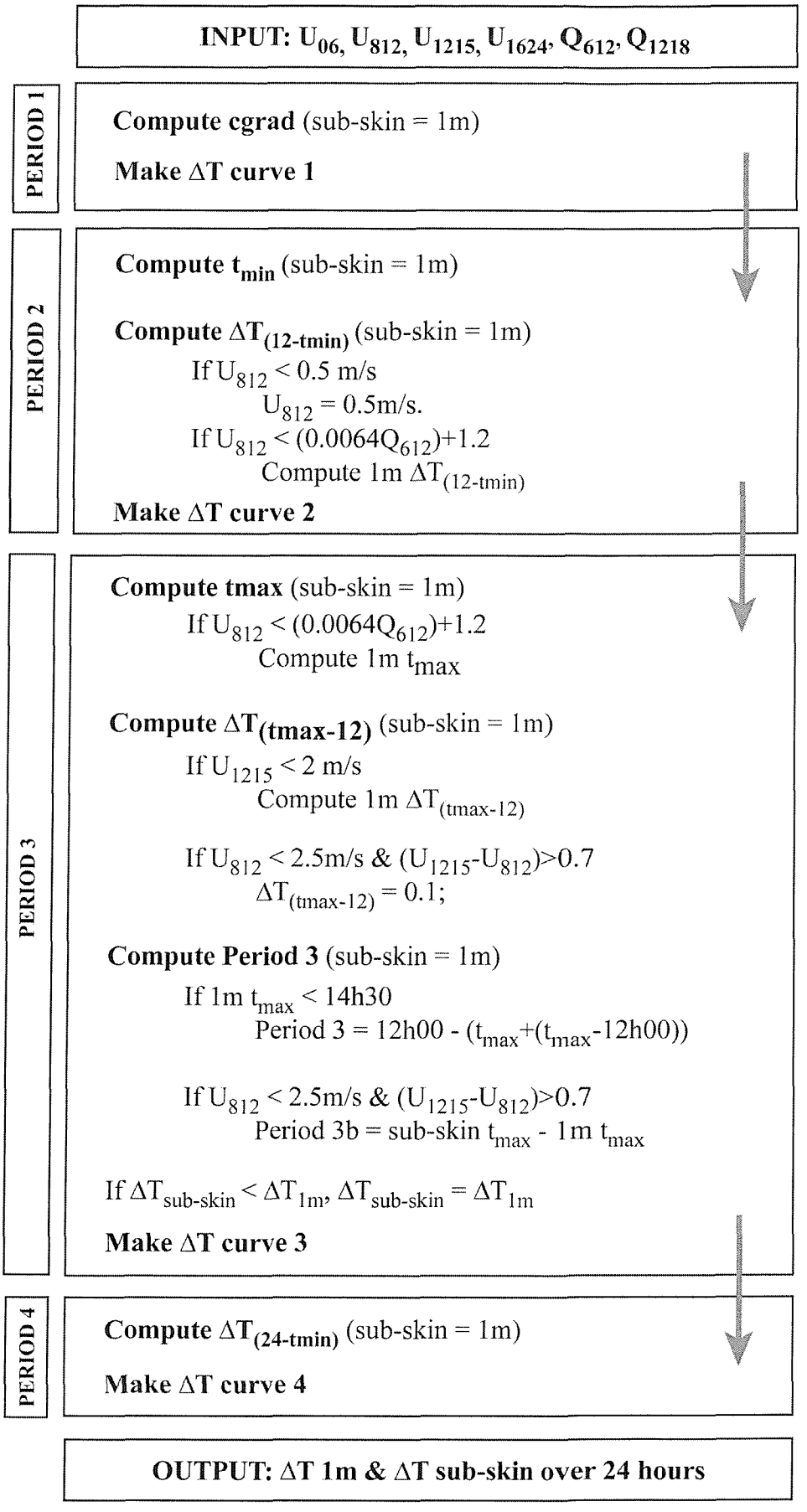

Appendix D: Flow diagram of diurnal warming parameterisation

REFERENCE LIST

Ajoy, K., P. Minnett, G. Podesta, R. Evans & K. Kilpatrick, Analysis of Pathfinder SST algorithm for global and regional conditions, *Proc. Indian Acad. Sci.*, **109**, 395-405, 2000.

Allen, M., Mutlow, C. T., Blumberg, G. M. C., Christy, J. R., McNider, R. T. and Llewellyn-Jones, D. T., Global change detection, *Nature*, **370**, 24-25, 1994.

Anderson, S. P., R. A. Weller & R. B. Lukas, Surface buoyancy forcing and the mixed layer of the western Pacific warm pool: observations and 1D model results, *J. Climate*, **9**, 3065-3085, 1996.

Bernie, D. J., S. J. Woolnough, J. M. Slingo & E. Guilyardi, Modelling diurnal and intraseasonal variability of the ocean mixed layer, submitted *J. Climate*, 2003.

Bohm, E., S. Marullo, & R. Santoleri, AVHRR detection of diurnal warming events in western Mediterranean Sea, *Int. J. Rem. Sens.*, **12**, 695-701, 1991.

Brown, O. B., J. W. Brown & R. H. Evans, Calibration of the Advanced Very High Resolution Radiometer infrared observations, *J. Geophys. Res.*, **90**, 11667-11678, 1985.

Cao, C., M. Weinreb & J. Sullivan, Solar contamination effects on the infrared channels of the Advanced Very High Resolution Radiometer, *J. Geophys. Res.*, **106**, 33,463-33,469, 2001.

Climate Variability & Prediction (CLIVAR) Implementation Plan, http://www.clivar.org/publications/other_pubs/iplan/iip/contents.htm, 1999.

Coppin, P. A., E. F. Bradley, I. J. Barton & J. S. Godfrey, Simultaneous observations of sea surface temperature in the western equatorial Pacific Ocean by bulk, radiative and satellite methods, *J. Geophys. Res.*, **96**, 3401-3409, 1991.

Cornillon, P. & L. Stramma, The distribution of diurnal sea surface warming events in the western Sargasso Sea, *J. Geophys. Res.*, **90**, 11,811-11,815, 1985.

Dai, A. & K. E. Trenberth, The diurnal cycle and its depiction in the Community Climate System Model, *J. Clim.*, **17**, 930-951, 2004.

Defant, A., Physical Oceanography, Volume 1, Pergamon Press, 729 pp, 1961.

Denman, K. L., A time-dependent model of the upper ocean, *J. Phys. Oceanog.*, **3**, 173-184, 1973.

Deschamps, P. Y. & R. Frouin, Large diurnal heating of the sea surface observed by the HCMR experiment, *J. Phys. Oceanog.*, **14**, 177-184, 1984.

Dickey, T. D. & J. J. Simpson, The influence of optical water type on the diurnal response of the upper ocean, *Tellus Ser. B*, **35**, 142-154, 1983.

Dickey, T., J. Marra, D. E. Sigurdson, R. A. Weller, C. S. Kinkade, S. E. Zedler, J. D. Wiggert & C. Langdon, Seasonal variability of bio-optical and physical properties in the Arabian Sea: October 1994-October 1995, *Deep Sea Res.*, Part II, **45**, 2001-2025, 1998.

Donlon, C. J., The GODAE High Resolution Sea Surface Temperature Pilot Project (GHRSST-PP), in *Proceedings of the International Symposium En route to GODAE*, Biarritz, France, 13-15th June, pp55-60, 2002a.

Donlon, C. J., P. J. Minnett, C. Gentemann, T. Nightingale, I, Barton, B. Ward & J. Murray, Towards improved validation of satellite sea surface skin temperature measurements for climate research, *J. Clim.*, **15**, 353-369, 2002b.

Donlon, C. J., The GODAE High Resolution Sea Surface Temperature – Pilot Project Development & Integration Plan, (available from GHRSST-PP Project Office, UK Met. Office), 2004a.

Donlon, C. J., The GODAE High Resolution Sea Surface Temperature – Pilot Project Data Specification Document, (available from GHRSST-PP Project Office, UK Met. Office), 2004b.

Emery, W. J., D. J. Baldwin, P. Schlussel & R. W. Reynolds, Accuracy of in situ sea surface temperatures used to calibrate infrared satellite measurements, *J. Geophys. Res.*, **106**, 2387-2405, 2001.

Easterling, D. R., J. L. Evans, P. Ya. Groisman, T. R. Karl, K. E. Kunkel & P. Ambenje, Observed variability and trends in extreme climatic events: a brief review, *Bull. Am. Met. Soc.*, **81**, 417-425, 2000.

Fairall, C. W., E. F. Bradley, D. P. Rogers, J. B. Edson & G. S. Young, Bulk parameterisation of air-sea fluxes for TOGA COARE, *J. Geophys. Res.*, **101**, 3747-3764, 1996a.

Fairall, C. W., E. F. Bradley, J. S. Godfrey, G. A. Wick, J. B. Edson & G. S. Young, Cool-skin and warm-layer effects on SST, *J. Geophys. Res.*, **101**, 1295-1308, 1996b.

Fairall, C. W., E. F. Bradley, Hare, J. E., Grachev, A. A. & J. B. Edson, Bulk parameterisation of air-sea fluxes: updates and verification for the COARE algorithm, *J. Climate*, **16**, 571-591, 2003.

Fischer, A. S., R. A. Weller, D. L. Rudnick, C. C. Erikson, C. M. Lee, K. H. Brink, C. A. Fox and R. R. Leben, Mesoscale eddies, coastal upwelling and the upper ocean heat budget in the Arabian Sea, *Deep Sea Research II*, **49**, 2231-2264, 2003.

Flament, P., J. Firing, M. Sawyer, and C. Trefois, Amplitude and horizontal structure of a large sea surface warming event during the Coastal Ocean Dynamics Experiment, *J. Phys. Oceanog*, **24**, 124-139, 1994.

Folland, C. K. & D. E. Parker, Correction of instrumental biases in historical sea surface temperature data, *Quart. J. Roy. Met. Soc.*, **121**, 319-167, 1995.

Gentemann, C. L., C. J. Donlon, A. C. Stuart-Menteth & F. J. Wentz, Diurnal signals in satellite sea surface temperature measurements, *Geophys. Res. Lett.*, **30**(3), 1140, doi:10.1029/2002GL016291, 2003.

Halpern, D. & R. K. Reed, Heat budget of the upper ocean under light winds, J. Phys. Oceanog., **6**, 972-975, 1976.

Hawkins, J. D., R. M. Clancy & J. F. Price, Use of AVHRR data to verify a system for forecasting diurnal variations of SST, *Int. J. Rem. Sens.*, **14**, 1347-1357, 1993.

Henderson-Sellers, A. & P. J. Robinson, Contemporary Climatology, Harlow, Longman, pp439, 1983.

Horrocks, L. A., A. Harris, R. Saunders, Modelling the diurnal thermocline for daytime bulk SST from the Advanced Along Track Scanning Radiometer, Met. Office Forecasting Research Technical Report No. 418, UK Met. Office, 2003a.

Horrocks, L. A., B. Candy, T. J. Nightingale, R. W. Saunders, A. O'Carroll & A. R. Harris, Parameterisations of the ocean skin effect and implications for satellite-based measurement of sea surface temperature, *J. Geophys. Res.*, **108**(3), 3096, doi:10.1029/2002JC001503, 2003b.

Houghton, J. T. et al., (Eds), *Climate Change 2001*, Intergovernmental Panel on Climate Change 2001, Cambridge University Press, New York, 2001.

Hurrell, J. W. & K. E. Trenberth, Global SST analyses – problems and implications for climate, *Bull. Am. Met. Soc.*, **80**, 2661-2677, 1999.

Inness, P. M. & J. M. Slingo, Simulation of Madden-Julian Oscillation in a general circulation model. Part 1: Comparison with observations and an atmosphere –only GCM, *J. Climate*, **16**, 345-364, 2003.

Ivanoff, A., *Ocean absorption of solar energy*, Chapter 5 Modelling and prediction of upper layers of the ocean (Kraus), Pergamon Press, 325pp, 1977.

Jerlov, N. G., *Optical Oceanography*, Elsevier, 194pp, 1968.

Jones, M. S., M. A. Saunders & T. H. Guymer, Reducing cloud contamination in ATSR averaged SST data, *J. Atmos. Oceanic Technol.*, **13**, 492-506, 1996.

Jones, P. D., T. M. Wigley & P. B. Wright, Global temperature variations between 1861-1984, *Nature*, **322**, 430-434, 1986.

Josey, S. A., E. C. Kent & P. K. Taylor, The Southampton Oceanography Centre (SOC) Ocean-Atmosphere Heat, Momentum and Freshwater Flux Atlas, Southampton Oceanography Centre Rep., 6, Southampton, U.K., 30pp + figures, 1998.

Kaiser, A. J. C, Heat balance in the upper ocean under light winds, *J. Phys. Oceanog.*, **8**, 1-12, 1978.

Kantha, L. H. & C. A. Clayson, An improved mixed layer model for geophysical applications, *J. Geophys. Res.*, **99**, 25235-25266, 1994.

Katsaros, K. B., A. Fiuza, F. Sousa & V. Amann, Surface temperature patterns and air-sea fluxes in the German Bight during MARSEN 1979, Phase 1, *J. Geophys. Res.*, **88**, 9871-9882, 1983.

Katsaros, K. B. & A. Soloviev, Vanishing horizontal sea surface temperature gradients at low wind speeds, *Bound. Layer Meteor.*, in press, 2004.

Katsaros, K. B., A. V. Soloviev, R. E. Weisberg & M. E. Luther, Reduced horizontal sea surface temperature gradients under conditions of clear sky and weak winds, *Bound. Layer Meteor.*, submitted, 2004.

Kawai, Y. & H. Kawamura, Evaluation of the diurnal warming of sea surface temperature using satellite-derived marine meteorological data, *J. Oceanography,* **58**, 805-814, 2002.

Kawai, Y. & H. Kawamura, Validation of daily amplitude of sea surface temperature evaluated with a parametric model using satellite data, *J. Oceanog.*, **59**, 637-644, 2003.

Kearns, E. J., A. Hanafin, R. H. Evans, P. J. Minnett & O. B. Brown, An independent assessment of Pathfinder AVHRR SST accuracy using the Marine Atmosphere Emitted Radiance Interferometer (M-AERI), *Bull. Am. Met. Soc.*, **81**, 1525-1536, 2000.

Kent, E. C., P. K. Taylor, B. S. Truscott & J. S. Hopkins, The accuracy of voluntary observing ships'meteorological observations – results of the VSOP-NA, *J. Atmos. Ocean. Technol.*, **10**, 591-608, 1993.

Kilpatrick, K. A., G. P. Podesta & R. Evans, Overview of NOAA/NASA AVHRR Pathfinder algorithm for SST and associated matchup database, *J. Geophys. Res,* 106, 9179-9197, 2001.

Kinkade, C. S., J. Marra, T. D. Dickey, C. Langdon, D. E. Sigurdson & R. A. Weller, Diel bio-optical variability observed from moored sensors in the Arabian Sea, *Deep Sea Research II*, **46**, 1813-1831, 1999.

Kondo, J., Y. Sasano & T. Ishii, On wind-driven current and temperature profiles with diurnal period in oceanic planetary boundary layer, *J. Phys. Oceanog.*, **9**, 360-372, 1979.

Kudryavtsev, V. N. & A. V. Soloviev, Slippery near-surafce layer of the ocean arising due to daytime solar heating, *J. Phys. Oceanog.*, **20**, 617-628, 1990.

Large, W., J. McWilliams & S. Donney, Oceanic vertical mixing: a review and a model with non-local boundary layer parameterization, *Review of Geophysics*, **32**, 363-403, 1994.

Lewis, M. R., M.-E. Carr, G. C. Feldmann, W. Esaias & C. McClain, Influence of penetrating solar radiation on the heat budget of the equatorial Pacific Ocean, *Nature*, **347**, 543-545, 1991.

Liou, K-N, Solar radiation at the top of the atmosphere, in An Introduction to Atmospheric Radiation, 26, 45-48, Academic Press, Inc., New York, 1980.

Liu, T., K. B. Katsaros & J. A. Businger, Bulk parameterisation of air-sea exchanges of heat and water vapour including the molecular constraints at the interface, *J. Atmos. Sciences*, **36**, 1722-1735, 1979.

Luterbacher, J., D. Dietrich, E. Xoplaki, M. Grosjean & H. Wanner, European seasonal and annual temperature variability, trends and extremes since 1500, *Science*, **303**, 1499-1503, 2004.

McCreary, J. P., K. E. Kohler, R. R. Hood, S. Smith, J. Kindle, A. S. Fischer & R. A. Weller, Influences of diurnal and intraseasonal forcing on mixed-layer and biological variability in the central Arabian Sea, *J. Geophys. Res.*, **106**, 7139-7155, 2001.

McNeil, C. L. & L. Merlivat, The warm oceanic surface layer: implications for CO_2 fluxes and surface gas measurements, *Geophys. Res. Lett.*, **23**, 3575-3578, 1996.

Mellor, G. & T. Yamada, Development of a turbulent closure model for geophysical fluid problems, *Rev. Geophys. & Space Phys.*, **20**, 851-875, 1982.

Merchant, C. J., A. R. Harris, M. J. Murray & A. M. Zavody, Toward the elimination of bias in satellite retrievals of sea surface temperature. 1. Theory, modelling and interalgorithm comparison, *J. Geophys. Res.*, **104**, 23565-23578, 1999.

Minnett, P. J., The regional optimisation of infrared measurements of SST from space, *J. Geophys. Res.*, **95**, 13497-13510, 1990.

Morel, A., Optical modelling of the upper ocean in relation to its biogenous matter content (case 1 waters), *J. Geophys. Res.*, **93**, 10749-10768, 1988.

Morel, A. & D. Antoine, Heating rate within the upper ocean in relation to its bio optical state. *J. Phys. Oceanog.*, **24**, 1652-1665, 1994.

Murtugudde, R., J. Beauchamp & A. Busalacchi, Effects of penetrative radiation on the upper tropical ocean circulation, *J. Climate*, **15**, 470-486, 2002.

Nakamoto, S. S. Prasanna Kumar, J. M. Oberhuber, K. Muneyama & R. Frouin., Chlorophyll modulation of sea surface temperature in the Arabian Sea in a mixed-layer isopycnal model. *Geophys. Res. Letters*, **105**, 3295-3306, 2000.

Nakamoto, S., S. Prasanna Kumar, J. M. Oberhuber, J. Ishizaka, K. Muneyama & R. Frouin, Response of the equatorial Pacific to chlorophyll pigment in a mixed layer isopycnal ocean general circulation model, *Geophys. Res. Letters*, **28**, 2021-2024, 2001.

Ohlmann, J. C., D. A. Siegel & C. Gaitier, Ocean mixed layer radiant heating and solar penetration: a global analysis, *J. Climate*, **9**, 2265-2280, 1996.

Ohlmann, J. C., D. A. Siegel & L. Washburn, Radiant heating of the western equatorial Pacific during TOGA-COARE, *J. Geophys. Res.*, **103**, 5379-5395, 1998.

Ohlmann, J. C., D. A. Siegel & C. D. Mobley, Ocean radiant heating:1. Optical influences, J. Phys. Oceanog., **30**, 1833-1848, 2000.

Ohlmann, J. C. & D. A. Siegel, Ocean Radiant Heating. Part II: Parameterising solar radiation transmission through the upper ocean. *J. Phys. Oceanog.*, **30**, 1849-1865, 2000.

Ostapoff, F., & S. Worthem, The intra-diurnal temperature variation in the upper ocean, *J. Phys. Oceanog.*, **4**, 601-612, 1974.

Pascal, R. W., S. A. Josey, D. Berry, A. Stuart-Menteth, RRS Charles Darwin Cruise CD135 Report, *Southampton Oceanography Centre Cruise Report*, No. **39**, 78pp, 2002.

Paulson, C. A. & J. J. Simpson, Irradiance measurements in the upper ocean, *J. Phys. Oceanog.*, **7**, 953-956, 1977.

Paulson, C. A. & J. J. Simpson, The temperature difference across the cool skin of the ocean, *J. Geophys. Res.*, **86**, 11044-11054, 1981.

Price, J. F., C. N. K. Mooers & J. C. Van Leer, Observations and storm induced mixed layer deepening, *J. Phys. Oceanog.*, **8**, 582-599, 1978.

Price, J. F., Observations of a rain-formed mixed layer, *J. Phys. Oceanog.*, **9**, 643-649, 1979.

Price, J. F., R. A. Weller & R. Pinkel, Diurnal cycling: Observations and models of the upper ocean response to diurnal heating, cooling and wind mixing, *J. Geophys. Res.*, **91**, 8411-8427, 1986.

Price, J. F., R. A. Weller, C. M. Boewrs & M. G. Briscoe, Diurnal response of SST observed at the long term upper ocean study (34N, 70W) in the Sargasso Sea, *J. Geophys. Res.*, **92**, 14,480-14,490, 1987.

Pritchard, M. & R. A. Weller, Near sea surface diurnal variability in the western equatorial Pacific Ocean during persistently low wind stress conditions, in preparation, 2004.

Privette, J. L., C. Fowler, G. A. Wick, D. Baldwin & W. J. Emery, Effects of orbital drift on Advanced Very High Resolution Radiometer products: normalised difference vegetation index and sea surface temperature, *Remote Sens. Environ.*, **53**, 164-171, 1995.

Ramp, S. R, R. W. Garwood, C. O. Davis and R. L. Snow, Surface heating and patchiness in the coastal ocean off central California during a wind relaxation event, *J. Geophys. Res.*, **96**, 14947-14957, 1991.

Reynolds, R. W. & T. M. Smith, Improved global sea surface temperature analyses using optimum interpolation, *J. Climate*, **7**, 929-948, 1994.

Reynolds, R. W., Specific contributions to the observing system: sea surface temperatures. *Proceedings of Ocean Obs. 1999*, 1999.

Robertson, J. E. & A. J. Watson, Thermal skin effect of the surface ocean and its implications for CO_2 uptake, *Nature*, **358**, 738-740, 1993.

Robinson, I. S. & C. J. Donlon, Global measurement of sea surface temperature from space: some new perspectives, *The Global Atmos. Ocean System*, **9**, 19-37, 2003.

Sathyendranath, S., A. D. Gouvela, S. R. Shetya, P. Ravindran & T. Platt, Biological control of surface temperature in the Arabian Sea. *Nature*, **349**, 54-56, 1991.

Saunders, P. M., The temperature at the ocean-air interface. *J. Atmos. Sciences,* **24**, 269-273, 1967.

Shinoda, T. & H. H. Hendon, Mixed Layer Modelling of Intraseasonal Variability in the Tropical Western Pacific and Indian Oceans, *J. Climate*, **11**, 2668-2685, 1998.

Shonting, D. H., Some observations of short-term heat transfer from the surface layers of the ocean, *Limnol. Oceanogr.*, **9**, 576-588, 1964.

Siegel, D. A. & T. D. Dickey, On the parameterisation of irradiance for open ocean photoprocesses, *J. Geophys. Res.*, **92**, 14648-14662, 1987.

Siegel, D. A., J. C. Ohlmann, L. Washburn, R. Bidigare, C. Nosse, E. Fields and Y. Zhou, Solar radiation, phytoplankton pigments and radiant heating of the equatorial Pacific warm pool, *J. Geophys. Res.*, **100**, 4485-4491, 1995.

Simpson, J. J. & T. D. Dickey, The relationship between downward irradiance and upper ocean structure, *J. Phys. Oceanog.*, **11**, 309-323, 1981.

Soloviev, A., On the vertical structure of the thin surface layer of the ocean during a weak wind, *Izv. Atmos. Oceanic Phys.*, **18**, 579-585, 1982.

Soloviev, A. & P. Schlussel, Evolution of cool skin and direct air-sea gas transfer coefficients during daytime, *Bound., Layer Meteor.*, **77**, 45-68, 1996.

Soloviev, A. & R. Lukas, Observation of large diurnal warming events in the near surface layer of the western equatorial warm pool, *Deep Sea Res.*, **44**, 1055-1076, 1997.

Stammer, D., F. Wentz & C. Gentemann, Validation of microwave SST measurements for climate purposes, *J. Climate*, **16**, 73-87, 2003.

Stommel, H., Observations of the diurnal thermocline, *Deep Sea Res.*, **16** (suppl), 269-284, 1969.

Stramma, L., P. Cornillon, R. A. Weller, J. F. Price & M. G. Briscoe, Large diurnal sea surface temperature variability: satellite and in situ measurements, *J Phys. Oceanogr.*, **56**, 345-358, 1986.

Stramska, M. & T. Dickey, Phytoplankton bloom and the vertical thermal structure of the upper ocean. *J. Marine Research*, **51**, 819-842, 1993.

Stuart-Menteth, A. C., I. S. Robinson & P. G. Challenor, A global study of diurnal warming using satellite derived sea surface temperature, *J. Geophys. Res.*, **108**(5), 3155, doi:10.1029/2002JC001534, 2003.

Takahashi, T., J. Olafsson, J. G. Goddard, D. W. Chipma & S. C. Sutherland, Seasonal variations of CO_2 and nutrients in the high latitude surface oceans: a comparative study, *Global Biogeochem. Cycles*, **7**, 843-878, 1993.

Tanahashi, S., H. Kawamura, T. Takahashi, and H. Yusa, Diurnal variations of sea surface temperature over the wide-ranging ocean using VISSR on board GMS, *J.Geophys. Res.*, 108(7), doi:1029/2002JC001313, 2003.

Walton, C. C., W. G. Pichel, J. F. Sapper & D. A. May, The development and operational application of nonlinear algorithms for the measurement of sea surface temperatures with the NOAA polar-orbiting environmental satellites, *J. Geophys. Res.*, **103**, 27999-28012, 1998.

Ward, B., R. Wanninkhof, P. J. Minnett, M. J. Head, SkinDeEP: A profiling instrument for upper decametre sea surface measurements, *J. Atmos. Oc. Technol.*, **21**, 207-222, 2004.

Webster, P. & R. Lukas, TOGA COARE: The Coupled Ocean-Atmosphere Response Experiment, *Bull. Am. Met. Soc.*, **73**, 1377-1416, 1992.

Webster, P. J., C. A. Clayson & J. A. Curry, Clouds, radiation and the diurnal cycle of SST in the tropical western Pacific, *J. Clim.*, **9**, 1712-1730, 1996.

Weller, R., A., M. F. Baumgartner, S. A. Josey, A. S. Fischer & J. C. Kindle, Atmospheric forcing in the Arabian Sea during 1994-1995: observations and comparisons with climatology and models, *Deep Sea Research II*, **45**, 1961-1999, 1998.

Wentz, F. J., A well-calibrated ocean algorithm for SSM/I, *J. Geophys. Res.*, **102**, 8703-8718, 1997.

Wick, G. A., W. J. Emery, L. H. Kantha and P. Schlussel, The behaviour of the bulk-skin sea surface temperature difference under varying wind speed and heat flux, *J Phys. Oceanog.*, **26**, 1969-1988, 1996.

Wick. G. A., J. C. Ohlmann, C. W. Fairall & A. T. Jessup, Improved oceanic cool skin corrections using a refined solar penetration model, in preparation, 2004.

Woodcock, A. H., Surface cooling and streaming in shallow fresh and salt waters, *J. Marine Res.*, **4**, 153-161, 1941.

Woolnough, S. J., J. M. Slingo & B. J. Hoskins, The organisation of tropical convection by intraseasonal sea surface temperature anomalies, *Quart. J. Roy. Meteor. Soc.*, **127**, 887-907, 2001.

Wu, X., W. P. Menzel & G. S. Wade, Estimation of sea surface temperatures using GOES-8/9 radiance measurements, *Bull. Am. Meteor. Soc.*, **80**, 1127-1138, 1999.

Yang, G. & J. Slingo, The diurnal cycle in the tropics, *Monthly Weather Review*, **129**, 784-801, 2001.

Yokoyama, R, S. Tanba & T. Souma, Air-sea interacting effects to the sea surface temperature observation by NOAA/AVHRR, *Int. J. Rem. Sens.*, **14**, 2631-2646, 1993.

Yokoyama, R., S. Tanba & T. Souma, Sea surface effects on the SST estimation by remote sensing, *Int. J. Rem. Sens.*, **16**, 227-238, 1995.

Yokoyama, R. & M. Konda, Sea surface effects on the sea surface temperature estimation by remote sensing – Part 2, *Int. J. Rem. Sens.*, **17**, 1293-1302, 1996.

Zeng, X. & R. E. Dickinson, Impact of diurnally varying skin temperature on surface fluxes over the tropical Pacific, *Geophys., Res., Letters*, **25**, 1411-1414, 1998.

Zeng, X., M. Zhao, R. E. Dickinson & Y. He, A multiyear hourly sea surface skin temperature data set derived from the TOGA TAO bulk temperature and wind speed over the tropical Pacific, *J. Geophys. Res.*, **104**, 1525-1536, 1999.

Zhang, C., Coherence between SST and atmospheric variability in western Pacific warm pool, Preprints, *Eighth Conf. On Air-Sea Interaction and Conf. On the Global Ocean-Atmosphere-Land System (GOALS)*, Atlanta, GA, Amer. Meteo. Soc., J112 J116, 1996.